La collana della Scuola di Alta Formazione Dottorale accoglie le migliori tesi di dottorato dell'Università degli Studi di Bergamo, insignite della dignità di stampa e sottoposte a procedura di *blind peer review*.

This research devises, implements and tests a discontinuous Galerkin (dG) and a Hybridizable Discontinuous Galerkin (HDG) framework for nonlinear elasticity problems featuring large deformations. The dG framework, stabilized with higher-order BR2 lifting operators and an adaptive strategy, encompasses not only compressible but also incompressible hyperelastic materials. The use of Lagrange multipliers for Dirichlet boundary conditions and agglomeration based h-multigrid preconditioners is proposed and the HDG framework is developed to solve problems involving contact constraints. Lagrange multipliers are introduced to enforce either Dirichlet boundary conditions or frictionless contact conditions. Several benchmark test cases are proposed to investigate some relevant computational aspects.

Luca Verzeroli is a mechanical engineer who obtained his PhD in Engineering and applied sciences (34th cycle) at the University of Bergamo. He is interested in numerical analysis and methods: his studies focused on the solution of Partial Differential Equations (PDEs) using conforming and non-conforming Finite Element Methods (FEMs) in the fields of Computational Solid and Fluid Mechanics (CSM and CFD). He also contributed to the development of some modules and routines for open-source libraries (i.e. SpaFEDTe) used not only for academic purposes but also for the solution of real-life problems.

ISBN: 978-88-97413-81-3
DOI: 10.13122/978-88-97413-81-3

Luca Verzeroli NONCONFORMING FINITE ELEMENTS METHODS

59

Collana della Scuola di Alta Formazione Dottorale

- 59 -

Luca Verzeroli

NONCONFORMING FINITE ELEMENTS METHODS FOR NONLINEAR ELASTICITY PROBLEMS

UNIVERSITÀ
DEGLI STUDI
DI BERGAMO

2023

Collana della Scuola di Alta Formazione Dottorale

- 59 -

Collana della Scuola di Alta Formazione Dottorale

Diretta da Paolo Cesaretti

Ogni volume è sottoposto a *blind peer review*.

ISSN: 2611-9927

Sito web: https://aisberg.unibg.it/handle/10446/130100

Luca Verzeroli

NONCONFORMING FINITE ELEMENTS METHODS FOR NONLINEAR ELASTICITY PROBLEMS
Featuring Finite Deformations and Frictionless Contact Constraints

Università degli Studi di Bergamo

2023

Nonconforming Finite Elements Methods for Nonlinear
Elasticity Problems Featuring Finite Deformations
and Frictionless Contact Constraints / Luca Verzeroli. – Bergamo :
Università degli Studi di Bergamo, 2023.
(Collana della Scuola di Alta Formazione Dottorale; 59)

ISBN: 978-88-97413-81-3
DOI: 10.13122/978-88-97413-81-3

Progetto grafico: Servizi Editoriali – Università degli Studi di Bergamo

via Salvecchio, 19
24129 Bergamo
Cod. Fiscale 80004350163
P. IVA 01612800167

https://aisberg.unibg.it/handle/10446/258489

Acknowledgements

I would like to express my deep and sincere gratitude to my supervisor, prof. Lorenzo Botti, that inspired me during the entire PhD program with his passion for the scientific research. Together, we acknowledge Serioplast (www.serioplast.com) for the idea of starting this challenging research project and for the financial support. I am also grateful to Paolo Innocenti and Massimo Rosati for supervising this work with interest and contagious enthusiasm.

"Happiness can be found,

even in the darkest of times,

if one only remembers

to turn on the light."
A. P. W. B. Dumbledore

To my family and Celia

Table of Contents

Chapter 1. Introduction

1.1 Motivation

Extrusion Blow Moulding (EBM) and Stretch Blow Moulding (SBM) are two of the main manufacturing processes involved in the production of rigid plastic packages for the home care, personal hygiene, food&beverage and automotive markets. EBM and SBM consist in deforming and blowing a hot plastic material of standardized shape until contact with a mould is reached, hence providing the final desired shape. As shown in Fig. 1, EBM and SBM can be distinguished according to the type and the shape of the polymers introduced in the blowing machine.

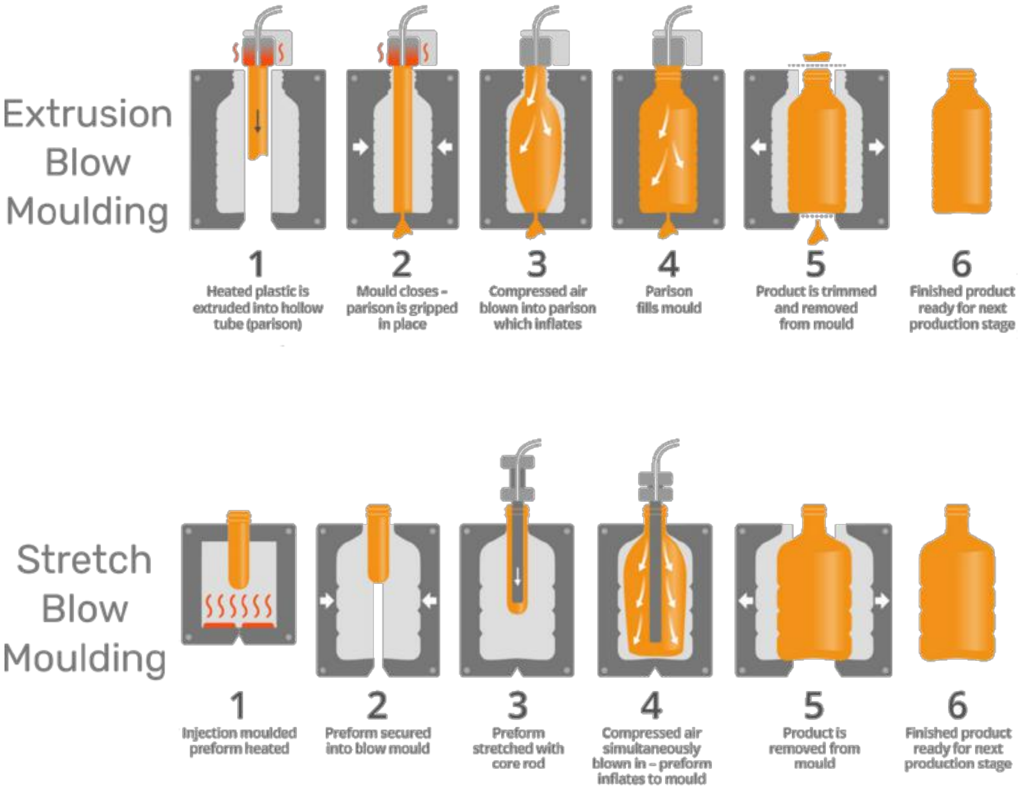

Figure 1: The sequence of steps involved in EBM and SBM manufacturing processes.

In EBM, the polymeric raw material (usually HDPE or PP), additives and pigments are mixed, melted and extruded through a die in the shape of a parison (a tube-like piece of plastic). On the other hand, SBM normally employs PET preforms, intermediate injection-moulded products with a fully formed bottle/jar neck and a thick tube attached. Preforms are heated in an oven and then stretched with a rod while the pressurized air is insufflated.

Before starting the mass production of new plastic containers, several process parameters have to be adjusted: e.g. polymer temperature, parison thickness, blowing time, cooling time, mould features. Since also polymer properties and weather conditions might influence the final result, no general recipes exist. The task of finding the optimal setting requires experienced operators and a trial and error approach. The process parameters have a crucial influence on the quality of packages which is asserted by means of extensive testing having the goal to evaluate the tightness ("leak test"), the resistance to axial load ("top load") and impacts ("drop test"). Clearly, package sturdiness is also affected by the material distribution and walls thickness: a uniform material distribution may avoid defects and weaker areas while uneven material distribution may increases weight and cost without benefits in terms of resistance.

Computational modelling is one of the possible approaches for investigating EBM and SBM with the goal to improve efficiency of the overall process. Improvements in terms of machine design and setting and cycle time are expected and reduction of wastes as well as decrease in the number of laboratory samples are envisaged. We mention three use-case scenarios:

- **R&D decision-making process**: once the final shape of a bottle-like product is identified, the R&D team has to set up the production process. The common approach, currently in use, consists of engineering the machinery components (*e.g.* the mould) according to past experience. This leads to a trial and error procedure made of mould prototypes and continuous adjustments. On the other hand, blow moulding simulation may help engineers to test different setups by means of a virtual reality approach.

- **Search for parameters setting**: an accurate simulation of blow moulding may be a tool that accelerates the definition of those process parameters that are essential to obtain a final product featuring all the desired mechanical properties. For example, technicians may investigate the final material distribution and bottle thickness by varying the input parameters of numerical simulations.

- **Mechanical simulations**: the outputs of blow moulding simulations may be employed to verify the quality of the final product without implementing the entire process. By means of the numerical counterpart of the aforementioned tests, engineers may investigate the mechanical properties in order to examine the feasibility of the entire project.

This work aims to evaluate if nonconforming Finite Element Methods are able to handle the crucial challenges involved in blow moulding simulations such as nonlinear constitutive laws in the finite deformation regime, incompressibility of materials and contact boundary conditions. Further developments are required to validate the accuracy of the results in real-life computations and to make the simulation tools usable in the engineering practice. The present work is to be considered as a promising starting point towards this ambitious goal.

1.2 Structure of the work

The work is organized as follows:

- **Chapter 6** introduces some basic notions of continuum mechanics that will serve as foundations of the computational modelling approaches devised in the following chapters. The kinematical description of all admissible body motions as well as volume and area transformations are presented for introducing the Lagrangian formulation of the basic mechanical principles of mass and linear momentum conservation. A constitutive relation between the stress and the strain has to be provided in order to close the elasticity problem. Thus, restricting our attention to hyperelasticity, constitutive laws are deduced from the definition of a strain energy function such that the expressions for the Piola stress tensors and the fourth-order elasticity tensors are derived for Saint Venant-Kirchhoff and neo-Hookean material models.

- **Chapter 3** reviews the methodological steps leading to the discretized versions of the continuous elasticity problem for hyperelastic materials. The problem of finding the numerical solution is formulated as the minimization of an energy functional encompassing both the internal energy contribution and the work of external forces. As a result, the static equilibrium of hyperelastic bodies undergoing large deformation is found by seeking the solution that zeros the directional derivatives of the energy functional. Optionally, the energy functional might be constrained by enforcing the incompressibility of the material, thereby enabling the description of isochoric motions. Lagrange multipliers are introduced in the formulation with the aim of imposing Dirichlet and contact boundary conditions. Three state-of-the-art nonconforming finite element formulations are considered as discrete counterparts of the weak forms: a new BR2 dG formulation, the HDG formulation proposed by Kabaria [1] and the HHO scheme devised by Abbas *et al.* [2]. The schemes are obtained by inserting in the local residuals of the Lagrangian equation of motion the reconstructed gradient operator for the discretization at hand, and possibly coupling with the incompressibility and Lagrange multipliers constraints. The resulting nonlinear system of equations is solved by means of an incremental load method, and each substep is equipped with the classical Newton method. Accordingly, the final deformed solution is reached through a sequence of intermediate equilibrium configurations. To complete the schemes formulation, Jacobian operators are derived.

- **Chapter 4** presents the numerical validation of the BR2 dG formulation for finite hyperelastic deformations. First of all, the numerical convergence rates is verified for each hyperelastic constitutive law challenging 3D manufactured solutions either in the compressible or incompressible regime. Then, 2D and 3D test cases are performed in order to analyse the behaviour of the formulation in presence of severe mesh distortions. Moreover, we investigate how the adaptive stabilization strategy influences the number of iterations of an agglomeration based h-multigrid preconditioned GMRES solver. The use of Lagrange Multiplier for applying Dirichlet boundary conditions allows to strongly reduce the number of steps required by the incremental method to reach the final solution.

- **Chapter 5** reports a brief numerical validation of HDG and HHO implementations for finite hyperelastic deformation in the compressible regime. 2D and 3D manufactured solutions are tested and the convergence rates are evaluated and tabulated.

- **Chapter 6** aims to provide the basic concepts for the description of the contact between bodies undergoing large deformations. In particular, we concentrate on the simulation of the frictionless contact between a rigid obstacle and a deformable body. The previously introduced energy functionals are modified by adding the work of Lagrange multipliers on the contact surfaces identified by means of an active set strategy. Once the weak form of the static equilibrium is obtained, the HDG formulation of the elasticity problems with frictionless contact is proposed. To conclude, the active set strategy for finding and following the contact areas between a deformable hyperelastic body and a obstacle boundary surface is presented in details.

- **Chapter 7** reports the numerical validation of the HDG formulation for hyperelastic deformations and frictionless contact. The analytical descriptions of some obstacle surfaces are introduced such that all geometrical functions, required by the linearization procedure, are derived. Consequently, two and three dimensional nonlinear elasticity problems featuring frictionless contact with the rigid obstacles are solved demonstrating the effectiveness of the active set strategy proposed in the previous chapter.

- **Chapter 8** collects the final remarks and proposes some future developments.

1.3 Progress beyond the state of the art

The dG framework for finite deformations of elastic solids based on a Bassi-Rebay (BR2) formulation is the main novelty of the present work. The framework relies on the following ingredients: 1. BR2 dG discretization of the Lagrangian equation of motion for hyperelastic materials; 2. BR2 dG discretization of the incompressibility constraint in Lagrangian formulation; 3. implementation of the Lagrange multipliers method for the imposition of Dirichlet boundary conditions; 4. adaptive stabilization strategy based on the spectrum of the fourth-order elasticity tensor; 5. agglomeration based h-multigrid solution strategy for the fully coupled formulation. We remark that the first, third and fifth aforementioned ingredients are novel contributions.

The attractive features of the proposed dG framework are: 1. ability of dealing with compressible and incompressible hyperelastic materials; 2. comparing with BR1 formulations, BR2 dG discretizations reduce the computational cost thanks to a more compact stencil; 3. higher-order lifting operators for the BR2 stabilization term allow to get rid of non-local stabilization parameters based on the number of faces; 4. Lagrange multipliers method for imposing Dirichlet boundary conditions reduces the number of incremental steps required by the globalization strategy by orders of magnitude, moreover the number of incremental steps is insensitive to mesh density and polynomial degree; 5. thanks to the adaptive stabilization strategy, stability is guaranteed in a broad range of test case configurations; 6. the performance of the state-of-the-art agglomeration based h-multigrid solution strategy is insensitive to the user-dependent stabilization parameters appearing in the adaptive stabilization technique.

Among the aforementioned features the imposition of Dirichlet boundary conditions by means of Lagrange multipliers deserves additional remarks. In this work we show that additional stabilization terms based on the jumps of the Lagrange multipliers on the edges of the boundary mesh are required to achieve stability. The stabilization needs to be carefully introduced avoiding the *sharp corners* of the boundary mesh, that is the edges where the surface normal happens to be discontinuous, see Chap. 3 for additional details. This observation is also the main motivation for relying on a HDG framework for dealing with computational contact mechanics. Indeed, since the sharp corners evolve during the computation, a formulation which does not require Lagrange multipliers stabilization is highly beneficial in practice.

The HDG framework for finite deformations of elastic solids featuring contact constraints is the second main novelty of the present work. The attractive features of the proposed HDG framework are: 1. ability of dealing with compressible and quasi-incompressible Saint Venant-Kirchhoff and neo-Hookean hyperelastic materials; 2. implementation of the Lagrange multipliers method for the imposition of Dirichlet boundary conditions; 3. ability of dealing with non-penetration frictionless contact constraints by means of Lagrange multipliers method; 4. as opposite to dG discretization, imposition of boundary conditions by means of Lagrange multipliers does not require additional stabilization.

Chapter 2. Fundamentals of Continuum Mechanics

This chapter introduces basic concepts of continuum mechanics that are the foundations of the computational modelling approaches devised in this work. Many authors inspired this brief introduction: among them, we appreciate the manuscripts of Odgen [3], Ciarlet [4] and Gurtin *et al.* [5] and Tadmor *et al.* [6].

Kinematics plays a crucial role in the Lagrangian formulation of the elasticity problem. The mathematical tools that allow to describe all geometrically admissible body motions are presented in Sec. 2.1: the mapping between a reference and a deformed configuration is delineated in Sec. 2.1.1, how volume and area transform during the deformation in Sec. 2.1.2 and the measures of strain in Sec. 2.1.3. The *basic mechanical principles* governing body motions, at the reference and at the deformed configuration, are derived in Sec. 2.2: the continuity equation is stated in Sec. 2.2.1 while the conservation of linear momentum in Sec. 2.2.2. The relation between the stress and the strain represents a key point in the description of the behavior of a body undergoing deformation. In this work, we consider only the *hyperelastic* materials described in Sec. 2.3. Hyperelastic constitutive laws are deduced from the definition of a strain energy function, see Sec. 2.3.1, from which the expressions for the Piola-Kirchhoff stress tensor are derived, see Sec. 2.3.2. Finally, in Sec. 2.3.3, the concept of the fourth-order elasticity tensor is introduced and it will be useful in the context of the linearization of the nonlinear elasticity problem in Chap. 3.

2.1 Kinematics

Kinematics is one of the branch of physics that describes body motion (or system of bodies) forgetting the causes and effects induced by external forces. The description of a body undergoing finite deformations may rely on two alternative ways of representing the relevant physical properties leading to the so called Eulerian (or spatial) and Lagrangian (or material) descriptions. The former one renders the system behavior at a spatial position, whereas the latter follows the behavior of a material particle. Differently from fluid mechanics that is almost exclusively based on spatial descriptions, solid mechanics relies often on the material description in order to develop constitutive laws and describe physical properties of material particles. For this reason, hereinafter, we will introduce the mathematical tools and transformations useful to formulate the elasticity problem from a Lagrangian point of view.

2.1.1 Body Motions

A body may be identified as the closed region $\Omega \in \mathbb{R}^d$ of the Euclidean space of dimension $d \in 2, 3$. When it occupies a fixed arbitrary reference configuration, we may refers to Ω as the **reference body**.

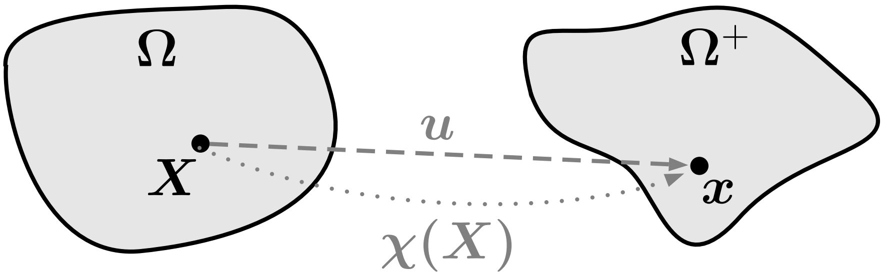

Figure 2: The mapping of the reference body Ω into its deformed configuration Ω^+.

Relying on the Fig. 2, the body Ω consists of a set of **material points** (or particles) labelled with the coordinates $\boldsymbol{X} = \{X_i,\ i \in 1, \ldots, d\}$. The **motion** of the body relocates each material point in a new place in the space, namely the **spatial point** $\boldsymbol{x} = \{x_i,\ i \in 1, \ldots, d\}$. The motion can be mathematically described with a sufficiently smooth function $\mathcal{X} : \Omega \times \mathbb{R}_{\geq 0} \rightarrow \mathbb{R}^d$ dependent on $\boldsymbol{X}$ and the time t

$$\boldsymbol{x} = \mathcal{X}(\boldsymbol{X}, t).$$

Restricting the attention to a certain instant of time $\bar{t}$, the function $\mathcal{X}(\boldsymbol{X}, \bar{t})$ indicates the **deformation** of the body. Obviously, the *reference* configuration is recovered setting $\bar{t} = 0$, so, $\mathcal{X}(\boldsymbol{X}, 0) = \boldsymbol{X}$, otherwise, the *deformed* (or *current*) configuration at time $\bar{t}$ is retrieve as $\Omega^+ := \{\mathcal{X}(\boldsymbol{X}, \bar{t}), \boldsymbol{X} \in \Omega, \bar{t} \in \mathbb{R}_{>0}\}$.

A basic assumption in continuum mechanics is that $\mathcal{X}$ has to be an injective function, namely a one-to-one mapping. The consequence is that two distinct material points never collapse into one or, in other words, they can not occupy the same position in the space, so, the body does not penetrate itself. This also implies that $\mathcal{X}$ is invertible so that

$$\boldsymbol{X} = \mathcal{X}^{-1}(\boldsymbol{x}, t)$$

is a mapping of the deformed body Ω^+ onto the reference body Ω.

REMARK. We try to use capital letters only for the quantities defined on the reference configuration. If it is not possible, we distinguish quantities of the deformed configuration adding the apex “+”.

Introducing the gradient operator in the reference configuration

$$\nabla_{\boldsymbol{X}}(\bullet) = \frac{\partial(\bullet)}{\partial \boldsymbol{X}}, \quad \nabla_{\boldsymbol{X}}(\bullet)_j = \frac{\partial(\bullet)}{\partial X_j},$$

the tensor field $\boldsymbol{F} : \Omega \times \mathbb{R}_{\geq 0} \rightarrow \mathbb{R}^{d\times d}$

$$\boldsymbol{F} \coloneqq \boldsymbol{F}(\boldsymbol{X}, t) = \nabla_{\boldsymbol{X}} \mathcal{X} = \nabla_{\boldsymbol{X}} \boldsymbol{x}, \quad F_{ij} = \frac{\partial \mathcal{X}_i}{\partial X_j} = \frac{\partial x_i}{\partial X_j}$$

is referred to as the **deformation gradient**. In order to explain the meaning of $\boldsymbol{F}$, we consider two distinct points $\boldsymbol{X}, \boldsymbol{Y} \in \Omega$ that are mapped in $\boldsymbol{x}, \boldsymbol{y} \in \Omega^+$. The difference $\boldsymbol{y} - \boldsymbol{x}$ may be expressed through a first-order Taylor expansion as

$$\boldsymbol{y} - \boldsymbol{x} = \mathcal{X}(\boldsymbol{Y}, t) - \mathcal{X}(\boldsymbol{X}, t) = \frac{\partial \mathcal{X}(\boldsymbol{X})}{\partial \boldsymbol{X}}(\boldsymbol{Y} - \boldsymbol{X}) + o(|\boldsymbol{Y} - \boldsymbol{X}|) \tag{2.1}$$

Taking $(\boldsymbol{Y} - \boldsymbol{X}) \rightarrow 0$, we obtain the expression

$$d\boldsymbol{x} = \boldsymbol{F}(\boldsymbol{X}, t) d\boldsymbol{X} \tag{2.2}$$

which gives an asymptotic meaning to the previous Eq. (2.1). So, as shown in Eq. (2.2), $\boldsymbol{F}$ depicts how the neighbourhood of a material point is changing during the deformation; consequently, it plays a crucial role in the formulation of the strain tensors (see Sec. 2.1.3).

The basic hypothesis of continuum mechanics is stated requiring that

$$J(\boldsymbol{X}, t) \coloneqq \det\left(\nabla_{\boldsymbol{X}} \mathcal{X}\right) = \det \boldsymbol{F} > 0$$

where $J : \Omega \times \mathbb{R}_{\geq 0} \rightarrow \mathbb{R}_{>0}$ is the *volumetric Jacobian* of the mapping $\mathcal{X}$ at the material point $\boldsymbol{X}$ and time t. Accordingly, if $J = 0$, $\mathcal{X}$ maps a volume into a surface or into a point and if $J < 0$, $\mathcal{X}$ represents a body with negative volume. As previously stated, the latter configurations are not physically acceptable.

An alternative way to describe the motion of a body is reported in Fig. 2: it consists of using the *displacement*, namely the mapping function $\boldsymbol{u} : \Omega \times \mathbb{R}_{\geq 0} \rightarrow \mathbb{R}^d$

$$\boldsymbol{u} = \boldsymbol{u}(\boldsymbol{X}, t) = \boldsymbol{x} - \boldsymbol{X} = \mathcal{X} - \boldsymbol{X}.$$

Accordingly, the deformation gradient can be re-written as

$$\boldsymbol{F} = \boldsymbol{F}(\boldsymbol{u}) = \nabla_{\boldsymbol{X}} \mathcal{X} = \nabla_{\boldsymbol{X}}(\boldsymbol{u} + \boldsymbol{X}) = \nabla_{\boldsymbol{X}} \boldsymbol{u} + \mathbf{1}$$

where $\mathbf{1}$ is the identity second-order tensor (*i.e.* $\mathbf{1}_{ij} = \delta_{ij}$, where δ_{ij} is the Kronecker delta and $\mathbf{1}\boldsymbol{v} = \boldsymbol{v}$). The two different mapping functions, $\mathcal{X}$ and $\boldsymbol{u}$, have the same role in the sense that both unknowns can be employed to formulate the elasticity problem.

2.1.2 Transformation of volume and area

Expressions (2.1) and (2.2) suggest the introduction of the linear transformation

$$\boldsymbol{v}(\boldsymbol{x},t) = \boldsymbol{F}(\boldsymbol{X},t)\,\boldsymbol{V}(\boldsymbol{X}) \tag{2.3}$$

where $\boldsymbol{V}$ denotes a *temporally constant* material vector field and $\boldsymbol{v}$ a spatial vector field, see also [5]. Eq. (2.3) states that the quantity $\boldsymbol{v}$ (*i.e.* the infinitesimal fiber, curves, tangents, planes, bases) is embedded in the deforming body Ω^+. Consequently, $\boldsymbol{v}$ is said to convect with the body and Eq. (2.3) is also mentioned as the **covariant transformation**.

Bearing in mind that the tensor $\boldsymbol{F}$ does not conserve the length and angles between vectors, an orthonormal basis in the reference configuration may not be orthonormal in the deformed configuration. In fact, in a 3D space, while each couple of vectors of a basis lies on a plane that convects with the body, the vector out of the couple is, usually, not perpendicular to that plane. This is the typical behaviour of a normal vector $\boldsymbol{N}$ in a reference configuration (see [5]). Its counterpart $\boldsymbol{n}$ in a deformed configuration is computed introducing the **contravariant** transformation

$$\boldsymbol{n}(\boldsymbol{x},t) = \boldsymbol{F}^{-\intercal}(\boldsymbol{X},t)\,\boldsymbol{N}(\boldsymbol{X}).$$

We remark that the vectors $\boldsymbol{N}$ and $\boldsymbol{n}$ are assumed to be also versors when $\boldsymbol{N}\cdot\boldsymbol{N} = 1$ and $\boldsymbol{n}\cdot\boldsymbol{n} = 1$. For the purpose of introducing the *transformation of volume*, an infinitesimal volume element dV in the material configuration Ω is considered. As depicted in Fig. 3a, dV may be computed as

$$dV = (\ell\boldsymbol{E}_1 \times \ell\boldsymbol{E}_2)\cdot\ell\boldsymbol{E}_3 = \ell^3$$

where ℓ is the infinitesimal length of an edge and $\boldsymbol{E}_i$ is an orthonormal basis defined in Ω.

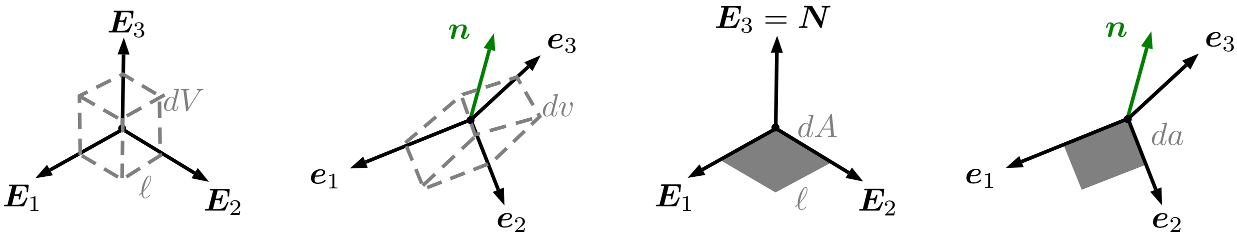

(a) Deformation of volume **(b)** Deformation of area

Figure 3: Deformation of volume and area.

Now, using Eq. (2.3), dV is mapped into the infinitesimal deformed volume element dv

$$dv = \ell^3(\boldsymbol{e}_1 \times \boldsymbol{e}_2)\cdot\boldsymbol{e}_3 = \ell^3(\boldsymbol{F}\boldsymbol{E}_1 \times \boldsymbol{F}\boldsymbol{E}_2)\cdot\boldsymbol{F}\boldsymbol{E}_3$$

in which $\boldsymbol{e}_i$ is an (generally non-orthonormal) basis defined in Ω^+. Using the definition of determinant of a second-order tensor field, we obtain

$$\frac{dv}{dV} = \frac{\cancel{\ell^3}\,(\boldsymbol{F}\boldsymbol{E}_1 \times \boldsymbol{F}\boldsymbol{E}_2) \cdot \boldsymbol{F}\boldsymbol{E}_3}{\cancel{\ell^3}\,(\boldsymbol{E}_1 \times \boldsymbol{E}_2) \cdot \boldsymbol{E}_3} = \det \boldsymbol{F} = J$$

from which we derive the formula for volume transformation

$$dv = J dV. \tag{2.4}$$

Mimicking the steps followed for the volume transformation, consider the basis $\{\boldsymbol{E}_1, \boldsymbol{E}_2, \boldsymbol{E}_3 = \boldsymbol{N}\}$ (with $|\boldsymbol{N}| = 1$) in Ω, as reported in Fig. 3b. The infinitesimal area element dA in Ω is

$$dA = |\ell \boldsymbol{E}_1 \times \ell \boldsymbol{E}_2| = \ell^2 |\boldsymbol{N}| = \ell^2.$$

On the other hand, the infinitesimal deformed area element

$$da = |\ell \boldsymbol{e}_1 \times \ell \boldsymbol{e}_2| = \ell^2 |\boldsymbol{F}\boldsymbol{E}_1 \times \boldsymbol{F}\boldsymbol{E}_2|$$

may be re-written[1]

$$da = \ell^2 J |\boldsymbol{F}^{-\top} \boldsymbol{N}|.$$

Therefore, from the ratio $\frac{da}{dA}$, we also obtain the so-called *Nanson's formula* for the area transformation

$$da = J |\boldsymbol{F}^{-\top} \boldsymbol{N}| dA. \tag{2.5}$$

The ratio

$$j = \frac{da}{dA}$$

is also referred to as the *areal Jacobian*.

2.1.3 Measures of strain

The measure of the deformation of a body with respect to a arbitrarily chosen reference configuration is outlined as *strain*. In general, the strain quantifies the change in form and size of a body.

One of the possible description of the strain is given by the *right Cauchy-Green tensor* defined as

$$\boldsymbol{C} = \boldsymbol{F}^{\top} \boldsymbol{F}.$$

---

[1] From tensor algebra, the identity $\boldsymbol{S}\boldsymbol{v} \times \boldsymbol{S}\boldsymbol{w} = \det \boldsymbol{S}\, \boldsymbol{S}^{-\top} (\boldsymbol{v} \times \boldsymbol{w}) = \mathbf{Cof}(\boldsymbol{S})(\boldsymbol{v} \times \boldsymbol{w})$ is given for an invertible tensor $\boldsymbol{S}$ and two vector $\boldsymbol{v}$ and $\boldsymbol{w}$. The quantity $\mathbf{Cof}(\boldsymbol{S})$ is also known as the **cofactor** of the tensor $\boldsymbol{S}$. Using $\boldsymbol{S} = \boldsymbol{F}$, $J = \det(\boldsymbol{F})$ and $\boldsymbol{E}_1 \times \boldsymbol{E}_2 = \boldsymbol{N}$, we obtain the expression for da.

Let be $\{\boldsymbol{E}_1, \boldsymbol{E}_2, \boldsymbol{E}_3\}$ and $\{\boldsymbol{e}_1, \boldsymbol{e}_2, \boldsymbol{e}_3\}$ two basis, respectively, in the reference and deformed configurations, such as $\boldsymbol{e}_i = \boldsymbol{F}\boldsymbol{E}_i$. Focusing on the scalar product

$$\boldsymbol{e}_i \cdot \boldsymbol{e}_j = \boldsymbol{F}\boldsymbol{E}_i \cdot \boldsymbol{F}\boldsymbol{E}_j = \boldsymbol{E}_i(\boldsymbol{F}^\intercal \boldsymbol{F})\boldsymbol{E}_j = C_{ij},$$

the physical meaning of the tensor $\boldsymbol{C}$ may be recovered. In fact, the diagonal terms C_{ii} provides information about the stretch[2] in the direction of $\boldsymbol{e}_i$ while the out of diagonal terms C_{ij} describes the changes in angle between $\boldsymbol{e}_i$ and $\boldsymbol{e}_j$ (if $C_{ij} = 0\,\forall i, j = 1, \ldots, 3,\ i \neq j$ orthogonality is preserved).
In the case of null displacement, $\boldsymbol{C} = \boldsymbol{1}$. Thereby, it is often preferable to introduce the *Green-Lagrange tensor*

$$\boldsymbol{E} = \frac{1}{2}(\boldsymbol{C} - \boldsymbol{1})$$

so that the strain is zero when $\boldsymbol{u} = \boldsymbol{0}$. Moreover, from the latter expression, the small deformation strain definition may be recovered cancelling out the second-order term $(\nabla_{\boldsymbol{X}}\boldsymbol{u}\,(\nabla_{\boldsymbol{X}}\boldsymbol{u})^\intercal)$.

2.2 Basic mechanical principles

The balance laws for mass and linear momentum will be derived in local and integral forms for the purpose of describing the motion of a body undergoing finite deformation. The conservation equations will be firstly stated in the deformed configuration and then cast in the reference configuration so that the problem can be analysed from a Lagrangian point of view. Moreover, the concept of stress is firstly defined using the well-known Cauchy stress tensor and then, introducing suitable push-back operators, using the Piola-Kirchhoff stress tensors.

2.2.1 Continuity equation

Let be $\rho(\boldsymbol{X}) : \Omega \to \mathbb{R}_{>0}$ and $\rho^+(\boldsymbol{x}, t) : \Omega^+ \times \mathbb{R}_{>0} \to \mathbb{R}_{>0}$ the density of the material of the body, respectively, in the reference and deformed configurations. The continuity equation in the current configuration is obtained imposing

$$\frac{d}{dt}\int_{\Omega^+} \rho^+(\boldsymbol{x}, t)\, dv = 0. \tag{2.6}$$

Requiring that the time derivative in Eq. (2.6) is null corresponds to set that the integral of the density ρ^+ in Ω^+ is equal to the integral of the *reference* density ρ in Ω, *i.e.*

$$\int_{\Omega^+} \rho^+(\boldsymbol{x}, t)\, dv = \int_{\Omega} \rho(\boldsymbol{X})\, dV. \tag{2.7}$$

---

[2] Remember that the tensor $\boldsymbol{F}$ does not preserve length and angle between vectors. If $\boldsymbol{L}$ is a vector of length $|\boldsymbol{L}|$ and $\boldsymbol{l} = \boldsymbol{F}\boldsymbol{L}$ its counterpart in the deformed configuration, the quantity $\boldsymbol{\lambda} = \frac{\boldsymbol{l}}{|\boldsymbol{L}|}$ define the stretch in direction of $\boldsymbol{l}$.

Now, the integral presented at the left-hand side of Eq. (2.7) may be computed in the current configuration changing the integration variable with the transformation of volume (2.4) obtaining

$$\begin{aligned}\int_{\Omega^+} \rho^+(\boldsymbol{x},t)\,dv &= \int_{\Omega} \rho^+(\mathcal{X}(\boldsymbol{X},t),t)\,J(\mathcal{X}(\boldsymbol{X},t),t)dV\\ &= \int_{\Omega} \rho^+(\boldsymbol{X},t)\,J(\boldsymbol{X},t)dV.\end{aligned} \tag{2.8}$$

So, combining Eqs. (2.7) and (2.8), we obtain the continuity equation in the reference configuration

$$\int_{\Omega} \Big(\rho^+(\boldsymbol{X},t)\,J(\boldsymbol{X},t) - \rho(\boldsymbol{X})\Big)\,dV = 0$$

or, alternatively, using the localization theorem (see [5])

$$\rho^+(\boldsymbol{X},t) = \frac{\rho(\boldsymbol{X})}{J(\boldsymbol{X},t)}. \tag{2.9}$$

The basic hypothesis of continuum mechanics that no two material points of the same neighbourhood may occupy the same spatial point at a given time can be stated as follows

$$J = \frac{\rho(\boldsymbol{X})}{\rho^+(\boldsymbol{X},t)} > 0. \tag{2.10}$$

2.2.2 Conservation of linear momentum

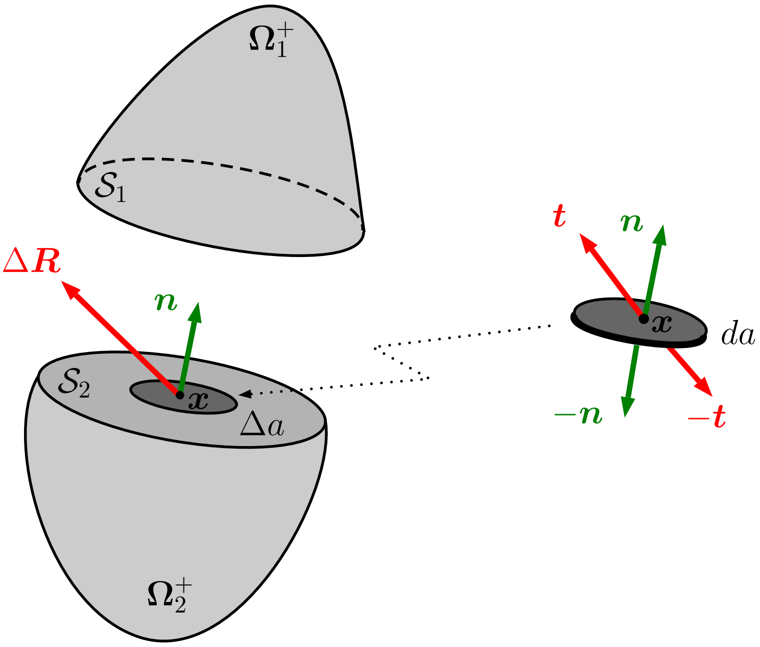

Figure 4: Traction vector.

A general deformable body is considered at its current configuration Ω^+. In order to develop the concept of stress, it is necessary to study the forces exchanged through the surface $\mathcal{S}$ between the regions Ω_1^+ and Ω_2^+ obtained splitting the body Ω^+, see Fig. 4. We identify with Δa the element of area in the neighbourhood of $\boldsymbol{x}$, a spatial point at time t in which the vector $\boldsymbol{n} = \boldsymbol{n}(\boldsymbol{x}, t)$ is the normal pointing outward the surface $\mathcal{S}$. According to the Cauchy's hypothesis (see [5]), if $\Delta\boldsymbol{R}$ is the resultant force on this area, the traction vector $\boldsymbol{t}$ at $\boldsymbol{x}$ with normal vector $\boldsymbol{n}$ is defined as

$$\boldsymbol{t} = \boldsymbol{t}(\boldsymbol{n}(\boldsymbol{x}, t), \boldsymbol{x}, t) = \lim_{\Delta a \to 0} \frac{\Delta\boldsymbol{R}}{\Delta a}.$$

The relationship between $\boldsymbol{t}$ and $\boldsymbol{n}$ must be such that it satisfies Newton's third law of action and reaction, namely $\boldsymbol{t}(-\boldsymbol{n}(\boldsymbol{x}, t), \boldsymbol{x}, t) = -\boldsymbol{t}(\boldsymbol{n}(\boldsymbol{x}, t), \boldsymbol{x}, t)$, see Fig. 4 on the right.

The static equilibrium equation of the deformed body Ω^+ subjected to the body force $\boldsymbol{f}^+ = \boldsymbol{f}^+(\boldsymbol{x}, t)$ (*i.e.* the gravity force field) per unit volume and the traction forces $\boldsymbol{t}$ (*i.e.* contact and friction forces) per unit area action on the boundary surface $\partial\Omega^+$ is derived. Note that $\boldsymbol{f}^+ = \rho^+\widetilde{\boldsymbol{f}}$, where $\widetilde{\boldsymbol{f}}$ is the force per unit mass. Ignoring, for simplicity, inertia forces, the translational equilibrium is obtained satisfying the Newton's law, namely, the sum of all forces acting on the body vanishes such that

$$\int_{\partial\Omega^+} \boldsymbol{t}\, da + \int_{\Omega^+} \boldsymbol{f}^+ dv = 0. \tag{2.11}$$

As stated by the Cauchy's theorem for the existence of stress (see [5]), a consequence of the balance of forces (2.11) is that there exists a spatial tensor field $\boldsymbol{\sigma} : \Omega^+ \times \mathbb{R}_{>0} \to \mathbb{R}^{d\times d}$, called the *Cauchy stress tensor*, such that

$$\boldsymbol{t}(\boldsymbol{n}(\boldsymbol{x}, t), \boldsymbol{x}, t) = \boldsymbol{\sigma}(\boldsymbol{x}, t)\boldsymbol{n}(\boldsymbol{x}, t). \tag{2.12}$$

Introducing the definition (2.12) and using the divergence (or Gauss) theorem, the first term of Eq. (2.11) can be transformed into a volume integral

$$\int_{\partial\Omega^+} \boldsymbol{t}\, da = \int_{\partial\Omega^+} \boldsymbol{\sigma}\boldsymbol{n}\, da = \int_{\Omega^+} \nabla_{\boldsymbol{x}} \cdot \boldsymbol{\sigma}\, dv,$$

where $\nabla_{\boldsymbol{x}}$ is the gradient operator in the deformed configuration

$$\nabla_{\boldsymbol{x}}(\bullet) = \frac{\partial(\bullet)}{\partial\boldsymbol{x}}, \quad \nabla_{\boldsymbol{x}}(\bullet)_j = \frac{\partial(\bullet)}{\partial x_j}.$$

Thus, local force balance in the deformed configuration is obtained

$$\nabla_{\boldsymbol{x}} \cdot \boldsymbol{\sigma} + \boldsymbol{f}^+ = 0.$$

The Lagrangian approach requires the reformulation of (2.11) in the reference configuration. First of all, we work on the term $\int_{\partial\Omega^+} \boldsymbol{t} da$. Using the Nanson's formula (2.5), we cast the integral over $\partial\Omega^+$ into an integral over $\partial\Omega$ (the boundary surface in the reference configuration) such that

$$\int_{\partial\Omega^+} \boldsymbol{\sigma}\boldsymbol{n}\, da = \int_{\partial\Omega} J\boldsymbol{\sigma}\boldsymbol{F}^{-\top}\boldsymbol{N}\, dA$$

from which we define the *first Piola-Kirchhoff stress tensor*

$$\boldsymbol{P} := J\boldsymbol{\sigma}\boldsymbol{F}^{-\intercal}. \tag{2.13}$$

Secondly, employing Eq. (2.4), the integral of the body forces over the deformed volume is transformed in

$$\int_{\Omega^+} \boldsymbol{f}^+ dv = \int_{\Omega} \boldsymbol{f}^+ J dV = \int_{\Omega} J\rho^+ \widetilde{\boldsymbol{f}} dV = \int_{\Omega} \rho \widetilde{\boldsymbol{f}}\, dV = \int_{\Omega} \boldsymbol{f}\, dV$$

where $\boldsymbol{f}(\boldsymbol{X}, t) : \Omega \times \mathbb{R}_{>0} \to \mathbb{R}^d$ is the Lagrangian description of body forces per unit volume in the reference configuration. Collecting the results,

$$\int_{\partial\Omega} \boldsymbol{P}\boldsymbol{N}\, dA + \int_{\Omega} \boldsymbol{f}\, dV = 0$$

and applying once again the divergence theorem, we get the local force balance in the reference configuration

$$\nabla_{\boldsymbol{X}} \cdot \boldsymbol{P} + \boldsymbol{f} = 0. \tag{2.14}$$

At the end of this section, we introduce the *second Piola-Kirchhoff stress tensor*[3] defined as follows

$$\boldsymbol{S} = \boldsymbol{F}^{-1}\boldsymbol{P} \tag{2.15}$$

As opposite to $\boldsymbol{P}$, the tensor $\boldsymbol{S}$ is objective (independent from the frame of reference, see [5]) and it will be used in the next section as basic ingredient to formulate the constitutive laws of hyperelastic materials.

2.3 Hyperelasticity

The equilibrium equations derived in Sec. 2.2.2 are written in terms of the Piola-Kirchhoff stress that measures the internal response of a deforming body subjected to external forces. Now, in order to close the problem, it is necessary to express $\boldsymbol{P}$ (or equivalently, $\boldsymbol{S}$) in terms of some measure of deformation such as, for instance, the strain tensors described in Sec. 2.1.3. The relationships between the stress and the strain are known as *constitutive equations* that, obviously, are dependent on the type of material under consideration. In this section, the constitutive equations will be established in the context of **hyperelastic** materials. We will restrict our investigation to the Saint Venant-Kirchhoff and the neo-Hookean materials.

In general, hyperelastic models find application in modelling polymeric or rubbery elastic response. Despite of the existence of several alternative material descriptions, the theory of hyperelastic material

---

[3] The introduction of the second Piola-Kirchhoff stress tensor $\boldsymbol{S}$ is also explained in the context of the power-conjugate pairing. See [5] for further details.

provides simple constitutive equations that may represent the basis for more complex material models such as elastoplasticity, viscoplasticity, and viscoelasticity.

2.3.1 Strain energy function

As accurately described by Hackett (2018) [7], hyperelasticity is the finite strain constitutive theory which describes the mechanical behavior of *elastic* solids with the use of *only one* material function. The hyperelastic response is said to be fully path independent and reversible. In fact, the stress depends only on the current level of the strain because it is independent from the history of the material point. Moreover, the original shape is recovered upon unloading the body. This also implies the absence of energy dissipation in the process of deformation, so, all energy expended during the deformation is stored in the body and it is completely released unloading the system.

Introduced by George Green (1793–1841), the unique material function describing hyperelastic material is known as the **strain-energy** (or **stored-energy**) function $w(\boldsymbol{F}) : \mathbb{R}^{d\times d} \longrightarrow \mathbb{R}$. A more general expression, suitable also for incompressible material, is $w(\boldsymbol{F}, q) : \mathbb{R}^{d\times d} \times \mathbb{R} \longrightarrow \mathbb{R}$, defined as follows

$$w = w(\boldsymbol{F}, q) \coloneqq \widehat{w}(\boldsymbol{F}) + q(J-1) \tag{2.16}$$

where q is an arbitrary Lagrange multiplier which differs from zero only in case of fully incompressible material. In fact, the additional terms are used in the description of isochoric deformations in order to satisfy, simultaneously, Eq. (2.14) and the incompressibility constraint

$$J = 1 \tag{2.17}$$

which directly follows from Eq. (2.9).

The **Saint Venant-Kirchhoff (SVK)** constitutive law is employed in those engineering applications involving small strains and large rotations. SVK provides the natural extension of linear elasticity to finite deformations (see *e.g.* [4]). Introducing the Lamé material parameters μ and λ and remembering the strain definition (2.1.3), the SVK strain-energy function is

$$(\mathrm{SVK}) : \widehat{w}(\boldsymbol{F}) = \mu\, \boldsymbol{E} : \boldsymbol{E} + \frac{1}{2}\lambda(\mathrm{tr}\,(\boldsymbol{E}))^2. \tag{2.18}$$

For future use, remember that μ and λ can be written in terms of the Poisson's coefficient ν and the Young's modulus E through the following relations

$$\mu = \frac{E}{2(1+\nu)}, \qquad \lambda = \frac{\nu E}{(1+\nu)(1-2\nu)}. \tag{2.19}$$

Some values of μ and λ for realistic materials are tabulated in [4].

A **neo-Hookean (NHK)** constitutive law is a particular case of the Mooney-Rivlin material description[4] that is typically used to characterize isotropic rubber-like materials undergoing large strains. The stored-energy function of a fully incompressible neo-Hookean material is defined using only the first invariant[5] of the strain tensor $\boldsymbol{C}$, such that

$$(\text{NHK-I}) : \widehat{w}(\boldsymbol{F}) = \frac{\mu}{2}(\operatorname{tr}(\boldsymbol{C}) - d). \tag{2.20}$$

where d is the geometrical dimension of the problem.

Removing the restriction (2.17) on the incompressibility and adding to (2.20) a suitable function of J (for further information see Brink and Stein (1996) [8] and Pence and Gou (2015) [9]), the extension to the compressible regime of the NHK-I model reads

$$(\text{NHK-C}) : \widehat{w}(\boldsymbol{F}) = \frac{\mu}{2}(\operatorname{tr}(\boldsymbol{C}) - d) - \mu \ln J + \frac{\lambda}{2}\Theta^2(J), \tag{2.21}$$

where, for example,

$$\Theta(J) = \begin{cases} J - 1, & \text{[8, Eq. 4.10], see also [10]} \\ \ln(J) & \text{[8, Eq. 4.11].} \end{cases}$$

In order to investigate the robustness of the numerical methods respect to mesh distortion, the standard NHK-C law (2.21) may be modified to reduce the rate of the strain-energy growth with respect to the deformation gradient. This permits to investigate, for example, the *cavitation* phenomena. In solid mechanics, the term cavitation refers to the formation and rapid expansion of voids that occurs when a solid is subjected to sufficiently large tensile stresses that produce significant deformation near cavities. Some experiments on the cavitation are reported by *e.g.* Gent and Lindley [11] where unusual internal flaws appear in vulcanized rubber cylinders under a well-defined relatively small tensile load. So, as proposed by [2] and [1], we define

$$(\text{NHK-CAV}) : \widehat{w}(\boldsymbol{F}) = \frac{2\mu}{3^{5/4}}(\operatorname{tr}(\boldsymbol{C}))^{\frac{3}{4}} - \mu \ln J + \frac{\lambda}{2}(\ln J)^2. \tag{2.22}$$

2.3.2 Piola-Kirchhoff stress tensors

As explained in [3], the stress state of hyperelastic materials in the reference configuration may be formulated using the strain-energy function (2.16) such that

$$\boldsymbol{P} = \frac{\partial w}{\partial \boldsymbol{F}}. \tag{2.23}$$

---

[4] See [7].

[5] The invariants of $\boldsymbol{C}$ are: $I_1 = \operatorname{tr}(\boldsymbol{C})$, $I_2 = \frac{1}{2}[(\operatorname{tr}(\boldsymbol{C}))^2 - \operatorname{tr}(\boldsymbol{C}^2)]$ and $I_3 = \det \boldsymbol{C}$. In general, the isotropic elastic properties of a hyperelastic material models may be described in terms of a strain-energy function $w = w(I_1, I_2, I_3)$.

A convenient definition of the first Piola-Kirchhoff stress tensor, equivalent to the one given in (2.23), reads

$$\boldsymbol{P} = \boldsymbol{P}(\boldsymbol{F}, p) = \boldsymbol{F}\boldsymbol{S} - p\, J\, \boldsymbol{F}^{-\top}, \tag{2.24}$$

where the second Piola-Kirchhoff stress (2.15) tensor may be obtained, from the strain-energy function, as follows

$$\boldsymbol{S} = \frac{\partial w(\boldsymbol{F})}{\partial \boldsymbol{E}} = 2\frac{\partial w(\boldsymbol{F})}{\partial \boldsymbol{C}}, \tag{2.25}$$

and $p = -q$ is the hydrostatic pressure. The use of the strain tensors $\boldsymbol{E}$ and $\boldsymbol{C}$ in Eq. (2.25) is motivated by the fact that they are suitable for expressing the stress-deformation relation. For those materials introduced in Sec. 2.3.1, the expressions of $\boldsymbol{S}$ can be derived introducing the definitions (2.18), (2.20), (2.21) and (2.22) into (2.25) to get

$$\text{(SVK)} : \boldsymbol{S} = 2\mu\boldsymbol{E} + \lambda(\operatorname{tr}(\boldsymbol{E}))\boldsymbol{1}; \tag{2.26}$$

$$\text{(NHK-I)} : \boldsymbol{S} = \mu\boldsymbol{1}; \tag{2.27}$$

$$\text{(NHK-C)} : \boldsymbol{S} = \mu(\boldsymbol{1} - \boldsymbol{C}^{-1}) + \lambda J\Theta(J)\Theta'(J)\boldsymbol{C}^{-1}; \tag{2.28}$$

$$\text{(NHK-CAV)} : \boldsymbol{S} = \frac{\mu}{3^{1/4}}\operatorname{tr}(\boldsymbol{C})^{-\frac{1}{4}}\,\boldsymbol{1} - \mu\boldsymbol{C}^{-1} + \lambda\ln(J)\boldsymbol{C}^{-1}. \tag{2.29}$$

Plugging (2.26)-(2.29) into (2.24), the final expression of $\boldsymbol{P}$ is obtained.

For future use, we define SVK-C and SVK-I in order to distinguish the Saint Venant-Kirchhoff (SVK) law used in the compressible or in the fully incompressible regime (requiring Eq. (2.17) to be satisfied).

2.3.3 Fourth-order elasticity tensor

The linearization, typically obtained with the use of the Newton's method (see Sec. 3.6), of the system of nonlinear equations deriving from the elasticity problem requires the definition of the so-called **fourth-order elasticity tensor** $\mathbb{A} : \mathbb{R}^{d\times d} \times \mathbb{R} \to \mathbb{R}^{d\times d\times d\times d}$. It may be related to the strain-energy function and computed as follows

$$\mathbb{A} = \mathbb{A}(\boldsymbol{F}, p) \coloneqq \frac{\partial}{\partial \boldsymbol{F}}\frac{\partial w}{\partial \boldsymbol{F}} = \frac{\partial \boldsymbol{P}}{\partial \boldsymbol{F}}. \tag{2.30}$$

Employing the definition (2.24), the tensor coefficients $\mathbb{A}_{ijkl}$, such that

$$\mathbb{A} = \mathbb{A}_{ijkl}\, \boldsymbol{E}_i \otimes \boldsymbol{E}_j \otimes \boldsymbol{E}_k \otimes \boldsymbol{E}_l,$$

reads

$$\mathbb{A}_{ijkl} = \frac{\partial}{\partial F_{kl}}(\boldsymbol{F}\boldsymbol{S})_{ij} - p\frac{\partial}{\partial F_{kl}}\left(J\,F^{-\top}_{ij}\right) =$$
$$= \delta_{ik}S_{lj} + F_{im}\frac{\partial S_{mj}}{\partial F_{kl}} - p\,J\left(F^{-\top}_{kl}F^{-\top}_{ij} - F^{-\top}_{il}F^{-1}_{jk}\right),$$

where $\boldsymbol{S}$ depends on the material model (see Eqs. (2.26)-(2.29)). To complete the definition of $\mathbb{A}$, the following relations are helpful

$$\frac{\partial E_{qr}}{\partial F_{kl}} = \frac{1}{2}\frac{\partial C_{qr}}{\partial F_{kl}} = \frac{1}{2}\left(\delta_{ql}F_{kr} + \delta_{rl}F_{kq}\right),$$

and

$$\frac{\partial S_{mj}}{\partial F_{kl}} = \frac{\partial S_{mj}}{\partial E_{qr}}\frac{\partial E_{qr}}{\partial F_{kl}} \quad \text{or} \quad \frac{\partial S_{mj}}{\partial F_{kl}} = \frac{\partial S_{mj}}{\partial C_{qr}}\frac{\partial C_{qr}}{\partial F_{kl}}$$

where

$$\text{SVK}: \frac{\partial S_{mj}}{\partial E_{qr}} = 2\mu\delta_{mq}\delta_{jr} + \lambda\delta_{mj}\delta_{qr};$$
$$\text{NHK-I}: \frac{\partial S_{mj}}{\partial C_{qr}} = 0;$$
$$\text{NHK-C}: \frac{\partial S_{mj}}{\partial C_{qr}} = \mu C^{-1}_{mq}C^{-1}_{rj} +$$
$$+ \lambda J\left(-\Theta\Theta' C^{-1}_{mq}C^{-1}_{rj} + \frac{1}{2}\left(\Theta\Theta' + J\Theta'^2 + J\Theta\Theta''\right)C^{-1}_{qr}C^{-1}_{mj}\right);$$
$$\text{NHK-CAV}: \frac{\partial S_{mj}}{\partial C_{qr}} = -\frac{1}{4}\frac{\mu}{3^{1/4}}\mathrm{tr}\,(\boldsymbol{C})^{-\frac{5}{4}}\,\delta_{mj}\delta_{qr} + \mu C^{-1}_{mq}C^{-1}_{rj} +$$
$$+ \lambda\left(-\ln(J)\,C^{-1}_{mq}C^{-1}_{rj} + \frac{1}{2}C^{-1}_{qr}C^{-1}_{mj}\right).$$

Chapter 3. Nonconforming Numerical Methods for Nonlinear Elasticity

Discontinuous *Galerkin (dG) methods* are widely employed in the field of Computational Fluid Dynamics (CFD) where they are appreciated for their turbulence modelling capabilities. In the last few decades, the interest in dG formulations for Computational Solid Mechanics (CSM) has been growing due to the following attractive features: robustness with respect to mesh distortion, ability to deal with arbitrarily unstructured polytopal elements meshes, possibility to locally increase the accuracy by raising the polynomial degree in those regions where the solution is expected to be smooth, availability of locking-free formulations in the incompressible and nearly-incompressible limits. Despite those appealing properties the success of dG methods among CSM practitioners has been rather scarce, possibly because of the increased memory footprint and the lack of efficient solution strategies. An obvious downturn is related to the lack of dG modules in CSM commercial codes.

Several dG discretizations of *linear elasticity* problems have been proposed and analysed in literature. The hp-error analysis was first considered by Riviere *et al.* [12] and Hansbo *et al.* [13] analysed the nearly and fully incompressible limits introducing a locking-free mixed formulation. A Bassi-Rebay (BR2) dG method was proposed by Lew *et al.* [14] and Cockburn *et al.* [15] introduced a Local Discontinuous Galerkin (LDG) method. Other locking-free implementations have been proposed by Wihler [16, 17] and hp-adaptivity was considered by Houston *et al.* [18]. Beam and plate modelling was tackled by Celiker [19, 20] while Kirchhoff-Love linear shells were investigated by Guzey *et al.* [21] and Noels [22]. Kaufmann *et al.* [23] exploited dG flexibility to simulate deformable bodies based on arbitrarily shaped polyhedral elements meshes. Plasticity problems in the small deformation regime were studied by Djoko *et al.* [24, 25].

Concerning the use of dG formulations in the context of *nonlinear elasticity* problems, the following research efforts deserve to be mentioned. In 2006 Noels and Radovitzky [26] tackled large strains of hyperelastic bodies and Eyck and Lew [27] proposed a dG formulation based on the Bassi-Rebay (BR1) [28] gradient reconstruction. A novel adaptive stabilization approach for the latter formulation was proposed in Eyck *et al.* [29, 30]. Whiteley [31] investigated locking phenomena in nonlinear elasticity showing the advantage of dG methods in the incompressible limit. Baroli *et al.* [32] devised a total Lagrangian Interior Penalty (IP) dG formulation for incompressible and anisotropic soft living materials. Challenging application oriented contributions are collected in what follows. Becker and Noel [33] modelled cracks initiation and propagation by means of Kirchhoff-Love shell elements. McBride and Reddy [34] introduced a logarithmic hyper-elastoplastic model for the finite-deformation regime. Liu *et al.* [35] tackled hypo- and hyper-elastoplastic problems through an updated Lagrangian formulation. Feistauer *et al.* [36] employed a spatial dG discretization for an elasto-dynamic system. To conclude, Kosis *et al.* [37] considered a space-time dG formulations of the Fluid-Structure-Interaction (FSI) problem involving a compressible Newtonian fluid and a Saint Venant-Kirchhoff material.

More recently, the introduction of *Hybridizable Discontinuous Galerkin methods (HDG)* has further increased the popularity of discontinuous Finite Element methods among CSM practitioners. HDG was first presented in Cockburn *et al.* [38] for the solution of second order elliptic problems. Soon *et al.* [39] describe the application HDG to linear elasticity problems and provide numerical evidence suggesting that the method is free of volumetric locking. Nguyen *et al.* [40] investigate the attractive feature of the method for the numerical simulation of wave phenomena in acoustics and elastodynamics. Nguyen and Peraire [41] proposed an HDG framework for continuum mechanics. A superconvergent HDG methods for linear elasticity based on weak stress symmetry formulations is proposed in Cockburn *et al.* [42]. Kabaria *et al.* [1] proposed an HDG method for nonlinear elasticity and a suitable stabilization strategy was later proposed by Cockburn and Shen [43]. Terrana *et al.* [44] applied HDG methods to thin structures presenting buckling phenomena.

Hybrid High-Order (HHO) methods have been developed in the last decade alongside the HDG methods. The interested reader may find a collection of possible application in the manuscript of Di Pietro and Droniou [45]. The method was firstly presented in Di Pietro and Ern [46] which proposes an arbitrary-order locking-free method for linear elasticity. Botti *et al.* [47] analysed a HHO for nonlinear elasticity with small deformations. The HHO method is employed in Bonaldi *et al.* [48] to solve the fourth-order elliptic problems arising from the mechanical modelling of Kirchhoff-Love plates. Abbas *et al.* [2] presented a stabilized and an unstabilized HHO method for finite deformations of hyperelastic materials. HHO methods has been applied to incremental associative plasticity and elastoplastic deformations in Abbas *et al.* [49, 50] while Chouly *et al.* [51] applied HHO methods to contact mechanics. In Botti *et al.* [52], the nonlinear elasticity operator is discretized with the HHO method for the solution of poroelasticity problems.

Based on a Lagrangian formulation of the equation of motion, three nonconforming discretizations of the nonlinear elasticity problem are introduced in this chapter.

In Sec. 3.2, we describe the mesh settings, namely the formal description of all sets of elements or faces used to properly define the local and global residuals of the discretized Lagrangian equation of motion, possibly coupled with incompressibility and Lagrange multipliers constraints.

The discrete problem is tackled considering a dG, a HDG and a HHO formulation. The dG formulation is derived in Sec. 3.3 where the BR2 gradient reconstruction is employed to discretize the elasticity problem for either compressible or incompressible hyperelastic materials. The proper amount of stabilization is ensured with the adaptive strategy presented in Sec. 3.3.1 and based on the spectrum of the fourth-order elasticity tensor.
The HDG and the HHO formulations for nonlinear elasticity problems involving only compressible materials are reported, respectively, in Sec. 3.4 and Sec. 3.5.

Globalisation of Newton's method is achieved by means of an incremental load method, described in Sec. 3.6. As a result, a sequence of intermediate linearized equilibrium configurations converging to the final solution is obtained. The derivation of the Jacobian operators is described in Sec. 3.6.1 for the dG, in Sec. 3.6.2 for the HDG and in Sec. 3.6.3 for the HHO formulation.

3.1 Nonlinear elasticity problem

Referring to Fig. 5, an elastic continuum body in the reference configuration occupies the bounded connected domain $\Omega \in \mathbb{R}^d$, $d \in 2, 3$, with Lipschitz continuous boundary $\partial\Omega$. The material points $\boldsymbol{X} \in \Omega$ are mapped into spatial points $\boldsymbol{x} = \boldsymbol{X} + \boldsymbol{u}(\boldsymbol{X})$, where $\boldsymbol{u} : \Omega \rightarrow \mathbb{R}^d$ is the displacement mapping. The body in deformed configuration occupies $\Omega^+ := \{\boldsymbol{X} + \boldsymbol{u}(\boldsymbol{X}), \boldsymbol{X} \in \Omega\}$. We consider the surface $\partial\Omega$ divided into the Neumann boundary $\partial\Omega_{\mathrm{N}}$ and the Dirichlet boundary $\partial\Omega_{\mathrm{D}}$. It is assumed that both $\partial\Omega_{\mathrm{D}}$ and $\partial\Omega_{\mathrm{N}}$ have non-zero $(d-1)$-dimensional Hausdorff measure and $\partial\Omega = \overline{\partial\Omega_{\mathrm{D}}} \bigcup \overline{\partial\Omega_{\mathrm{N}}}$ with $\partial\Omega_{\mathrm{D}} \bigcap \partial\Omega_{\mathrm{N}} = \emptyset$.

The elasticity problem can be obtained supplementing the force balance (2.14) with suitable boundary conditions. Accordingly, the elasticity problem consists of finding the displacement mapping $\boldsymbol{u}$ such

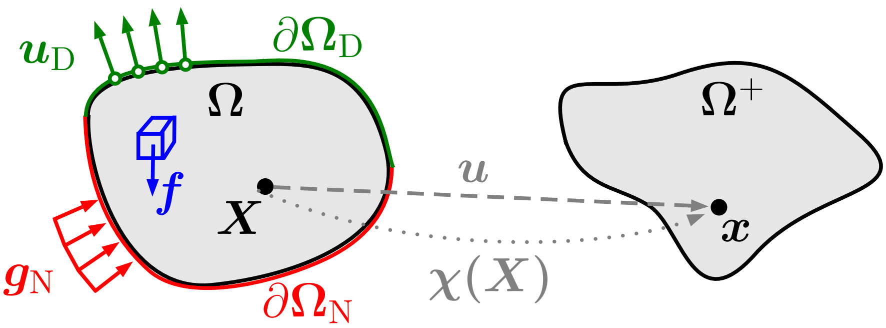

Figure 5: The mapping of the reference body Ω into its deformed configuration Ω^+ and the external loads applied on the boundary surface $\partial\Omega$ and in the volume.

that

$$-\nabla_{\boldsymbol{X}} \cdot \boldsymbol{P} = \boldsymbol{f} \qquad \text{in } \Omega, \tag{3.1a}$$

$$\boldsymbol{u} = \boldsymbol{u}_\mathrm{D} \qquad \text{on } \partial\Omega_\mathrm{D}, \tag{3.1b}$$

$$\boldsymbol{P}\boldsymbol{N} = \mathbf{T}_\mathrm{N} \qquad \text{on } \partial\Omega_\mathrm{N}, \tag{3.1c}$$

where $\boldsymbol{N}$ is the unit normal vector pointing out of $\partial\Omega$, $\boldsymbol{f} : \Omega \to \mathbb{R}^d$ is the known body force, $\boldsymbol{T}_\mathrm{N}$ is the traction force imposed on $\partial\Omega_\mathrm{N}$, $\boldsymbol{u}_\mathrm{D}$ is the displacement vector imposed on $\partial\Omega_\mathrm{D}$ and $\boldsymbol{P}$, from Eq. (2.13), is the first Piola-Kirchhoff stress tensor: a stress measure that describes the response of the body to the external solicitations $\boldsymbol{f}, \boldsymbol{T}_\mathrm{N}$, and $\boldsymbol{u}_\mathrm{D}$. The unknown of the problem $\boldsymbol{u}$ is hidden in the definition of $\boldsymbol{P}$. Restricting the attention on the hyperelastic materials introduced in Sec. 2.3, the stress tensor $\boldsymbol{P}(\boldsymbol{F}, p)$ in Eq. (2.24) is given as a function of the deformation gradient $\boldsymbol{F}(\boldsymbol{u})$, see Eq. (2.1.1). The hydrostatic pressure p is introduced in order to cope with the incompressibility constraint (2.17).

In this work, we focus on the the static equilibrium of hyperelastic bodies undergoing isochoric large deformation. The compressible regime will be recovered as a particular case of isochoric motion.

Let $\boldsymbol{V}$ be the set of all kinematically admissible displacements which satisfy the Dirichlet condition (3.1b) and Q be the set of admissible Lagrange multipliers. Summing up the contributions to the system energy, namely, the stored energy from Eq. (2.16) and the work of body and surface forces, we define the *energy functional* $\mathcal{W} : \boldsymbol{V} \times Q \to \mathbb{R}$ such that

$$\mathcal{W}(\boldsymbol{v}, q) = \int_\Omega w(\boldsymbol{F}(\boldsymbol{v}), q) - \int_\Omega \boldsymbol{f} \cdot \boldsymbol{v} - \int_{\partial\Omega_\mathrm{N}} \boldsymbol{T}_\mathrm{N} \cdot \boldsymbol{v}. \tag{3.2}$$

The static equilibrium of problem (3.1) **constrained** by $J = 1$ consists in finding $(\boldsymbol{u}, p) \in \boldsymbol{V} \times Q$ which satisfy the following weak form of the Euler-Lagrange equations

$$\begin{aligned} 0 = \frac{d}{d\epsilon}\mathcal{W}(\boldsymbol{u} + \epsilon\delta\boldsymbol{v}, p)\Big|_{\epsilon=0} &= \int_\Omega \boldsymbol{P}(\boldsymbol{F}(\boldsymbol{u}), p) : \nabla_{\boldsymbol{X}}(\delta\boldsymbol{v}) + \\ &\quad - \int_\Omega \boldsymbol{f} \cdot \delta\boldsymbol{v} - \int_{\partial\Omega_\mathrm{N}} \boldsymbol{T}_\mathrm{N} \cdot \delta\boldsymbol{v}, \qquad (3.3a) \\ 0 = \frac{d}{d\epsilon}\mathcal{W}(\boldsymbol{u}, p + \epsilon\delta q)\Big|_{\epsilon=0} &= \int_\Omega (J - 1)\,\delta q, \qquad (3.3b) \end{aligned}$$

for all virtual displacements $\delta\boldsymbol{v}$ that satisfy a Dirichlet condition on $\partial\Omega_\mathrm{D}$ and for all δq. In the left-hand terms of (3.3), we have introduced the notation for the directional derivative, see Bonet *et al.* [53]. According to (3.3), $(\boldsymbol{u}, p)$ is a stationary point of $\mathcal{W}(\boldsymbol{v}, q)$ in Eq. (3.2).

In case of compressible-material models, the strain-energy function (2.16) reads $w : \mathbb{R}^{d\times d} \longrightarrow \mathbb{R}$ with $w = w(\boldsymbol{F})$, similarly, the energy functional (3.2) is $\mathcal{W} : \boldsymbol{V} \longrightarrow \mathbb{R}$ with $\mathcal{W} = \mathcal{W}(\boldsymbol{v})$. The static equilibrium of the *unconstrained* problem (3.1) consists in finding $\boldsymbol{u} \in \boldsymbol{V}$ which satisfy the following weak form of the Euler-Lagrange equations

$$\begin{aligned} 0 = \frac{d}{d\epsilon}\mathcal{W}(\boldsymbol{u} + \epsilon\delta\boldsymbol{v})\Big|_{\epsilon=0} &= \int_\Omega \boldsymbol{P}(\boldsymbol{F}(\boldsymbol{u})) : \nabla_{\boldsymbol{X}}(\delta\boldsymbol{v}) + \\ &\quad - \int_\Omega \boldsymbol{f} \cdot \delta\boldsymbol{v} - \int_{\partial\Omega_\mathrm{N}} \boldsymbol{T}_\mathrm{N} \cdot \delta\boldsymbol{v}. \end{aligned}$$

In the following, we consider the possibility to impose the Dirichlet boundary condition using the Lagrange Multipliers method. Let $\partial\Omega_\mathrm{D}$ be divided in some non-overlapping partitions (see Sec. 3.2.1 and Sec. 3.2.2 for further details). Among them, we identify with $\partial\Omega_{\mathrm{D}_\mathrm{L}}$ the partition on which the boundary conditions are imposed by the means of the Lagrange multipliers method (see Babuška [54]). Let $\boldsymbol{S}$ be an additional set of admissible Lagrange multipliers. Adding the work of Lagrange multipliers to the energy functional (3.2), we define another *energy functional* $\mathcal{W}_\lambda : \boldsymbol{V} \times Q \times \boldsymbol{S} \longrightarrow \mathbb{R}$ such that

$$\begin{aligned} \mathcal{W}_\lambda(\boldsymbol{v}, q, \boldsymbol{\lambda}) = \int_\Omega w(\boldsymbol{F}(\boldsymbol{v}), q) - \int_\Omega \boldsymbol{f} \cdot \boldsymbol{v} + \\ - \int_{\partial\Omega_\mathrm{N}} \boldsymbol{T}_\mathrm{N} \cdot \boldsymbol{v} + \int_{\partial\Omega_{\mathrm{D}_\mathrm{L}}} \boldsymbol{\lambda} \cdot (\boldsymbol{v} - \boldsymbol{u}_\mathrm{D}). \end{aligned} \qquad (3.4)$$

Thus, the static equilibrium of problem (3.1) constrained by $J = 1$ and using the Lagrange multiplier method for the imposition of the Dirichlet boundary conditions consists in finding $(\boldsymbol{u}, p, \boldsymbol{\lambda}) \in \boldsymbol{V} \times Q \times \boldsymbol{S}$

which satisfy the following weak form of the Euler-Lagrange equations

$$\begin{aligned}
0 = \frac{d}{d\epsilon}\mathcal{W}_\lambda(\boldsymbol{u}+\epsilon\delta\boldsymbol{v}, p, \boldsymbol{\lambda})\Big|_{\epsilon=0} &= \int_\Omega \boldsymbol{P}(\boldsymbol{F}(\boldsymbol{u}), p) : \nabla_{\boldsymbol{X}}(\delta\boldsymbol{v}) + \\
&- \int_\Omega \boldsymbol{f}\cdot\delta\boldsymbol{v} - \int_{\partial\Omega_{\mathrm{N}}} \boldsymbol{T}_{\mathrm{N}}\cdot\delta\boldsymbol{v} + \\
&+ \int_{\partial\Omega_{\mathrm{D_L}}} \boldsymbol{\lambda}\cdot\delta\boldsymbol{v}, \\
0 = \frac{d}{d\epsilon}\mathcal{W}_\lambda(\boldsymbol{u}, p+\epsilon\delta q, \boldsymbol{\lambda})\Big|_{\epsilon=0} &= \int_\Omega (J-1)\,\delta q, \\
0 = \frac{d}{d\epsilon}\mathcal{W}_\lambda(\boldsymbol{u}, p, \boldsymbol{\lambda}+\epsilon\delta\boldsymbol{\lambda})\Big|_{\epsilon=0} &= \int_{\partial\Omega_{\mathrm{D_L}}} \delta\boldsymbol{\lambda}\cdot(\boldsymbol{u}-\boldsymbol{u}_{\mathrm{D}}).
\end{aligned}$$

Similarly for compressible-material models, the energy functional (3.4) becomes $\mathcal{W}_\lambda : \boldsymbol{V}\times\boldsymbol{S}\to\mathbb{R}$ with $\mathcal{W}_\lambda = \mathcal{W}_\lambda(\boldsymbol{v}, \boldsymbol{\lambda})$. In this case, the static equilibrium of the unconstrained problem (3.1) consists in finding $(\boldsymbol{u}\times\boldsymbol{\lambda}) \in \boldsymbol{V}\times\boldsymbol{S}$ which satisfy the following weak form of the Euler-Lagrange equations

$$\begin{aligned}
0 = \frac{d}{d\epsilon}\mathcal{W}_\lambda(\boldsymbol{u}+\epsilon\delta\boldsymbol{v}, \lambda)\Big|_{\epsilon=0} &= \int_\Omega \boldsymbol{P}(\boldsymbol{F}(\boldsymbol{u})) : \nabla_{\boldsymbol{X}}(\delta\boldsymbol{v}) + \\
&- \int_\Omega \boldsymbol{f}\cdot\delta\boldsymbol{v} - \int_{\partial\Omega_{\mathrm{N}}} \boldsymbol{T}_{\mathrm{N}}\cdot\delta\boldsymbol{v} + \\
&+ \int_{\partial\Omega_{\mathrm{D_L}}} \boldsymbol{\lambda}\cdot\delta\boldsymbol{v}, \\
0 = \frac{d}{d\epsilon}\mathcal{W}_\lambda(\boldsymbol{u}, \boldsymbol{\lambda}+\epsilon\delta\boldsymbol{\lambda})\Big|_{\epsilon=0} &= \int_{\partial\Omega_{\mathrm{D_L}}} \delta\boldsymbol{\lambda}\cdot(\boldsymbol{u}-\boldsymbol{u}_{\mathrm{D}}).
\end{aligned}$$

3.2 Mesh settings

3.2.1 Mesh setting for dG methods

For the dG method in Sec. 3.3, we define a spatial mesh $\mathcal{T}_h$ as a finite collection of disjoint mesh elements where $\mathrm{T}\in\mathcal{T}_h$ is a *mesh element* of diameter h_T and meshstep size $h := \max_{\mathrm{T}\in\mathcal{T}_h} h_\mathrm{T} > 0$. The set $\mathcal{T}_h$ is such that $\bigcup_{\mathrm{T}\in\mathcal{T}_h}\overline{T} = \overline{\Omega}_h$, and either one of the following two conditions is satisfied

$$\begin{aligned}
&\Omega_h \equiv \Omega, \\
&\Omega_h \text{ is a suitable approximation of } \Omega, \text{ meaning that } \lim_{h\to 0}\Omega_h = \Omega.
\end{aligned} \tag{3.6}$$

The mesh skeleton $\bigcup_{\mathrm{T}\in\mathcal{T}_h}\partial\mathrm{T}$ is partitioned into a finite collection of mesh faces $\mathcal{F}_h$ such that, for each $\mathrm{F}\in\mathcal{F}_h$, one of the following two conditions is satisfied:

(i) There exist $\mathrm{T}, \mathrm{T}' \in \mathcal{T}_h$, with $\mathrm{T}\neq\mathrm{T}'$, such that $\mathrm{F} = \partial\mathrm{T}\cap\partial\mathrm{T}'$, meaning that F is an *internal face*.

(ii) There is $\mathrm{T}\in\mathcal{T}_h$ such that $\mathrm{F} = \partial\mathrm{T}\cap\partial\Omega_h$, meaning that F is a *boundary face*.

For each mesh element $\mathrm{T} \in \mathcal{T}_h$, the set $\mathcal{F}_{\mathrm{T}} = \{\mathrm{F} \in \mathcal{F}_h : \mathrm{F} \subset \partial\mathrm{T}\}$ denotes the faces composing the element boundary $\partial\mathrm{T}$.

We will consider two strategies for imposing Dirichlet boundary conditions, namely the Nitsche method and the Lagrange multipliers method. Thus, let $\partial\Omega_{h,\mathrm{D}} = \partial\Omega_{h,\mathrm{D_N}} \bigcup \partial\Omega_{h,\mathrm{D_L}}$, where $\partial\Omega_{h,\mathrm{D_N}}$ and $\partial\Omega_{h,\mathrm{D_L}}$ are, respectively, the Nitsche and the Lagrange multipliers partitions of the Dirichlet boundary. Consequently, we define four disjoint subsets of the set $\mathcal{F}_{\mathrm{T}}$:

1. $\mathcal{F}_{\mathrm{T}}^{\mathrm{D_N}} = \{\mathrm{F} \in \mathcal{F}_{\mathrm{T}} : \mathrm{F} \subset \partial\Omega_{h,\mathrm{D_N}}\}$: the set of Dirichlet faces where boundary conditions are weakly enforced using Nitsche method;
2. $\mathcal{F}_{\mathrm{T}}^{\mathrm{D_L}} = \{\mathrm{F} \in \mathcal{F}_{\mathrm{T}} : \mathrm{F} \subset \partial\Omega_{h,\mathrm{D_L}}\}$: the set of Dirichlet faces where boundary conditions are enforced using Lagrange multipliers;
3. $\mathcal{F}_{\mathrm{T}}^{\mathrm{N}} = \{\mathrm{F} \in \mathcal{F}_{\mathrm{T}} : \mathrm{F} \subset \partial\Omega_{h,\mathrm{N}}\}$: the set of Neumann boundary faces;
4. $\mathcal{F}_{\mathrm{T}}^{\mathrm{i}} := \mathcal{F}_{\mathrm{T}} \setminus \left(\mathcal{F}_{\mathrm{T}}^{\mathrm{D}} \cup \mathcal{F}_{\mathrm{T}}^{\mathrm{N}}\right)$: the set of internal faces.

For future use, we also set $\mathcal{F}_{\mathrm{T}}^{\mathrm{i,D_N}} := \mathcal{F}_{\mathrm{T}}^{\mathrm{i}} \cup \mathcal{F}_{\mathrm{T}}^{\mathrm{D_N}}$.
For all $T \in \mathcal{T}_h$ and all $F \in \mathcal{F}_{\mathrm{T}}$, $\boldsymbol{n}_{\mathrm{TF}}$ denotes the normal vector to F pointing out of T. We remark that is case of boundary faces $\boldsymbol{n}_{\mathrm{TF}}$ can be equal to $\boldsymbol{N}$ or an approximation of $\boldsymbol{N}$, see (3.6).

Settings for Dirichlet BCs imposed by means of the Lagrange multipliers method

The Lagrange multipliers method requires further settings. $\partial\Omega_{h,\mathrm{D_L}}$ is partitioned into smooth patches $\Pi_{h,n}$, $n = 1, ..., N$, such that

1. $\bigcup_{\Pi_{h,n} \in \partial\Omega_{h,\mathrm{D_L}}} \overline{\Pi}_{h,n} = \overline{\partial\Omega}_{h,\mathrm{D_L}}$;
2. the normal vector $\boldsymbol{N}$ varies continuously over $\Pi_n = \lim_{h\to 0} \Pi_{h,n}$.

We define the sharp corners of $\partial\Omega_{h,\mathrm{D_L}}$ as $\Gamma_h^i := \partial\Pi_{h,n} \cap \partial\Pi_{h,l}$, with $n, l = 1, ..., N, n \neq l$. The boundary of $\partial\Omega_{h,\mathrm{D_L}}$ is defined as follows

$$\Gamma_h^b := \left(\partial\Omega_{h,\mathrm{D_L}} \cap \partial\Omega_{h,\mathrm{D_N}}\right) \bigcup \left(\partial\Omega_{h,\mathrm{D_L}} \cap \partial\Omega_{h,\mathrm{N}}\right).$$

To conclude we let $\Gamma_h = \Gamma_h^i \bigcup \Gamma_h^b$ be the set collecting all the sharp corners and the boundary of $\partial\Omega_{h,\mathrm{D_L}}$.

Let $\mathcal{F}_h^{\mathrm{D_L}}$ be the set collecting all Dirichlet boundary faces where the Lagrange multipliers method is employed. The edges composing the face boundary are collected in the set $\mathcal{E}_{\mathrm{F}}$ for each mesh face $\mathrm{F} \in \mathcal{F}_h^{\mathrm{D_L}}$ such that $\bigcup_{\mathrm{E}\in\mathcal{E}_{\mathrm{F}}} \overline{\mathrm{E}} = \partial\mathrm{F}$. We define two disjoint subsets of the set $\mathcal{E}_{\mathrm{F}}$:

1. $\mathcal{E}_{\mathrm{F}}^{b} = \{\mathrm{E} \in \mathcal{E}_{\mathrm{F}} : \mathrm{E} \subset \Gamma_h\}$: the set of *boundary edges*;

2. $\mathcal{E}_{\mathrm{F}}^{\mathrm{i}} \coloneqq \mathcal{E}_{\mathrm{F}} \setminus \mathcal{E}_{\mathrm{F}}^{b}$: the set of *internal edges*.

3.2.2 Mesh setting for HDG and HHO methods

For the HDG method in Sec. 3.4 and the HHO methods in Sec. 3.5, we define the spatial mesh $\mathcal{M}_h \coloneqq (\mathcal{T}_h, \mathcal{F}_h)$ where $\mathcal{T}_h$ is finite collection of polygonal (if $d = 2$) or polyhedral (if $d = 3$) elements such that $h \coloneqq \max_{\mathrm{T}\in\mathcal{T}_h} h_{\mathrm{T}} > 0$ denotes the meshstep size, while $\mathcal{F}_h$ is a finite collection of line segments (if $d = 2$) or polygonal faces (if $d = 3$). For the sake of brevity, in what follows the term “face” will be used in both two and three space dimensions.

We remark that, while in the dG setting faces are possibly non-planar and even non-connected, HDG and HHO methods are more restrictive with respect to mesh faces definition. In particular, a face F is a non-empty open connected subset of a hyperplane of $\mathbb{R}^d$ and the $(d-1)$-dimensional Hausdorff measure of its relative boundary $\overline{\mathrm{F}} \setminus \mathrm{F}$ is zero (see [45, Definition 1.4]).

For each mesh element $\mathrm{T} \in \mathcal{T}_h$, the faces contained in the element boundary $\partial\mathrm{T}$ are collected in the set $\mathcal{F}_{\mathrm{T}}$. We will impose Dirichlet boundary conditions strongly or using again the Lagrange multipliers method, so, let $\partial\Omega_{h,\mathrm{D}} = \partial\Omega_{h,\mathrm{D_S}} \bigcup \partial\Omega_{h,\mathrm{D_L}}$, where $\partial\Omega_{h,\mathrm{D_S}}$ and $\partial\Omega_{h,\mathrm{D_L}}$ are, respectively, the “strong” and the Lagrange multipliers partitions of the Dirichlet boundary. Subsequently, we define four disjoint subsets of the set $\mathcal{F}_{\mathrm{T}}$:

1. $\mathcal{F}_{\mathrm{T}}^{\mathrm{D_S}} = \{\mathrm{F} \in \mathcal{F}_{\mathrm{T}} : \mathrm{F} \subset \partial\Omega_{h,\mathrm{D_S}}\}$: the set of Dirichlet faces where boundary conditions are strongly enforced;

2. $\mathcal{F}_{\mathrm{T}}^{\mathrm{D_L}} = \{\mathrm{F} \in \mathcal{F}_{\mathrm{T}} : \mathrm{F} \subset \partial\Omega_{h,\mathrm{D_L}}\}$: the set of Dirichlet faces where boundary conditions are enforced using Lagrange multipliers;

3. $\mathcal{F}_{\mathrm{T}}^{\mathrm{N}} = \{\mathrm{F} \in \mathcal{F}_{\mathrm{T}} : \mathrm{F} \subset \partial\Omega_{h,\mathrm{N}}\}$: the set of Neumann boundary faces;

4. $\mathcal{F}_{\mathrm{T}}^{\mathrm{i}} \coloneqq \mathcal{F}_{\mathrm{T}} \setminus \left(\mathcal{F}_{\mathrm{T}}^{\mathrm{D}} \cup \mathcal{F}_{\mathrm{T}}^{\mathrm{N}}\right)$: the set of internal faces.

For all $T \in \mathcal{T}_h$ and all $F \in \mathcal{F}_{\mathrm{T}}$, $\boldsymbol{n}_{\mathrm{TF}}$ denotes the normal vector to F pointing out of T. We remark that is case of boundary faces $\boldsymbol{n}_{\mathrm{TF}}$ can be equal to $\boldsymbol{N}$ or an approximation of $\boldsymbol{N}$, see (3.6).

3.2.3 Numerical integration over reference mesh entities

In order to be able to numerically integrate over mesh elements, mesh faces and mesh edges, we require that, for any Y element or face:

1. there exists a reference entity $\widehat{Y}$ of standardized shape and a polynomial mapping $\Psi_Y : \widehat{Y} \longrightarrow Y$ such that $Y = \Psi_Y(\widehat{Y})$;
2. quadrature rules of arbitrary order are available on the reference entity $\widehat{Y}$.

From the geometrical viewpoint reference entities read as follows

$$\widehat{Y} = \begin{cases} \text{point}, & \text{if } Y \in \mathcal{E}_h, \\ \text{line segment}, & \text{if } Y \in \mathcal{F}_h, \\ \text{polygon}, & \text{if } Y \in \mathcal{T}_h, \end{cases} \text{ if } d = 2;$$

$$\widehat{Y} = \begin{cases} \text{line segment}, & \text{if } Y \in \mathcal{E}_h, \\ \text{polygon}, & \text{if } Y \in \mathcal{F}_h, \\ \text{polyhedron}, & \text{if } Y \in \mathcal{T}_h, \end{cases} \text{ if } d = 3.$$

3.3 Discontinuous Galerkin formulation

We are going to formulate a dG framework that relies on a BR2 discretization of the Lagrangian equation of motion for compressible and incompressible hyperelastic materials. We also account for the implementation of the Lagrange multipliers method for the imposition of Dirichlet boundary conditions (BCs).

Let $\mathbb{P}^{\ell}_{d}$ be the space of d-variate polynomials of total degree $\leq \ell$. For each $\mathrm{T} \in \mathcal{T}_h$, we denote by $\mathcal{P}^{\ell}(\mathrm{T})$ the space spanned by the restriction of $\mathbb{P}^{\ell}_{d}$ to T and by $\mathcal{P}^{\ell}(\mathrm{F})$ the space spanned by the restriction of $\mathbb{P}^{\ell}_{d-1}$ to F. Fix a polynomial degree $k \geq 1$ and let $\mathrm{T} \in \mathcal{T}_h$. We define the *local discrete gradient* $\mathfrak{G}^k_{\mathrm{T}} : H^1(\mathcal{T}_h)^d \to \mathcal{P}^k(\mathrm{T})^{d\times d}$ such that, for all $\boldsymbol{v} \in H^1(\mathcal{T}_h)^d$,

$$\begin{aligned}\int_{\mathrm{T}} \mathfrak{G}^k_{\mathrm{T}}(\boldsymbol{v}) : \boldsymbol{\tau} \coloneqq \int_{\mathrm{T}} \nabla_{\boldsymbol{X}} \boldsymbol{v}_{|\mathrm{T}} : \boldsymbol{\tau} + \\ - \sum_{\mathrm{F}\in\mathcal{F}^{\mathrm{i},\mathrm{D_N}}_{\mathrm{T}}} \frac{1}{2} \int_{\mathrm{F}} (\boldsymbol{n}_{\mathrm{TF}} \otimes [\![\boldsymbol{v}]\!]_{\mathrm{TF}}) : \boldsymbol{\tau} \qquad \forall \boldsymbol{\tau} \in \mathcal{P}^k(\mathrm{T})^{d\times d},\end{aligned}$$

where, for each $\mathrm{F} \in \mathcal{F}^{\mathrm{i},\mathrm{D_N}}_{\mathrm{T}}$, the jump of $\boldsymbol{v}$ across F is defined as

$$[\![\boldsymbol{v}]\!]_{\mathrm{TF}} \coloneqq \begin{cases} \boldsymbol{v}_{|\mathrm{T}} - \boldsymbol{v}_{|\mathrm{T}'} & \text{if } \mathrm{F} \in \mathcal{F}^{\mathrm{i}}_{\mathrm{T}} \cap \mathrm{F}^{\mathrm{i}}_{\mathrm{T}'} \text{ with } \mathrm{T}, \mathrm{T}' \in \mathcal{T}_h, \mathrm{T} \neq \mathrm{T}', \\ 2(\boldsymbol{v}_{|\mathrm{T}} - \boldsymbol{g}_{\mathrm{D}}) & \text{if } \mathrm{F} \in \mathcal{F}^{\mathrm{D_N}}_{\mathrm{T}}. \end{cases} \tag{3.7}$$

Introducing, for any $\mathrm{F} \in \mathcal{F}^{\mathrm{i},\mathrm{D_N}}_{\mathrm{T}}$ and any integer $\ell \geq 0$, the jump lifting operator $\mathfrak{R}^{\ell}_{\mathrm{FT}} : L^2(\mathrm{F})^d \to \mathcal{P}^{\ell}(\mathrm{T})^{d\times d}$ such that, for all $\boldsymbol{\varphi} \in L^2(\mathrm{F})^d$ and all $\boldsymbol{\tau} \in \mathcal{P}^{\ell}(\mathrm{T})^{d\times d}$,

$$\int_{\mathrm{T}} \mathfrak{R}^{\ell}_{\mathrm{FT}}(\boldsymbol{\varphi}) : \boldsymbol{\tau} = \frac{1}{2} \int_{\mathrm{F}} (\boldsymbol{n}_{\mathrm{TF}} \otimes \boldsymbol{\varphi}) : \boldsymbol{\tau},$$

it holds, for all $\boldsymbol{v} \in H^1(\mathcal{T}_h)^d$,

$$\mathfrak{G}_T^k(\boldsymbol{v}) = \nabla_{\boldsymbol{X}} \boldsymbol{v}_{|T} - \sum_{\mathrm{F} \in \mathcal{F}_{\mathrm{T}}^{\mathrm{i},\mathrm{D}_\mathrm{N}}} \mathfrak{R}_{\mathrm{FT}}^k \left([\![\boldsymbol{v}]\!]_{\mathrm{TF}} \right).$$

Based on definition (2.1.1), we introduce two discrete dG versions of the deformation gradient

$$\begin{aligned} \text{for any } \mathrm{T} \in \mathcal{T}_h : \mathfrak{F}_{\mathrm{T}}^k(\boldsymbol{v}) \quad &:= \mathfrak{G}_{\mathrm{T}}^k(\boldsymbol{v}) + \mathbf{1}; \\ \text{for any } \mathrm{T} \in \mathcal{T}_h,\ \mathrm{F} \in \mathcal{F}_{\mathrm{T}}^{\mathrm{i},\mathrm{D}_\mathrm{N}} : \mathfrak{F}_{\mathrm{TF}}^{k+1}(\boldsymbol{v}) &:= \nabla_{\boldsymbol{X}} \boldsymbol{v}_{|\mathrm{T}} - \mathfrak{R}_{\mathrm{FT}}^{k+1} \left([\![\boldsymbol{v}]\!]_{\mathrm{TF}} \right) + \mathbf{1}. \end{aligned}$$

We remark that $\mathfrak{F}_{\mathrm{T}}^k$ relies on jump contributions over $\partial\mathrm{T}$ and jump lifting operator of degree k, while $\mathfrak{F}_{\mathrm{TF}}^{k+1}$ relies solely on the jump lifting operator of degree $k{+}1$ over F. The idea to employ $k{+}1$ lifting operators to get rid of stabilization parameters was first proposed by John *et al.* [55] in the context of LDG discretizations of the Laplace operator with rigorous analysis covering the case of simplicial meshes.

We introduce the scalar- and vector-valued *broken* polynomial spaces

$$\begin{aligned} \mathcal{P}^k(\mathcal{T}_h) &:= \left\{ q_h = (q_{\mathrm{T}})_{\mathrm{T} \in \mathcal{T}_h} : q_T \in \mathcal{P}^k(\mathrm{T}) \text{ for all } \mathrm{T} \in \mathcal{T}_h \right\}, \\ \mathcal{P}^k(\mathcal{T}_h)^d &:= \left\{ \boldsymbol{v}_h = (\boldsymbol{v}_{\mathrm{T}})_{\mathrm{T} \in \mathcal{T}_h} : \boldsymbol{v}_{\mathrm{T}} \in \mathcal{P}^k(\mathrm{T})^d \text{ for all } \mathrm{T} \in \mathcal{T}_h \right\}. \end{aligned}$$

and the vector-valued polynomial space for Lagrange multipliers over Dirichlet boundaries

$$\mathcal{P}^k(\mathcal{F}_h^{\mathrm{D}_\mathrm{L}})^d := \left\{ \widehat{\boldsymbol{s}}_h = (\widehat{\boldsymbol{s}}_{\mathrm{F}})_{\mathrm{F} \in \mathcal{F}_h^{\mathrm{D}_\mathrm{L}}} : \widehat{\boldsymbol{s}}_{\mathrm{F}} \in \mathcal{P}^k(\mathrm{F})^d \text{ for all } \mathrm{F} \in \mathcal{F}_h^{\mathrm{D}_\mathrm{L}} \right\}.$$

Let the $k \geq 1$ denote the polynomial degree, let a mesh element $\mathrm{T} \in \mathcal{T}_h$ and a mesh face $\mathrm{F} \in \mathcal{F}_h^{\mathrm{D}_\mathrm{L}}$ be fixed. Given $(\boldsymbol{u}_h, p_h, \widehat{\boldsymbol{\lambda}}_h) \in \mathcal{P}^k(\mathcal{T}_h)^d \times \mathcal{P}^k(\mathcal{T}_h) \times \mathcal{P}^k(\mathcal{F}_h^{\mathrm{D}_\mathrm{L}})^d$, we define the local residuals

- $r_{\mathrm{T}}^{\mathrm{dG,Lem}}\left((\boldsymbol{u}_h, p_h, \widehat{\boldsymbol{\lambda}}_h); \bullet\right) : \mathcal{P}^k(\mathrm{T})^d \to \mathbb{R}$ of the discrete Lagrangian equation of motion,
- $r_{\mathrm{T}}^{\mathrm{dG,ic}}((\boldsymbol{u}_h, p_h); \bullet) : \mathcal{P}^k(\mathrm{T}) \to \mathbb{R}$ of the discrete incompressibility constraint,
- $r_{\mathrm{F}}^{\mathrm{dG,D_L}}\left((\boldsymbol{u}_h, \widehat{\lambda}_h); \bullet\right) : \mathcal{P}^k(\mathrm{F})^d \to \mathbb{R}$ of the constraints on Dirichlet boundary,

such that: for all $\boldsymbol{v}_{\mathrm{T}} \in \mathcal{P}^k(\mathrm{T})^d$, all $q_{\mathrm{T}} \in \mathcal{P}^k(\mathrm{T})$ and all $\widehat{\boldsymbol{s}}_{\mathrm{F}} \in \mathcal{P}^k(\mathrm{F})$

$$\begin{aligned}
r_{\mathrm{T}}^{\mathrm{dG,Lem}}\left((\boldsymbol{u}_h, p_h, \widehat{\boldsymbol{\lambda}}_h); \boldsymbol{v}_{\mathrm{T}}\right) \coloneqq & \int_{\mathrm{T}} \boldsymbol{P}(\boldsymbol{\mathfrak{F}}_{\mathrm{T}}^k(\boldsymbol{u}_h), p_h) : \nabla_{\boldsymbol{X}} \boldsymbol{v}_{\mathrm{T}} + \\
& - \sum_{\mathrm{F} \in \mathcal{F}_{\mathrm{T}}^{i,\mathrm{D_N}}} \int_{\mathrm{F}} \left[\{\!\{\boldsymbol{P}(\boldsymbol{\mathfrak{F}}_{\mathrm{TF}}^{k+1}(\boldsymbol{u}_h), p_h)\}\!\}_{\mathrm{F}}\, \boldsymbol{n}_{\mathrm{TF}}\right] \cdot \boldsymbol{v}_{\mathrm{T}} + \\
& + \sum_{\mathrm{F} \in \mathcal{F}_{\mathrm{T}}^{i,\mathrm{D_N}}} \int_{\mathrm{F}} \eta_{\mathrm{F}} \left[\{\!\{\boldsymbol{\mathfrak{R}}_{\mathrm{FT}}^k([\![\boldsymbol{u}]\!]_{\mathrm{TF}})\}\!\}_{\mathrm{F}}\, \boldsymbol{n}_{\mathrm{TF}}\right] \cdot \boldsymbol{v}_{\mathrm{T}} + \\
& - \int_{\mathrm{T}} \boldsymbol{f} \cdot \boldsymbol{v}_{\mathrm{T}} - \sum_{\mathrm{F} \in \mathcal{F}_{\mathrm{T}}^{\mathrm{N}}} \int_{\mathrm{F}} \boldsymbol{T}_{\mathrm{N}} \cdot \boldsymbol{v}_{\mathrm{T}} - \sum_{\mathrm{F} \in \mathcal{F}_{\mathrm{T}}^{\mathrm{D_L}}} \int_{\mathrm{F}} \widehat{\boldsymbol{\lambda}}_h \cdot \boldsymbol{v}_{\mathrm{T}},
\end{aligned} \tag{3.8}$$

$$\begin{aligned}
r_{\mathrm{T}}^{\mathrm{dG,ic}}((\boldsymbol{u}_h, p_h); q_{\mathrm{T}}) \coloneqq & \int_{\mathrm{T}} (\det(\boldsymbol{\mathfrak{F}}_{\mathrm{T}}^k(\boldsymbol{u}_h)) - 1)\, q_{\mathrm{T}} + \\
& + \sum_{F \in \mathcal{F}_{\mathrm{T}}^{\mathrm{i}}} \int_{\mathrm{F}} \eta_{\mathrm{LBB}}\, h_{\mathrm{F}}\, [\![p_h]\!]_{\mathrm{TF}}\, q_{\mathrm{T}},
\end{aligned} \tag{3.9}$$

$$r_{\mathrm{F}}^{\mathrm{dG,D_L}}\left((\boldsymbol{u}_h, \widehat{\boldsymbol{\lambda}}_h); \widehat{\boldsymbol{s}}_{\mathrm{F}}\right) \coloneqq \int_{\mathrm{F}} (\boldsymbol{u}_h - \boldsymbol{u}_{\mathrm{D}}) \cdot \widehat{\boldsymbol{s}}_{\mathrm{F}} + \sum_{\mathrm{E} \in \mathcal{E}_{\mathrm{F}}^{i}} \int_{\mathrm{E}} \eta_{\widehat{\boldsymbol{\lambda}}}\, h_{\mathrm{E}}\, [\![\widehat{\boldsymbol{\lambda}}_h]\!]_{\mathrm{FE}} \cdot \widehat{\boldsymbol{s}}_{\mathrm{F}}. \tag{3.10}$$

The average operator in Eq. (3.8) is such that, for all $\varphi \in H^1(\mathcal{T}_h)$ and all $F \in \mathcal{F}_h$,

$$\{\!\{\varphi\}\!\}_F \coloneqq \begin{cases} \frac{1}{2}\left(\varphi_{|\mathrm{T}} + \varphi_{|\mathrm{T}'}\right) & \text{if } \mathrm{F} \in \mathcal{F}_{\mathrm{T}}^{\mathrm{i}} \cap \mathrm{F}_{\mathrm{T}'}^{\mathrm{i}}, \text{ with } \mathrm{T}, \mathrm{T}' \in \mathcal{T}_h,\, \mathrm{T} \neq \mathrm{T}', \\ \varphi_{|\mathrm{F}} & \text{otherwise.} \end{cases}$$

with the understanding that $\{\!\{\bullet\}\!\}_{\mathrm{F}}$ acts component-wise when applied to vector and tensor functions. Furthermore, for any $\mathrm{E} \in \mathcal{E}_{\mathrm{F}}^{\mathrm{i}}$, the edge jump operator in Eq. (3.10) reads

$$[\![\boldsymbol{v}]\!]_{\mathrm{FE}} \coloneqq \boldsymbol{v}_{|\mathrm{F}} - \boldsymbol{v}_{|\mathrm{F}'} \quad \text{if } \mathrm{E} \in \mathcal{E}_{\mathrm{F}} \cap \mathrm{E}_{\mathrm{F}'} \text{ with } \mathrm{F}, \mathrm{F}' \in \mathcal{F}_h^{\mathrm{D_L}},\, \mathrm{F} \neq \mathrm{F}'.$$

With h_{F} and h_{E}, we denote the diameter of a face or an edge, respectively. Note that $h_{\mathrm{E}} = 1$ if $d = 2$.

The local residuals in (3.8)-(3.10) contain several stabilization terms and user-dependent stabilization parameters $\eta_{(\bullet)} > 0$ dictated by stability requirements. The first term in the second line of (3.8) is a stabilization term inspired by [56], where it was introduced to ensure coercivity of the BR1 formulation proposed by Bassi and Rebay [28], see also [57]. The adaptive stabilization parameter η_F is computed as proposed by Eyck and co-workers [27,30], who first introduced the idea of adaptive stabilization in the context of BR1 dG discretizations of nonlinear elasticity problems. A comprehensive description of the procedure involved in the computation of η_F will be given in Sec. 3.3.1. The last term in (3.9), endowed with stabilization parameter η_{LBB}, ensures LBB stability by penalizing the pressure jumps across internal faces, see [58] and [32]. The second term in (3.10), endowed with stabilization parameter $\eta_{\widehat{\lambda}}$, penalizes the Lagrange multipliers jumps across *internal edges* of Dirichlet boundaries. We remark that, for the sake of consistency of the dG formulation, we do not penalize the jumps over the sharp corners Γ_h^i. Indeed, since $\widehat{\boldsymbol{\lambda}}_h$ approximates the stress vector $\boldsymbol{PN}$ and the normal vector $\boldsymbol{N}$ is discontinuous at the sharp corners Γ_h^i, Lagrange multipliers are discontinuous over each $\mathrm{E} \in \mathcal{E}_{\mathrm{F}}^b \cap \Gamma_h^i$. Definitions of $\mathcal{E}_{\mathrm{F}}^{\mathrm{i}}$, $\mathcal{E}_{\mathrm{F}}^b$ and Γ_h^i are given in Sec. 3.2.1.

Assembling *element-by-element* the local residuals (3.8) and (3.9), the two global residuals $r_h^{\mathrm{dG,Lem}}\left((\boldsymbol{u}_h, p_h, \widehat{\boldsymbol{\lambda}}_h); \bullet\right) : \mathcal{P}^k(\mathcal{T}_h)^d \to \mathbb{R}$ and $r_h^{\mathrm{dG,ic}}\left((\boldsymbol{u}_h, p_h); \bullet\right) : \mathcal{P}^k(\mathcal{T}_h) \to \mathbb{R}$ are obtained i.e.

$$r_h^{\mathrm{dG,Lem}}\left((\boldsymbol{u}_h, p_h, \widehat{\boldsymbol{\lambda}}_h); \boldsymbol{v}_h\right) \coloneqq \sum_{\mathrm{T}\in\mathcal{T}_h} r_{\mathrm{T}}^{\mathrm{dG,Lem}}\left((\boldsymbol{u}_h, p_h, \widehat{\boldsymbol{\lambda}}_h); \boldsymbol{v}_{h|\mathrm{T}}\right),$$

$$r_h^{\mathrm{dG,ic}}\left((\boldsymbol{u}_h, p_h); q_h\right) \coloneqq \sum_{\mathrm{T}\in\mathcal{T}_h} r_{\mathrm{T}}^{\mathrm{dG,ic}}\left((\boldsymbol{u}_h, p_h); q_{h|\mathrm{T}}\right).$$

Similarly, the global residual $r_h^{\mathrm{dG,D_L}}\left((\boldsymbol{u}_h, \widehat{\boldsymbol{\lambda}}_h); \bullet\right) : \mathcal{P}^k(\mathcal{F}_h^{\mathrm{D_L}})^d \to \mathbb{R}$ is obtained assembling *face-by-face* the local residual (3.10), *i.e.*

$$r_h^{\mathrm{dG,D_L}}\left((\boldsymbol{u}_h, \widehat{\boldsymbol{\lambda}}_h); \widehat{\boldsymbol{s}}_h\right) \coloneqq \sum_{\mathrm{F}\in\mathcal{F}_h^{\mathrm{D_L}}} r_{\mathrm{F}}^{\mathrm{dG,D_L}}\left((\boldsymbol{u}_h, \widehat{\boldsymbol{\lambda}}_h); \widehat{\boldsymbol{s}}_{h|\mathrm{F}}\right).$$

Define, for the sake of brevity

$$\boldsymbol{W}_{\mathrm{ie},h}^{\mathrm{dG},k} = \mathcal{P}^k(\mathcal{T}_h)^d \times \mathcal{P}^k(\mathcal{T}_h) \times \mathcal{P}^k(\mathcal{F}_h^{\mathrm{D_L}})^d,$$

$$\boldsymbol{W}_{\mathrm{ce},h}^{\mathrm{dG},k} = \mathcal{P}^k(\mathcal{T}_h)^d \times \mathcal{P}^k(\mathcal{F}_h^{\mathrm{D_L}})^d.$$

The discrete nonlinear elasticity problems reads as follows:

- **Incompressible material**: find $(\boldsymbol{u}_h, p_h, \widehat{\boldsymbol{\lambda}}_h) \in \boldsymbol{W}_{ie,h}^{\mathrm{dG},k}$ such that

  $$r_{\mathrm{ie},h}^{\mathrm{dG}}\left((\boldsymbol{u}_h, p_h, \widehat{\boldsymbol{\lambda}}_h); (\boldsymbol{v}_h, q_h, \widehat{\boldsymbol{s}}_h)\right) = 0 \qquad \forall(\boldsymbol{v}_h, q_h, \widehat{\boldsymbol{s}}_h) \in \boldsymbol{W}_{ie,h}^{\mathrm{dG},k}, \tag{3.11}$$

  where, given $(\boldsymbol{u}_h, p_h, \widehat{\boldsymbol{s}}_h) \in \boldsymbol{W}_{ie,h}^{\mathrm{dG},k}$, $r_{\mathrm{ie},h}^{\mathrm{dG}}\left((\boldsymbol{u}_h, p_h, \widehat{\boldsymbol{\lambda}}_h); \bullet\right) : \boldsymbol{W}_{ie,h}^{\mathrm{dG},k} \to \mathbb{R}$ is such that $\forall(\boldsymbol{v}_h, q_h, \widehat{\boldsymbol{s}}_h) \in \boldsymbol{W}_{ie,h}^{\mathrm{dG},k}$

  $$\begin{aligned} r_{\mathrm{ie},h}^{\mathrm{dG}}\left((\boldsymbol{u}_h, p_h, \widehat{\boldsymbol{\lambda}}_h); (\boldsymbol{v}_h, q_h, \widehat{\boldsymbol{s}}_h)\right) = {} & r_h^{\mathrm{dG,Lem}}\left((\boldsymbol{u}_h, p_h, \widehat{\boldsymbol{\lambda}}_h); \boldsymbol{v}_h\right) + \\ & + r_h^{\mathrm{dG,ic}}\left((\boldsymbol{u}_h, p_h); q_h\right) + \\ & + r_h^{\mathrm{dG,D_L}}\left((\boldsymbol{u}_h, \widehat{\boldsymbol{\lambda}}_h); \widehat{\boldsymbol{s}}_h\right); \end{aligned} \tag{3.12}$$

- **Compressible material**: find $(\boldsymbol{u}_h, \widehat{\boldsymbol{\lambda}}_h) \in \boldsymbol{W}^{\mathrm{dG},k}_{ce,h}$ such that

$$r^{\mathrm{dG}}_{\mathrm{ce},h}\left((\boldsymbol{u}_h, \widehat{\boldsymbol{\lambda}}_h); (\boldsymbol{v}_h, \widehat{\boldsymbol{s}}_h)\right) = 0 \qquad \forall (\boldsymbol{v}_h, \widehat{\boldsymbol{s}}_h) \in \boldsymbol{W}^{\mathrm{dG},k}_{ce,h}, \tag{3.13}$$

where, given $(\boldsymbol{u}_h, \widehat{\boldsymbol{\lambda}}_h) \in \boldsymbol{W}^{\mathrm{dG},k}_{ce,h}$, $r^{\mathrm{dG}}_{\mathrm{ce},h}\left((\boldsymbol{u}_h, \widehat{\boldsymbol{\lambda}}_h); \bullet\right) : \boldsymbol{W}^{\mathrm{dG},k}_{ce,h} \to \mathbb{R}$ is such that $\forall (\boldsymbol{v}_h, \widehat{\boldsymbol{s}}_h) \in \boldsymbol{W}^{\mathrm{dG},k}_{ce,h}$

$$r^{\mathrm{dG}}_{\mathrm{ce},h}\left(\boldsymbol{u}_h; \boldsymbol{v}_h\right) = r^{\mathrm{dG,Lem}}_{h}\left((\boldsymbol{u}_h, \widehat{\boldsymbol{\lambda}}_h); (\boldsymbol{v}_h, \widehat{\boldsymbol{s}}_h)\right) + r^{\mathrm{dG,D_L}}_{h}\left((\boldsymbol{u}_h, \widehat{\boldsymbol{\lambda}}_h); \widehat{\boldsymbol{s}}_h\right). \tag{3.14}$$

3.3.1 Adaptive stabilization for dG methods

If, on the one hand, the amount of stabilization required to ensure the coercivity of dG formulations can be precisely estimated in the context of linear elasticity problems, see [14] and [16], on the other hand, penalty parameters are not known a priori in the case of finite deformations of hyperelastic materials, see [29] and [43]. This is an uncomfortable situation as excessive stabilization worsen the condition number of system matrices and insufficient stabilization severely affects the robustness of numerical schemes. As a result, a tedious trial and error approach would often be required in practice. The adaptive stabilization strategies proposed and analysed by Eyck and co-workers [27]- [30] in the context of BR1 dG formulations are a crucial tool for mitigating this drawback.

The adaptive stabilization introduced in (3.8), can be considered the natural extension of the approach proposed in [30] to the BR2 dG discretization. The stabilization parameter η_{F} is defined as follows

$$\eta_{\mathrm{F}} = \epsilon + \beta\, \lambda_{\mathrm{F}}$$

where $\epsilon, \beta \geq 0$ are user-dependent parameters. Let a mesh element $\mathrm{T} \in \mathcal{T}_h$ and a mesh face $\mathrm{F} \in \mathcal{F}^{\mathrm{i,D_N}}_{\mathrm{T}}$ be fixed, for each point $\boldsymbol{X} \in \mathrm{F}$

$$\lambda_{\mathrm{TF}}(\boldsymbol{X}) = \max\left\{0, -\min_{0 \neq \boldsymbol{G} \in \mathbb{R}^{d\times d}} \frac{\boldsymbol{G} : \mathbb{A}(\mathfrak{F}^{k+1}_{\mathrm{TF}}(\boldsymbol{u}_h(\boldsymbol{X})), p_h) : \boldsymbol{G}}{\boldsymbol{G} : \boldsymbol{G}}\right\}$$

and

$$\lambda_{\mathrm{F}} = \begin{cases} \frac{\overline{\lambda}_{\mathrm{TF}} + \overline{\lambda}_{\mathrm{T'F}}}{2} & \text{if } \mathrm{F} \in \mathcal{F}^{\mathrm{i}}_{\mathrm{T}} \cap \mathrm{F}^{\mathrm{i}}_{\mathrm{T'}} \text{ with } \mathrm{T}, \mathrm{T'} \in \mathcal{T}_h,\ \mathrm{T} \neq \mathrm{T'}, \\ \overline{\lambda}_{\mathrm{TF}} & \text{if } \mathrm{F} \in \mathcal{F}^{\mathrm{D_N}}_{\mathrm{T}}. \end{cases}$$

where $\mathbb{A}$ is the fourth-order elasticity tensor described in Sec. 2.3.3 and $\overline{\lambda}_{\mathrm{TF}}$ is the mean value of $\lambda_{\mathrm{TF}}(\boldsymbol{X})$ over F.

As detailed in Itskov [59, 60], the nine (in 3D, six in 2D) eigenvalues λ_i of $\mathbb{A}$ can be obtained solving the characteristic equation

$$\det\left(\underline{\mathbb{A} - \lambda \mathbb{I}}\right) = 0 \tag{3.15}$$

where $\mathbb{I} = \delta_{ik}\delta_{jl}\,\boldsymbol{E}_i \otimes \boldsymbol{E}_j \otimes \boldsymbol{E}_k \otimes \boldsymbol{E}_l$ is the fourth-order identity tensor and the underline $\underline{\bullet}$ indicates one of the possible matrix form of a fourth-order tensor such that

$$\underline{\mathbb{A}} = \begin{bmatrix}
\mathbb{A}_{0000} & \mathbb{A}_{0001} & \mathbb{A}_{0002} & \mathbb{A}_{0010} & \mathbb{A}_{0011} & \mathbb{A}_{0012} & \mathbb{A}_{0020} & \mathbb{A}_{0021} & \mathbb{A}_{0022} \\
\mathbb{A}_{0100} & \mathbb{A}_{0101} & \mathbb{A}_{0102} & \mathbb{A}_{0110} & \mathbb{A}_{0111} & \mathbb{A}_{0112} & \mathbb{A}_{0120} & \mathbb{A}_{0121} & \mathbb{A}_{0122} \\
\mathbb{A}_{0200} & \mathbb{A}_{0201} & \mathbb{A}_{0202} & \mathbb{A}_{0210} & \mathbb{A}_{0211} & \mathbb{A}_{0212} & \mathbb{A}_{0220} & \mathbb{A}_{0221} & \mathbb{A}_{0222} \\
\mathbb{A}_{1000} & \mathbb{A}_{1001} & \mathbb{A}_{1002} & \mathbb{A}_{1010} & \mathbb{A}_{1011} & \mathbb{A}_{1012} & \mathbb{A}_{1020} & \mathbb{A}_{1021} & \mathbb{A}_{1022} \\
\mathbb{A}_{1100} & \mathbb{A}_{1101} & \mathbb{A}_{1102} & \mathbb{A}_{1110} & \mathbb{A}_{1111} & \mathbb{A}_{1112} & \mathbb{A}_{1120} & \mathbb{A}_{1121} & \mathbb{A}_{1122} \\
\mathbb{A}_{1200} & \mathbb{A}_{1201} & \mathbb{A}_{1202} & \mathbb{A}_{1210} & \mathbb{A}_{1211} & \mathbb{A}_{1212} & \mathbb{A}_{1220} & \mathbb{A}_{1221} & \mathbb{A}_{1222} \\
\mathbb{A}_{2000} & \mathbb{A}_{2001} & \mathbb{A}_{2002} & \mathbb{A}_{2010} & \mathbb{A}_{2011} & \mathbb{A}_{2012} & \mathbb{A}_{2020} & \mathbb{A}_{2021} & \mathbb{A}_{2022} \\
\mathbb{A}_{2100} & \mathbb{A}_{2101} & \mathbb{A}_{2102} & \mathbb{A}_{2110} & \mathbb{A}_{2111} & \mathbb{A}_{2112} & \mathbb{A}_{2120} & \mathbb{A}_{2121} & \mathbb{A}_{2122} \\
\mathbb{A}_{2200} & \mathbb{A}_{2201} & \mathbb{A}_{2202} & \mathbb{A}_{2210} & \mathbb{A}_{2211} & \mathbb{A}_{2212} & \mathbb{A}_{2220} & \mathbb{A}_{2221} & \mathbb{A}_{2222}
\end{bmatrix}$$

and

$$\underline{\mathbb{I}} = \begin{bmatrix}
1 & 0 & 0 & 0 & 0 & 0 & 0 & 0 & 0 \\
0 & 1 & 0 & 0 & 0 & 0 & 0 & 0 & 0 \\
0 & 0 & 1 & 0 & 0 & 0 & 0 & 0 & 0 \\
0 & 0 & 0 & 1 & 0 & 0 & 0 & 0 & 0 \\
0 & 0 & 0 & 0 & 1 & 0 & 0 & 0 & 0 \\
0 & 0 & 0 & 0 & 0 & 1 & 0 & 0 & 0 \\
0 & 0 & 0 & 0 & 0 & 0 & 1 & 0 & 0 \\
0 & 0 & 0 & 0 & 0 & 0 & 0 & 1 & 0 \\
0 & 0 & 0 & 0 & 0 & 0 & 0 & 0 & 1
\end{bmatrix}.$$

Problem (3.15) is solved for each quadrature point of each mesh face at the first step of each Newton iteration involved in the globalisation strategy presented in Sec. 3.6.

3.4 Hybridizable Discontinuous Galerkin formulation

Hybridizable Discontinuous Galerkin (HDG) methods are based on the following key features:

- **discrete unknowns** that are broken polynomials over mesh elements and mesh faces;
- **local gradient reconstruction** solving local problems involving element and element faces unknowns;
- **stabilization operators** that rely on the jump between the trace of element unknowns and face unknowns.

In the following, we present the HDG method for nonlinear elasticity problems originally introduced by Kabaria *et al.* [1]. We also consider the possibility to enforce Dirichlet boundary conditions using the Lagrange Multiplier method.

Let $\mathbb{P}_d^\ell$ be the space of d-variate polynomials of total degree $\leq \ell$. We denote by $\mathcal{P}^\ell(\mathrm{T})$ the space spanned by the restriction to T of functions in $\mathbb{P}_d^\ell$ and by $\mathcal{P}^\ell(\mathrm{F})$ the space spanned by the restriction to F of functions in $\mathbb{P}_{d-1}^\ell$.

Let $k \geq 1$ be a fixed polynomial degree. In addition to element-based unknowns $\boldsymbol{v}_\mathrm{T} \in \mathcal{P}^k(\mathrm{T})^d$, the HDG methods also introduces, over the element boundary $\partial\mathrm{T}$, the unknowns $\boldsymbol{v}_{\partial\mathrm{T}} \in \mathcal{P}^k(\mathcal{F}_\mathrm{T})^d = \bigtimes_{\mathrm{F}\in\mathcal{F}_\mathrm{T}} \mathcal{P}^k(\mathrm{F})$ such that $\boldsymbol{v}_{\partial\mathrm{T}} = (\boldsymbol{v}_\mathrm{F})_{\mathrm{F}\in\mathcal{F}_\mathrm{T}}$ and $\boldsymbol{v}_\mathrm{F} \in \mathcal{P}^k(\mathrm{F})^d$. For future use, we define $\boldsymbol{v}_{\partial\mathrm{T}_\mathrm{L}} = (\boldsymbol{v}_\mathrm{F})_{\mathrm{F}\in\mathcal{F}_\mathrm{T}^{\mathrm{D_L}}}$ with $\boldsymbol{v}_{\partial\mathrm{T}_\mathrm{L}} \in \mathcal{P}^k(\mathcal{F}_\mathrm{T}^{\mathrm{D_L}})^d = \bigtimes_{\mathrm{F}\in\mathcal{F}_\mathrm{T}^{\mathrm{D_L}}} \mathcal{P}^k(\mathrm{F})$.
So, $(\boldsymbol{v}_\mathrm{T}, \boldsymbol{v}_{\partial\mathrm{T}})$ identifies the pair of HDG local degrees of freedom that lives in

$$\boldsymbol{U}_\mathrm{T}^k := \mathcal{P}^k(\mathrm{T})^d \times \mathcal{P}^k(\mathcal{F}_\mathrm{T})^d.$$

For future use, we also define the global HDG space as

$$\boldsymbol{U}_h^k := \mathcal{P}^k(\mathcal{T}_h)^d \times \mathcal{P}^k(\mathcal{F}_h)^d \tag{3.16}$$

where

$$\mathcal{P}^k(\mathcal{T}_h)^d := \bigtimes_{\mathrm{T}\in\mathcal{T}_h} \mathcal{P}^k(\mathrm{T})^d,$$
$$\mathcal{P}^k(\mathcal{F}_h)^d := \bigtimes_{\mathrm{F}\in\mathcal{F}_h} \mathcal{P}^k(\mathrm{F})^d,$$

so that an element of $\boldsymbol{U}_h^k$ will be denoted as $(\boldsymbol{v}_{\mathcal{T}_h}, \boldsymbol{v}_{\mathcal{F}_h})$.

The value of discrete face unknowns $\boldsymbol{v}_\mathrm{F} \in \mathcal{F}_h^{\mathrm{D_S}}$ on the Dirichlet boundary may be enforced strongly relying on the modified space

$$\boldsymbol{U}_h^{k,\mathrm{D_S}} := \left\{(\boldsymbol{v}_{\mathcal{T}_h}, \boldsymbol{v}_{\mathcal{F}_h}) \in \boldsymbol{U}_h^k : \boldsymbol{v}_\mathrm{F} = \boldsymbol{\Pi}_\mathrm{F}^k(\boldsymbol{u}_\mathrm{D}), \forall \mathrm{F} \in \mathcal{F}_h^{\mathrm{D_S}}\right\}$$

where $\boldsymbol{\Pi}_\mathrm{F}^k$ is the L^2-orthogonal projector on $\mathcal{P}^k(\mathrm{F})^d$.

In each mesh cell $\mathrm{T} \in \mathcal{T}_h$, the local gradient reconstruction is enabled by an operator $\mathcal{G}_\mathrm{T}^k : \boldsymbol{U}_\mathrm{T}^k \to \mathcal{P}^k(\mathrm{T})^{d\times d}$. The *local reconstructed gradient* $\mathcal{G}_\mathrm{T}^k(\boldsymbol{v}_\mathrm{T}, \boldsymbol{v}_{\partial\mathrm{T}}) \in \mathcal{P}^k(\mathrm{T})^{d\times d}$ is obtained solving the problem

$$\int_\mathrm{T} \mathcal{G}_\mathrm{T}(\boldsymbol{v}_\mathrm{T}, \boldsymbol{v}_{\partial\mathrm{T}}) : \boldsymbol{\tau} = \int_\mathrm{T} \nabla_{\boldsymbol{X}} \boldsymbol{v}_\mathrm{T} : \boldsymbol{\tau} + \sum_{\mathrm{F}\in\mathcal{F}_\mathrm{T}} \int_\mathrm{F} (\boldsymbol{v}_\mathrm{F} - \boldsymbol{v}_\mathrm{T}) \cdot \boldsymbol{\tau}\, \boldsymbol{n}_\mathrm{TF} \tag{3.17}$$

for all $\boldsymbol{\tau} \in \mathcal{P}^k(\mathrm{T})^{d\times d}$. This problem requires to solve a small linear system involving the inversion of a mass matrix associated with the basis of polynomial space $\mathcal{P}^k(\mathrm{T})^{d\times d}$. Being $\mathscr{G}^k_{\mathrm{T}}$ a local operator, the reconstruction of the gradient on each cell is a task suitable for parallel computation.
Being the gradient locally reconstructed in the polynomial space $\mathcal{P}^k(\mathrm{T})^{d\times d}$, the semi-norm $|(\boldsymbol{v}_{\mathrm{T}}, \boldsymbol{v}_{\partial\mathrm{T}})|_T$ for all $(\boldsymbol{v}_{\mathrm{T}}, \boldsymbol{v}_{\partial\mathrm{T}}) \in \boldsymbol{U}^k_{\mathrm{T}}$ is not controlled by the norm $\|\mathscr{G}^k_{\mathrm{T}}(\boldsymbol{v}_{\mathrm{T}}, \boldsymbol{v}_{\partial\mathrm{T}})\|_{L^2(\mathrm{T})}$ and a stabilization term is required (see [2]).

The HDG stabilization term is based on the operator $\widetilde{\mathfrak{s}}^k_{\partial\mathrm{T}} : \boldsymbol{U}^k_{\mathrm{T}} \to \mathcal{P}^k(\mathcal{F}_{\mathrm{T}})^d$ where

$$\widetilde{\mathfrak{s}}^k_{\partial\mathrm{T}}(\boldsymbol{v}_{\mathrm{T}}, \boldsymbol{v}_{\partial\mathrm{T}}) = \boldsymbol{v}_{\mathrm{T}} - \boldsymbol{v}_{\partial\mathrm{T}}$$

when the same polynomial order k is used for both element and face unknowns[1]. The reader can find the alternative HHO version of this stabilization term in Sec. 3.5.2.

Before introducing the local residual used to solve the nonlinear elasticity problem, we define the discrete HDG version of the local deformation gradient

$$\mathscr{F}^k_{\mathrm{T}}(\boldsymbol{v}_{\mathrm{T}}, \boldsymbol{v}_{\partial\mathrm{T}}) \coloneqq \mathscr{G}^k_{\mathrm{T}}(\boldsymbol{v}_{\mathrm{T}}, \boldsymbol{v}_{\partial\mathrm{T}}) + \mathbf{1}$$

where $\mathscr{G}^k_{\mathrm{T}}$ from Eq. (3.17).

Now, given $(\boldsymbol{u}_{\mathrm{T}}, \boldsymbol{u}_{\partial\mathrm{T}}, \widehat{\boldsymbol{\lambda}}_{\partial\mathrm{T}_{\mathrm{L}}}) \in \boldsymbol{U}^k_{\mathrm{T}} \times \mathcal{P}^k(\mathcal{F}^{\mathrm{D_L}}_{\mathrm{T}})^d$, we are ready to introduce the local residual $r^{\mathrm{HDG,Lem}}_{\mathrm{T}}((\boldsymbol{u}_{\mathrm{T}}, \boldsymbol{u}_{\partial\mathrm{T}}, \widehat{\boldsymbol{\lambda}}_{\partial\mathrm{T}_{\mathrm{L}}}); \bullet) : \boldsymbol{U}^k_{\mathrm{T}} \to \mathbb{R}$ of the discrete Lagrangian equation of motion

$$\begin{aligned}
& r^{\mathrm{HDG,Lem}}_{\mathrm{T}}((\boldsymbol{u}_{\mathrm{T}}, \boldsymbol{u}_{\partial\mathrm{T}}, \widehat{\boldsymbol{\lambda}}_{\partial\mathrm{T}_{\mathrm{L}}}); (\boldsymbol{v}_{\mathrm{T}}, \boldsymbol{v}_{\partial\mathrm{T}})) = \\
& = \int_{\mathrm{T}} \boldsymbol{P}(\mathscr{F}^k_{\mathrm{T}}(\boldsymbol{u}_{\mathrm{T}}, \boldsymbol{u}_{\partial\mathrm{T}})) \cdot \mathscr{G}^k_{\mathrm{T}}(\boldsymbol{v}_{\mathrm{T}}, \boldsymbol{v}_{\partial\mathrm{T}}) + \\
& + \int_{\partial\mathrm{T}} \xi\, \widetilde{\mathfrak{s}}^k_{\partial\mathrm{T}}(\boldsymbol{u}_{\mathrm{T}}, \boldsymbol{u}_{\partial\mathrm{T}}) : \widetilde{\mathfrak{s}}^k_{\partial\mathrm{T}}(\boldsymbol{v}_{\mathrm{T}}, \boldsymbol{v}_{\partial\mathrm{T}}) + \\
& - \int_{\mathrm{T}} \boldsymbol{f} \cdot \boldsymbol{v}_{\mathrm{T}} - \sum_{\mathrm{F}\in\mathcal{F}^{\mathrm{N}}_{\mathrm{T}}} \int_{\mathrm{F}} \boldsymbol{T}_{\mathrm{N}} \cdot \boldsymbol{v}_{\mathrm{F}} + \\
& - \sum_{\mathrm{F}\in\mathcal{F}^{\mathrm{D_L}}_{\mathrm{T}}} \int_{\mathrm{F}} \widehat{\boldsymbol{\lambda}}_{\mathrm{F}} \cdot \boldsymbol{v}_{\mathrm{F}}
\end{aligned} \tag{3.18}$$

where, in the second line, ξ is a user-dependent parameter that should be tweaked to ensure coercivity of the method.

---

[1] The stabilization operator becomes $\widetilde{\boldsymbol{S}}^k_{\partial\mathrm{T}} = \boldsymbol{\Pi}^k_{\partial\mathrm{T}}(\boldsymbol{v}_{\partial\mathrm{T}} - \boldsymbol{v}_{\mathrm{T}})$ when cell unknowns are of order $k+1$.

Enforcing the Dirichlet boundary conditions with the Lagrange multiplier method requires the definition of the local residual $r_{\mathrm{F}}^{\mathrm{HDG,D_L}}(\boldsymbol{u}_{\mathrm{F}};\bullet) : \mathcal{P}^k(\mathrm{F})^d \to \mathbb{R}$ of the constraint, such that

$$r_{\mathrm{F}}^{\mathrm{HDG,D_L}}(\boldsymbol{u}_{\mathrm{F}};\widehat{\boldsymbol{s}}_{\mathrm{F}}) \coloneqq \int_{\mathrm{F}} (\boldsymbol{u}_{\mathrm{F}} - \boldsymbol{u}_{\mathrm{D}}) \cdot \widehat{\boldsymbol{s}}_{\mathrm{F}}. \tag{3.19}$$

Define, for the sake of brevity,

$$\boldsymbol{W}_{\mathrm{ce},h}^{\mathrm{HDG},k} = \boldsymbol{U}_h^{k,\mathrm{D_S}} \times \mathcal{P}^k(\mathcal{F}_h^{\mathrm{D_L}})^d$$

and let be $(\boldsymbol{u}_{\mathcal{T}_h}, \boldsymbol{u}_{\mathcal{F}_h}, \widehat{\boldsymbol{\lambda}}_{\mathcal{F}_h^{\mathrm{D_L}}}) \in \boldsymbol{W}_{\mathrm{ce},h}^{\mathrm{HDG},k}$.
The global residuals $r_h^{\mathrm{HDG,Lem}}((\boldsymbol{u}_{\mathcal{T}_h}, \boldsymbol{u}_{\mathcal{F}_h}, \widehat{\boldsymbol{\lambda}}_{\mathcal{F}_h^{\mathrm{D_L}}});\bullet) : \boldsymbol{U}_h^k \to \mathbb{R}$ is obtained assembling *element-by-element* the local residual (3.18), such that

$$\begin{aligned} & r_h^{\mathrm{HDG,Lem}}\left((\boldsymbol{u}_{\mathcal{T}_h}, \boldsymbol{u}_{\mathcal{F}_h}, \widehat{\boldsymbol{\lambda}}_{\mathcal{F}_h^{\mathrm{D_L}}});(\boldsymbol{v}_{\mathcal{T}_h}, \boldsymbol{v}_{\mathcal{F}_h})\right) \coloneqq \\ & \coloneqq \sum_{\mathrm{T}\in\mathcal{T}_h} r_{\mathrm{T}}^{\mathrm{HDG,Lem}}\left((\boldsymbol{u}_{\mathcal{T}_h|\mathrm{T}}, \boldsymbol{u}_{\mathcal{F}_h|\partial\mathrm{T}}, \widehat{\boldsymbol{\lambda}}_{\mathcal{F}_h^{\mathrm{D_L}}|\partial\mathrm{T_L}});(\boldsymbol{v}_{\mathcal{T}_h|\mathrm{T}}, \boldsymbol{v}_{\mathcal{F}_h|\partial\mathrm{T}})\right). \end{aligned} \tag{3.20}$$

Analogously, assembling *face-by-face* the local residual (3.19), the global residual $r_h^{\mathrm{HDG,D_L}}(\boldsymbol{u}_h;\bullet) : \mathcal{P}^k(\mathcal{F}_h^{\mathrm{D_L}})^d \to \mathbb{R}$ is i.e.

$$r_h^{\mathrm{HDG,D_L}}\left(\boldsymbol{u}_{\mathcal{F}_h};\widehat{\boldsymbol{s}}_{\mathcal{F}_h^{\mathrm{D_L}}}\right) \coloneqq \sum_{\mathrm{F}\in\mathcal{F}_h^{\mathrm{D_L}}} r_{\mathrm{F}}^{\mathrm{HDG,D_L}}\left(\boldsymbol{u}_{\mathcal{F}_h|\mathrm{F}};\widehat{\boldsymbol{s}}_{\mathcal{F}_h^{\mathrm{D_L}}|\mathrm{F}}\right). \tag{3.21}$$

Adding the global residual (3.21) of the Lagrange multipliers constraint to Eq. (3.20), the HDG discretization of the nonlinear elasticity problem with compressible constitutive law reads as find $(\boldsymbol{u}_{\mathcal{T}_h}, \boldsymbol{u}_{\mathcal{F}_h}, \widehat{\boldsymbol{\lambda}}_{\mathcal{F}_h^{\mathrm{D_L}}}) \in \boldsymbol{W}_{\mathrm{ce},h}^{\mathrm{HDG},k}$ such that

$$r_{\mathrm{ce},h}^{\mathrm{HDG}}\left((\boldsymbol{u}_{\mathcal{T}_h}, \boldsymbol{u}_{\mathcal{F}_h}, \widehat{\boldsymbol{\lambda}}_{\mathcal{F}_h^{\mathrm{D_L}}});(\boldsymbol{v}_{\mathcal{T}_h}, \boldsymbol{v}_{\mathcal{F}_h}, \widehat{\boldsymbol{s}}_{\mathcal{F}_h^{\mathrm{D_L}}})\right) = 0 \tag{3.22}$$

for all $(\boldsymbol{v}_{\mathcal{T}_h}, \boldsymbol{v}_{\mathcal{F}_h}, \widehat{\boldsymbol{s}}_{\mathcal{F}_h^{\mathrm{D_L}}}) \in \boldsymbol{W}_{\mathrm{ce},h}^{\mathrm{HDG},k}$ and where $r_{\mathrm{ce},h}^{\mathrm{HDG}}\left((\boldsymbol{u}_{\mathcal{T}_h}, \boldsymbol{u}_{\mathcal{F}_h}, \widehat{\boldsymbol{\lambda}}_{\mathcal{F}_h^{\mathrm{D_L}}});\bullet\right) : \boldsymbol{W}_{\mathrm{ce},h}^{\mathrm{HDG},k} \to \mathbb{R}$ is such that for all $(\boldsymbol{v}_{\mathcal{T}_h}, \boldsymbol{v}_{\mathcal{F}_h}, \widehat{\boldsymbol{s}}_{\mathcal{F}_h^{\mathrm{D_L}}}) \in \boldsymbol{W}_{\mathrm{ce},h}^{\mathrm{HDG},k}$

$$\begin{aligned} & r_{\mathrm{ce},h}^{\mathrm{HDG}}\left((\boldsymbol{u}_{\mathcal{T}_h}, \boldsymbol{u}_{\mathcal{F}_h}, \widehat{\boldsymbol{\lambda}}_{\mathcal{F}_h^{\mathrm{D_L}}});(\boldsymbol{v}_{\mathcal{T}_h}, \boldsymbol{v}_{\mathcal{F}_h}, \widehat{\boldsymbol{s}}_{\mathcal{F}_h^{\mathrm{D_L}}})\right) = \\ & = r_h^{\mathrm{HDG,Lem}}\left((\boldsymbol{u}_{\mathcal{T}_h}, \boldsymbol{u}_{\mathcal{F}_h}, \widehat{\boldsymbol{\lambda}}_{\mathcal{F}_h^{\mathrm{D_L}}});(\boldsymbol{v}_{\mathcal{T}_h}, \boldsymbol{v}_{\mathcal{F}_h})\right) + \\ & + r_h^{\mathrm{HDG,D_L}}\left(\boldsymbol{u}_{\mathcal{F}_h};\widehat{\boldsymbol{s}}_{\mathcal{F}_h^{\mathrm{D_L}}}\right). \end{aligned} \tag{3.23}$$

3.5 Hybrid High-Order formulations

Similarly to HDG methods, Hybrid High-Order (HHO) methods rely on discrete unknowns over mesh element and mesh faces, local gradient reconstruction and stabilization terms. Two HHO methods, based on the original formulation introduced in [2], are here presented accounting for the possibility to enforce Dirichlet boundary conditions using the Lagrange Multiplier method.

HHO and HDG formulations differ for the space in which the gradient is reconstructed (uHHO in Sec. 3.5.1) or for the stabilization term (sHHO in Sec. 3.5.2). As reported in [2], in each mesh cell $\mathrm{T} \in \mathcal{T}_h$, the discrete deformation gradient $\mathscr{F}^k_{\mathrm{T}}(\boldsymbol{v}_{\mathrm{T}}, \boldsymbol{v}_{\partial\mathrm{T}}) := \mathscr{G}^k_{\mathrm{T}}(\boldsymbol{v}_{\mathrm{T}}, \boldsymbol{v}_{\partial\mathrm{T}}) + \boldsymbol{1}$ is based on the local gradient reconstruction enabled by the operator $\mathscr{G}^k_{\mathrm{T}} : \boldsymbol{U}^k_{\mathrm{T}} \to \mathcal{R}(\mathrm{T})^{d\times d}$ from Eq. (3.17). $\mathcal{R}(\mathrm{T})^{d\times d}$ may coincides with one of the following spaces: $\mathcal{P}^{k+1}(\mathrm{T})^{d\times d}$ or $(\mathbb{RTN}^k_d(\mathrm{T}))^{d\times d}$ in the context of the unstabilized methods and $\mathcal{P}^k(\mathrm{T})^{d\times d}$ in the context of stabilized methods.

3.5.1 Unstabilized HHO method

Set $\mathcal{R}(\mathrm{T})^{d\times d} = \mathcal{P}^{k+1}(\mathrm{T})^{d\times d}$ such that the local discrete gradient $\mathscr{G}^k_{\mathrm{T}}(\boldsymbol{v}_{\mathrm{T}}, \boldsymbol{v}_{\partial\mathrm{T}})$ is reconstructed in $\mathcal{P}^{k+1}(\mathrm{T})^{d\times d}$ (the use of the RTN space is not investigated in this work, see *e.g.* [2] for further details). Given $(\boldsymbol{u}_{\mathrm{T}}, \boldsymbol{u}_{\partial\mathrm{T}}, \widehat{\boldsymbol{\lambda}}_{\partial\mathrm{T}_{\mathrm{L}}}) \in \boldsymbol{U}^k_{\mathrm{T}} \times \mathcal{P}^k(\mathcal{F}^{\mathrm{D_L}}_{\mathrm{T}})^d$, the local residual of the discrete Lagrangian equation of motion $r^{\mathrm{uHHO,Lem}}_{\mathrm{T}}((\boldsymbol{u}_{\mathrm{T}}, \boldsymbol{u}_{\partial\mathrm{T}}, \widehat{\boldsymbol{\lambda}}_{\partial\mathrm{T}_{\mathrm{L}}}), \bullet) : \boldsymbol{U}^k_{\mathrm{T}} \to \mathbb{R}$ reads

$$
\begin{aligned}
&r^{\mathrm{uHHO,Lem}}_{\mathrm{T}}((\boldsymbol{u}_{\mathrm{T}}, \boldsymbol{u}_{\partial\mathrm{T}}, \widehat{\boldsymbol{\lambda}}_{\partial\mathrm{T}_{\mathrm{L}}}); (\boldsymbol{v}_{\mathrm{T}}, \boldsymbol{v}_{\partial\mathrm{T}})) = \\
&= \int_{\mathrm{T}} \boldsymbol{P}(\mathscr{F}^k_{\mathrm{T}}(\boldsymbol{u}_{\mathrm{T}}, \boldsymbol{u}_{\partial\mathrm{T}}), 0) : \mathscr{G}^k_{\mathrm{T}}(\boldsymbol{v}_{\mathrm{T}}, \boldsymbol{v}_{\partial\mathrm{T}}) + \\
&- \int_{\mathrm{T}} \boldsymbol{f} \cdot \boldsymbol{v}_{\mathrm{T}} - \sum_{\mathrm{F}\in\mathcal{F}^{\mathrm{N}}_{\mathrm{T}}} \int_{\mathrm{F}} \boldsymbol{T}_{\mathrm{N}} \cdot \boldsymbol{v}_{\mathrm{F}} + \\
&- \sum_{\mathrm{F}\in\mathcal{F}^{\mathrm{D_L}}_{\mathrm{T}}} \int_{\mathrm{F}} \widehat{\boldsymbol{\lambda}}_{\mathrm{F}} \cdot \boldsymbol{v}_{\mathrm{F}}.
\end{aligned}
\tag{3.24}
$$

Enforcing the Dirichlet boundary conditions with the Lagrange multiplier method requires the definition of the local residual $r^{\mathrm{HHO,D_L}}_{\mathrm{F}}(\boldsymbol{u}_{\mathrm{F}}; \bullet) : \mathcal{P}^k(\mathrm{F})^d \to \mathbb{R}$ of the constraint, such that

$$
r^{\mathrm{HHO,D_L}}_{\mathrm{F}}(\boldsymbol{u}_{\mathrm{F}}; \widehat{\boldsymbol{s}}_{\mathrm{F}}) := \int_{\mathrm{F}} (\boldsymbol{u}_{\mathrm{F}} - \boldsymbol{u}_{\mathrm{D}}) \cdot \widehat{\boldsymbol{s}}_{\mathrm{F}}. \tag{3.25}
$$

where $\boldsymbol{u}_{\mathrm{F}} \in \mathcal{P}^k(\mathcal{F}^{\mathrm{D_L}}_{\mathrm{T}})^d$.

Define, for the sake of brevity,

$$
\boldsymbol{W}^{\mathrm{HHO},k}_{\mathrm{ce},h} = \boldsymbol{U}^{k,\mathrm{Ds}}_h \times \mathcal{P}^k(\mathcal{F}^{\mathrm{D_L}}_h)^d
$$

and let be $(\boldsymbol{u}_{\mathcal{T}_h}, \boldsymbol{u}_{\mathcal{F}_h}, \widehat{\boldsymbol{\lambda}}_{\mathcal{F}^{\mathrm{D_L}}_h}) \in \boldsymbol{W}^{\mathrm{HHO},k}_{\mathrm{ce},h}$.

The global residuals $r^{\mathrm{uHHO,Lem}}_h((\boldsymbol{u}_{\mathcal{T}_h}, \boldsymbol{u}_{\mathcal{F}_h}, \widehat{\boldsymbol{\lambda}}_{\mathcal{F}^{\mathrm{D_L}}_h}); \bullet) : \boldsymbol{U}^k_h \to \mathbb{R}$ is obtained assembling *element-by-element* the local residual (3.24) i.e.

$$
\begin{aligned}
&r^{\mathrm{uHHO,Lem}}_h \left((\boldsymbol{u}_{\mathcal{T}_h}, \boldsymbol{u}_{\mathcal{F}_h}, \widehat{\boldsymbol{\lambda}}_{\mathcal{F}^{\mathrm{D_L}}_h}); (\boldsymbol{v}_{\mathcal{T}_h}, \boldsymbol{v}_{\mathcal{F}_h}) \right) := \\
&:= \sum_{\mathrm{T}\in\mathcal{T}_h} r^{\mathrm{uHHO,Lem}}_{\mathrm{T}} \left((\boldsymbol{u}_{\mathcal{T}_h|\mathrm{T}}, \boldsymbol{u}_{\mathcal{F}_h|\partial\mathrm{T}}, \widehat{\boldsymbol{\lambda}}_{\mathcal{F}^{\mathrm{D_L}}_h|\partial\mathrm{T}_{\mathrm{L}}}); (\boldsymbol{v}_{\mathcal{T}_h|\mathrm{T}}, \boldsymbol{v}_{\mathcal{F}_h|\partial\mathrm{T}}) \right).
\end{aligned}
\tag{3.26}
$$

Analogously, the global residual $r_h^{\mathrm{HHO,D_L}}(\boldsymbol{u}_{\mathcal{F}_h};\bullet) : \mathcal{P}^k(\mathcal{F}_h^{\mathrm{D_L}})^d \to \mathbb{R}$ is retrieved assembling *face-by-face* the local residual (3.25), i.e.

$$r_h^{\mathrm{HHO,D_L}}\left(\boldsymbol{u}_{\mathcal{F}_h};\widehat{\boldsymbol{s}}_{\mathcal{F}_h^{\mathrm{D_L}}}\right) \coloneqq \sum_{\mathrm{F}\in\mathcal{F}_h^{\mathrm{D_L}}} r_{\mathrm{F}}^{\mathrm{HHO,D_L}}\left(\boldsymbol{u}_{\mathcal{F}_h|\mathrm{F}};\widehat{\boldsymbol{s}}_{\mathcal{F}_h^{\mathrm{D_L}}|\mathrm{F}}\right). \tag{3.27}$$

Given $(\boldsymbol{u}_{\mathcal{T}_h},\, \boldsymbol{u}_{\mathcal{F}_h}, \widehat{\boldsymbol{\lambda}}_{\mathcal{F}_h^{\mathrm{D_L}}}) \in \boldsymbol{W}_{\mathrm{ce},h}^{\mathrm{HHO},k}$, the uHHO discretization of the nonlinear compressible elasticity problem reads as find $(\boldsymbol{u}_{\mathcal{T}_h},\, \boldsymbol{u}_{\mathcal{F}_h}, \widehat{\boldsymbol{\lambda}}_{\mathcal{F}_h^{\mathrm{D_L}}}) \in \boldsymbol{W}_{\mathrm{ce},h}^{\mathrm{HHO},k}$ such that

$$r_{\mathrm{ce},h}^{\mathrm{uHHO}}\left((\boldsymbol{u}_{\mathcal{T}_h},\, \boldsymbol{u}_{\mathcal{F}_h}, \widehat{\boldsymbol{\lambda}}_{\mathcal{F}_h^{\mathrm{D_L}}});(\boldsymbol{v}_{\mathcal{T}_h},\, \boldsymbol{v}_{\mathcal{F}_h}, \widehat{\boldsymbol{s}}_{\mathcal{F}_h^{\mathrm{D_L}}})\right) = 0 \tag{3.28}$$

for all $(\boldsymbol{v}_{\mathcal{T}_h},\, \boldsymbol{v}_{\mathcal{F}_h}, \widehat{\boldsymbol{s}}_{\mathcal{F}_h^{\mathrm{D_L}}}) \in \boldsymbol{W}_{\mathrm{ce},h}^{\mathrm{HHO},k}$ and where $r_{\mathrm{ce},h}^{\mathrm{uHHO}}\left((\boldsymbol{u}_{\mathcal{T}_h},\, \boldsymbol{u}_{\mathcal{F}_h}, \widehat{\boldsymbol{\lambda}}_{\mathcal{F}_h^{\mathrm{D_L}}});\bullet\right) : \boldsymbol{W}_{\mathrm{ce},h}^{\mathrm{HHO},k} \to \mathbb{R}$ is such that for all $(\boldsymbol{v}_{\mathcal{T}_h},\, \boldsymbol{v}_{\mathcal{F}_h}, \widehat{\boldsymbol{s}}_{\mathcal{F}_h^{\mathrm{D_L}}}) \in \boldsymbol{W}_{\mathrm{ce},h}^{\mathrm{HHO},k}$

$$\begin{aligned} &r_{\mathrm{ce},h}^{\mathrm{uHHO}}\left((\boldsymbol{u}_{\mathcal{T}_h},\, \boldsymbol{u}_{\mathcal{F}_h}, \widehat{\boldsymbol{\lambda}}_{\mathcal{F}_h^{\mathrm{D_L}}});(\boldsymbol{v}_{\mathcal{T}_h},\, \boldsymbol{v}_{\mathcal{F}_h}, \widehat{\boldsymbol{s}}_{\mathcal{F}_h^{\mathrm{D_L}}})\right) = \\ &= r_h^{\mathrm{uHHO,Lem}}\left((\boldsymbol{u}_{\mathcal{T}_h},\, \boldsymbol{u}_{\mathcal{F}_h}, \widehat{\boldsymbol{\lambda}}_{\mathcal{F}_h^{\mathrm{D_L}}});(\boldsymbol{v}_{\mathcal{T}_h},\, \boldsymbol{v}_{\mathcal{F}_h})\right) + \\ &+ r_h^{\mathrm{HHO,D_L}}\left(\boldsymbol{u}_{\mathcal{F}_h};\widehat{\boldsymbol{s}}_{\mathcal{F}_h^{\mathrm{D_L}}}\right). \end{aligned}$$

3.5.2 Stabilized HHO method

The gradient is reconstructed locally in the polynomial space $\mathcal{R}(\mathrm{T})^{d\times d} = \mathcal{P}^k(\mathrm{T})^{d\times d}$ for all $\mathrm{T}\in\mathcal{T}_h$.

The HHO stabilization term is based on the definition of the *local displacement reconstruction* operator $\boldsymbol{D}_{\mathrm{T}}^{k+1} : \boldsymbol{U}_{\mathrm{T}}^k \to \mathcal{P}^{k+1}(\mathrm{T})^d$. The reconstructed displacements $\boldsymbol{D}_{\mathrm{T}}^{k+1}(\boldsymbol{v}_{\mathrm{T}},\, \boldsymbol{v}_{\partial\mathrm{T}}) \in \mathcal{P}^{k+1}(\mathrm{T})^d$ is obtained solving a Neumann problem in T such than, for all $\boldsymbol{w}\in\mathcal{P}^{k+1}(\mathrm{T})^d$

$$\begin{aligned} \int_{\mathrm{T}} \nabla_{\boldsymbol{X}} \boldsymbol{D}_{\mathrm{T}}^{k+1}(\boldsymbol{v}_{\mathrm{T}},\, \boldsymbol{v}_{\partial\mathrm{T}}) : \nabla_{\boldsymbol{X}}\boldsymbol{w} = \int_{\mathrm{T}} &\nabla_{\boldsymbol{X}}\boldsymbol{v}_{\mathrm{T}} : \nabla_{\boldsymbol{X}}\boldsymbol{w} \\ &+ \sum_{\mathrm{F}\in\mathcal{F}_{\mathrm{T}}} \int_{\mathrm{F}} (\boldsymbol{v}_{\mathrm{F}} - \boldsymbol{v}_{\mathrm{T}}) \cdot \nabla_{\boldsymbol{X}}\boldsymbol{w}\, \boldsymbol{n}_{\mathrm{TF}} \end{aligned}$$

and additionally enforcing that

$$\int_{\mathrm{T}} \boldsymbol{D}_{\mathrm{T}}^{k+1}(\boldsymbol{v}_{\mathrm{T}},\, \boldsymbol{v}_{\partial\mathrm{T}})\, d\mathrm{T} = \int_{\mathrm{T}} \boldsymbol{v}_{\mathrm{T}}\, d\mathrm{T}.$$

The stabilization term is based on the usual operator for HHO methods $\mathfrak{s}_{\partial\mathrm{T}}^k : \boldsymbol{U}_{\mathrm{T}}^k \to \mathcal{P}^k(\mathcal{F}_{\mathrm{T}})^d$ such that, for all $(\boldsymbol{v}_{\mathrm{T}},\, \boldsymbol{v}_{\partial\mathrm{T}}) \in \boldsymbol{U}_{\mathrm{T}}^k$,

$$\begin{aligned} \mathfrak{s}_{\partial\mathrm{T}}^k(\boldsymbol{v}_{\mathrm{T}},\, \boldsymbol{v}_{\partial\mathrm{T}}) = \boldsymbol{\Pi}_{\partial\mathrm{T}}^k\Big(&\boldsymbol{v}_{\partial\mathrm{T}} - \boldsymbol{D}_{\mathrm{T}}^{k+1}(\boldsymbol{v}_{\mathrm{T}},\, \boldsymbol{v}_{\partial\mathrm{T}})_{|\partial\mathrm{T}} + \\ &- \big(\boldsymbol{v}_{\mathrm{T}} - \boldsymbol{\Pi}_{\mathrm{T}}^k(\boldsymbol{D}_{\mathrm{T}}^{k+1}(\boldsymbol{v}_{\mathrm{T}},\, \boldsymbol{v}_{\partial\mathrm{T}}))\big)_{|\partial\mathrm{T}}\Big). \end{aligned} \tag{3.29}$$

Now, given $(\boldsymbol{u}_{\mathrm{T}},\, \boldsymbol{u}_{\partial\mathrm{T}}, \widehat{\boldsymbol{\lambda}}_{\partial\mathrm{T}_{\mathrm{L}}}) \in \boldsymbol{U}_{\mathrm{T}}^{k} \times \mathcal{P}^{k}(\mathcal{F}_{\mathrm{T}}^{\mathrm{D_L}})^{d}$, we are ready to introduce the local residual $r_{\mathrm{T}}^{\mathrm{sHHO,Lem}}((\boldsymbol{u}_{\mathrm{T}},\, \boldsymbol{u}_{\partial\mathrm{T}}, \widehat{\boldsymbol{\lambda}}_{\partial\mathrm{T}_{\mathrm{L}}}), \bullet) : \boldsymbol{U}_{\mathrm{T}}^{k} \to \mathbb{R}$ of the discrete Lagrangian equation of motion

$$\begin{aligned} & r_{\mathrm{T}}^{\mathrm{sHHO,Lem}}((\boldsymbol{u}_{\mathrm{T}},\, \boldsymbol{u}_{\partial\mathrm{T}}, \widehat{\boldsymbol{\lambda}}_{\partial\mathrm{T}_{\mathrm{L}}}); (\boldsymbol{v}_{\mathrm{T}},\, \boldsymbol{v}_{\partial\mathrm{T}})) = \\ & = \int_{\mathrm{T}} \boldsymbol{P}(\mathscr{F}_{\mathrm{T}}^{k}(\boldsymbol{u}_{\mathrm{T}},\, \boldsymbol{u}_{\partial\mathrm{T}})) : \mathscr{G}_{\mathrm{T}}^{k}(\boldsymbol{v}_{\mathrm{T}},\, \boldsymbol{v}_{\partial\mathrm{T}}) + \\ & + \int_{\partial\mathrm{T}} \frac{\kappa}{h_{\partial\mathrm{T}}}\, \mathfrak{s}_{\partial\mathrm{T}}^{k}(\boldsymbol{u}_{\mathrm{T}},\, \boldsymbol{u}_{\partial\mathrm{T}}) \cdot \mathfrak{s}_{\partial\mathrm{T}}^{k}(\boldsymbol{v}_{\mathrm{T}},\, \boldsymbol{v}_{\partial\mathrm{T}}) + \\ & - \int_{\mathrm{T}} \boldsymbol{f} \cdot \boldsymbol{v}_{\mathrm{T}} - \sum_{\mathrm{F}\in\mathcal{F}_{\mathrm{T}}^{\mathrm{N}}} \int_{\mathrm{F}} \boldsymbol{T}_{\mathrm{N}} \cdot \boldsymbol{v}_{\mathrm{F}} + \\ & - \sum_{\mathrm{F}\in\mathcal{F}_{\mathrm{T}}^{\mathrm{D_L}}} \int_{\mathrm{F}} \widehat{\boldsymbol{\lambda}}_{\mathrm{F}} \cdot \boldsymbol{v}_{\mathrm{F}} \end{aligned} \tag{3.30}$$

where $h_{\partial\mathrm{T}}$ is such that $h_{\partial\mathrm{T}|\mathrm{F}} = h_{\mathrm{F}}$ with h_{F} the face diameter of F and $\kappa = \kappa_0\, \mu$ with κ_0 a user-dependent parameter for scaling the stabilization.

As in previous paragraphs, let be $(\boldsymbol{u}_{\mathcal{T}_h},\, \boldsymbol{u}_{\mathcal{F}_h}, \widehat{\boldsymbol{\lambda}}_{\mathcal{F}_h^{\mathrm{D_L}}}) \in \boldsymbol{W}_{\mathrm{ce},h}^{\mathrm{HHO},k}$, assembling *element-by-element* the local residual (3.30), the global residuals $r_{h}^{\mathrm{sHHO,Lem}}((\boldsymbol{u}_{\mathcal{T}_h},\, \boldsymbol{u}_{\mathcal{F}_h}, \widehat{\boldsymbol{\lambda}}_{\mathcal{F}_h^{\mathrm{D_L}}}); \bullet) : \boldsymbol{U}_{h}^{k} \to \mathbb{R}$ is i.e.

$$\begin{aligned} & r_{h}^{\mathrm{sHHO,Lem}}\left((\boldsymbol{u}_{\mathcal{T}_h},\, \boldsymbol{u}_{\mathcal{F}_h}, \widehat{\boldsymbol{\lambda}}_{\mathcal{F}_h^{\mathrm{D_L}}}); (\boldsymbol{v}_{\mathcal{T}_h},\, \boldsymbol{v}_{\mathcal{F}_h})\right) := \\ & := \sum_{\mathrm{T}\in\mathcal{T}_h} r_{\mathrm{T}}^{\mathrm{sHHO,Lem}}\left((\boldsymbol{u}_{\mathcal{T}_h|\mathrm{T}},\, \boldsymbol{u}_{\mathcal{F}_h|\partial\mathrm{T}}, \widehat{\boldsymbol{\lambda}}_{\mathcal{F}_h^{\mathrm{D_L}}|\partial\mathrm{T}_{\mathrm{L}}}); (\boldsymbol{v}_{\mathcal{T}_h|\mathrm{T}},\, \boldsymbol{v}_{\mathcal{F}_h|\partial\mathrm{T}})\right). \end{aligned} \tag{3.31}$$

Adding the global residual (3.27) of the Lagrange multipliers constraint, the sHHO discretization of the nonlinear elasticity problem with compressible constitutive law reads as find $(\boldsymbol{u}_{\mathcal{T}_h},\, \boldsymbol{u}_{\mathcal{F}_h}, \widehat{\boldsymbol{\lambda}}_{\mathcal{F}_h^{\mathrm{D_L}}}) \in \boldsymbol{W}_{\mathrm{ce},h}^{\mathrm{HHO},k}$ such that

$$r_{\mathrm{ce},h}^{\mathrm{sHHO}}\left((\boldsymbol{u}_{\mathcal{T}_h},\, \boldsymbol{u}_{\mathcal{F}_h}, \widehat{\boldsymbol{\lambda}}_{\mathcal{F}_h^{\mathrm{D_L}}}); (\boldsymbol{v}_{\mathcal{T}_h},\, \boldsymbol{v}_{\mathcal{F}_h}, \widehat{\boldsymbol{s}}_{\mathcal{F}_h^{\mathrm{D_L}}})\right) = 0 \tag{3.32}$$

for all $(\boldsymbol{v}_{\mathcal{T}_h},\, \boldsymbol{v}_{\mathcal{F}_h}, \widehat{\boldsymbol{s}}_{\mathcal{F}_h^{\mathrm{D_L}}}) \in \boldsymbol{W}_{\mathrm{ce},h}^{\mathrm{HHO},k}$ and where $r_{\mathrm{ce},h}^{\mathrm{sHHO}}\left((\boldsymbol{u}_{\mathcal{T}_h},\, \boldsymbol{u}_{\mathcal{F}_h}, \widehat{\boldsymbol{\lambda}}_{\mathcal{F}_h^{\mathrm{D_L}}}); \bullet\right) : \boldsymbol{W}_{\mathrm{ce},h}^{\mathrm{HHO},k} \to \mathbb{R}$ is such that for all $(\boldsymbol{v}_{\mathcal{T}_h},\, \boldsymbol{v}_{\mathcal{F}_h}, \widehat{\boldsymbol{s}}_{\mathcal{F}_h^{\mathrm{D_L}}}) \in \boldsymbol{W}_{\mathrm{ce},h}^{\mathrm{HHO},k}$

$$\begin{aligned} & r_{\mathrm{ce},h}^{\mathrm{sHHO}}\left((\boldsymbol{u}_{\mathcal{T}_h},\, \boldsymbol{u}_{\mathcal{F}_h}, \widehat{\boldsymbol{\lambda}}_{\mathcal{F}_h^{\mathrm{D_L}}}); (\boldsymbol{v}_{\mathcal{T}_h},\, \boldsymbol{v}_{\mathcal{F}_h}, \widehat{\boldsymbol{s}}_{\mathcal{F}_h^{\mathrm{D_L}}})\right) = \\ & = r_{h}^{\mathrm{sHHO,Lem}}\left((\boldsymbol{u}_{\mathcal{T}_h},\, \boldsymbol{u}_{\mathcal{F}_h}, \widehat{\boldsymbol{\lambda}}_{\mathcal{F}_h^{\mathrm{D_L}}}); (\boldsymbol{v}_{\mathcal{T}_h},\, \boldsymbol{v}_{\mathcal{F}_h})\right) + \\ & + r_{h}^{\mathrm{HHO,D_L}}\left(\boldsymbol{u}_{\mathcal{F}_h}; \widehat{\boldsymbol{s}}_{\mathcal{F}_h^{\mathrm{D_L}}}\right). \end{aligned}$$

3.6 Incremental load method

Problems (3.11), (3.13), (3.22), (3.28) and (3.32) are solved by means of Newton's method. The same procedure is employed for dG, HDG and HHO methods, so, we neglect the apices (dG, HDG, uHHO and sHHO) for sake of simplicity.

In order to globalize the convergence of the Newton iteration towards the equilibrium configuration, we adopt the **incremental method**, see *e.g.* [4]. The idea is to define a quasi-static loading path that allows to reach the final configuration by passing through a sequence of intermediate equilibrium states. To this end, an incremental percentage of the external solicitation is imposed at each intermediate step $i = 1, \dots N-1$, where N is the step corresponding to the final configuration. In particular, for $i = 1, 2 \dots, N$, we apply Newton's method to solve the following problem: find $\boldsymbol{w}_h^i \in \boldsymbol{W}_{\bullet,h}^k$ such that

$$\tilde{r}_{\bullet,h}^i(\boldsymbol{w}_h^i; \boldsymbol{z}_h) = 0, \quad \forall \boldsymbol{z}_h \in \boldsymbol{W}_{\bullet,h}^k \tag{3.33}$$

where $\tilde{r}_{\bullet,h}^i(*;*)$ is one of the residuals defined in (3.12)-(3.14)-(3.23), *i.e.* $\bullet \in \{\text{ce,ie}\}$, but the external solicitations in (3.8), see also (3.7), and (3.18) are replaced by

$$\tilde{\boldsymbol{f}} = \frac{i}{N}\boldsymbol{f}, \qquad \tilde{\boldsymbol{t}}_{\text{N}} = \frac{i}{N}\boldsymbol{t}_{\text{N}}, \qquad \tilde{\boldsymbol{u}}_{\text{D}} = \frac{i}{N}\boldsymbol{u}_{\text{D}}.$$

Clearly, $\boldsymbol{w}_h^N$ is the solution of one of the problems in (3.11)-(3.13)-(3.22). Nevertheless, since each state of the sequence is incremental with respect to the previous configuration, convergence of Newton's method is guaranteed providing N big enough.

As described in Alg. 3.1, **Newton's method** applied to problem (3.33) reads:

```
Set the initial guess $\boldsymbol{w}_h^i = \boldsymbol{w}_h^{i-1}$;
while $\delta\boldsymbol{w}_h$ is too large do
    find $\delta\boldsymbol{w}_h \in \boldsymbol{W}_{\bullet,h}^k$ such that:
        $\left(\boldsymbol{J}_{\bullet,h}(\boldsymbol{w}_h^i)\delta\boldsymbol{w}_h, \boldsymbol{z}_h\right)_{L^2(\Omega)} = -\tilde{r}_{\bullet,h}^i(\boldsymbol{w}_h^i; \boldsymbol{z}_h), \quad \forall \boldsymbol{z}_h \in \boldsymbol{W}_{\bullet,h}^k;$    (3.34)
    set $\boldsymbol{w}_h^i$ += $\delta\boldsymbol{w}_h$;
end
```

Algorithm 3.1: Newton method's procedure.

where, for each $\boldsymbol{w}_h \in \boldsymbol{W}_{\bullet,h}^k$, the Jacobian operator $\boldsymbol{J}_{\bullet,h} : \boldsymbol{W}_{\bullet,h}^k \to \boldsymbol{W}_{\bullet,h}^k$ is defined such that

$$\left(\boldsymbol{J}_{\bullet,h}(\boldsymbol{w}_h)\boldsymbol{y}_h, \boldsymbol{z}_h\right)_{L^2(\Omega)} = \frac{d}{d\epsilon}\tilde{r}_{\bullet,h}(\boldsymbol{w}_h + \epsilon\boldsymbol{y}_h; \boldsymbol{z}_h)\bigg|_{\epsilon=0}, \qquad \forall \boldsymbol{y}_h, \boldsymbol{z}_h \in \boldsymbol{W}_{\bullet,h}^k.$$

In what follows, we present the Jacobian operators for all the nonconforming methods introduced in this work. In particular, the entire derivation is proposed only for the dG formulation. However, this procedure is valid for all the other discretizations.

3.6.1 Derivation of Jacobian operators for dG formulations

In the incompressible regime, the Jacobian operator is stated as

$$
\begin{aligned}
\left(\boldsymbol{J}^{\mathrm{dG}}_{\mathrm{ie},h}(\boldsymbol{w}_h)\delta\boldsymbol{w}_h, \boldsymbol{z}_h\right)_{L^2(\Omega)} = \sum_{\mathrm{T}\in\mathcal{T}_h} \frac{\partial}{\partial\epsilon}\Bigg(& r^{\mathrm{dG,Lem}}_{\mathrm{T}}\left((\boldsymbol{u}_h + \epsilon\delta\boldsymbol{u}_h, p_h, \widehat{\boldsymbol{\lambda}}_h); \boldsymbol{v}_{\mathrm{T}}\right) + \\
& + r^{\mathrm{dG,Lem}}_{\mathrm{T}}\left((\boldsymbol{u}_h, p_h + \epsilon\delta p_h, \widehat{\boldsymbol{\lambda}}_h); \boldsymbol{v}_{\mathrm{T}}\right) + \\
& + r^{\mathrm{dG,Lem}}_{\mathrm{T}}\left((\boldsymbol{u}_h, p_h, \widehat{\boldsymbol{\lambda}}_h + \epsilon\delta\widehat{\boldsymbol{\lambda}}_h); \boldsymbol{v}_{\mathrm{T}}\right) + \\
& + r^{\mathrm{dG,ic}}_{\mathrm{T}}\left((\boldsymbol{u}_h + \epsilon\delta\boldsymbol{u}_h, p_h); q_{h|\mathrm{T}}\right) + \\
& + r^{\mathrm{dG,ic}}_{\mathrm{T}}\left((\boldsymbol{u}_h, p_h + \epsilon\delta p_h); q_{h|\mathrm{T}}\right) + \\
& + r^{\mathrm{dG,D_L}}_{h}\left((\boldsymbol{u}_h + \epsilon\delta\boldsymbol{u}_h, \widehat{\boldsymbol{\lambda}}_h); \widehat{\boldsymbol{s}}_h\right) + \\
& + r^{\mathrm{dG,D_L}}_{h}\left((\boldsymbol{u}_h, \widehat{\boldsymbol{\lambda}}_h + \epsilon\delta\widehat{\boldsymbol{\lambda}}_h); \widehat{\boldsymbol{s}}_h\right)\Bigg)\Bigg|_{\epsilon=0}.
\end{aligned}
\tag{3.35}
$$

On the other hand, in the compressible regime,

$$
\begin{aligned}
\left(\boldsymbol{J}^{\mathrm{dG}}_{\mathrm{ce},h}(\boldsymbol{u}_h)\delta\boldsymbol{u}_h, \boldsymbol{v}_h\right)_{L^2(\Omega)} = \sum_{\mathrm{T}\in\mathcal{T}_h} \frac{\partial}{\partial\epsilon}\Bigg(& r^{\mathrm{dG,Lem}}_{\mathrm{T}}\left((\boldsymbol{u}_h + \epsilon\delta\boldsymbol{u}_h, 0, \widehat{\boldsymbol{\lambda}}_h); \boldsymbol{v}_{\mathrm{T}}\right) + \\
& + r^{\mathrm{dG,Lem}}_{\mathrm{T}}\left((\boldsymbol{u}_h, 0, \widehat{\boldsymbol{\lambda}}_h + \epsilon\delta\widehat{\boldsymbol{\lambda}}_h); \boldsymbol{v}_{\mathrm{T}}\right) + \\
& + r^{\mathrm{dG,D_L}}_{h}\left((\boldsymbol{u}_h + \epsilon\delta\boldsymbol{u}_h, \widehat{\boldsymbol{\lambda}}_h); \widehat{\boldsymbol{s}}_h\right) + \\
& + r^{\mathrm{dG,D_L}}_{h}\left((\boldsymbol{u}_h, \widehat{\boldsymbol{\lambda}}_h + \epsilon\delta\widehat{\boldsymbol{\lambda}}_h); \widehat{\boldsymbol{s}}_h\right)\Bigg)\Bigg|_{\epsilon=0}.
\end{aligned}
\tag{3.36}
$$

The computation of directional derivatives of local residuals in Eqs. (3.35) and (3.36) are presented. Firstly, we consider the residual of the discrete Lagrangian equation of motion. The directional derivative respect to $\boldsymbol{u}_h$ reads

$$
\begin{aligned}
& \frac{\partial}{\partial\epsilon} r^{\mathrm{dG,Lem}}_{\mathrm{T}}\left((\boldsymbol{u}_h + \epsilon\delta\boldsymbol{u}_h, p_h, \widehat{\boldsymbol{\lambda}}_h); \boldsymbol{v}_{\mathrm{T}}\right)\Bigg|_{\epsilon=0} = \\
& = \int_{\mathrm{T}} \left(\frac{\partial\boldsymbol{\mathfrak{F}}^k_{\mathrm{T}}(\boldsymbol{u}_h + \epsilon\delta\boldsymbol{u}_h)}{\partial\epsilon} : \frac{\partial\boldsymbol{P}(\boldsymbol{\mathfrak{F}}^k_{\mathrm{T}}(\boldsymbol{u}_h + \epsilon\delta\boldsymbol{u}_h), p_h)}{\partial\boldsymbol{\mathfrak{F}}^k_{\mathrm{T}}(\boldsymbol{u}_h + \epsilon\delta\boldsymbol{u}_h)}\right)\Bigg|_{\epsilon=0} : \nabla_{\boldsymbol{X}}\boldsymbol{v}_{\mathrm{T}} + \\
& - \sum_{\mathrm{F}\in\mathcal{F}^{i,\mathrm{D_N}}_{\mathrm{T}}} \int_{\mathrm{F}} \left[\left\{\!\!\left\{\frac{\partial\boldsymbol{\mathfrak{F}}^{k+1}_{\mathrm{TF}}(\boldsymbol{u}_h + \epsilon\delta\boldsymbol{u}_h)}{\partial\epsilon} : \frac{\partial\boldsymbol{P}(\boldsymbol{\mathfrak{F}}^{k+1}_{\mathrm{TF}}(\boldsymbol{u}_h + \epsilon\delta\boldsymbol{u}_h), p_h)}{\partial\boldsymbol{\mathfrak{F}}^{k+1}_{\mathrm{TF}}(\boldsymbol{u}_h + \epsilon\delta\boldsymbol{u}_h)}\right\}\!\!\right\}_{\mathrm{F}} \boldsymbol{n}_{\mathrm{TF}}\right]_{\epsilon=0} \cdot \boldsymbol{v}_{\mathrm{T}} + \\
& + \sum_{\mathrm{F}\in\mathcal{F}^{i,\mathrm{D_N}}_{\mathrm{T}}} \int_{\mathrm{F}} \eta_{\mathrm{F}} \left\{\!\!\left\{\frac{\partial\boldsymbol{\mathfrak{R}}^k_{\mathrm{FT}}([\![\boldsymbol{u}_h + \epsilon\delta\boldsymbol{u}_h]\!]_{\mathrm{TF}})}{\partial\epsilon}\Bigg|_{\epsilon=0} \boldsymbol{n}_{\mathrm{TF}}\right\}\!\!\right\}_{\mathrm{F}} \cdot \boldsymbol{v}_{\mathrm{T}}.
\end{aligned}
$$

We first compute the directional derivatives of the discrete deformation gradient

$$\left.\frac{\partial \boldsymbol{\mathfrak{F}}^k_{\mathrm{T}}(\boldsymbol{u}_h+\epsilon\delta\boldsymbol{u}_h)}{\partial\epsilon}\right|_{\epsilon=0} = \boldsymbol{\mathfrak{G}}^k_T(\delta\boldsymbol{u}_h),$$

$$\left.\frac{\partial \boldsymbol{\mathfrak{F}}^{k+1}_{\mathrm{TF}}(\boldsymbol{u}_h+\epsilon\delta\boldsymbol{u}_h)}{\partial\epsilon}\right|_{\epsilon=0} = \nabla_{\boldsymbol{X}}\delta\boldsymbol{u}_{|\mathrm{T}} - \boldsymbol{\mathfrak{R}}^{k+1}_{\mathrm{FT}}([\![\delta\boldsymbol{u}_h]\!]_{\mathrm{TF}}).$$

From the definition of $\mathbb{A}$, the fourth-order elasticity tensor (see Sec. 2.3.3 for further information), we are able to infer

$$\left.\frac{\partial \boldsymbol{P}(\boldsymbol{\mathfrak{F}}^k_{\mathrm{T}}(\boldsymbol{u}_h+\epsilon\delta\boldsymbol{u}_h),p_h)}{\partial\boldsymbol{\mathfrak{F}}^k_{\mathrm{T}}(\boldsymbol{u}_h+\epsilon\delta\boldsymbol{u}_h)}\right|_{\epsilon=0} = \mathbb{A}(\boldsymbol{\mathfrak{F}}^k_{\mathrm{T}}(\boldsymbol{u}_h),p_h),$$

$$\left.\frac{\partial \boldsymbol{P}(\boldsymbol{\mathfrak{F}}^{k+1}_{\mathrm{TF}}(\boldsymbol{u}_h+\epsilon\delta\boldsymbol{u}_h),p_h)}{\partial\boldsymbol{\mathfrak{F}}^{k+1}_{\mathrm{TF}}(\boldsymbol{u}_h+\epsilon\delta\boldsymbol{u}_h)}\right|_{\epsilon=0} = \mathbb{A}(\boldsymbol{\mathfrak{F}}^{k+1}_{\mathrm{TF}}(\boldsymbol{u}_h),p_h).$$

Moreover, being $\boldsymbol{\mathfrak{R}}^k_{\mathrm{FT}}$ a linear operator, we get

$$\begin{aligned}\left.\frac{\partial}{\partial\epsilon}\boldsymbol{\mathfrak{R}}^k_{\mathrm{FT}}([\![\boldsymbol{u}_h+\epsilon\delta\boldsymbol{u}_h]\!]_{\mathrm{TF}})\right|_{\epsilon=0} &= \left.\frac{\partial}{\partial\epsilon}\left(\boldsymbol{\mathfrak{R}}^k_{\mathrm{FT}}([\![\boldsymbol{u}_h]\!]_{\mathrm{TF}})+\boldsymbol{\mathfrak{R}}^k_{\mathrm{FT}}([\![\epsilon\delta\boldsymbol{u}_h]\!]_{\mathrm{TF}})\right)\right|_{\epsilon=0}\\ &= \left.\frac{\partial}{\partial\epsilon}\left(\epsilon\ \boldsymbol{\mathfrak{R}}^k_{\mathrm{FT}}([\![\delta\boldsymbol{u}_h]\!]_{\mathrm{TF}})\right)\right|_{\epsilon=0}\\ &= \boldsymbol{\mathfrak{R}}^k_{\mathrm{FT}}([\![\delta\boldsymbol{u}_h]\!]_{\mathrm{TF}}).\end{aligned}$$

Using the previous results, we finally obtain

$$\begin{aligned}&\left.\frac{\partial}{\partial\epsilon}r^{\mathrm{dG,Lem}}_{\mathrm{T}}((\boldsymbol{u}_h+\epsilon\delta\boldsymbol{u}_h,p_h);\boldsymbol{v}_{\mathrm{T}})\right|_{\epsilon=0} =\\ &= \sum_{\mathrm{T}\in\mathcal{T}_h}\Bigg(\int_{\mathrm{T}}\left[\boldsymbol{\mathfrak{G}}^k_T(\delta\boldsymbol{u}_h):\mathbb{A}(\boldsymbol{\mathfrak{F}}^k_{\mathrm{T}}(\boldsymbol{u}_h),p_h)\right]:\nabla_{\boldsymbol{X}}\boldsymbol{v}_{\mathrm{T}}+\\ &- \sum_{\mathrm{F}\in\mathcal{F}^{i,\mathrm{D_N}}_{\mathrm{T}}}\int_{\mathrm{F}}\left[\Big\{\!\!\Big\{\Big(\nabla_{\boldsymbol{X}}\delta\boldsymbol{u}_{|\mathrm{T}}-\boldsymbol{\mathfrak{R}}^{k+1}_{\mathrm{FT}}([\![\delta\boldsymbol{u}_h]\!]_{\mathrm{TF}})\Big):\mathbb{A}(\boldsymbol{\mathfrak{F}}^{k+1}_{\mathrm{TF}}(\boldsymbol{u}_h),p_h)\Big\}\!\!\Big\}_{\mathrm{F}}\boldsymbol{n}_{\mathrm{TF}}\right]\cdot\boldsymbol{v}_{\mathrm{T}}+\\ &+ \sum_{\mathrm{F}\in\mathcal{F}^{i,\mathrm{D_N}}_{\mathrm{T}}}\int_{\mathrm{F}}\eta_{\mathrm{F}}\ \left[\big\{\!\!\big\{\boldsymbol{\mathfrak{R}}^k_{\mathrm{FT}}([\![\delta\boldsymbol{u}_h]\!]_{\mathrm{TF}})\big\}\!\!\big\}_{\mathrm{F}}\boldsymbol{n}_{\mathrm{TF}}\right]\cdot\boldsymbol{v}_{\mathrm{T}}.\end{aligned}\tag{3.37}$$

The directional derivative respect to p_h reads

$$\begin{aligned}&\left.\frac{\partial}{\partial\epsilon}r^{\mathrm{dG,Lem}}_{\mathrm{T}}\left((\boldsymbol{u}_h,p_h+\epsilon\delta p_h,\widehat{\boldsymbol{\lambda}}_h);\boldsymbol{v}_{\mathrm{T}}\right)\right|_{\epsilon=0} =\\ &= \int_{\mathrm{T}}\left.\frac{\partial\boldsymbol{P}(\boldsymbol{\mathfrak{F}}^k_{\mathrm{T}}(\boldsymbol{u}_h),p_h+\epsilon\delta p_h)}{\partial\epsilon}\right|_{\epsilon=0}:\nabla_{\boldsymbol{X}}\boldsymbol{v}_{\mathrm{T}}+\\ &- \sum_{\mathrm{F}\in\mathcal{F}^{i,\mathrm{D_N}}_{\mathrm{T}}}\int_{\mathrm{F}}\left[\left\{\!\!\!\left\{\left.\frac{\partial\boldsymbol{P}(\boldsymbol{\mathfrak{F}}^{k+1}_{\mathrm{TF}}(\boldsymbol{u}_h),p_h+\epsilon\delta p_h)}{\partial\epsilon}\right|_{\epsilon=0}\right\}\!\!\!\right\}_{\mathrm{F}}\boldsymbol{n}_{\mathrm{TF}}\right]\cdot\boldsymbol{v}_{\mathrm{T}},\end{aligned}$$

where

$$\left.\frac{\partial\boldsymbol{P}(\boldsymbol{\mathfrak{F}}^k_{\mathrm{T}}(\boldsymbol{u}_h),p_h+\epsilon\delta p_h)}{\partial\epsilon}\right|_{\epsilon=0} = -\delta p_h\ \det(\boldsymbol{\mathfrak{F}}^k_{\mathrm{T}}(\boldsymbol{u}_h))\ [\boldsymbol{\mathfrak{F}}^k_{\mathrm{T}}(\boldsymbol{u}_h)]^{-\intercal},$$

$$\left.\frac{\partial \boldsymbol{P}(\boldsymbol{\mathfrak{F}}_{\mathrm{TF}}^{k+1}(\boldsymbol{u}_h), p_h + \epsilon \delta p_h)}{\partial \epsilon}\right|_{\epsilon=0} = -\delta p_h \ \det(\boldsymbol{\mathfrak{F}}_{\mathrm{TF}}^{k+1}(\boldsymbol{u}_h)) \ [\boldsymbol{\mathfrak{F}}_{\mathrm{TF}}^{k+1}(\boldsymbol{u}_h)]^{-\intercal}.$$

This leads to the following result

$$\begin{aligned}
&\frac{\partial}{\partial \epsilon} r_{\mathrm{T}}^{\mathrm{dG,Lem}} \left((\boldsymbol{u}_h, p_h + \epsilon \delta p_h, \widehat{\boldsymbol{\lambda}}_h); \boldsymbol{v}_{\mathrm{T}}\right)\Big|_{\epsilon=0} = \\
&= -\int_{\mathrm{T}} \delta p_h \ \det(\boldsymbol{\mathfrak{F}}_{\mathrm{T}}^{k}(\boldsymbol{u}_h)) \ [\boldsymbol{\mathfrak{F}}_{\mathrm{T}}^{k}(\boldsymbol{u}_h)]^{-\intercal} : \nabla_{\boldsymbol{X}} \boldsymbol{v}_{\mathrm{T}} + \\
&- \sum_{\mathrm{F} \in \mathcal{F}_{\mathrm{T}}^{i,\mathrm{D_N}}} \int_{\mathrm{F}} \left[\left\{\!\!\left\{ \delta p_h \ \det(\boldsymbol{\mathfrak{F}}_{\mathrm{TF}}^{k+1}(\boldsymbol{u}_h)) \ [\boldsymbol{\mathfrak{F}}_{\mathrm{TF}}^{k+1}(\boldsymbol{u}_h)]^{-\intercal} \right\}\!\!\right\}_{\mathrm{F}} \boldsymbol{n}_{\mathrm{TF}}\right] \cdot \boldsymbol{v}_{\mathrm{T}}.
\end{aligned} \tag{3.38}$$

The directional derivative respect to $\widehat{\boldsymbol{\lambda}}_h$ reads

$$\begin{aligned}
&\frac{\partial}{\partial \epsilon} r_{\mathrm{T}}^{\mathrm{dG,Lem}} \left((\boldsymbol{u}_h, p_h, \widehat{\boldsymbol{\lambda}}_h + \epsilon \delta \widehat{\boldsymbol{\lambda}}_h); \boldsymbol{v}_{\mathrm{T}}\right)\Big|_{\epsilon=0} = \\
&= - \sum_{\mathrm{F} \in \mathcal{F}_{\mathrm{T}}^{\mathrm{D_L}}} \int_{\mathrm{F}} \frac{\partial}{\partial \epsilon} (\widehat{\boldsymbol{\lambda}}_h + \epsilon \delta \widehat{\boldsymbol{\lambda}}_h)\Big|_{\epsilon=0} \cdot \boldsymbol{v}_{\mathrm{T}} = \\
&= - \sum_{\mathrm{F} \in \mathcal{F}_{\mathrm{T}}^{\mathrm{D_L}}} \int_{\mathrm{F}} \delta \widehat{\boldsymbol{\lambda}}_h \cdot \boldsymbol{v}_{\mathrm{T}}.
\end{aligned} \tag{3.39}$$

Let's now compute the directional derivatives of the residual of the incompressibility constraint. The directional derivative respect to $\boldsymbol{u}_h$ reads

$$\begin{aligned}
&\frac{\partial}{\partial \epsilon} r_{\mathrm{T}}^{\mathrm{dG,ic}} \left((\boldsymbol{u}_h + \epsilon \delta \boldsymbol{u}_h, p_h); q_{h|\mathrm{T}}\right)\Big|_{\epsilon=0} = \\
&= \int_{\mathrm{T}} \left(\frac{\partial \det(\boldsymbol{\mathfrak{F}}_{\mathrm{T}}^{k}(\boldsymbol{u}_h + \epsilon \delta \boldsymbol{u}_h))}{\partial \boldsymbol{\mathfrak{F}}_{\mathrm{T}}^{k}(\boldsymbol{u}_h + \epsilon \delta \boldsymbol{u}_h)} : \frac{\partial \boldsymbol{\mathfrak{F}}_{\mathrm{T}}^{k}(\boldsymbol{u}_h + \epsilon \delta \boldsymbol{u}_h)}{\partial \epsilon} \right)\Bigg|_{\epsilon=0} q_{\mathrm{T}}
\end{aligned}$$

with

$$\left.\frac{\partial \det(\boldsymbol{\mathfrak{F}}_{\mathrm{T}}^{k}(\boldsymbol{u}_h + \epsilon \delta \boldsymbol{u}_h))}{\partial \boldsymbol{\mathfrak{F}}_{\mathrm{T}}^{k}(\boldsymbol{u}_h + \epsilon \delta \boldsymbol{u}_h)}\right|_{\epsilon=0} = \det(\boldsymbol{\mathfrak{F}}_{\mathrm{T}}^{k}(\boldsymbol{u}_h)) [\boldsymbol{\mathfrak{F}}_{\mathrm{T}}^{k}(\boldsymbol{u}_h)]^{-\intercal}$$

such that

$$\begin{aligned}
&\frac{\partial}{\partial \epsilon} r_{\mathrm{T}}^{\mathrm{dG,ic}} \left((\boldsymbol{u}_h + \epsilon \delta \boldsymbol{u}_h, p_h); q_{h|\mathrm{T}}\right)\Big|_{\epsilon=0} = \\
&= \int_{\mathrm{T}} \left(\det(\boldsymbol{\mathfrak{F}}_{\mathrm{T}}^{k}(\boldsymbol{u}_h)) [\boldsymbol{\mathfrak{F}}_{\mathrm{T}}^{k}(\boldsymbol{u}_h)]^{-\intercal} : \boldsymbol{\mathfrak{G}}_{T}^{k}(\delta \boldsymbol{u}_h) \right) q_{\mathrm{T}}.
\end{aligned} \tag{3.40}$$

Similarly, the directional derivative respect to p_h reads

$$\begin{aligned} &\frac{\partial}{\partial \epsilon} r_{\mathrm{T}}^{\mathrm{dG,ic}}((\boldsymbol{u}_h, p_h + \epsilon \delta p_h); q_{h|\mathrm{T}})\Big|_{\epsilon=0} = \\ &= \sum_{F \in \mathcal{F}_{\mathrm{T}}^{\mathrm{i}}} \int_{\mathrm{F}} \eta_{\mathrm{LBB}}\, h_{\mathrm{F}} \left[\!\!\left[\frac{\partial p_h + \epsilon \delta p_h}{\partial \epsilon}\Big|_{\epsilon=0} \right]\!\!\right]_{\mathrm{TF}} q_{\mathrm{T}} = \\ &= \sum_{F \in \mathcal{F}_{\mathrm{T}}^{\mathrm{i}}} \int_{\mathrm{F}} \eta_{\mathrm{LBB}}\, h_{\mathrm{F}} [\![\delta p_h]\!]_{\mathrm{TF}}\, q_{\mathrm{T}}. \end{aligned} \tag{3.41}$$

Finally, we compute the directional derivatives of the residual of the Lagrange multiplier constraint with its stabilizing term. The directional derivative respect to $\boldsymbol{u}_h$ reads

$$\begin{aligned} \frac{\partial}{\partial \epsilon} r_h^{\mathrm{dG,D_L}} \left((\boldsymbol{u}_h + \epsilon \delta \boldsymbol{u}_h, \widehat{\boldsymbol{\lambda}}_h); \widehat{\boldsymbol{s}}_h \right)\Big|_{\epsilon=0} &= \int_{\mathrm{F}} \frac{\partial}{\partial \epsilon} (\boldsymbol{u}_h + \epsilon \delta \boldsymbol{u}_h - \boldsymbol{g}_{\mathrm{D}})\Big|_{\epsilon=0} \cdot \widehat{\boldsymbol{s}}_{\mathrm{F}} = \\ &= \int_{\mathrm{F}} \delta \boldsymbol{u}_h \cdot \widehat{\boldsymbol{s}}_{\mathrm{F}} \end{aligned} \tag{3.42}$$

while, the directional derivative respect to $\widehat{\boldsymbol{\lambda}}_h$ reads

$$\begin{aligned} &\frac{\partial}{\partial \epsilon} r_h^{\mathrm{dG,D_L}} \left((\boldsymbol{u}_h, \widehat{\boldsymbol{\lambda}}_h + \epsilon \delta \widehat{\boldsymbol{\lambda}}_h); \widehat{\boldsymbol{s}}_h \right)\Big|_{\epsilon=0} = \\ &= \sum_{\mathrm{E} \in \mathcal{E}_{\mathrm{F}}^{i}} \int_{\mathrm{E}} \eta_{\widehat{\lambda}}\, h_{\mathrm{E}} \left[\!\!\left[\frac{\partial \widehat{\boldsymbol{\lambda}}_h + \epsilon \delta \widehat{\boldsymbol{\lambda}}_h}{\partial \epsilon}\Big|_{\epsilon=0} \right]\!\!\right]_{\mathrm{FE}} \cdot \widehat{\boldsymbol{s}}_{\mathrm{F}} = \\ &= \sum_{\mathrm{E} \in \mathcal{E}_{\mathrm{F}}^{i}} \int_{\mathrm{E}} \eta_{\widehat{\lambda}}\, h_{\mathrm{E}} [\![\delta \widehat{\boldsymbol{\lambda}}_h]\!]_{\mathrm{FE}} \cdot \widehat{\boldsymbol{s}}_{\mathrm{F}}. \end{aligned} \tag{3.43}$$

According to the definitions in Sec. 2.3.3, the dG formulation in Sec. 3.3 and gathering the information from Eqs. (3.37)-(3.43), the dG version of the Jacobian operator for the incompressible regime reads

$$
\begin{aligned}
&\left(\boldsymbol{J}^{\mathrm{dG}}_{\mathrm{ie},h}(\boldsymbol{w}_h)\delta\boldsymbol{w}_h, \boldsymbol{z}_h\right)_{L^2(\Omega)} = \\
&= \sum_{\mathrm{T}\in\mathcal{T}_h}\Bigg(\int_{\mathrm{T}}\left[\mathfrak{G}^k_T(\delta\boldsymbol{u}_h) : \mathbb{A}(\mathfrak{F}^k_{\mathrm{T}}(\boldsymbol{u}_h), p_h)\right] : \nabla_{\boldsymbol{X}}\boldsymbol{v}_{\mathrm{T}} + \\
&- \sum_{\mathrm{F}\in\mathcal{F}^{i,\mathrm{D_N}}_{\mathrm{T}}}\int_{\mathrm{F}}\left[\left\{\!\!\left\{\left(\nabla_{\boldsymbol{X}}\delta\boldsymbol{u}_{h|\mathrm{T}} - \mathfrak{R}^{k+1}_{\mathrm{FT}}(\llbracket\delta\boldsymbol{u}_h\rrbracket_{\mathrm{TF}})\right) : \mathbb{A}(\mathfrak{F}^{k+1}_{\mathrm{TF}}(\boldsymbol{u}_h), p_h)\right\}\!\!\right\}_{\mathrm{F}}\boldsymbol{n}_{\mathrm{TF}}\right]\cdot\boldsymbol{v}_{\mathrm{T}} + \\
&+ \sum_{\mathrm{F}\in\mathcal{F}^{i,\mathrm{D_N}}_{\mathrm{T}}}\int_{\mathrm{F}}\eta_{\mathrm{F}}\,\left[\{\!\!\{\mathfrak{R}^k_{\mathrm{FT}}(\llbracket\delta\boldsymbol{u}_h\rrbracket_{\mathrm{TF}})\}\!\!\}_{\mathrm{F}}\,\boldsymbol{n}_{\mathrm{TF}}\right]\cdot\boldsymbol{v}_{\mathrm{T}} + \\
&- \int_{\mathrm{T}}\delta p_h\,\det(\mathfrak{F}^k_{\mathrm{T}}(\boldsymbol{u}_h))\,[\mathfrak{F}^k_{\mathrm{T}}(\boldsymbol{u}_h)]^{-\intercal} : \nabla_{\boldsymbol{X}}\boldsymbol{v}_{\mathrm{T}} + \\
&- \sum_{\mathrm{F}\in\mathcal{F}^{i,\mathrm{D_N}}_{\mathrm{T}}}\int_{\mathrm{F}}\left[\{\!\!\{\delta p_h\,\det(\mathfrak{F}^{k+1}_{\mathrm{TF}}(\boldsymbol{u}_h))\,[\mathfrak{F}^{k+1}_{\mathrm{TF}}(\boldsymbol{u}_h)]^{-\intercal}\}\!\!\}_{\mathrm{F}}\,\boldsymbol{n}_{\mathrm{TF}}\right]\cdot\boldsymbol{v}_{\mathrm{T}} + \\
&+ \int_{\mathrm{T}}\left(\det(\mathfrak{F}^k_{\mathrm{T}}(\boldsymbol{u}_h))[\mathfrak{F}^k_{\mathrm{T}}(\boldsymbol{u}_h)]^{-\intercal} : \mathfrak{G}^k_T(\delta\boldsymbol{u}_h)\right)\,q_{\mathrm{T}} + \sum_{F\in\mathcal{F}^{\mathrm{i}}_{\mathrm{T}}}\int_{\mathrm{F}}\eta_{\mathrm{LBB}}\,h_{\mathrm{F}}\,\llbracket\delta p_h\rrbracket_{\mathrm{TF}}\,q_{\mathrm{T}}\Bigg) + \\
&+ \sum_{\mathrm{F}\in\mathcal{F}^{\mathrm{D_L}}_h}\left(-\int_{\mathrm{F}}\delta\widehat{\boldsymbol{\lambda}}_h\cdot\boldsymbol{v}_{\mathrm{T}} + \int_{\mathrm{F}}\delta\boldsymbol{u}_h\cdot\widehat{\boldsymbol{s}}_{\mathrm{F}} + \sum_{\mathrm{E}\in\mathcal{E}^i_{\mathrm{F}}}\int_{\mathrm{E}}\eta_{\widehat{\boldsymbol{\lambda}}}\,h_{\mathrm{E}}\,\llbracket\delta\widehat{\boldsymbol{\lambda}}_h\rrbracket_{\mathrm{FE}}\cdot\widehat{\boldsymbol{s}}_{\mathrm{F}}\right).
\end{aligned}
$$

We remark that the compressible regime can be retrieved setting $p_h = 0$ such that

$$
\begin{aligned}
&\left(\boldsymbol{J}^{\mathrm{dG}}_{\mathrm{ce},h}(\boldsymbol{w}_h)\delta\boldsymbol{w}_h, \boldsymbol{z}_h\right)_{L^2(\Omega)} = \\
&= \sum_{\mathrm{T}\in\mathcal{T}_h}\Bigg(\int_{\mathrm{T}}\left[\mathfrak{G}^k_T(\delta\boldsymbol{u}_h) : \mathbb{A}(\mathfrak{F}^k_{\mathrm{T}}(\boldsymbol{u}_h))\right] : \nabla_{\boldsymbol{X}}\boldsymbol{v}_{\mathrm{T}} + \\
&- \sum_{\mathrm{F}\in\mathcal{F}^{i,\mathrm{D_N}}_{\mathrm{T}}}\int_{\mathrm{F}}\left[\left\{\!\!\left\{\left(\nabla_{\boldsymbol{X}}\delta\boldsymbol{u}_{h|\mathrm{T}} - \mathfrak{R}^{k+1}_{\mathrm{FT}}(\llbracket\delta\boldsymbol{u}_h\rrbracket_{\mathrm{TF}})\right) : \mathbb{A}(\mathfrak{F}^{k+1}_{\mathrm{TF}}(\boldsymbol{u}_h))\right\}\!\!\right\}_{\mathrm{F}}\boldsymbol{n}_{\mathrm{TF}}\right]\cdot\boldsymbol{v}_{\mathrm{T}} + \\
&+ \sum_{\mathrm{F}\in\mathcal{F}^{i,\mathrm{D_N}}_{\mathrm{T}}}\int_{\mathrm{F}}\eta_{\mathrm{F}}\,\{\!\!\{\mathfrak{R}^k_{\mathrm{FT}}(\llbracket\delta\boldsymbol{u}_h\rrbracket_{\mathrm{TF}})\,\boldsymbol{n}_{\mathrm{TF}}\}\!\!\}_{\mathrm{F}}\cdot\boldsymbol{v}_{\mathrm{T}}\Bigg) + \\
&+ \sum_{\mathrm{F}\in\mathcal{F}^{\mathrm{D_L}}_h}\left(-\int_{\mathrm{F}}\delta\widehat{\boldsymbol{\lambda}}_h\cdot\boldsymbol{v}_{\mathrm{T}} + \int_{\mathrm{F}}\delta\boldsymbol{u}_h\cdot\widehat{\boldsymbol{s}}_{\mathrm{F}} + \sum_{\mathrm{E}\in\mathcal{E}^i_{\mathrm{F}}}\int_{\mathrm{E}}\eta_{\widehat{\boldsymbol{\lambda}}}\,h_{\mathrm{E}}\,\llbracket\delta\widehat{\boldsymbol{\lambda}}_h\rrbracket_{\mathrm{FE}}\cdot\widehat{\boldsymbol{s}}_{\mathrm{F}}\right).
\end{aligned}
$$

3.6.2 Jacobian operator for HDG formulations

Coherently with the definitions in Sec. 3.4, the procedure described in Sec. 3.6.1 for the derivation of the Jacobian operator of dG formulations can be also applied to HDG obtaining

$$\begin{aligned}
&\left(\boldsymbol{J}^{\mathrm{HDG}}_{\mathrm{ce},h}(\boldsymbol{w}_h)\delta\boldsymbol{w}_h, \boldsymbol{z}_h\right)_{L^2(\Omega)} = \\
&\qquad = \sum_{\mathrm{T}\in\mathcal{T}_h}\Bigg(\int_{\mathrm{T}}\left[\boldsymbol{\mathscr{G}}^k_T(\delta\boldsymbol{u}_{\mathcal{T}_h|\mathrm{T}}, \delta\boldsymbol{u}_{\mathcal{F}_h|\partial\mathrm{T}}) : \mathbb{A}(\boldsymbol{\mathscr{F}}^k_{\mathrm{T}}(\boldsymbol{u}_{\mathcal{T}_h|\mathrm{T}}))\right] : \boldsymbol{\mathscr{G}}^k_T(\boldsymbol{v}_{\mathcal{T}_h|\mathrm{T}}, \boldsymbol{v}_{\mathcal{F}_h|\partial\mathrm{T}}) + \\
&\qquad\qquad + \int_{\partial\mathrm{T}}\xi\,\widetilde{\boldsymbol{\mathfrak{s}}}^k_{\partial\mathrm{T}}(\delta\boldsymbol{u}_{\mathcal{T}_h|\mathrm{T}}, \delta\boldsymbol{u}_{\mathcal{F}_h|\partial\mathrm{T}})\cdot\widetilde{\boldsymbol{\mathfrak{s}}}^k_{\partial\mathrm{T}}(\boldsymbol{v}_{\mathcal{T}_h|\mathrm{T}}, \boldsymbol{v}_{\mathcal{F}_h|\partial\mathrm{T}})\Bigg) + \\
&\qquad + \sum_{\mathrm{F}\in\mathcal{F}_h^{\mathrm{D_L}}}\left(-\int_{\mathrm{F}}\delta\widehat{\boldsymbol{\lambda}}_{\mathcal{F}_h^{\mathrm{D_L}}|\mathrm{F}}\cdot\boldsymbol{v}_{\mathcal{F}_h|\mathrm{F}} + \int_{\mathrm{F}}\delta\boldsymbol{u}_{\mathcal{F}_h|\mathrm{F}}\cdot\widehat{\boldsymbol{s}}_{\mathcal{F}_h^{\mathrm{D_L}}|\mathrm{F}}\right).
\end{aligned}$$

Being a hybrid approximation method, the problem (3.34) can be solved using the *static condensation* (or Schur complement) technique. The latter consists of expressing the local cell unknowns $\boldsymbol{u}_{\mathrm{T}}$ in terms of local face unknowns $\boldsymbol{u}_{\partial\mathrm{T}}$. As a result, eliminating the cell unknowns, the static condensation technique allows to reduce (3.34) to a linear system in term of face unknowns only. Further information on the topic are presented in the HHO literature *e.g.* the manuscript [45] and in [2].

3.6.3 Jacobian operator for HHO formulations

Computing the directional derivatives of the global residuals (3.28) and (3.32) following the procedure described in Sec. 3.6.1 for dG methods, the Jacobian operator for the uHHO formulation reads

$$\begin{aligned}
&\left(\boldsymbol{J}^{\mathrm{uHHO}}_{\mathrm{ce},h}(\boldsymbol{w}_h)\delta\boldsymbol{w}_h, \boldsymbol{z}_h\right)_{L^2(\Omega)} = \\
&\qquad = \sum_{\mathrm{T}\in\mathcal{T}_h}\int_{\mathrm{T}}\left[\boldsymbol{\mathscr{G}}^k_T(\delta\boldsymbol{u}_{\mathcal{T}_h|\mathrm{T}}, \delta\boldsymbol{u}_{\mathcal{F}_h|\partial\mathrm{T}}) : \mathbb{A}(\boldsymbol{\mathscr{F}}^k_{\mathrm{T}}(\boldsymbol{u}_{\mathcal{T}_h|\mathrm{T}}))\right] : \boldsymbol{\mathscr{G}}^k_T(\boldsymbol{v}_{\mathcal{T}_h|\mathrm{T}}, \boldsymbol{v}_{\mathcal{F}_h|\partial\mathrm{T}}) + \\
&\qquad + \sum_{\mathrm{F}\in\mathcal{F}_h^{\mathrm{D_L}}}\left(-\int_{\mathrm{F}}\delta\widehat{\boldsymbol{\lambda}}_{\mathcal{F}_h^{\mathrm{D_L}}|\mathrm{F}}\cdot\boldsymbol{v}_{\mathcal{F}_h|\mathrm{F}} + \int_{\mathrm{F}}\delta\boldsymbol{u}_{\mathcal{F}_h|\mathrm{F}}\cdot\widehat{\boldsymbol{s}}_{\mathcal{F}_h^{\mathrm{D_L}}|\mathrm{F}}\right),
\end{aligned}$$

and for the sHHO formulation reads

$$\begin{aligned}
&\left(\boldsymbol{J}^{\mathrm{sHHO}}_{\mathrm{ce},h}(\boldsymbol{w}_h)\delta\boldsymbol{w}_h, \boldsymbol{z}_h\right)_{L^2(\Omega)} = \\
&\qquad = \sum_{\mathrm{T}\in\mathcal{T}_h}\Bigg(\int_{\mathrm{T}}\left[\boldsymbol{\mathscr{G}}^k_T(\delta\boldsymbol{u}_{\mathcal{T}_h|\mathrm{T}}, \delta\boldsymbol{u}_{\mathcal{F}_h|\partial\mathrm{T}}) : \mathbb{A}(\boldsymbol{\mathscr{F}}^k_{\mathrm{T}}(\boldsymbol{u}_{\mathcal{T}_h|\mathrm{T}}))\right] : \boldsymbol{\mathscr{G}}^k_T(\boldsymbol{v}_{\mathcal{T}_h|\mathrm{T}}, \boldsymbol{v}_{\mathcal{F}_h|\partial\mathrm{T}}) + \\
&\qquad\qquad + \int_{\partial\mathrm{T}}\frac{\kappa}{h_{\partial\mathrm{T}}}\boldsymbol{\mathfrak{s}}^k_{\partial\mathrm{T}}(\delta\boldsymbol{u}_{\mathcal{T}_h|\mathrm{T}}, \delta\boldsymbol{u}_{\mathcal{F}_h|\partial\mathrm{T}})\cdot\boldsymbol{\mathfrak{s}}^k_{\partial\mathrm{T}}(\boldsymbol{v}_{\mathcal{T}_h|\mathrm{T}}, \boldsymbol{v}_{\mathcal{F}_h|\partial\mathrm{T}})\Bigg) + \\
&\qquad + \sum_{\mathrm{F}\in\mathcal{F}_h^{\mathrm{D_L}}}\left(-\int_{\mathrm{F}}\delta\widehat{\boldsymbol{\lambda}}_{\mathcal{F}_h^{\mathrm{D_L}}|\mathrm{F}}\cdot\boldsymbol{v}_{\mathcal{F}_h|\mathrm{F}} + \int_{\mathrm{F}}\delta\boldsymbol{u}_{\mathcal{F}_h|\mathrm{F}}\cdot\widehat{\boldsymbol{s}}_{\mathcal{F}_h^{\mathrm{D_L}}|\mathrm{F}}\right).
\end{aligned}$$

3.7 Conclusions

In this chapter, we presented state-of-the-art nonconforming finite element schemes for nonlinear elasticity problems. Numerical validation of dG formulations and evaluation of the efficiency of the incremental load method will be considered in Chap. 4. Numerical validation of HDG and HHO formulations will be considered in Chap. 5.

The possibility to enforce Dirichlet boundary conditions by means of Lagrange multipliers has been discussed for all the numerical schemes. Interestingly HHO and HDG formulations do not require additional penalty terms for the jumps of Lagrange multipliers over boundary edges in order to achieve stability. This basic observation has important practical consequences in the field of computational contact mechanics. Indeed, stabilization terms require to track and identify the sharp corners of the computational domain boundary whose evolution along the deformation path is also influenced by the geometry of obstacles the body comes into contact with. Based on this observation HDG formulations will be the preferred choice in Chap. 6, where a framework for nonlinear elasticity problems featuring frictionless contact constraints will be introduced.

Chapter 4. Numerical Validation of BR2 Discontinuous Galerkin Formulations for Finite Hyperelastic Deformations

The BR2 dG framework for finite deformations of elastic solids presented in Chap. 3 is, herein, validated and tested. The numerical investigation performed on challenging 2D and 3D test cases will focus on the effectiveness of the dG framework in practice.

At each loading step of the incremental method, we have to solve a sequence of linear systems as expected from Newton's method. The linear solver efficiency is crucial for the performance of the solution strategy, especially for isochoric deformation. An agglomeration based h-multigrid preconditioned GMRES solver is employed to compute the solution of the linear systems. We demonstrate that, thanks to the combination of adaptive stabilisation and multigrid solution strategy, the efficacy of the solver is maintained over a wide range of stabilization parameters values. Accordingly, the burden of choosing the stabilization coefficients is streamlined. Moreover, we show that imposing Dirichlet boundary conditions by means of Lagrange multipliers significantly improves the robustness of Newton's method globalisation strategy and reduces the computational cost.

As a first point, we verify the numerical convergence rates for each of the constitutive laws in (2.18)-(2.20) based on manufactured 3D solutions. To this end, the L^2 error norms of the displacement and the displacement gradient are tabulated varying the mesh size h and the polynomial degree k. Afterwords, we challenge the stabilization strategy performing three specifically conceived 2D computations: the *parabolic indentation problem*, see Sec. 4.3.1, the *beam deformation*, see Sec. 4.3.2 and the *cavitating voids*, see Sec. 4.3.3. Notice that the constitutive law in Eq. (2.22) is not included in numerical convergence tests cases and is employed solely for the cavitating voids test case of Sec. 4.3.3. Moreover, we investigate *volumetric locking* in the nearly incompressible regime performing the *Cook's membrane test*, see Sec. 4.3.4. To conclude, we tackle 3D computations and analyse the robustness of the h-multigrid solution strategy with respect to the stabilization parameter. Sec. 4.4.1 and Sec. 4.4.2 consider the *torsion of a square-section bar* and the *deformation of a hollow cylinder* subjected to the rotation of its top surface, respectively.

All numerical test cases require the setup of the incremental strategy presented in Sec. 3.6 whose crucial parameter is the number of loading steps. On the one hand, an underestimated number of increments leads to Newton's method convergence failure and breakdown of the solution strategy, on the other hand, an overestimated number of increments causes an excessive computational cost. Converge failure is often associated with $\det(\mathfrak{F}_{\mathrm{T}}^{k}(\boldsymbol{u})) \leq 0$ or $\det(\mathfrak{F}_{\mathrm{TF}}^{k+1}(\boldsymbol{u})) \leq 0$, meaning that the fundamental hypothesis stated in Eq. (2.10) is violated. While the number of increments can be adaptively chosen by splitting the problematic step until Eq. (2.10) is satisfied (almost) everywhere in the domain, we rely on equispaced increments in all the numerical test cases presented hereafter. The goal is to show how different test cases are handled in terms of number of increments and to stress the crucial role of the strategy employed for imposing Dirichlet boundary conditions, see Sec. 4.1.

At each successful loading path step, Newton iteration achieves a relative residual decrease of ten orders of magnitude in less than eight iterations (usually between four and six). The sequence of linearised equation systems can be solved with either a direct or an iterative solver. In the latter case, due to poor performance of standard Incomplete Lower Upper (ILU) factorization preconditioners, we adopt the h-multigrid agglomeration based solution strategy proposed in Botti *et al.* [61]. As a distinctive feature, h-coarsened mesh sequences are generated on the fly by recursive agglomeration of the fine grid and, accordingly, arbitrarily unstructured grids can be handled as an input of the agglomeration strategy. The cost of numerical integration over agglomerated elements is mitigated by using element-by-element L^2 projections to build coarse grid operators, with projection operators computed and stored once-and-for-all in a preprocessing phase. The performance of the h-multigrid preconditioned iterative solver will be evaluated in terms of number of iterations required to reach a eight orders of magnitude drop of the relative residual norm. We remark that the h-multigrid solution strategy has not been implemented and tested in combination with boundary conditions enforced by means of Lagrange multipliers, accordingly a direct solver is employed instead.

4.1 Influence of Dirichlet boundary conditions on the incremental load method

The BR2 formulations of Sec. 3.3 admit the imposition of Dirichlet Boundary Conditions (BCs) by means of Nitsche method and Lagrange multipliers method. Interestingly, the strategy based on Lagrange multipliers is the most effective, leading to increased robustness of the incremental load method. The following reasoning provides an intuitive explanation for the aforementioned behavior. When using Nitsche method for Dirichlet BCs the occurrence of null or negative Jacobian values, namely $\det(\mathfrak{F}_{\mathrm{TF}}^{k+1}(\boldsymbol{u})) \leq 0$, is often triggered by the action of lifting operators on Dirichlet boundaries, see Eq. (3.3) and definition (3.7). On internal faces, the jumps magnitude is controlled mainly by the discretization parameters: in particular we expect the jumps to shrink while increasing the polynomial degree k and decreasing the mesh step size h. As opposite, on Dirichlet boundary faces, since

Newton's method initial guess is the solution of the previous incremental step, jumps magnitude is dictated primarily by the number of increments of the incremental load method, see also (3.6).

The number of incremental steps for BR2 formulations with Nitsche method and Lagrange multipliers method Dirichlet BCS are reported in Tab. 1, where manufactured solutions are considered, and Tab. 2, where we tabulate data for realistic test cases. In Tab. 1, it is possible to appreciate that, in case of Nitsche method, increasingly higher step counts are required as the mesh is refined and the polynomial degree increases. As opposite, in case of Lagrange multipliers method, three loading steps are employed irrespectively of discretization parameters. The results of Tab. 2 confirm that Lagrange multipliers method leads to an astonishing decrease of the number of steps in all test cases. We remark that the Lagrange multiplier method has not been tested in the incompressible regime, further investigation will be carried in future works.

Finally, in Tab. 3, we provide an overview of the stabilization parameters settings for each of the test cases presented in Sec. 4.3 and Sec. 4.4.

4.2 Evaluation of convergence rates

Convergence tests consider the neo-Hookean (NHK) and Saint Venant-Kirchhoff (SVK) constitutive models in both the compressible (-C) and the incompressible (-I) regime. Numerical solutions are obtained over a four grids h-refined mesh sequence of the unit cube $\Omega : [0,1]^3$. The uniform hexahedral elements have diameter h ranging from 0.25 (coarse mesh) to 0.03125 (fine mesh), halving h at each refinement step, as shown in Fig. 6.

We apply first, second and third degree BR2 dG discretizations and enforce boundary conditions based on smooth analytical displacement fields, see Sec. 4.2.1 and Sec. 4.2.2. Dirichlet boundary conditions based on the exact displacement are imposed with Nitsche method or Lagrange multipliers method on five of the six surfaces composing $\partial\Omega$. A Neumann boundary condition based on the exact deformation gradient is imposed on the unaccounted surface. Convergence is evaluated based on the L^2-norm of the error on the displacement, the displacement gradient and, eventually, the pressure. Forcing terms are computed based on analytical solutions by means of SageMath [62], an open-source library featuring symbolic calculus.

4.2.1 Compressible materials

Let's denote by $\boldsymbol{X} = (X, Y, Z)$ the Cartesian coordinates in the reference configuration and by u, v, w the three components of the displacement vector $\boldsymbol{u}$.

		Number of increments in the loading path			
		BCs enforced by Nitsche method			BCs enforced by Lagrange multipliers
Model	**Mesh**	$k = 1$	$k = 2$	$k = 3$	$k = 1, 2, 3$
NHK-C	coarse	100	400	400	3
	fine	400	800	800	
NHK-I	coarse	400	400	400	-
	fine	800	1000	1500	
SVK-C	coarse	400	800	800	3
	fine	800	2000	2500	
SVK-I	coarse	400	400	800	-
	fine	1500	2000	2000	

Table 1: Number of increments in the loading path for the manufactured solutions of Sec. 4.2. We consider any combination of neo-Hookean and Saint Venant-Kirchhoff constitutive models with compressible and incompressible materials. Results are given considering the coarsest and the finest grid of the Cartesian grids sequence (4^3 and 32^3 hexahedral elements, respectively) for different polynomial degrees $k = \{1, 2, 3\}$.

		Number of increments in the loading path	
Test case	**Material model**	**BCs enforced by Nitsche method**	**BCs enforced by Lagrange multipliers**
Parabolic indentation	NHK-C	60	2
	NHK-I / SVK-I	40	-
Cook's membrane	NHK-C / NHK-I	30	30
Beam deformation	NHK-C	600	15
Cavitating voids	NHK-CAV	-	100
Bar torsion	NHK-C / SVK-C	15 – 60	10
	NHK-I / SVK-I	15 – 80	-
Cylinder top face rotation	NHK-C	1000	30
	NHK-I	650	-

Table 2: Number of increments in the loading path for all 2D and 3D test cases considered in Sec. 4.3 and Sec. 4.4. In case of Bar torsion the number of incremental steps was fine tuned according to the polynomial degree, see Sec. 4.4.1 for additional details.

Test case	β	ϵ	$\eta_{\mathbf{LBB}}$	$\eta_{\widehat{\lambda}}$
Convergence tests	1	0	1	1
Parabolic indentation	0	0	1	1
Cook's membrane	0–10	0	1	1
Beam deformation	1	1	-	1
Cavitating voids	1	1	-	1
Bar torsion	0–5	0	1	1
Cylinder top face rotation	4	1	1	1

Table 3: Stabilization parameters for all 2D and 3D test cases considered in Sec. 4.3 and Sec. 4.4. In case of Bar torsion β was fine tuned according to the polynomial degree, see Sec. 4.4.1 for additional details.

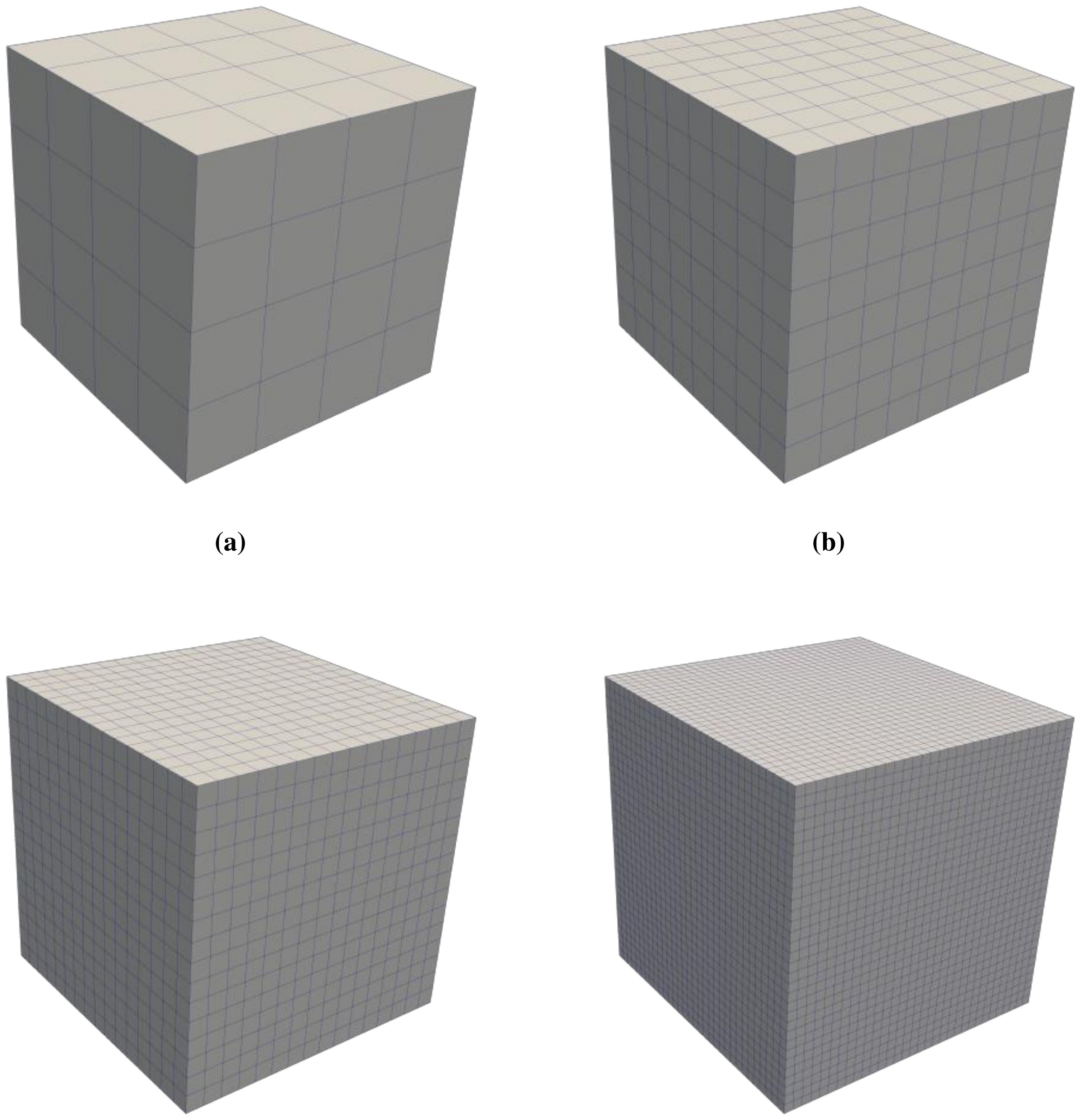

(a) (b) (c) (d)

Figure 6: Four grids h-refined mesh sequence of a unit cube $\Omega : [0,1]^3$ used in 3D convergence tests.

In the compressible regime, we consider the following displacement field proposed by Abbas *et al.* [2]

$$\begin{cases} u(\boldsymbol{X}) = \left(\dfrac{1}{\lambda} + \alpha\right) X + \psi(Y) \\ v(\boldsymbol{X}) = -\left(\dfrac{1}{\lambda} + \dfrac{\alpha + \gamma + \alpha\gamma}{1 + \alpha + \gamma + \alpha\gamma}\right) Y \\ w(\boldsymbol{X}) = \left(\dfrac{1}{\lambda} + \gamma\right) Z + \omega(X) + \xi(Y) \end{cases}$$

where $\alpha = \gamma = 0.1$, $\psi(Y) = \alpha \sin(\pi Y)$, $\omega(X) = \gamma \sin(\pi X)$ and $\xi(Y) = 0$. Relevant parameters of the NHK-C and SVK-C constitutive laws are defined setting $\mu = 1$ and $\lambda = 10$, which corresponds to a Poisson's ration of $\nu \simeq 0.455$. The adaptive stabilization parameters are taken as $\beta = 1$ and $\epsilon = 0$, respectively. In case of Dirichlet boundary conditions enforced by means of Lagrange multipliers, we set $\eta_{\widehat{\lambda}} = 1$. Asymptotic convergence rates of order $k + 1$ and k for the displacement and the displacement gradient can be appreciated in Tab. 4 and Tab. 5 for the NHK-C and the SVK-C model, respectively.

4.2.2 Incompressible nonlinear elasticity

The fully incompressible nonlinear elasticity problem is defined according to the following isochoric displacement field

$$\begin{cases} u(\boldsymbol{X}) = (a^2 - 1)X + \dfrac{b}{2}\sin^2(Y) + \dfrac{c}{2}\sin^2(Z) \\ v(\boldsymbol{X}) = \left(\dfrac{1}{a} - 1\right) Y \\ w(\boldsymbol{X}) = \left(\dfrac{1}{a} - 1\right) Z \end{cases}$$

where $a = 1.1$, $b = 1$ and $c = 1$. The pressure field reads $p = \frac{1}{3}\mathrm{tr}\,(\boldsymbol{\sigma})$, where $\boldsymbol{\sigma} = \frac{1}{J}\boldsymbol{F}\boldsymbol{S}\boldsymbol{F}^{\intercal}$ is the Cauchy stress tensor. Based on the NHK-I model, the exact pressure reads

$$p^{\text{NHK-I}} = \frac{c^2\cos^2(Z)\sin^2(Z)\mu + b^2\cos^2(Y)\sin^2(Y)\mu + a^4\mu + \frac{2\mu}{a^2}}{3}.$$

Based on the SVK-I model, the exact pressure reads

$$\begin{aligned} p^{\text{SVK}} = \frac{1}{6}\mu\Big(&2\cos^4(Z)\sin^4(Z) + \Big(4\cos^2(Y)\sin^2(Y) + 6\Big)\cos^2(Z)\sin^2(Z) + \\ &+ 2\cos^4(Y)\sin^4(Y) + 6\cos^2(Y)\sin^2(Y)\Big) + \\ +\frac{1}{6}\lambda\Big(&\cos^4(Z)\sin^4(Z) + \Big(2\cos^2(Y)\sin^2(Y) + 3\Big)\cos^2(Z)\sin^2(Z) + \\ &+ \cos^4(Y)\sin^4(Y) + 3\cos^2(Y)\sin^2(Y)\Big). \end{aligned}$$

card($\mathcal{T}_h$)	$\Vert\boldsymbol{u}-\boldsymbol{u}_h\Vert_{L^2(\Omega)}$	**rate**	$\Vert\nabla_{\boldsymbol{X}}(\boldsymbol{u}-\boldsymbol{u}_h)\Vert_{L^2(\Omega)}$	**rate**	$\Vert\boldsymbol{u}-\boldsymbol{u}_h\Vert_{L^2(\Omega)}$	**rate**	$\Vert\nabla_{\boldsymbol{X}}(\boldsymbol{u}-\boldsymbol{u}_h)\Vert_{L^2(\Omega)}$	**rate**
	$k = 1$, BCs by Nitsche method				$k = 1$, BCs by Lagrange multipliers method			
64	2.457e-03	-	7.116e-02	-	2.622e-03	-	7.250e-02	-
512	6.104e-04	2.00	3.561e-02	0.99	6.126e-04	2.10	3.565e-02	1.02
4096	1.536e-04	1.99	1.781e-02	0.99	1.538e-04	1.99	1.780e-02	1.00
32768	3.853e-05	1.99	8.903e-03	1.00	3.858e-05	1.99	8.904e-03	1.00
	$k = 2$, BCs by Nitsche method				$k = 2$, BCs by Lagrange multipliers method			
64	2.241e-04	-	7.374e-03	-	6.589e-04	-	1.295e-02	-
512	2.859e-05	2.97	1.838e-03	2.00	4.982e-05	3.73	2.323e-03	2.48
4096	3.568e-06	3.00	4.580e-04	2.00	4.484e-06	3.47	4.944e-04	2.23
32768	4.421e-07	3.01	1.141e-04	2.00	4.765e-07	3.23	1.165e-04	2.09
	$k = 3$, BCs by Nitsche method				$k = 3$, BCs by Lagrange multipliers method			
64	1.130e-05	-	4.926e-04	-	1.257e-05	-	5.400e-04	-
512	7.462e-07	3.92	6.110e-05	3.01	7.480e-07	4.07	6.183e-05	3.13
4096	4.796e-08	3.96	7.579e-06	3.00	4.794e-08	3.96	7.598e-06	3.02
32768	3.043e-09	3.98	9.420e-07	3.00	$\star$	-	$\star$	-

Table 4: Errors and convergence rates for BR2 dG discretizations of degree $k = \{1, 2, 3\}$ over a h-refined mesh sequence of the unit cube, NHK-C constitutive model. $\star$ indicates unavailable data due to excessive memory consumption of the LU solver.

card($\mathcal{T}_h$)	$\|\boldsymbol{u}-\boldsymbol{u}_h\|_{L^2(\Omega)}$	**rate**	$\|\nabla_{\boldsymbol{X}}(\boldsymbol{u}-\boldsymbol{u}_h)\|_{L^2(\Omega)}$	**rate**	$\|\boldsymbol{u}-\boldsymbol{u}_h\|_{L^2(\Omega)}$	**rate**	$\|\nabla_{\boldsymbol{X}}(\boldsymbol{u}-\boldsymbol{u}_h)\|_{L^2(\Omega)}$	**rate**
	$k = 1$, BCs by Nitsche method				$k = 1$, BCs by Lagrange multipliers method			
64	2.486e-03	-	7.117e-02	-	2.648e-03	-	7.248e-02	-
512	6.211e-04	2.00	3.562e-02	0.99	6.259e-04	2.08	3.567e-02	1.02
4096	1.558e-04	1.99	1.781e-02	1.00	1.562e-04	1.99	1.781e-02	1.00
32768	3.901e-05	1.99	8.904e-03	1.00	3.906e-05	1.99	8.904e-03	1.00
	$k = 2$, BCs by Nitsche method				$k = 2$, BCs by Lagrange multipliers method			
64	2.170e-04	-	7.345e-03	-	6.217e-04	-	1.262e-02	-
512	2.789e-05	2.99	1.831e-03	2.00	4.810e-05	3.69	2.283e-03	2.47
4096	3.504e-06	2.99	4.566e-04	2.00	4.401e-06	3.45	4.909e-04	2.22
32768	4.383e-07	2.99	1.140e-04	2.00	4.731e-07	3.22	1.162e-04	2.08
	$k = 3$, BCs by Nitsche method				$k = 3$, BCs by Lagrange multipliers method			
64	1.138e-05	-	4.894e-04	-	1.261e-05	-	5.385e-04	-
512	7.513e-07	3.92	6.069e-05	3.01	7.516e-07	4.07	6.186e-05	3.12
4096	4.818e-08	3.96	7.542e-06	3.00	4.804e-08	3.97	7.600e-06	3.03
32768	3.049e-09	3.98	9.396e-07	3.00	$\star$	-	$\star$	-

Table 5: Errors and convergence rates for BR2 dG discretizations of degree $k = \{1, 2, 3\}$ over a h-refined mesh sequence of the unit cube, SVK-C constitutive model. $\star$ indicates unavailable data due to excessive memory consumption of the LU solver.

As in the previous section, the adaptive stabilization parameters are set as $\beta = 1$ and $\epsilon = 0$, while pressure jumps stabilization coefficient is taken as $\eta_{\mathrm{LBB}} = 1$. Similarly to the compressible regime, asymptotic convergence rates of order $k + 1$ and k are observed for the displacement and the displacement gradient over h-refined meshes. The pressure error in L^2-norm exhibits a rate of convergence between k and $k + 1$. Convergence results are reported in Tab. 6 and Tab. 7 for the NHK-I and SVK-I models, respectively.

4.3 2D simulations

4.3.1 Parabolic indentation problem

The 2D *parabolic indentation* problem imposes a severe deformation of parabolic shape to the top surface of a unit-length square computational domain $\Omega : [0, 1]^2$. As proposed by Eyck and coworkers [29], the parabolic profile reads $v(\boldsymbol{X}) = 3(X - 0.5)^2$ and the bottom surface is clamped. The computational mesh consist of 512 triangular elements and we consider a first degree BR2 dG discretization. Dirichlet boundary conditions are imposed on the top and bottom surfaces while homogeneous Neumann boundary conditions are enforced on the rest of the boundary. We set $\beta = 0$ and $\epsilon = 0$, meaning that the adaptive stabilization strategy is switched-off, and, in the incompressible regime, we also set $\eta_{\mathrm{LBB}} = 1$.

The deformed states obtained with all constitutive models relevant for this configuration are depicted in Fig. 7, material parameters reads $\mu = \lambda = 0.4$. When using the SVK-C model, Newton's method fails to converge when reaching 50% of the loading path, irrespectively of the amount of stabilization introduced. Accordingly, the final configuration is not attained. This behavior can be explained by noticing that, as opposite to the NHK-C model, the SVK strain-energy function (2.18) lacks of any term preventing the onset of negative Jacobian values, see also [4]. We remark that the SVK-I model is successful, because $\det(\boldsymbol{F})$=1 is weakly enforced in accordance with the incompressibility constraint.

4.3.2 2D beam deformation

As proposed by Eyck and co-workers [30], we challenge the adaptive stabilisation strategy considering the deformation of a 2D beam: the bottom surface is clamped while the upper surface of the beam is first rotated by $\pi/2$ and, then, translated in the direction orthogonal to the beam axis. We consider a NHK-C constitutive law and we set $\nu = 0.3$ and $E = 1$. The computational mesh consists of 110 triangular elements and we employ a $k = 1$ BR2 dG discretization. Dirichlet boundary conditions

card($\mathcal{T}_h$)	$\|\boldsymbol{u}-\boldsymbol{u}_h\|_{L^2(\Omega)}$	**rate**	$\|p-p_h\|_{L^2(\Omega)}$	**rate**	$\|\nabla_{\boldsymbol{X}}(\boldsymbol{u}-\boldsymbol{u}_h)\|_{L^2(\Omega)}$	**rate**
	k = 1, BCs by Nitsche method					
64	2.665e-03	-	3.137e-02	-	6.589e-02	-
512	6.531e-04	2.02	1.002e-02	1.64	3.270e-02	1.01
4096	1.638e-04	1.99	2.764e-03	1.85	1.628e-02	1.01
32768	4.122e-05	1.99	7.464e-04	1.88	8.129e-03	1.00
	k = 2, BCs by Nitsche method					
64	1.801e-04	-	2.612e-03	-	5.165e-03	-
512	2.246e-05	3.00	2.882e-04	3.18	1.279e-03	2.01
4096	2.808e-06	2.99	3.338e-05	3.11	3.187e-04	2.01
32768	3.514e-07	2.99	4.405e-06	2.92	7.958e-05	2.00
	k = 3, BCs by Nitsche method					
64	4.257e-06	-	5.952e-05	-	1.817e-04	-
512	2.782e-07	3.94	4.538e-06	3.73	2.252e-05	3.01
4096	1.780e-08	3.97	3.392e-07	3.74	2.794e-06	3.01
32768	1.126e-09	3.98	2.709e-08	3.65	3.478e-07	3.00

Table 6: Errors and convergence rates for BR2 dG discretizations of degree $k = \{1, 2, 3\}$ over a h-refined mesh sequence of the unit cube, NHK-I constitutive model.

card($\mathcal{T}_h$)	$\|\boldsymbol{u}-\boldsymbol{u}_h\|_{L^2(\Omega)}$	**rate**	$\|p-p_h\|_{L^2(\Omega)}$	**rate**	$\|\nabla_{\boldsymbol{X}}(\boldsymbol{u}-\boldsymbol{u}_h)\|_{L^2(\Omega)}$	**rate**
	k = 1, BCs by Nitsche method					
64	2.596e-03	-	3.691e-02	-	6.555e-02	-
512	6.522e-04	1.99	1.437e-02	1.36	3.265e-02	1.01
4096	1.653e-04	1.98	4.348e-03	1.72	1.628e-02	1.00
32768	4.181e-05	1.98	1.180e-03	1.88	8.128e-03	1.00
	k = 2, BCs by Nitsche method					
64	1.707e-04	-	4.901e-03	-	5.175e-03	-
512	2.127e-05	3.01	6.606e-04	2.89	1.282e-03	2.01
4096	2.660e-06	2.99	1.339e-04	2.30	3.195e-04	2.00
32768	3.328e-07	2.99	3.227e-05	2.05	7.977e-05	2.00
	k = 3, BCs by Nitsche method					
64	4.248e-06	-	1.020e-04	-	1.814e-04	-
512	2.779e-07	3.93	6.755e-06	3.92	2.248e-05	3.01
4096	1.779e-08	3.97	4.701e-07	3.85	2.792e-06	3.01
32768	1.126e-09	3.98	3.463e-08	3.76	3.477e-07	3.00

Table 7: Errors and convergence rates for BR2 dG discretizations of degree $k = \{1, 2, 3\}$ over a h-refined mesh sequence of the unit cube, SVK-I constitutive model.

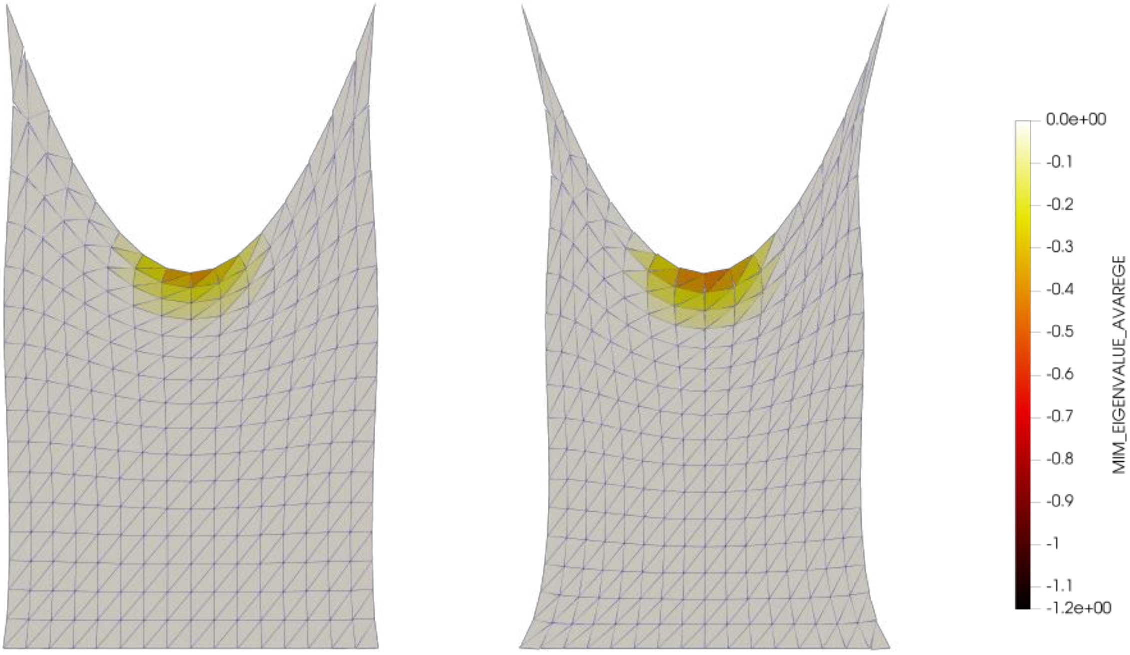

(a) NHK-C **(b)** NHK-I

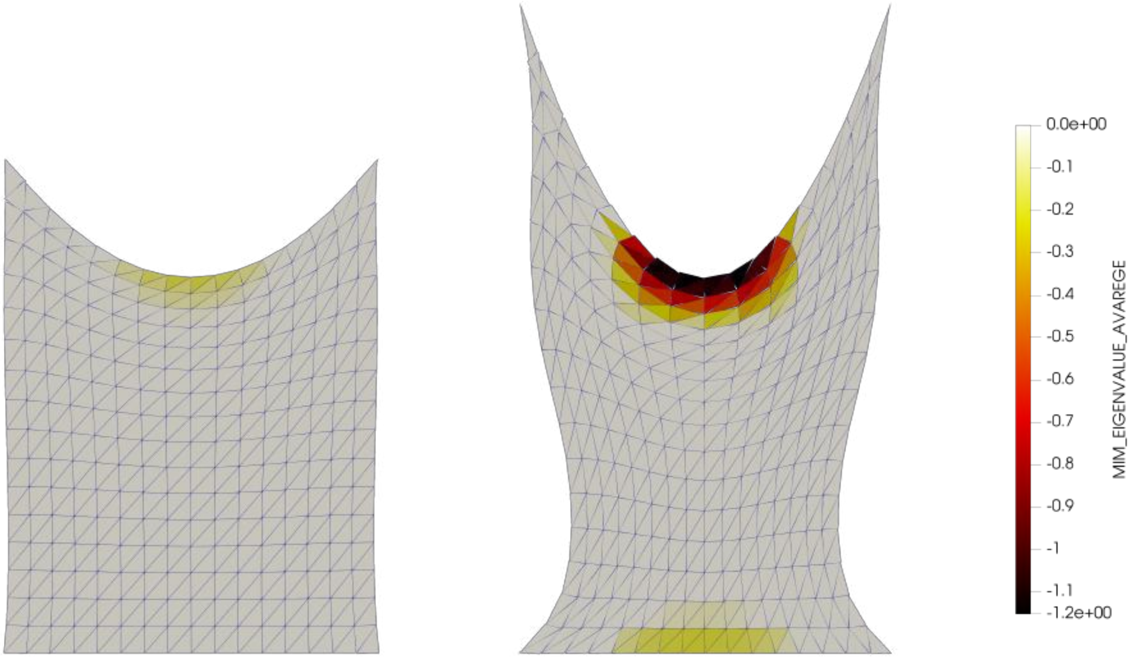

(c) SVK-C **(d)** SVK-I

Figure 7: Deformed configurations of the parabolic indentation problem using NHK and the SVK constitutive models. Images are colour coded based on the minimum negative eigenvalue of the fourth order elasticity tensor $\mathbb{A}$.

are imposed on the top and bottom surfaces while homogeneous Neumann boundary conditions are enforced on the rest of the boundary.

Fig. 8 depicts the beam deformation by showing a sequence of deformed states consistent with the loading path. Deformed states are colour-coded with minimum negative eigenvalues of the elasticity tensor allowing to appreciate that compression of the beam material triggers the adaptive stabilization strategy.

In order to study the influence of the stabilization parameter on the performance of the h-multigrid solution strategy, we run a series of test varying β in the interval $[0, 200]$ for each ϵ in $\{0, 1, 10, 20\}$. For each combination of β and ϵ, the history of total linear solver iterations recorded along the loading path, counting of 600 incremental steps, is depicted in Fig. **??**. Furthermore, the average and maximum number of Newton iteration as well as the average and maximum number of linear solver iterations are tabulated in Tab. 8.

We remark that, in the range $0 \leq \beta \leq 200$, the number of linear solver iterations is pretty stable, and setting $\epsilon = 1$ reduces the number of Newton iteration resulting in a decrease of the total number of the linear solver iterations per incremental step.

4.3.3 Cavitating voids

In solid mechanics, the term *cavitation* refers to the formation and rapid expansion of voids that occurs when a solid is subjected to sufficiently large tensile stresses. Some experiments on the cavitation are reported by Gent and Lindley *e.g.* [11] where unusual internal flaws appear in vulcanized rubber cylinders under a well-defined relatively small tensile load. Since, during the growth of voids, significant deformation occurs near the cavities, the numerical simulation of cavitation requires numerical methods that are robust respect to mesh distortion. A Crouzeix-Raviart nonconforming finite element method was presented in Xu and Henao [63] while, more recently, the cavitation problem has been studied using HDG [1] and HHO [2] discretizations. The interested reader may refer to the review by Xu *et al.* [63].

We consider a unit radius disk centered at the origin with two holes: the first centered at $C_1 = (-0.3, 0, 0)$ with radius 0.25 and the second centered at $C_2 = (0.3, 0, 0)$ with radius 0.2. The disc is expanded by imposing Dirichlet boundary conditions $\boldsymbol{g}_{\mathrm{D}} = (\alpha - 1)\boldsymbol{X}$, with $\alpha \geq 1$, on the outer surface ($|\boldsymbol{X}| = 1$ in reference configuration), while imposing traction-free Neumann boundary conditions on the inner walls of the holes. For cavitation to occur, we rely on the strain energy function in (2.22). Note that, with respect to the standard NHK-C law (2.21), NHK-CAV has been modified to reduce

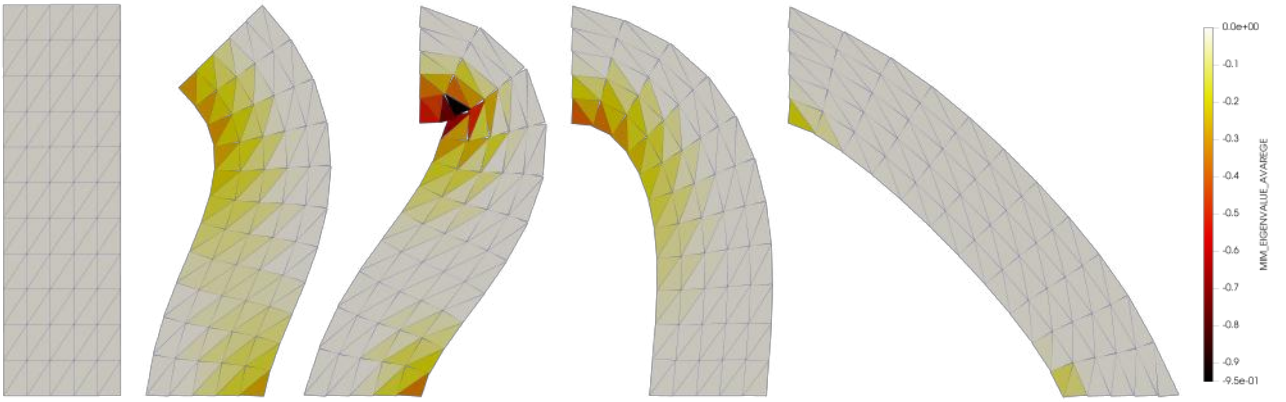

Figure 8: Deformation of a 2D NHK-C beam. Images are colour-coded based on the minimum negative eigenvalue of the fourth-order elasticity tensor $\mathbb{A}$.

ϵ			β										
			0	**1**	**2**	**4**	**8**	**16**	**30**	**50**	**100**	**150**	**200**
0	**Newton iterations**	**mean**	6	6	6	6	6	6	6	6	6	6	6
		max	7	7	7	8	8	8	9	9	10	10	10
	Linear Solver iterations	**mean**	4	4	4	4	4	4	4	4	5	5	5
		max	6	6	7	7	7	7	7	7	8	8	9
1	**Newton iterations**	**mean**	5	5	6	6	6	5	5	5	5	5	5
		max	6	7	7	7	7	7	7	7	8	8	8
	Linear Solver iterations	**mean**	4	4	4	4	4	4	4	4	5	5	5
		max	6	7	7	7	7	7	7	7	8	8	8
10	**Newton iterations**	**mean**	5	5	5	5	5	5	5	5	5	5	5
		max	5	5	5	5	5	5	5	6	6	6	5
	Linear Solver iterations	**mean**	5	5	5	5	5	5	5	5	6	6	6
		max	8	8	8	8	8	8	8	8	8	9	9
20	**Newton iterations**	**mean**	5	5	5	5	5	5	4	4	4	4	4
		max	5	5	5	5	5	5	5	5	5	5	5
	Linear Solver iterations	**mean**	6	6	6	6	6	6	6	6	7	7	7
		max	9	9	9	9	9	9	9	9	9	10	10

Table 8: 2D NHK-C beam: average and maximum number of Newton and linear solver iterations recorded along the loading path. Results are obtained varying the stabilization parameters β and ϵ in order to show their influence on the performance of the solution strategy.

the rate of the strain-energy growth with respect to the deformation gradient. In order to enable direct comparison with [1], we use the same material configuration setting $\mu = 0.1$ and $\lambda = 1$ and $\alpha = 4.7$. Fig. 10 reports the results obtained choosing $k = \{1, 2, 3\}$. It is interesting to remark that only higher-order $k = 2, 3$ dG discretizations are able to reach the final configuration while the first degree $k = 1$ discretization fails at 64% of the loading path due to the onset of negative Jacobian values, see Fig. 10a.

The adaptive stabilization parameters are set as $\beta = 1$ and $\epsilon = 1$, the latter helping Newton's method convergence rates. This test case requires 100 incremental steps with Dirichlet boundary conditions imposed by means of the Lagrange multipliers method, as opposite, we were unable to succeed with Dirichlet BCs imposed by means of Nitsche method. As reported in Tab. 2, 100 steps is the highest number of increments required among all test cases employing Lagrange multipliers. This confirms that the test case challenges the robustness of the numerical strategy. The final highly distorted computational mesh, consisting of 8982 triangular elements, is depicted in Fig. 11.

4.3.4 Cook's membrane

We consider the problem sketched in Fig. 12 where a tapered panel is clamped on the the left side and subjected to a shearing dead load $\boldsymbol{T}_\mathrm{N} = 0,0625\mathrm{N/mm}^2$ on the opposite end. This bending-dominated test case is known as *Cook's membrane*. Many authors (i.e. Simo and Armero (1992) [64] or Brink and Stein (1996) [8]) consider this problem as a benchmark to investigate the phenomenon of volumetric-locking.

In order to investigate possible locking phenomena in our dG formulation, we propose a comparison between the nearly (NHK-C) and the fully (NHK-I) incompressible models. For the nearly incompressible regime, a material with the volumetric function $\Theta(J) = J - 1$ is chosen for the purpose of comparing our results with those presented in [8]. The material parameters are assumed to be $\mu = 0.8\ \mathrm{N/mm}^2$ and $\lambda = 8000\ \mathrm{N/mm}^2$ so as the Poisson's ratio results $\nu = 0.49995$. Instead, for the fully incompressible regime, we consider a NHK-I material with $\mu = 0.8\mathrm{N/mm}^2$.

The stabilization parameter is increased while raising the polynomial degree, in particular we set $\beta = 3, 7, 10$ at $k = 1, 2, 3$, respectively. We remark the need for adaptive stabilization triggered by the stress singularity at the top left corner. Since increasing the polynomial degree the numerical solution approaches the singular solution, more stabilization is required. On the other hand, the fully incompressible material regime does not require to activate the adaptive stabilization strategy. In all test cases, we set $\epsilon = 0$ and, for the incompressible tests, $\eta_\mathrm{LBB} = 1$.

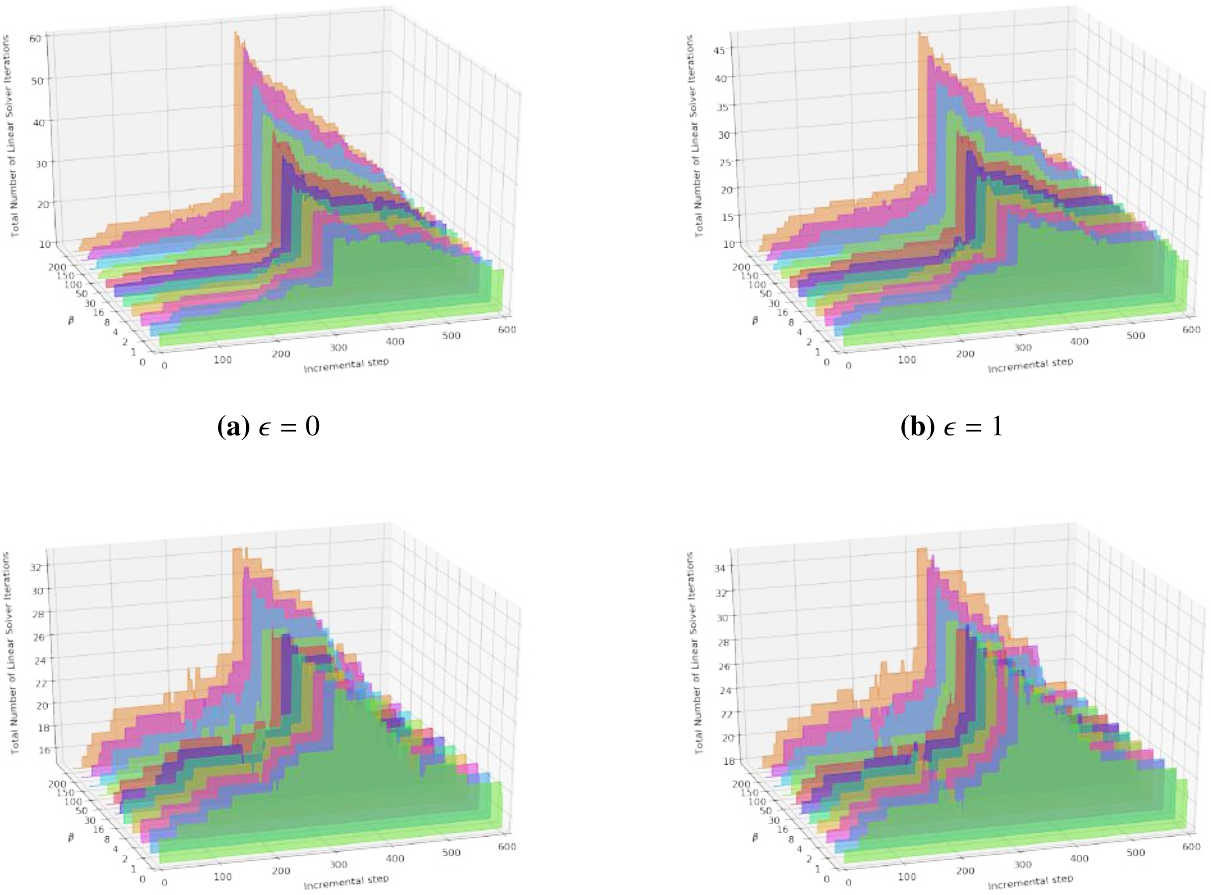

(a) $\epsilon = 0$

(b) $\epsilon = 1$

(c) $\epsilon = 10$

(d) $\epsilon = 20$

Figure 9: 2D NHK-C beam: total number of linear solver iterations recorded along the loading path (600 increments). Results are obtained varying the stabilization parameters β and ϵ in order to show their influence on the performance of the solution strategy.

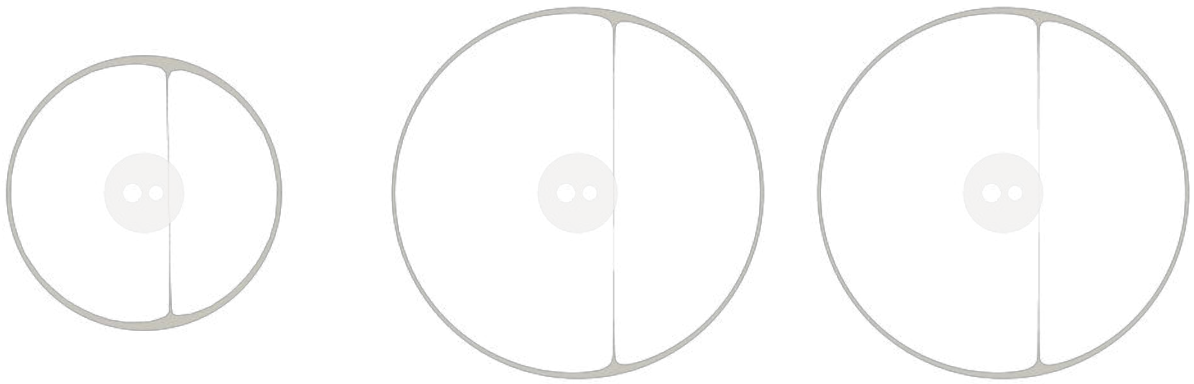

(a) $k = 1$

(b) $k = 2$

(c) $k = 3$

Figure 10: NHK-CAV disk with two holes subjected to tensile stresses. For each polynomial degree $k = \{1, 2, 3\}$ the reference configuration (small disk with circular holes) and deformed configurations (big disk with stretched holes) are shown.

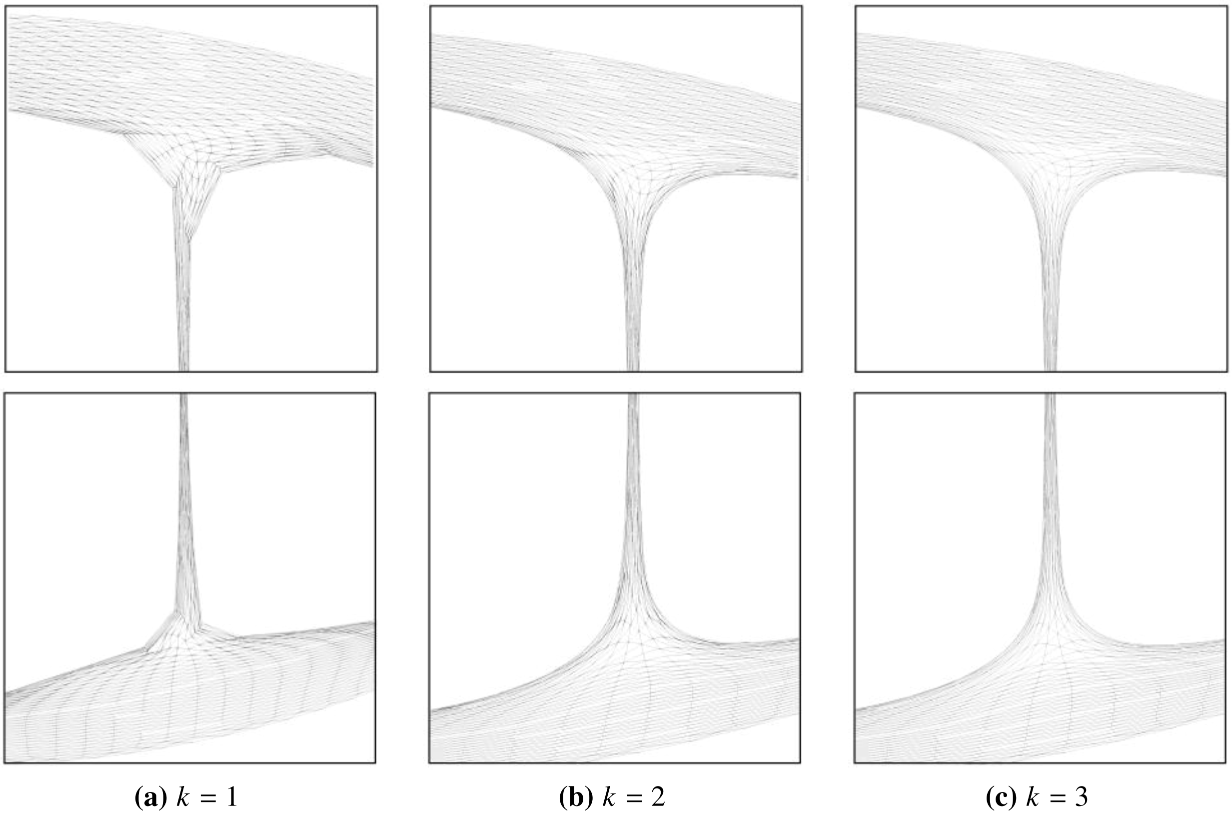

Figure 11: NHK-CAV disk with two holes subjected to tensile stresses. Details of the strip separating the two holes at different polynomial degrees $k = \{1, 2, 3\}$.

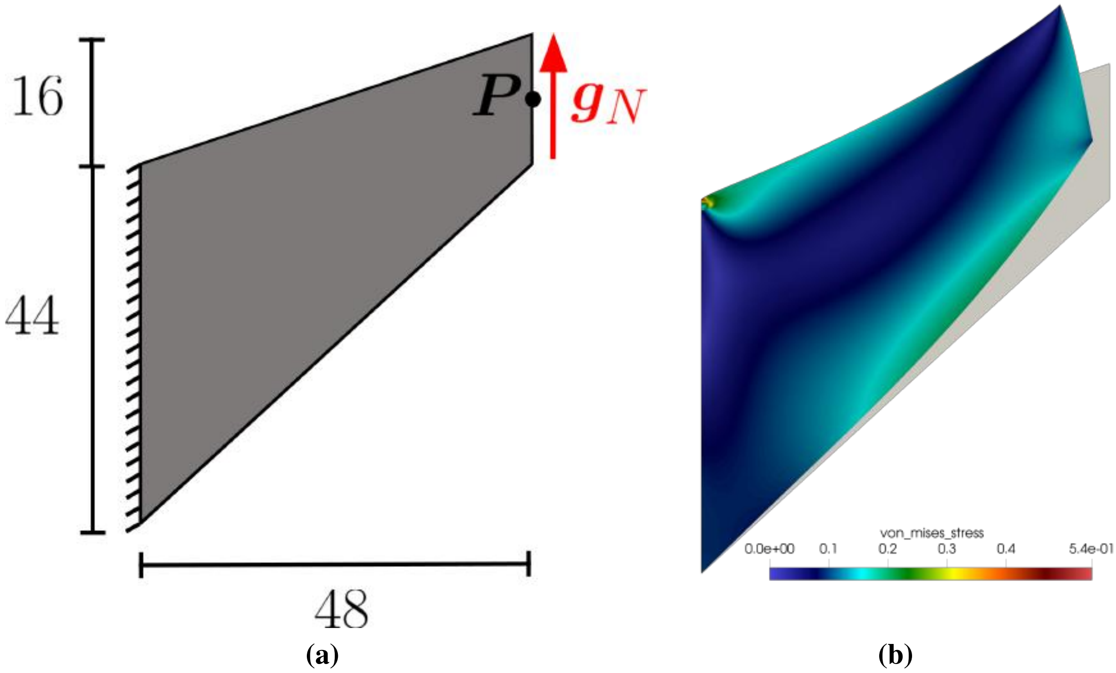

Figure 12: (a) Geometry of the Cook's membrane test: a clamped tapered panel subjected to a shearing load. (b) Third-order solution of the *Cook's membrane* (nearly incompressible neo-Hookean model (NHK-C, $\mu = 0.8$, $\lambda = 8000$ and $\Theta(J) = J - 1$)). Colours represent the von Mises stress distribution.

We consider triangular and quadrilateral mesh sequences of the computational domain identified according to the number of elements along each side of $\partial\Omega$. Triangular meshes are obtained splitting each quadrilateral element in two triangles. As an example, two 16×16 meshes are depicted in Fig. 13. The maximum vertical displacements detected at the point P (see Fig. 12) are tabulated in Tab. 9 considering NHK models in the nearly compressible limit and a sequence of four meshes (from 4 to 32 element per side).

It's worth noting that the locking phenomenon occurs only with quadrilateral elements ($k = 1$). Note that, the maximum displacement is underestimated with respect to the reference value of $\simeq$ 7mm reported in the literature. Locking is not visible for triangular elements with $k = \{1, 2, 3\}$ and square elements with $k = \{2, 3\}$. Further information on the topic can be found in [65] where a low-order locking-free hybrid dG element is presented.

An interesting result is reported in Tab. 10 in which we compare the values of the maximum vertical displacement obtained on a 16×16 mesh with the nearly and the fully incompressible models. The imposition of the incompressibility constraint (2.17) avoids the locking phenomenon (see the results obtained with first-order quadrilateral element). The discrepancy between the nearly and the fully incompressible models using quadrilateral meshes at $k = 1$ are plotted in Fig. 14.

4.4 3D simulations

4.4.1 Torsion of a square section bar

We consider a square section bar such that $H/L = 5$, where L is the edge length of the square cross-section and H is the extension of the bar in the axial direction. The mesh, consisting of 400 uniform hexahedral elements, is shown in Fig. 15. The bottom surface is clamped while the top surface is subjected to a 360 degrees plane rotation around its centroid. We employ the fully incompressible SVK-I model with material parameters $\mu = 1$ and $\lambda = 1$. We remark that this test case was successfully completed also based on the SVK-C, NHK-C and NHK-I constitutive laws but the results are not presented for the sake of conciseness. Dirichlet boundary conditions are imposed on the top and bottom surfaces while homogeneous Neumann boundary conditions are enforced on the rest of the boundary. Regarding the stabilization parameters, adaptive stabilization is mandatory only in the NHK-C case: we set $\beta = 1$ for $k = 1$, $\beta = 2$ for $k = 2$ and $\beta = 5$ for $k = 3$. Other relevant parameters are $\epsilon = 0$ and $\eta_{\mathrm{LBB}} = 1$ in the incompressible regime.

The results for the SVK-I model are displayed in Fig. 15 considering first, second and third degree BR2 dG discretizations. Increasing the polynomial degree reduces the amplitude of discontinuities in the displacement field resulting in a more precise representation of the geometry of the deformed bar. Furthermore, the regions where the stresses intensify are more accurately captured: note that, for $k = 1$, the stress is constant inside each mesh element.

4.4.2 Cylinder deformation

We consider a hollow cylinder such that $H/R = 4$ and $r = 0.7R$, where R and r are, respectively, the external and internal radius of the annulus cross-section and H is the extension of the cylinder in the axial direction. As proposed in [29], the top surface of the cylinder is rotated while keeping the bottom surface clamped. We consider both NHK-C and NHK-I constitutive laws with $\nu = 0.25$ and $E = 1$. Dirichlet boundary conditions are imposed on the top and bottom surfaces while homogeneous Neumann boundary conditions are enforced on the rest of the boundary.

Fig. 16 reports the computational mesh, consisting of 8906 tetrahedral elements, and the deformed configurations at different rotation angles α, with $0 \leq \alpha \leq \frac{\pi}{2}$, obtained for the compressible case with a first degree BR2 dG formulation. It is worth mentioning that for $\alpha \geq \frac{\pi}{4}$ the cylinder penetrates itself due to the lack of contact boundary conditions. Despite the lack of meaningfulness from the physical viewpoint, this result emphasises the capability of dealing with large deformations.

The stabilization parameters reads $\beta = 4$ and $\epsilon = 1$ and $\eta_{\text{LBB}} = 1$ for the incompressible model. In Fig. 17, deformed states are colour-coded with minimum negative eigenvalues of the fourth-order elasticity tensor allowing to appreciate that compression of the beam material triggers the adaptive stabilization strategy. Fig. 17b also depicts the deformed state reached at 65% of the entire rotation by the NHK-I cylinder. After approaching this configuration Newton's method struggles to converge irrespectively of the amount of stabilization introduced.

As we did for the beam deformation of Sec. 4.3.2, we analyse the influence of the stabilization parameter on the performance of the h-multigrid solution strategy. We consider a 1000 increments loading path and choose $\beta \in [0, 200]$ and $\epsilon \in \{0, 1, 10, 20\}$. In Fig. **??**, for each incremental step solved by Newton's method, we report the total number of linear solver iterations obtained varying β and ϵ. The average and maximum number of Newton iteration as well as the average and maximum number of linear solver iterations are tabulated in Tab. 11.

The iteration spike observed at around one fifth of the loading path is due to buckling of the cylinder. We remark that for $\beta < 4$ and $\epsilon = 0$ the computation fails due to an insufficient amount of stabilisation. In the range $4 \leq \beta \leq 50$, the runs are successful and we observe a mild increase of the number of linear solver iterations. An excessive amount of stabilization ($\beta > 50$) deteriorates the solver efficiency leading to a significant increase of the computational time.

4.5 Conclusions

We numerically validated the dG framework developed in Sec. 3.3 for the simulation of finite deformation based on compressible and incompressible hyperelastic material models. The framework relies on BR2 dG discretizations and allows to impose Dirichlet boundary conditions by means of Nitsche method and Lagrange multipliers. State of the art agglomeration based h-multigrid solution strategies have been successfully employed to improve efficiency of the solution strategy.

The proposed BR2 formulation provides the same attractive features of BR1 dG discretizations for a reduced computational cost thanks to a more compact stencil: each cell is coupled solely with its neighbouring elements instead of neighbours plus neighbours of neighbours. In order to better control the amount of stabilization the BR2 stabilization term relies on lifting operators defined in a polynomial space that is one degree higher than the polynomial space employed for test and trial functions. The approach has demonstrated effective over computational meshes composed of elements of standardized shape (triangles and quadrilaterals in 2D, tetrahedra and hexahedra in 3D) and allows to get rid of non-local stabilization parameters based on the number of faces.

We demonstrated that the Lagrange multiplier method for imposing Dirichlet boundary conditions is more effective than Nitsche method in the sense that the number of incremental step can be reduced by orders of magnitude. Moreover the number of increments is insensitive to mesh density and polynomial degree.

In order to achieve stability in a broader range of test case configurations, in particular is case of compression solicitations, the proposed BR2 implementation requires an adaptive stabilization strategy featuring user dependent stabilisation parameters. Nevertheless, since the performance of the multigrid solution strategy is pretty insensitive to those stabilization parameters, the computational expense is not affected by tuning the stabilization, as might be required when dealing with challenging applications.

Future research efforts will consider the possibility to utilize the proposed implementation within an unified high-order accurate framework for fluid-structure interaction where dG methods are employed both for computational fluid-dynamics and computational solid mechanics.

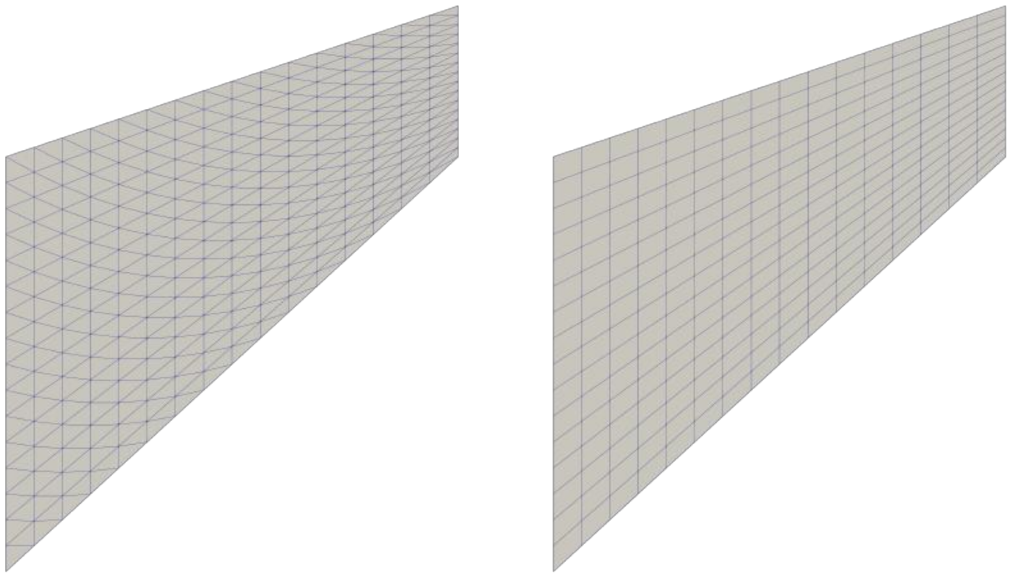

(a) (b)

Figure 13: Examples of meshes used in the Cook's membrane test: two 16×16 meshes with triangular (a) and quadrilateral (b) elements.

	TRI $k = 1$	**TRI** $k = 2$	**TRI** $k = 3$	**QUAD** $k = 1$	**QUAD** $k = 2$	**QUAD** $k = 3$
4×4	6.015	6.850	6.929	2.459	5.770	6.692
8×8	6.583	6.945	6.952	2.522	6.628	6.865
16×16	6.829	6.959	6.962	2.624	6.850	6.918
32×32	6.922	6.964	6.968	2.882	6.915	6.941

Table 9: Vertical maximum displacement at point P obtained solving the Cook's problem with different meshes (TRI, QUAD) and polynomial orders ($k = \{1, 2, 3\}$) considering the nearly incompressible constitutive law (NHK-C: $\mu = 0.8$, $\lambda = 8000$ and $\Theta(J) = J - 1$).

	Nearly Incompressible (NHK-C)	Fully incompressible (NHK-I)
TRI $k = 1$	6.829	6.938
TRI $k = 2$	6.959	6.983
TRI $k = 3$	6.962	6.983
QUAD $k = 1$	2.624	6.891
QUAD $k = 2$	6.850	6.985
QUAD $k = 3$	6.918	6.987

Table 10: Maximum vertical displacements at point P obtained solving the Cook's problem with different types of elements and polynomial orders. Results captured on 16×16 meshes.

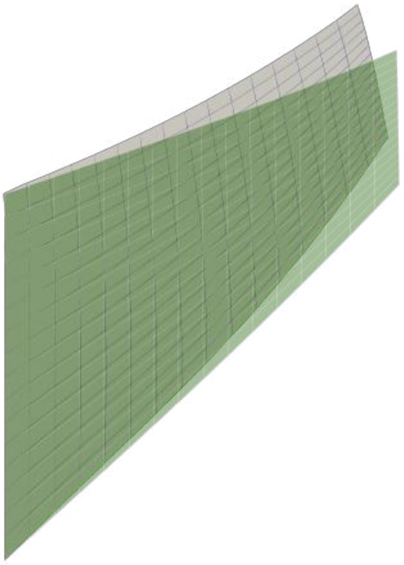

Figure 14: Deformed configurations of the Cook's membrane problem obtained with first-order square elements. In green, the nearly compressible and, in grey, the fully incompressible case.

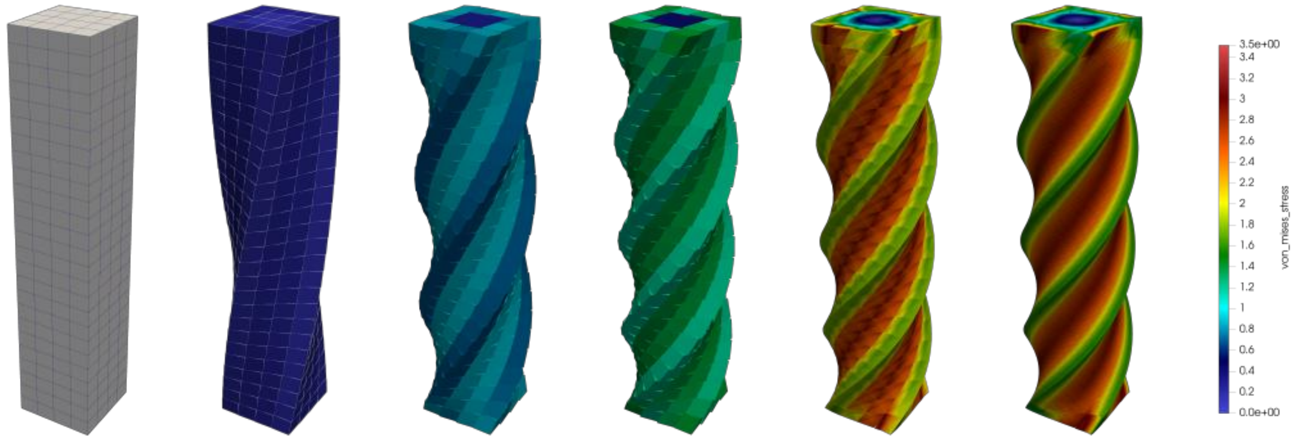

(a) 3D Mesh **(b)** $\alpha = \frac{\pi}{2}$ $k = 1$ **(c)** $\alpha = \frac{3\pi}{2}$ $k = 1$ **(d)** $\alpha = 2\pi$ $k = 1$ **(e)** $\alpha = 2\pi$ $k = 2$ **(f)** $\alpha = 2\pi$ $k = 3$

Figure 15: Torsion of a SVK-I square section bar. (a) Computational mesh; (b-f) Von Mises stress distribution for $k = 1, 2, 3$ when the top surface is rotated by an angle α.

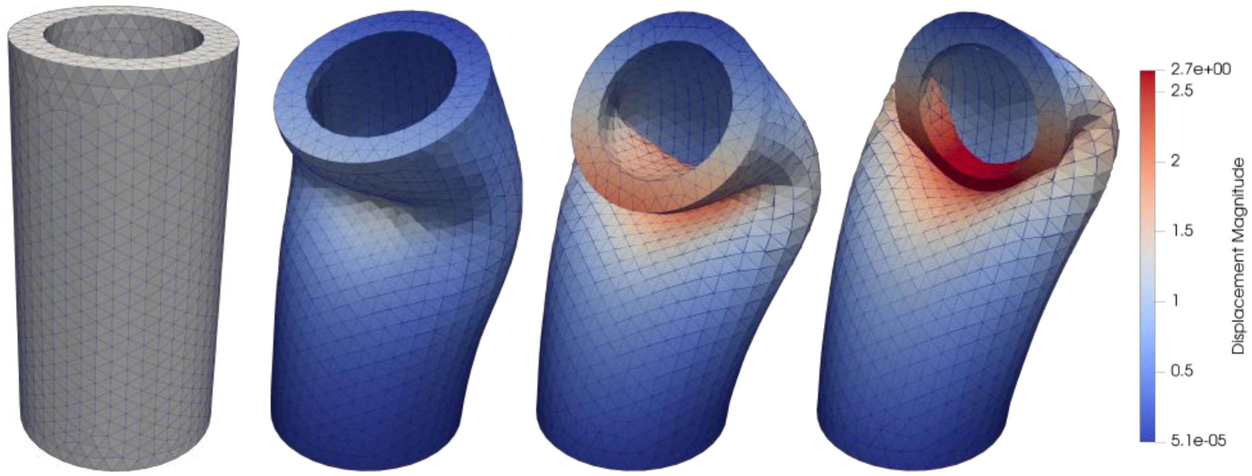

(a) $\alpha = 0$ **(b)** $\alpha = 0.15\pi$ **(c)** $\alpha = 0.30\pi$ **(d)** $\alpha = 0.5\pi$

Figure 16: Rotation of the top surface of a NHK-C hollow cylinder: sequence of equilibrium states obtained by the incremental load method while increasing the rotation angle α, $k = 1$.

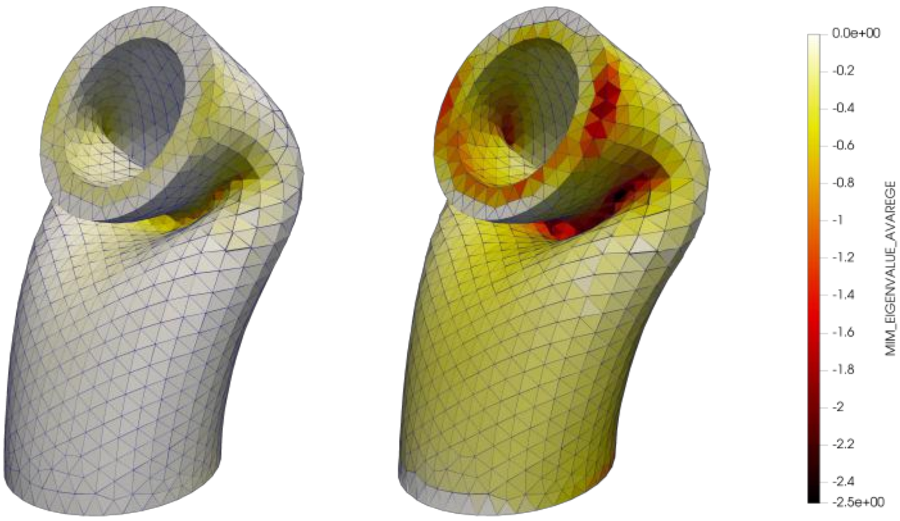

(a) NHK-C **(b)** NHK-I

Figure 17: Deformation of a hollow cylinder. *Left* and *right*: NHK-C and NHK-I constitutive laws, respectively. Images are colour-coded based on the minimum negative eigenvalue of the fourth-order elasticity tensor $\mathbb{A}$.

ϵ			β										
			0	**1**	**2**	**4**	**8**	**16**	**30**	**50**	**100**	**150**	**200**
0	**Newton iterations**	**mean**	-	-	-	5	5	5	4	4	4	4	4
		max	-	-	-	5	5	5	4	4	4	4	4
	Linear Solver iterations	**mean**	-	-	-	11	11	11	12	13	16	22	26
		max	-	-	-	20	20	22	25	28	46	58	64
1	**Newton iterations**	**mean**	-	5	5	5	5	5	4	4	4	4	4
		max	-	5	5	5	5	5	4	4	4	4	4
	Linear Solver iterations	**mean**	-	10	11	12	11	11	12	13	17	22	26
		max	-	19	20	20	21	22	25	29	41	54	65
10	**Newton iterations**	**mean**	5	5	5	5	5	4	4	4	4	4	4
		max	5	5	5	5	5	5	4	4	4	4	4
	Linear Solver iterations	**mean**	16	16	16	15	16	16	16	17	21	26	30
		max	26	26	26	26	27	28	30	35	49	60	72
20	**Newton iterations**	**mean**	5	5	5	5	4	4	4	4	4	4	4
		max	5	5	5	5	5	4	4	4	4	4	4
	Linear Solver iterations	**mean**	19	19	19	19	19	19	20	21	26	30	33
		max	33	33	33	33	34	36	40	47	58	68	73

Table 11: NHK-C cylinder: average and maximum number of Newton and linear solver iterations recorded along the loading path. Results are obtained varying the stabilization parameters β and ϵ in order to show their influence on the performance of the solution strategy.

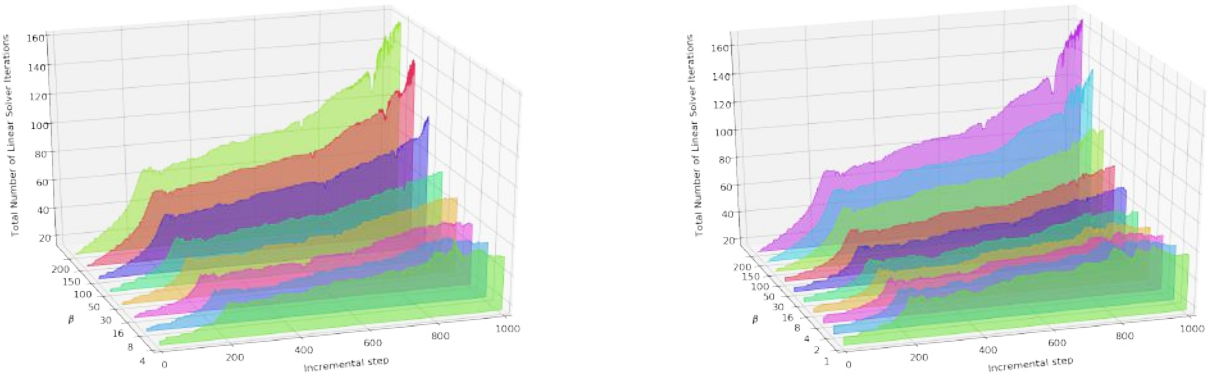

(a) $\epsilon = 0$

(b) $\epsilon = 1$

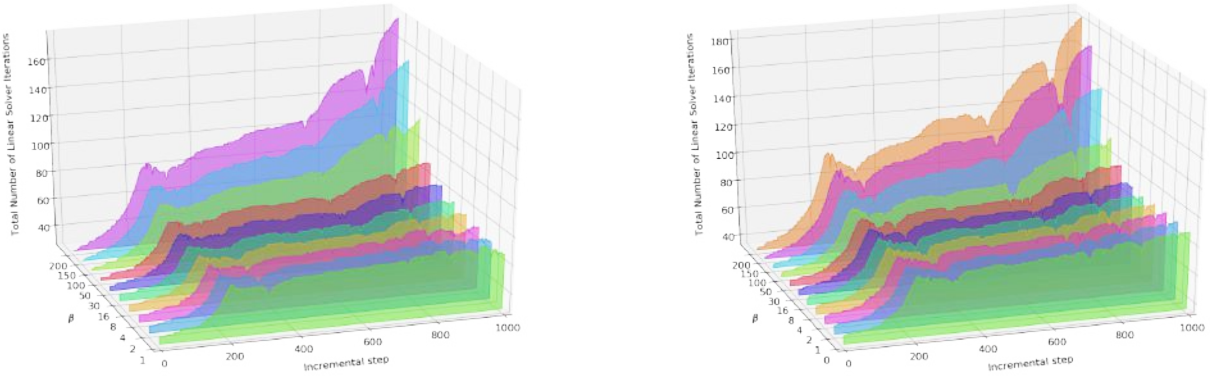

(c) $\epsilon = 10$

(d) $\epsilon = 20$

Figure 18: NHK-C cylinder: total number of linear solver iterations recorded along the loading path (1000 incremental steps). Results are obtained varying the stabilization parameters β and ϵ in order to show their influence on the performance of the solution strategy.

Chapter 5. Numerical Validation of Hybridizable Discontinuous Galerkin and Hybrid High-Order Formulations for Finite Hyperelastic Deformations

The HDG and the HHO implementations are verified computing the numerical convergence rates based on two and three dimensional analytical solutions. Errors in L^2 norm are tabulated in Sec. 5.1 over h-refined mesh sequences and varying the polynomial degree.

5.1 Evaluation of convergence rates

Convergence tests consider the neo-Hookean (NHK) constitutive model in the compressible (-C) regime. Numerical solutions are obtained over a five grids h-refined mesh sequence of a unit square $\Omega : [0, 1]^2$ in 2D and four grids of a unit cube $\Omega : [0, 1]^3$ in 3D.

In 2D, the uniform triangular elements have diameter h ranging from 0.113 (coarse mesh) to 0.00705 (fine mesh), dividing each triangle in four finer elements at each refinement step, as depicted in Fig. 19.

On the other hand, in 3D, the uniform tetrahedral elements have diameter h ranging from 0.14 (coarse mesh) to 0.0174 (fine mesh), dividing each tetrahedron in eight finer elements at each refinement step, as shown in Fig. 20.

We apply first, second and third degree HDG and HHO discretizations and enforce boundary conditions based on smooth analytical displacement fields, as presented in Sec. 5.1.1 and Sec. 5.1.2. Dirichlet boundary conditions based on the exact displacement are imposed by means of the Lagrange multipliers method on three of four and five of the six surfaces composing $\partial\Omega$, in 2D and 3D, respectively. A Neumann boundary condition based on the exact deformation gradient is imposed on the unaccounted surface. Convergence is evaluated based on the L^2-norm of the error on the displacement and the displacement gradient. Forcing terms are computed based on analytical solutions by means of SageMath [62], an open-source library featuring symbolic calculus.

5.1.1 2D convergence tests

Let's denote by $\boldsymbol{X} = (X, Y)$ the Cartesian coordinates in the reference configuration and by (u, v) the three components of the displacement vector $\boldsymbol{u}$.

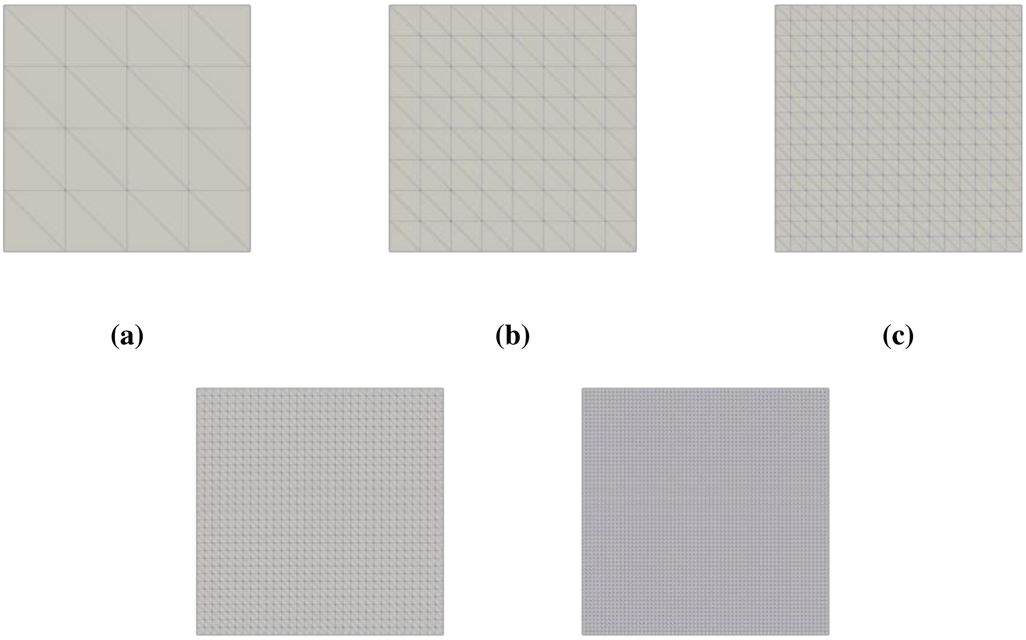

(a) (b) (c)

(d) (e)

Figure 19: Five grids h-refined mesh sequence of a unit square $\Omega : [0, 1]^2$ used in 2D convergence tests.

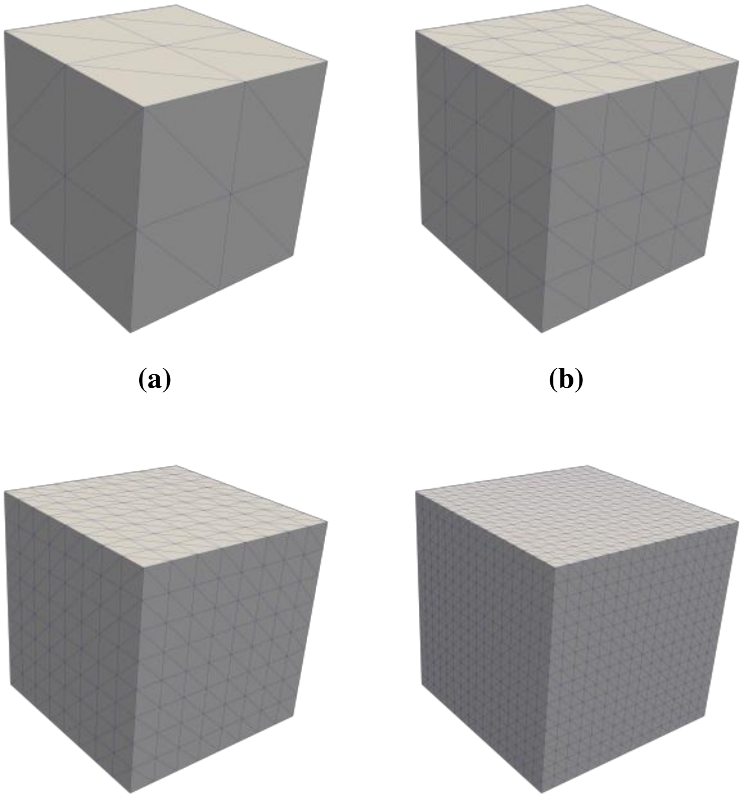

(a) (b)

(c) (d)

Figure 20: Four grids h-refined mesh sequence of a unit cube $\Omega : [0, 1]^3$ used in 3D convergence tests.

We consider the following displacement field

$$\begin{cases} u(\boldsymbol{X}) = -a\cos(x) + b\sin(y) \\ v(\boldsymbol{X}) = -c\cos(y) \end{cases}$$

with $a = b = c = 0.5$. Relevant parameters of the NHK-C constitutive law are defined setting $\mu = 1$ and $\lambda = 1$, which corresponds to a Poisson's ration of $\nu \simeq 0.25$. Regarding the stabilization parameter, we set $\xi = 1$ and $\kappa_0 = 2$, respectively, for the HDG and the sHHO formulation.

Let's first consider the displacement error in L^2 norm. Both HDG and uHHO show an asymptotic convergence rate of order $k + 1$, see Tabs. 12 and 13. Whereas, sHHO convergence rate is $k + 2$, see Tab. 14. Let's now consider the displacement gradient error in L^2 norm. uHHO and sHHO show an asymptotic convergence rate of order k and $k + 1$ respectively, see Tabs. 13 and 14. HDG error on the displacement gradient shows the tendency to superconverge with order $k + 1$, see Tab. 12, thereby overcoming by one order the expected convergence rate. Similar results were reported in [1].

5.1.2 3D convergence tests

Let's denote by $\boldsymbol{X} = (X, Y, Z)$ the Cartesian coordinates in the reference configuration and by (u, v, w) the three components of the displacement vector $\boldsymbol{u}$.
We consider the following displacement field proposed by Abbas *et al.* [2]

$$\begin{cases} u(\boldsymbol{X}) = \left(\dfrac{1}{\lambda} + \alpha\right) X + \psi(Y) \\ v(\boldsymbol{X}) = -\left(\dfrac{1}{\lambda} + \dfrac{\alpha + \gamma + \alpha\gamma}{1 + \alpha + \gamma + \alpha\gamma}\right) Y \\ w(\boldsymbol{X}) = \left(\dfrac{1}{\lambda} + \gamma\right) Z + \omega(X) + \xi(Y) \end{cases}$$

where $\alpha = \gamma = 0.1$, $\psi(Y) = \alpha\sin(\pi Y)$, $\omega(X) = \gamma\sin(\pi X)$ and $\xi(Y) = 0$. Relevant parameters of the NHK-C constitutive law are defined setting $\mu = 1$ and $\lambda = 10$, which corresponds to a Poisson's ratio of $\nu \simeq 0.455$. Concerning the stabilization parameter, we set $\xi = 10$ and $\kappa_0 = 1$, respectively, for the HDG and the sHHO formulation.

The convergence rates observed in 2D are confirmed for 3D test cases. HDG convergence rates are of order $k + 1$, both for the displacement and the displacement gradient, see Tab. 15. uHHO convergence rates are of order $k + 1$ and k for the displacement and the displacement gradient, respectively, see Tab. 16. sHHO convergence rate are one order higher than uHHO, see Tab. 17.

card$(\mathcal{T}_h)$	$\|\boldsymbol{u}-\boldsymbol{u}_h\|_{L^2(\Omega)}$	**rate**	$\|\nabla_{\boldsymbol{X}}(\boldsymbol{u}-\boldsymbol{u}_h)\|_{L^2(\Omega)}$	**rate**
$k = 1$				
32	1.954e-03	-	3.424e-03	-
128	4.875e-04	2.00	1.021e-03	1.74
512	1.217e-04	2.00	2.889e-04	1.82
2048	3.040e-05	2.00	7.939e-05	1.86
8192	7.598e-06	2.00	2.142e-05	1.88
$k = 2$				
32	2.959e-05	-	5.500e-05	-
128	3.694e-06	3.00	7.587e-06	2.85
512	4.611e-07	3.00	1.019e-06	2.89
2048	5.760e-08	3.00	1.343e-07	2.92
8192	7.197e-09	3.00	1.749e-08	2.94
$k = 3$				
32	5.229e-07	-	9.306e-07	-
128	3.256e-08	4.00	6.720e-08	3.79
512	2.032e-09	4.00	4.676e-09	3.84
2048	1.269e-10	4.00	3.146e-10	3.89
8192	7.927e-12	4.00	2.063e-11	3.93

Table 12: Errors and convergence rates for HDG discretizations of degree $k = \{1, 2, 3\}$ over a h-refined 2D mesh sequence of triangles, NHK-C constitutive model.

card$(\mathcal{T}_h)$	$\|\boldsymbol{u}-\boldsymbol{u}_h\|_{L^2(\Omega)}$	**rate**	$\|\nabla_{\boldsymbol{X}}(\boldsymbol{u}-\boldsymbol{u}_h)\|_{L^2(\Omega)}$	**rate**
$k = 1$				
32	1.234e-03	-	2.372e-02	-
128	3.087e-04	1.99	1.187e-02	0.99
512	7.717e-05	1.99	5.935e-03	0.99
2048	1.929e-05	2.00	2.968e-03	0.99
8192	4.823e-06	2.00	1.484e-03	0.99
$k = 2$				
32	2.582e-05	-	6.930e-04	-
128	3.226e-06	3.00	1.740e-04	1.99
512	4.033e-07	2.99	4.357e-05	1.99
2048	5.042e-08	2.99	1.090e-05	1.99
8192	6.304e-09	2.99	2.727e-06	1.99
$k = 3$				
32	3.791e-07	-	1.096e-05	-
128	2.365e-08	4.00	1.369e-06	3.00
512	1.477e-09	4.00	1.711e-07	3.00
2048	9.226e-11	4.00	2.138e-08	3.00
8192	5.765e-12	4.00	2.673e-09	3.00

Table 13: Errors and convergence rates for uHHO discretizations of degree $k = \{1, 2, 3\}$ over a h-refined 2D mesh sequence of triangles, NHK-C constitutive model.

card$(\mathcal{T}_h)$	$\|\boldsymbol{u}-\boldsymbol{u}_h\|_{L^2(\Omega)}$	**rate**	$\|\nabla_{\boldsymbol{X}}(\boldsymbol{u}-\boldsymbol{u}_h)\|_{L^2(\Omega)}$	**rate**
$k = 1$				
32	1.642e-04	-	3.501e-03	-
128	2.462e-05	2.73	1.025e-03	1.77
512	3.455e-06	2.83	2.849e-04	1.84
2048	4.667e-07	2.88	7.671e-05	1.89
8192	6.150e-08	2.92	2.020e-05	1.92
$k = 2$				
32	1.319e-06	-	4.888e-05	-
128	9.061e-08	3.86	6.647e-06	2.87
512	6.011e-09	3.91	8.769e-07	2.92
2048	3.897e-10	3.94	1.134e-07	2.95
8192	2.490e-11	3.96	1.447e-08	2.97
$k = 3$				
32	1.514e-08	-	8.060e-07	-
128	5.053e-10	4.90	5.674e-08	3.82
512	1.661e-11	4.92	3.837e-09	3.88
2048	5.375e-13	4.94	2.516e-10	3.93
8192	1.722e-14	4.96	1.617e-11	3.95

Table 14: Errors and convergence rates for sHHO discretizations of degree $k = \{1, 2, 3\}$ over a h-refined 2D mesh sequence of triangles, NHK-C constitutive model.

card$(\mathcal{T}_h)$	$\|\boldsymbol{u}-\boldsymbol{u}_h\|_{L^2(\Omega)}$	**rate**	$\|\nabla_{\boldsymbol{X}}(\boldsymbol{u}-\boldsymbol{u}_h)\|_{L^2(\Omega)}$	**rate**
$k = 1$				
48	6.347e-03	-	4.479e-02	-
384	1.566e-03	2.01	1.505e-02	1.57
3072	3.824e-04	2.03	4.475e-03	1.75
24576	9.423e-05	2.02	1.243e-03	1.84
$k = 2$				
48	8.070e-04	-	6.675e-03	-
384	9.903e-05	3.02	1.042e-03	2.67
3072	1.207e-05	3.03	1.506e-04	2.79
24576	1.490e-06	3.01	2.055e-05	2.87
$k = 3$				
48	7.636e-05	-	7.278e-04	-
384	4.674e-06	4.02	5.588e-05	3.70
3072	2.879e-07	4.02	3.942e-06	3.82
24576	1.787e-08	4.01	2.641e-07	3.89

Table 15: Errors and convergence rates for HDG discretizations of degree $k = \{1, 2, 3\}$ over a h-refined 3D mesh sequence of tetrahedra, NHK-C constitutive model.

card($\mathcal{T}_h$)	$\|\boldsymbol{u}-\boldsymbol{u}_h\|_{L^2(\Omega)}$	**rate**	$\|\nabla_{\boldsymbol{X}}(\boldsymbol{u}-\boldsymbol{u}_h)\|_{L^2(\Omega)}$	**rate**
$k = 1$				
48	6.788e-03	-	8.605e-02	-
384	1.742e-03	1.96	4.286e-02	1.00
3072	4.381e-04	1.99	2.138e-02	1.00
24576	1.098e-04	1.99	1.067e-02	1.00
$k = 2$				
48	8.644e-04	-	1.386e-02	-
384	1.133e-04	2.93	3.525e-03	1.97
3072	1.438e-05	2.97	8.833e-04	1.99
24576	1.809e-06	2.99	2.207e-04	2.00
$k = 3$				
48	8.091e-05	-	1.571e-03	-
384	5.118e-06	3.98	1.861e-04	2.98
3072	3.206e-07	3.99	2.488e-05	2.99
24576	2.004e-08	3.99	3.110e-06	2.99

Table 16: Errors and convergence rates for uHHO discretizations of degree $k = \{1, 2, 3\}$ over a h-refined 3D mesh sequence of tetrahedra, NHK-C constitutive model.

card($\mathcal{T}_h$)	$\|\boldsymbol{u}-\boldsymbol{u}_h\|_{L^2(\Omega)}$	**rate**	$\|\nabla_{\boldsymbol{X}}(\boldsymbol{u}-\boldsymbol{u}_h)\|_{L^2(\Omega)}$	**rate**
$k = 1$				
48	1.331e-03	-	2.160e-02	-
384	1.931e-04	2.78	5.947e-03	1.86
3072	2.629e-05	2.87	1.563e-03	1.92
24576	3.426e-06	2.93	4.001e-04	1.96
$k = 2$				
48	1.185e-04	-	2.761e-03	-
384	8.028e-06	3.88	3.733e-04	2.88
3072	5.180e-07	3.95	4.816e-05	2.95
24576	3.280e-08	3.98	6.098e-06	2.98
$k = 3$				
48	8.683e-06	-	2.645e-04	-
384	2.820e-07	4.94	1.764e-05	3.90
3072	8.952e-09	4.97	1.131e-06	3.96
24576	2.817e-10	4.99	7.148e-08	3.98

Table 17: Errors and convergence rates for sHHO discretizations of degree $k = \{1, 2, 3\}$ over a h-refined 3D mesh sequence of tetrahedra, NHK-C constitutive model.

5.2 Conclusions

In this chapter, we numerically validate the HDG and HHO methods of Sec. 3.4, Sec. 3.5.1 and Sec. 3.5.2 for the simulation of finite deformations based on compressible hyperelastic material models. In particular, the method of manufactured solutions has been successfully employed to verify and replicate the expected convergence rates on h-refined mesh sequences.

We do not consider HDG and HHO formulations for the computation of the challenging test cases performed by means of dG discretizations in Chap. 4. We remark that the development of efficient solution strategies and adaptive stabilisation strategies for HDG and HHO formulations is still an open field of research. Accordingly, a comparison based on efficiency of the solution strategy would be impractical and unfair.

In Chap. 6, the HDG formulation will be employed to extend the framework introduced in Chap. 3 to computational contact mechanics. In Chap. 7, challenging 2D and 3D computations involving contact with rigid obstacles will be proposed.

Chapter 6. Hybridizable Discontinuous Galerkin formulations for Computational Contact Mechanics

Many mechanical applications involve the contact between bodies undergoing large deformation: for instance, the blow moulding of polymers for the food&beverage or home care markets, the sheet metal forming and the crash test simulation for the automotive industry, the analysis of rolling contact of tyres for the transport industry, the drilling studies for the mining industry and so forth. Thus, the last decades have seen increasing interest in Computational Contact Mechanics (CCM). The latter is an interdisciplinary area that covers topics such as tribology (friction, lubrification, adhesion, wear), maths, computer science and physics. We refer to Laursen [66] and Wriggers [67] as introductory literature on CCM.

In this chapter, we aim to simulate the frictionless contact between a rigid obstacle and a deformable body through the imposition of the so-called non-penetration boundary condition. In order to track the portion of $\partial\Omega$ that comes into contact with the obstacle, we introduce the so called *active set strategy*. Moreover, the non-penetration condition for the entities belonging to the active set is enforced by the means of the Lagrange Multiplier method.

This chapter is organized as follows. Different numerical techniques used in CCM are illustrated in Sec. 6.1. The normal and the tangential contact constraints are introduce in Sec. 6.2. The weak form of the nonlinear elasticity problem with the normal contact constraint of non-penetration is derived in Sec. 6.3. Then, the weak form is discretized using the HDG method defining, in Sec. 6.4, the local and global residual and the Jacobian operator to solve the minimization problem. To conclude, the active set strategy employed in the numerical test cases is explained in Sec. 6.5.

6.1 Introduction

From a mathematical viewpoint,we deal with a nonlinear boundary value problem which incorporates the geometrical constraint of non-penetration and the frictional effects arising from the relative body motion. Interestingly, the contact constraint requires the solution of a variational inequality, introducing additional complexity to the nonlinear elasticity problem of Chap. 3.

Several numerical techniques have been developing since the '70s:

- **Lagrange Multipliers method**: introduces additional unknowns, namely the Lagrange multipliers (LMs), for the constraint enforcement. LMs act in the formulation as the normal and tangential unknown reaction forces exchanged between the bodies during the contact. The values assumed by LMs are retrieved from the solution of a saddle-point problem, so, the method introduces some numerical difficulties mitigated by the fact that the contact boundary constraint are exactly imposed and satisfied. Some examples are illustrated in Haslinger *et al.* [68], Wohlmuth [69] and Poop [70].

- **Penalty method**: replaces the set of inequalities associated to the contact problem with a non-linear system of equation introducing penalization parameters. The penalization adds contact rigidity associating large energies to those displacement solutions violating the contact constraint. Despite of its simplicity, the effectiveness of the method is strongly influenced by the choice of the penalty parameter. If the latter tends to infinity, the contact constraint are exactly satisfied but, obviously, the resulting linear system of equation is ill-conditioned. On the other hand, underestimated value of the penalty parameters lead to unacceptably violation of contact constraint. The interested reader may find some application in Kikuchi and Oden [71, 72].

- **Augmented Lagrangian method**: uses the concepts introduced in the two previous techniques obtaining a Lagrange formulation regularized with penalty terms. See Glowinski and Tallec [73], Zavarise and De Lorenzis [74] and Hild and Renard [75] for further information on the topic.

- **Nitsche method**: is a technique used to impose Dirichlet boundary conditions without increasing the number of unknowns as with the LM method (see Nitsche [76] and Sec. 3.3 where this method is employed in the context of dG formulation). With the Nitsche method, the contact boundary condition are imposed weakly on the body surface through a consistent term, eventually, regularized with a real parameters. In Chouly *et al.* [77] and Mlika [78] we find an interesting overview of recent result on Nitsche's method for contact problems.

We also mention direct elimination method, the barrier method, the formulation of constitutive equations and the perturbed Lagrange method, see [67] for additional details.

Most of the aforementioned methods need to be coupled with numerical strategies aiming to identify and follow the evolution in time of the contact portion of the boundary. These algorithms are often named active set strategies. We refer to De Lorenzis *et al.* [79] and Sec. 6.5 for further information.

6.2 Contact constraints

Bearing in mind the concepts illustrated in Chap. 2, the contact kinematical constraints will be derived hereinafter. Consider two (or more) bodies Ω_α approaching each other during a finite deformation process. Referring to Fig. 21, we observe that, for $\alpha = \{1, 2\}$, the bodies Ω_1 and Ω_2 come in contact on the boundary surface $\partial\Omega^+_{\mathrm{C}} = \partial\Omega^+_{1,\mathrm{C}} = \partial\Omega^+_{2,\mathrm{C}}$ in the deformed configuration.

The *contact surface* is defined as the place where two distinct material points, $\boldsymbol{X}_1$ and $\boldsymbol{X}_2$, occupy the same place of the space, namely the spatial points $\boldsymbol{x}_1 = \mathcal{X}_1(\boldsymbol{X}_1)$ and $\boldsymbol{x}_2 = \mathcal{X}_2(\boldsymbol{X}_2)$ coincides.

When the contact occurs, the two bodies exchange forces on the contact surface. These reaction forces produce on $\partial\Omega^+_{\mathrm{C}}$ an unknown stress $\boldsymbol{t}_{\mathrm{C}}$ that may be decomposed as

$$\boldsymbol{t}_{\mathrm{C}} = p_n \boldsymbol{n} + \boldsymbol{t}_T \tag{6.1}$$

where p_n is a pressure value, $\boldsymbol{n}$ is the normal vector defined on $\partial\Omega^+_{\mathrm{C}}$ and $\boldsymbol{t}_T$ is the tangential part of $\boldsymbol{t}$. CCM formulates kinematical contact relations in order to define the components of $\boldsymbol{t}_{\mathrm{C}}$.

The *normal contact kinematics* provides the geometrical constraint of non-penetration (see Sec. 6.2.1) or constitutive laws to assign a value to the pressure p_n. In several contact problem, the knowledge of micromechanical characteristics of the contact surface is essential for the proper treatment of physical phenomena. Based on experimental studies regarding materials microstructures several constitutive equations can be developed (see [67]).

The *tangential contact kinematics* completes the description of the contact reaction forces defining $\boldsymbol{t}_T$. Generally, two different situations has to be distinguished: the stick state and the sliding state, see Sec. 6.2.2.

6.2.1 Normal contact constraint

Assume that two bodies come in contact. For all spatial points $\boldsymbol{x}_1 \in \Omega^+_1$ and $\boldsymbol{x}_2 \in \Omega^+_2$ such that the segment $\overrightarrow{\boldsymbol{x}_2\boldsymbol{x}_1}$ does not intersect Ω^+_2, the *non-penetration condition* occurring in normal contact kinematics reads

$$(\boldsymbol{x}_2 - \boldsymbol{x}_1) \cdot \boldsymbol{n}_1 \geq 0,$$

where $\boldsymbol{n}_1$ is the normal vector at $\boldsymbol{x}_1$ pointing out of Ω^+_1. Under the assumption that the contact boundaries are convex surfaces, we may relate every point $\boldsymbol{x}_2$ on Ω^+_2 to its *closest-point projection* $\overline{\boldsymbol{x}}_1$ on $\partial\Omega^+_1$.

Let d be the scalar that identifies the distance between two points, $\boldsymbol{x}_a$ and $\boldsymbol{x}_b$, such that

$$d = \|\boldsymbol{x}_b - \boldsymbol{x}_a\|.$$

Referring to Fig. 22, the closest-point projection $\overline{\boldsymbol{x}}_1$ on Ω_1^+ of the point $\boldsymbol{x}_2$ on Ω_2^+ is defined via the minimum distance problem:

$$d_{\min}\left(\boldsymbol{x}_2\right) = \|\boldsymbol{x}_2 - \overline{\boldsymbol{x}}_1\| = \min_{\boldsymbol{x}_1 \subseteq \partial\Omega_1^+} \|\boldsymbol{x}_2 - \boldsymbol{x}_1\|. \tag{6.2}$$

Once the point $\overline{\boldsymbol{x}}_1$ is known for each point $\boldsymbol{x}_2 \in \partial\Omega_2^+$ by solving problem (6.2), the scalar function $g_n : \partial\Omega_2^+ \to \mathbb{R}$, representing the *normal gap* between Ω_1^+ and Ω_2^+, is defined as

$$g_n(\boldsymbol{x}_2) = (\boldsymbol{x}_2 - \overline{\boldsymbol{x}}_1) \cdot \overline{\boldsymbol{n}}_1,$$

where $\overline{\boldsymbol{n}}_1$ is the normal vector at $\overline{\boldsymbol{x}}_1$ pointing outward Ω_1^+, see Fig. 22. We remark that, according to (6.2), $\boldsymbol{x}_2 - \overline{\boldsymbol{x}}_1$ has the same direction of $\overline{\boldsymbol{n}}_1$. We refer to Wriggers [67, Sec. 4.1] for further details regarding the well-posedness of problem (6.2) and differentiability of the distance function.
Thereby, the *inequality constraint of the non-penetration condition* may be reformulated as

$$g_n(\boldsymbol{x}_2) \geq 0. \tag{6.3}$$

Eq. (6.3) represents a geometrical constraint that precludes Ω_2^+ to occupy the region of the space owned by Ω_1^+. When $g_n = 0$, namely Ω_1 and Ω_2 are in contact, the bodies exchange forces such that, for the action-reaction law, $\boldsymbol{t}_{1\mathrm{C}} = -\boldsymbol{t}_{2\mathrm{C}}$ at each contact point on $\partial\Omega_{\mathrm{C}}^+$.

In this situation, the pressure p_n assumes the meaning of contact pressure such that $p_n = p_{1n} = p_{2n}$, where $p_{\bullet n}$ is the contact pressure on $\partial\Omega_\bullet^+$. Under the hypothesis of non-adhesive contact, the contact pressure must be lower than zero, $p_n < 0$ (non-attractive, repulsive), when the normal gap is null $g_n = 0$. On the other hand, if there is a gap between the bodies, $g_n > 0$, the contact pressure vanishes, $p_n = 0$. These arguments are collected in the well-known Hertz-Signorini-Moreau condition that reads

$$g_n \geq 0, \qquad p_n \leq 0, \qquad g_n\, p_n = 0. \tag{6.4}$$

In the context of optimization theory, the conditions in (6.4) are also known as the Kuhn-Tucker-Karush condition, see [67].

Differently from $\boldsymbol{T}_{\mathrm{N}}$ on the Neumann boundary $\partial\Omega_{\mathrm{N}}$, the stress $\boldsymbol{t}_{\mathrm{C}}$ on Ω_{C}^+ is *not known a priori*. Thus, we have to choose, from the list presented in Sec. 6.1, a method that renders the contact boundary condition.
The Lagrange multiplier method reveals to be a valuable technique for the imposition of the contact constraints. Regarding the frictionless contact, where $\boldsymbol{t}_T = 0$, only the normal component of the

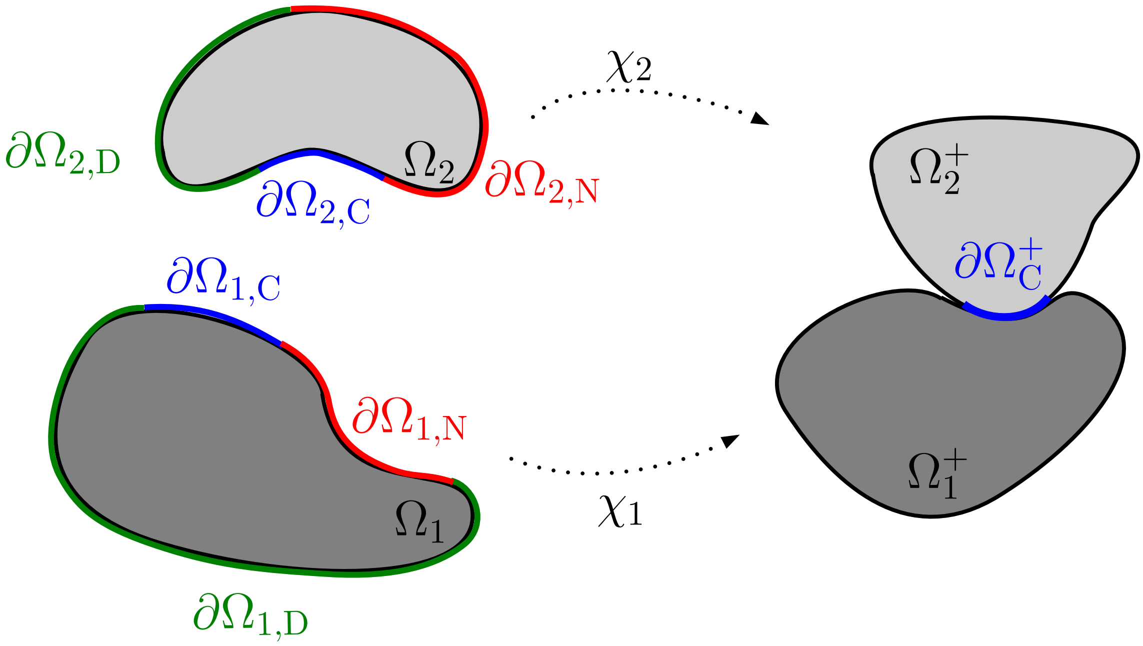

Figure 21: Contact between bodies undergoing finite deformation.

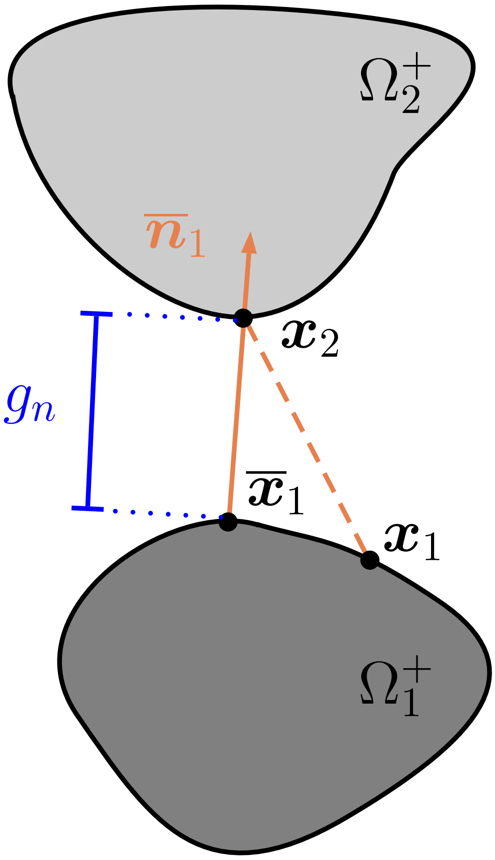

Figure 22: Closest-point projection $\overline{x}_1$ on Ω_1^+ of the point x_2 on Ω_2^+.

contact stress has to be identified, so that $\boldsymbol{t}_{\mathrm{C}} = p_n \boldsymbol{n}$. Thereby, we will introduce $\lambda_n \in S_n$ where S_n is the set of LMs constrained with the boundary condition $g_n = 0$. The aim of λ_n is to retrieve the value of the contact pressure p_n that avoids the penetration between the contacting bodies.

6.2.2 Tangential contact constraint

A simple tangential contact constraint is the *stick* condition in which no tangential relative displacements occurs in the contact zone. Usually, when the tangential forces are above a certain limit, the contacting surfaces no longer stick, but move relative to each other: this is called *sliding*. In order to deal with sliding, several constitutive laws relating tangential stress to contact pressure have been developed. In particular, we mention the Coulomb's law, requiring the introduction of proportionality coefficients for each material couple.

Stick and sliding are only two of the several tangential behaviours presented in literature (see *e.g.* [67] and [79]). Up to now, we disregard the tangential behaviour considering only the *frictionless contact* where the value of the tangential stress is known a priori because constant to zero ($\boldsymbol{t}_T = 0$). Further investigations are planned for future works.

6.3 Nonlinear elasticity problem with normal contact constraint

In this section, we derive the weak form of the contact boundary value problem including in the formulation the geometrical constrain of non-penetration (Sec. 6.2.1). The tangential contact is considered frictionless.

Even if the extension to multi body system is straightforward, we consider two bodies: Ω_1 and Ω_2. By hypotheses, Ω_1 is **rigid**, namely not deformable, and **fixed**, while Ω_2 undergoes finite deformation. During the deformation, Ω_1 and Ω_2 come in contact on the surface $\partial\Omega_{\mathrm{C}}^{+}$, see Fig. 21.
In the context of finite elastic deformations, unilateral frictionless contact problems consist in seeking the displacement mapping $\boldsymbol{u}$ such that

$$-\nabla_{\boldsymbol{X}} \cdot \boldsymbol{P} = \boldsymbol{f} \qquad \text{in } \Omega_2, \tag{6.5a}$$

$$\boldsymbol{u} = \boldsymbol{u}_{\mathrm{D}} \qquad \text{on } \partial\Omega_{2,\mathrm{D}}, \tag{6.5b}$$

$$\boldsymbol{P}\boldsymbol{N} = \mathbf{T}_{\mathrm{N}} \qquad \text{on } \partial\Omega_{2,\mathrm{N}}, \tag{6.5c}$$

$$\boldsymbol{P}(\mathbf{1} - \boldsymbol{N} \otimes \boldsymbol{N})\boldsymbol{N} = \mathbf{0} \qquad \text{on } \partial\Omega_{\widetilde{\mathrm{C}}}, \tag{6.5d}$$

$$g_n \geq 0,\ (\boldsymbol{P}\boldsymbol{N}) \cdot \boldsymbol{N} \leq 0,\ g_n\left[(\boldsymbol{P}\boldsymbol{N}) \cdot \boldsymbol{N}\right] = 0 \qquad \text{on } \partial\Omega_{\widetilde{\mathrm{C}}}, \tag{6.5e}$$

where $\partial\Omega_{\widetilde{\mathrm{C}}}$ is the contact boundary that can be divided in two non-overlapping partitions:

- $\partial\Omega_{\mathrm{C}}$: the contact interface, namely the portion of $\partial\Omega_{\widetilde{\mathrm{C}}}$ where the gap function *is zero*;
- $\partial\Omega_{!\mathrm{C}}$: the portion of $\partial\Omega_{\widetilde{\mathrm{C}}}$ where the gap function *is strictly positive*.

According to the hypothesis of frictionless contact, condition (6.5d) enforces a null tangential solicitation on $\partial\Omega^{+}_{\widetilde{\mathrm{C}}}$. The unilateral contact Signorini conditions in (6.5e) enforce non-penetration between the body and the obstacle providing compression or null normal solicitation on $\partial\Omega_{\widetilde{\mathrm{C}}}$ when the gap function is zero or strictly positive, respectively.

Based on Signorini conditions, it is possible to obtain a variational *inequality* which the solution of problem (6.5) has to fulfill, see *e.g.* [67, Sec. 6.2]. Nevertheless, reformulating the problem as a variational *equality* is computationally more convenient. Among several approaches, a reliable solution consists of combining the Lagrange Multipliers methods with an active set strategy providing a way to find the contact reaction forces and to track the contact interface along the deformation history. In the context of hyperelastic materials, the weak form is obtained as the minimization of a suitable energy functional, as described in what follows.

Mimicking the approach presented in Sec. 3.1 and assuming that $\partial\Omega^{+}_{\mathrm{C}}$ is known, we have to add to the energy functional of the system the contribution of the work of a Lagrange Multiplier satisfying $g_n(\boldsymbol{x}_2) = 0$ on $\partial\Omega^{+}_{\mathrm{C}}$. Thus, we introduce the energy functional $\mathcal{W}^{+}_{\mathrm{C}} : \boldsymbol{V} \times S^{+}_{n} \longrightarrow \mathbb{R}$ defined as

$$\mathcal{W}^{+}_{\mathrm{C}}(\boldsymbol{v}, \lambda^{+}_{n}) = \int_{\partial\Omega^{+}_{\mathrm{C}}} \lambda^{+}_{n} \left(g_n(\boldsymbol{x}_2(\boldsymbol{v})) - 0 \right) \tag{6.6}$$

where λ^{+}_{n} is a Lagrange Multiplier such that $\lambda^{+}_{n} = p_n$. For the purpose of applying the Lagrangian formulation developed in Sec. 3.1, the integral in Eq. (6.6) on the contact boundary surface has to be defined on the reference configuration. Thus, we introduce the energy functional $\mathcal{W}_{\mathrm{C}} : \boldsymbol{V} \times S_n \longrightarrow \mathbb{R}$ such that

$$\mathcal{W}_{\mathrm{C}}(\boldsymbol{v}, \lambda_n) = \int_{\partial\Omega_{\mathrm{C}}} \lambda_n \, g_n(\boldsymbol{X}_2 + \boldsymbol{v}) \tag{6.7}$$

where $\lambda_n = J|\boldsymbol{F}^{-\intercal}\boldsymbol{N}|\lambda^{+}_{n}$ is the counterpart of λ^{+}_{n} in the reference configuration obtained using the Nanson's formula (2.5) (see also [67]).

Let $\mathcal{W}_{2\lambda}(\boldsymbol{v}, \boldsymbol{\lambda}) = \mathcal{W}_{\lambda}(\boldsymbol{v}, 0, \boldsymbol{\lambda}) : \boldsymbol{V} \times \boldsymbol{S} \longrightarrow \mathbb{R}$ be the energy functional defined over the deforming body Ω_2, with $\mathcal{W}_{\lambda}$ from Eq. (3.4), and hydrostatic pressure set to zero since we do not enforce the incompressibility constraint. The contribution $\mathcal{W}_{\mathrm{C}}$ of the work of λ_n may be added to $\mathcal{W}_{2\lambda}$ such that the total energy function $\mathcal{W}^{\mathrm{TOT}}_{\mathrm{C}} : \boldsymbol{V} \times \boldsymbol{S} \times S_n \longrightarrow \mathbb{R}$ is stated as

$$\mathcal{W}^{\mathrm{TOT}}_{\mathrm{C}}(\boldsymbol{v}, \boldsymbol{\lambda}, \lambda_n) = \mathcal{W}_{2\lambda}(\boldsymbol{v}, \boldsymbol{\lambda}) + \mathcal{W}_{\mathrm{C}}(\boldsymbol{v}, \lambda_n) \tag{6.8}$$

where $\boldsymbol{V}$ is now the set of all admissible displacements fields that satisfy Dirichlet condition on $\partial\Omega_{2,\mathrm{D}}$ and non-penetration constraints on $\partial\Omega_{\mathrm{C}}^{+}$. It is interesting to remark that, since the contact surface $\partial\Omega_{\mathrm{C}}$ is known by assumption, the solution of (6.5) through the minimization of the energy functional (6.8) does not involve directly the *inequality* constraint (6.3). Instead, the inequality plays a role in the definition of $\partial\Omega_{\mathrm{C}}$, see Sec. 6.5.

In order to define the minimization problem, two directional derivatives of (6.7) have to be defined. The first term associated with the virtual work of λ_n along the variation of the gap function in the normal direction is *i.e.*

$$\frac{\partial}{\partial\epsilon}\mathcal{W}_{\mathrm{C}}(\boldsymbol{v}+\epsilon\delta\boldsymbol{v},\lambda_n)\bigg|_{\epsilon=0}=\int_{\partial\Omega_{\mathrm{C}}}\lambda_n\,\overline{\boldsymbol{n}}_1\cdot\delta\boldsymbol{v} \tag{6.9}$$

where

$$\overline{\boldsymbol{n}}_1=\overline{\boldsymbol{n}}_1(\boldsymbol{x}_2)=\overline{\boldsymbol{n}}_1(\boldsymbol{X}_2+\boldsymbol{u})=\frac{\partial g_n(\boldsymbol{x}_2)}{\partial\boldsymbol{x}_2}. \tag{6.10}$$

The normal gap g_n is a scalar function that describes the distance from a surface (in our case $\partial\Omega_1^{+}$). The gradient of this function points to the direction with the maximum rate of change of the normal gap. This happens perpendicularly to the surface which may be also described as the set of points where the distance is equal to zero, or $g_n=0$.

The second term is used to enforce the constraint of non-penetration in the normal direction

$$\frac{\partial}{\partial\epsilon}\mathcal{W}_{\mathrm{C}}(\boldsymbol{v},\lambda_n+\epsilon\delta\lambda_n)\bigg|_{\epsilon=0}=\int_{\partial\Omega_{\mathrm{C}}}\delta\lambda_n\,g_n(\boldsymbol{X}+\boldsymbol{v}). \tag{6.11}$$

Introducing the Lagrange multiplier method for the imposition of the Dirichlet boundary condition (6.5b) and for the normal contact constraint $g_n(\boldsymbol{x}_2)=0$ and using the definitions in Eqs. (6.9)-(6.11), the static equilibrium of problem (6.5) is stated as finding $(\boldsymbol{u},\boldsymbol{\lambda},\lambda_n)\in\boldsymbol{V}\times\boldsymbol{S}\times S_n$ which satisfy the following weak form of the Euler-Lagrange equations

$$\begin{aligned}
0=\frac{d}{d\epsilon}\mathcal{W}_{\mathrm{C}}^{\mathrm{TOT}}(\boldsymbol{u}+\epsilon\delta\boldsymbol{v},\boldsymbol{\lambda},\lambda_n)\bigg|_{\epsilon=0}&=\int_{\Omega}\boldsymbol{P}(\boldsymbol{F}(\boldsymbol{u})):\nabla_{\boldsymbol{X}}(\delta\boldsymbol{v})+\\
&-\int_{\Omega}\boldsymbol{f}\cdot\delta\boldsymbol{v}-\int_{\partial\Omega_{\mathrm{N}}}\boldsymbol{T}_{\mathrm{N}}\cdot\delta\boldsymbol{v}+\\
&+\int_{\partial\Omega_{\mathrm{D_L}}}\boldsymbol{\lambda}\cdot\delta\boldsymbol{v}+\\
&+\int_{\partial\Omega_{\mathrm{C}}}\lambda_n\,\overline{\boldsymbol{n}}_1(\boldsymbol{X}_2+\boldsymbol{u})\cdot\delta\boldsymbol{v},
\end{aligned} \tag{6.12a}$$

$$0=\frac{d}{d\epsilon}\mathcal{W}_{\mathrm{C}}^{\mathrm{TOT}}(\boldsymbol{u},\boldsymbol{\lambda}+\epsilon\delta\boldsymbol{\lambda},\lambda_n)\bigg|_{\epsilon=0}=\int_{\partial\Omega_{\mathrm{D_L}}}\delta\boldsymbol{\lambda}\cdot(\boldsymbol{u}-\boldsymbol{u}_{\mathrm{D}}), \tag{6.12b}$$

$$0=\frac{d}{d\epsilon}\mathcal{W}_{\mathrm{C}}^{\mathrm{TOT}}(\boldsymbol{u},\boldsymbol{\lambda},\lambda_n+\epsilon\delta\lambda_n)\bigg|_{\epsilon=0}=\int_{\partial\Omega_{\mathrm{C}}}\delta\lambda_n\,g_n(\boldsymbol{X}_2+\boldsymbol{u}), \tag{6.12c}$$

for all virtual displacements $\delta\boldsymbol{v}$ that satisfy a homogeneous Dirichlet condition on $\partial\Omega_{\mathrm{D}}$ and the non-penetration condition on Ω_{C}^{+} and for all $\delta\boldsymbol{\lambda}$ and $\delta\lambda_n$.

6.4 HDG method for contact mechanics

This section is dedicated to the use of the HDG method to discretize the contact problem introduced in the previous section. In what follows, starting from the system of equations (6.12), the residual and the Jacobian operator of the Lagrangian equation of motion are derived.

Keeping in mind the the mesh setting of the HDG method introduced in Sec. 3.2.2, an additional subset of the set of element faces $\mathcal{F}_\mathrm{T}$ is required to specialize the formulations including the surface integral terms on the contact interface $\partial\Omega_{h,\mathrm{C}}$. Accordingly, we define $\mathcal{F}_\mathrm{T}^\mathrm{C} = \{\mathrm{F} \in \mathcal{F}_\mathrm{T} : \mathrm{F} \subset \partial\Omega_{h,\mathrm{C}}\}$ as the set of active faces. For future use, we also define $v_{\partial\mathrm{T}_\mathrm{C}} = (v_\mathrm{F})_{\mathrm{F}\in\mathcal{F}_\mathrm{T}^\mathrm{C}}$ with $v_{\partial\mathrm{T}_\mathrm{C}} \in \mathcal{P}^k(\mathcal{F}_\mathrm{T}^\mathrm{C}) = \mathop{\times}_{\mathrm{F}\in\mathcal{F}_\mathrm{T}^\mathrm{C}} \mathcal{P}^k(\mathrm{F})$.

Firstly, we introduce the local residual $r_\mathrm{T}^{\mathrm{HDG,Lem}}((\boldsymbol{u}_\mathrm{T},\, \boldsymbol{u}_{\partial\mathrm{T}}, \widehat{\boldsymbol{\lambda}}_{\partial\mathrm{T}_\mathrm{L}}, (\widehat{\lambda}_n)_{\partial\mathrm{T}_\mathrm{C}}), \bullet) : \boldsymbol{U}_\mathrm{T}^k \to \mathbb{R}$ of the Lagrangian equation of motion:

$$\begin{aligned}
&r_\mathrm{T}^{\mathrm{HDG,Lem}}\Big((\boldsymbol{u}_\mathrm{T},\, \boldsymbol{u}_{\partial\mathrm{T}}, \widehat{\boldsymbol{\lambda}}_{\partial\mathrm{T}_\mathrm{L}}, (\widehat{\lambda}_n)_{\partial\mathrm{T}_\mathrm{C}}); (\boldsymbol{v}_\mathrm{T},\, \boldsymbol{v}_{\partial\mathrm{T}})\Big) = \\
&= \int_\mathrm{T} \boldsymbol{P}(\mathscr{F}_\mathrm{T}^k(\boldsymbol{u}_\mathrm{T},\, \boldsymbol{u}_{\partial\mathrm{T}})) : \mathscr{G}_\mathrm{T}^k(\boldsymbol{v}_\mathrm{T},\, \boldsymbol{v}_{\partial\mathrm{T}}) + \\
&+ \int_{\partial\mathrm{T}} \xi\, \widetilde{\mathfrak{s}}_{\partial\mathrm{T}}^k(\boldsymbol{u}_\mathrm{T},\, \boldsymbol{u}_{\partial\mathrm{T}}) \cdot \widetilde{\mathfrak{s}}_{\partial\mathrm{T}}^k(\boldsymbol{v}_\mathrm{T},\, \boldsymbol{v}_{\partial\mathrm{T}}) + \\
&- \int_\mathrm{T} \boldsymbol{f} \cdot \boldsymbol{v}_\mathrm{T} - \sum_{\mathrm{F}\in\mathcal{F}_\mathrm{T}^\mathrm{N}} \int_\mathrm{F} \boldsymbol{T}_\mathrm{N} \cdot \boldsymbol{v}_\mathrm{F} + \\
&- \sum_{\mathrm{F}\in\mathcal{F}_\mathrm{T}^{\mathrm{D_L}}} \int_\mathrm{F} \widehat{\boldsymbol{\lambda}}_\mathrm{F} \cdot \boldsymbol{v}_\mathrm{F} + \sum_{\mathrm{F}\in\mathcal{F}_\mathrm{T}^\mathrm{C}} \int_\mathrm{F} \widehat{\lambda}_n\, \overline{\boldsymbol{n}}_1(\boldsymbol{X}_2 + \boldsymbol{u}_\mathrm{F}) \cdot \boldsymbol{v}_\mathrm{F}
\end{aligned} \tag{6.13}$$

so that a comparison with (3.18) shows the addition of the last term in order to take into account the non-penetration boundary condition.

Secondly, we define the local residual $r_\mathrm{F}^{\mathrm{HDG,C}}(\boldsymbol{u}_\mathrm{F}; \bullet) : \mathcal{P}^k(\mathrm{F}) \to \mathbb{R}$ of Lagrange Multiplier constraint as follows

$$r_\mathrm{F}^{\mathrm{HDG,C}}(\boldsymbol{u}_\mathrm{F}; \widehat{s}_\mathrm{F}) \coloneqq \int_\mathrm{F} \widehat{s}_\mathrm{F}\, g_n(\boldsymbol{X}_2 + \boldsymbol{u}_\mathrm{F}). \tag{6.14}$$

The global residuals $r_h^{\mathrm{HDG,Lem}}((\boldsymbol{u}_{\mathcal{T}_h},\, \boldsymbol{u}_{\mathcal{F}_h}, \widehat{\boldsymbol{\lambda}}_{\mathcal{F}_h^{\mathrm{D_L}}}, (\widehat{\lambda}_n)_{\mathcal{F}_h^\mathrm{C}}); \bullet) : \boldsymbol{U}_h^k \to \mathbb{R}$ obtained assembling *element-by-element* the local residual (6.13) is

$$\begin{aligned}
&r_h^{\mathrm{HDG,Lem}}\Big((\boldsymbol{u}_{\mathcal{T}_h},\, \boldsymbol{u}_{\mathcal{F}_h}, \widehat{\boldsymbol{\lambda}}_{\mathcal{F}_h^{\mathrm{D_L}}}, (\widehat{\lambda}_n)_{\mathcal{F}_h^\mathrm{C}}); (\boldsymbol{v}_{\mathcal{T}_h},\, \boldsymbol{v}_{\mathcal{F}_h})\Big) \coloneqq \\
&\coloneqq \sum_{\mathrm{T}\in\mathcal{T}_h} r_\mathrm{T}^{\mathrm{HDG,Lem}}\Big((\boldsymbol{u}_{\mathcal{T}_h|\mathrm{T}},\, \boldsymbol{u}_{\mathcal{F}_h|\partial\mathrm{T}}, \widehat{\boldsymbol{\lambda}}_{\mathcal{F}_h^{\mathrm{D_L}}|\partial\mathrm{T}_\mathrm{L}}, (\widehat{\lambda}_n)_{\mathcal{F}_h^\mathrm{C}|\partial\mathrm{T}_\mathrm{C}}); (\boldsymbol{v}_{\mathcal{T}_h|\mathrm{T}},\, \boldsymbol{v}_{\mathcal{F}_h|\partial\mathrm{T}})\Big).
\end{aligned} \tag{6.15}$$

Then, the global residual $r_h^{\mathrm{HDG,C}}\left(\boldsymbol{u}_{\mathcal{F}_h};\bullet\right):\mathcal{P}^k(\mathcal{F}_h^{\mathrm{C}})\to\mathbb{R}$ is obtained assembling *face-by-face* the local residual (6.14), *i.e.*

$$r_h^{\mathrm{HDG,C}}\left(\boldsymbol{u}_{\mathcal{F}_h};\widehat{s}_{\mathcal{F}_h^{\mathrm{C}}}\right)\coloneqq\sum_{\mathrm{F}\in\mathcal{F}_h^{\mathrm{C}}} r_{\mathrm{F}}^{\mathrm{HDG,C}}\left(\boldsymbol{u}_{\mathcal{F}_h|\mathrm{F}};\widehat{s}_{\mathcal{F}_h^{\mathrm{HDG,C}}|\mathrm{F}}\right). \tag{6.16}$$

Defining, for the sake of brevity, the global HDG space

$$\boldsymbol{W}_{\mathrm{ce},h}^{\mathrm{HDG},k}=\boldsymbol{U}_h^{k,\mathrm{D_S}}\times\mathcal{P}^k(\mathcal{F}_h^{\mathrm{D_L}})^d\times\mathcal{P}^k(\mathcal{F}_h^{\mathrm{C}}),$$

the HDG discretization of the nonlinear elasticity problem with compressible constitutive laws and the non-penetration condition on the contact surface is obtained summing up the global residuals (6.15) and (6.16), and reads as find the unknowns $(\boldsymbol{u}_{\mathcal{T}_h},\,\boldsymbol{u}_{\mathcal{F}_h},\widehat{\boldsymbol{\lambda}}_{\mathcal{F}_h^{\mathrm{D_L}}},(\widehat{\lambda}_n)_{\mathcal{F}_h^{\mathrm{C}}})\in\boldsymbol{W}_{\mathrm{ce},h}^{\mathrm{HDG},k}$ such that for all $(\boldsymbol{v}_{\mathcal{T}_h},\,\boldsymbol{v}_{\mathcal{F}_h},\widehat{\boldsymbol{s}}_{\mathcal{F}_h^{\mathrm{D_L}}},\widehat{s}_{\mathcal{F}_h^{\mathrm{C}}})\in\boldsymbol{W}_{\mathrm{ce},h}^{\mathrm{HDG},k}$

$$r_{\mathrm{ce},h}^{\mathrm{HDG,C}}\left((\boldsymbol{u}_{\mathcal{T}_h},\,\boldsymbol{u}_{\mathcal{F}_h},\widehat{\boldsymbol{\lambda}}_{\mathcal{F}_h^{\mathrm{D_L}}},(\widehat{\lambda}_n)_{\mathcal{F}_h^{\mathrm{C}}});(\boldsymbol{v}_{\mathcal{T}_h},\,\boldsymbol{v}_{\mathcal{F}_h},\widehat{\boldsymbol{s}}_{\mathcal{F}_h^{\mathrm{D_L}}},\widehat{s}_{\mathcal{F}_h^{\mathrm{C}}})\right)=0 \tag{6.17}$$

where the residual $r_{\mathrm{ce},h}^{\mathrm{HDG,C}}\left((\boldsymbol{u}_{\mathcal{T}_h},\,\boldsymbol{u}_{\mathcal{F}_h},\widehat{\boldsymbol{\lambda}}_{\mathcal{F}_h^{\mathrm{D_L}}},(\widehat{\lambda}_n)_{\mathcal{F}_h^{\mathrm{C}}});\bullet\right):\boldsymbol{W}_{\mathrm{ce},h}^{\mathrm{HDG},k}\to\mathbb{R}$ is such that for all $(\boldsymbol{v}_{\mathcal{T}_h},\,\boldsymbol{v}_{\mathcal{F}_h},\widehat{\boldsymbol{s}}_{\mathcal{F}_h^{\mathrm{D_L}}},\widehat{s}_{\mathcal{F}_h^{\mathrm{C}}})\in\boldsymbol{W}_{\mathrm{ce},h}^{\mathrm{HDG},k}$,

$$\begin{aligned}&r_{\mathrm{ce},h}^{\mathrm{HDG,C}}\left((\boldsymbol{u}_{\mathcal{T}_h},\,\boldsymbol{u}_{\mathcal{F}_h},\widehat{\boldsymbol{\lambda}}_{\mathcal{F}_h^{\mathrm{D_L}}},(\widehat{\lambda}_n)_{\mathcal{F}_h^{\mathrm{C}}});(\boldsymbol{v}_{\mathcal{T}_h},\,\boldsymbol{v}_{\mathcal{F}_h},\widehat{\boldsymbol{s}}_{\mathcal{F}_h^{\mathrm{D_L}}},\widehat{s}_{\mathcal{F}_h^{\mathrm{C}}})\right)=\\&=r_h^{\mathrm{HDG,Lem}}\left((\boldsymbol{u}_{\mathcal{T}_h},\,\boldsymbol{u}_{\mathcal{F}_h},\widehat{\boldsymbol{\lambda}}_{\mathcal{F}_h^{\mathrm{D_L}}},(\widehat{\lambda}_n)_{\mathcal{F}_h^{\mathrm{C}}});(\boldsymbol{v}_{\mathcal{T}_h},\,\boldsymbol{v}_{\mathcal{F}_h})\right)+\\&+r_h^{\mathrm{HDG,D_L}}\left(\boldsymbol{u}_{\mathcal{F}_h};\widehat{\boldsymbol{s}}_{\mathcal{F}_h^{\mathrm{D_L}}}\right)+r_h^{\mathrm{HDG,C}}\left(\boldsymbol{u}_{\mathcal{F}_h};\widehat{s}_{\mathcal{F}_h^{\mathrm{C}}}\right).\end{aligned} \tag{6.18}$$

Eq. (6.17) can be rewritten in the form $r_h(\boldsymbol{w}_h;\boldsymbol{z}_h)=0$ (see Eq. (3.33)) introducing, for the sake of notation, $\boldsymbol{w}_h=(\boldsymbol{u}_{\mathcal{T}_h},\,\boldsymbol{u}_{\mathcal{F}_h},\widehat{\boldsymbol{\lambda}}_{\mathcal{F}_h^{\mathrm{D_L}}},(\widehat{\lambda}_n)_{\mathcal{F}_h^{\mathrm{C}}})\in\boldsymbol{W}_{\mathrm{ce},h}^{\mathrm{HDG},k}$ and $\boldsymbol{z}_h=(\boldsymbol{v}_{\mathcal{T}_h},\,\boldsymbol{v}_{\mathcal{F}_h},\widehat{\boldsymbol{s}}_{\mathcal{F}_h^{\mathrm{D_L}}},\widehat{s}_{\mathcal{F}_h^{\mathrm{C}}})\in\boldsymbol{W}_{\mathrm{ce},h}^{\mathrm{HDG},k}$. Thus, the solution of the nonlinear elasticity problem may be retrieved using the incremental method developed in Sec. 3.6. The latter requires the computation of the Jacobian operator for the linearization of the nonlinear elastic problem. So, first of all, we need to compute the directional derivatives of the local residuals (6.13) and (6.14) with the same procedure presented for dG methods in Sec. 3.6.1.

Accordingly, we get the Jacobian operator

$$
\begin{aligned}
&\left(\boldsymbol{J}^{\mathrm{HDG,C}}_{\mathrm{ce},h}(\boldsymbol{w}_h)\delta\boldsymbol{w}_h,\boldsymbol{z}_h\right)_{L^2(\Omega)} = \\
&= \sum_{\mathrm{T}\in\mathcal{T}_h}\left(\int_{\mathrm{T}}\left[\boldsymbol{\mathscr{G}}^k_T(\delta\boldsymbol{u}_{\mathcal{T}_h|\mathrm{T}},\,\delta\boldsymbol{u}_{\mathcal{F}_h|\partial\mathrm{T}}):\mathbb{A}(\boldsymbol{\mathscr{F}}^k_{\mathrm{T}}(\boldsymbol{u}_{\mathcal{T}_h|\mathrm{T}}),0)\right]:\boldsymbol{\mathscr{G}}^k_T(\boldsymbol{v}_{\mathcal{T}_h|\mathrm{T}},\,\boldsymbol{v}_{\mathcal{F}_h|\partial\mathrm{T}})+\right.\\
&\left.+\int_{\partial\mathrm{T}}\xi\,\widetilde{\boldsymbol{\mathfrak{s}}}^k_{\partial\mathrm{T}}(\delta\boldsymbol{u}_{\mathcal{T}_h|\mathrm{T}},\,\delta\boldsymbol{u}_{\mathcal{F}_h|\partial\mathrm{T}})\cdot\widetilde{\boldsymbol{\mathfrak{s}}}^k_{\partial\mathrm{T}}(\boldsymbol{v}_{\mathcal{T}_h|\mathrm{T}},\,\boldsymbol{v}_{\mathcal{F}_h|\partial\mathrm{T}})\right)+\\
&+\sum_{\mathrm{F}\in\mathcal{F}_h^{\mathrm{D_L}}}\left(-\int_{\mathrm{F}}\delta\widehat{\boldsymbol{\lambda}}_{\mathcal{F}_h^{\mathrm{D_L}}|\mathrm{F}}\cdot\boldsymbol{v}_{\mathcal{F}_h|\mathrm{F}}+\int_{\mathrm{F}}\delta\boldsymbol{u}_{\mathcal{F}_h|\mathrm{F}}\cdot\widehat{\boldsymbol{s}}_{\mathcal{F}_h^{\mathrm{D_L}}|\mathrm{F}}\right)+ \qquad (6.19)\\
&+\sum_{\mathrm{F}\in\mathcal{F}_h^{\mathrm{C}}}\left(\int_{\mathrm{F}}(\lambda_n)_{\mathcal{F}_h^{\mathrm{C}}|\mathrm{F}}\left(\boldsymbol{H}_{g_n}(\boldsymbol{X}+\boldsymbol{u}_{\mathcal{F}_h|\mathrm{F}})\,\delta\boldsymbol{u}_{\mathcal{F}_h|\mathrm{F}}\right)\cdot\boldsymbol{v}_{\mathcal{F}_h|\mathrm{F}}+\right.\\
&\left.+\int_{\mathrm{F}}\widehat{s}_{\mathcal{F}_h^{\mathrm{C}}|\mathrm{F}}\,\overline{\boldsymbol{n}}_1(\boldsymbol{X}+\boldsymbol{u}_{\mathcal{F}_h|\mathrm{F}})\cdot\delta\boldsymbol{u}_{\mathcal{F}_h|\mathrm{F}}+\int_{\mathrm{F}}\delta\lambda_{\mathcal{F}_h^{\mathrm{C}}|\mathrm{F}}\,\overline{\boldsymbol{n}}_1(\boldsymbol{X}_2+\boldsymbol{u}_{\mathcal{F}_h|\mathrm{F}})\cdot\boldsymbol{v}_{\mathcal{F}_h|\mathrm{F}}\right).
\end{aligned}
$$

where $\boldsymbol{H}_{g_n}$ is the Hessian matrix of the normal gap g_n related to the curvature of the boundary surface $\partial\Omega_1$ which is defined as

$$
\boldsymbol{H}_{\bullet}(\boldsymbol{x}) = \begin{bmatrix} \frac{\partial^2\bullet}{\partial x^2} & \frac{\partial^2\bullet}{\partial x\partial y} & \frac{\partial^2\bullet}{\partial x\partial z} \\ \frac{\partial^2\bullet}{\partial y\partial x} & \frac{\partial^2\bullet}{\partial y^2} & \frac{\partial^2\bullet}{\partial y\partial z} \\ \frac{\partial^2\bullet}{\partial z\partial x} & \frac{\partial^2\bullet}{\partial z\partial y} & \frac{\partial^2\bullet}{\partial z^2} \end{bmatrix}. \qquad (6.20)
$$

6.5 Active set strategy

In this section, we present the strategy aimed at identifying and following the evolution of the contact surface $\partial\Omega_{\mathrm{C}}$ all along the body deformation. A brief overview of the main available contact discretization methods within the Finite Element Method is presented in [79].

The incremental method introduced in Sec. 3.6 for computing the equilibrium of elastic bodies undergoing finite deformations has to be modified, in fact, only after the surface $\partial\Omega_{\mathrm{C}}$ has been identified, we are able to apply the Newton's method for the solution of (6.5). To this end, the incremental method is currently equipped with an *active set strategy* encompassing contact with a rigid body. The *active set* is the region of the boundary surfaces, namely a sub-set of boundary faces, where the contact boundary conditions are "active". A suitable search strategy is required to identify the active set.

Initialized at the beginning of the computation (possibly as the empty set), the active set $\mathcal{F}_h^{\mathrm{C}}$ is repeatedly updated along the deformation history as described in what follows:

1. defining $\mathcal{F}_h^b$ the the set collecting all boundary faces, a face $\mathrm{F} \in \mathcal{F}_h^b \setminus \mathcal{F}_h^{\mathrm{C}}$ is included in the active set if the average value of the gap functions over it is zero or negative;
2. a face $\mathrm{F} \in \mathcal{F}_h^{\mathrm{C}}$ is excluded from the active set if the average pressure over it is zero or positive.

Clearly, the first active set update condition ensures non-penetration while the second avoids the onset of adhesion forces.

The modified incremental method with the active set strategy is summarized in the Alg. 6.1 which is used in the numerical results presented in Sec. 7.1 and Sec. 7.2.

```
for $i = 1 \rightarrow N$ do                                                   // Incremental method
    Set the initial guess $\boldsymbol{w}_h^i = \boldsymbol{w}_h^{i-1}$;
    do                                                                       // Active set strategy
        while $\delta \boldsymbol{w}_h$ is too large do                       // Newton method
            find $\delta \boldsymbol{w}_h \in \boldsymbol{W}_{\mathrm{ce},h}^{\mathrm{HDG},k}$ such that:
                $\left(\boldsymbol{J}_{\mathrm{ce},h}^{\mathrm{HDG,C}}(\boldsymbol{w}_h^i)\delta \boldsymbol{w}_h, \boldsymbol{z}_h\right)_{L^2(\Omega)} = -\tilde{r}_{\mathrm{ce},h}^{\mathrm{HDG,C},i}(\boldsymbol{w}_h^i; \boldsymbol{z}_h), \quad \forall \boldsymbol{z}_h \in \boldsymbol{W}_{\mathrm{ce},h}^{\mathrm{HDG},k};$
            set $\boldsymbol{w}_h^i \mathrel{+}= \delta \boldsymbol{w}_h$;
        end
        Compute $\widehat{\mathcal{F}_h^{\mathrm{C}}} = \left\{\mathrm{F} \in \mathcal{F}_h^b \setminus \mathcal{F}_h^{\mathrm{C}} : \int_{\mathrm{F}} g_n \leq 0\right\}$;
        Compute $\widetilde{\mathcal{F}_h^{\mathrm{C}}} = \left\{\mathrm{F} \in \mathcal{F}_h^{\mathrm{C}} : \int_{\mathrm{F}} \lambda_n \geq 0\right\}$;
        Set $\mathcal{F}_h^{\mathrm{C}} = \mathcal{F}_h^{\mathrm{C}} \cup \widehat{\mathcal{F}_h^{\mathrm{C}}}$;
        Set $\mathcal{F}_h^{\mathrm{C}} = \mathcal{F}_h^{\mathrm{C}} \setminus \widetilde{\mathcal{F}_h^{\mathrm{C}}}$;
    while $\widehat{\mathcal{F}_h^{\mathrm{C}}} = \widetilde{\mathcal{F}_h^{\mathrm{C}}} = \emptyset$;
end
```

Algorithm 6.1: The incremental method of Sec. 3.6 equipped with an active set strategy to solve nonlinear elasticity problems at large deformation and with the normal contact constraints of non-penetration.

In the inner loop, Newton's method (see Alg. 3.1) is employed to solve an incremental step where the active set is kept fixed despite the gap function may change due to deformation. Upon Newton convergence, the active set is updated. If any boundary face has been added or removed from the active set, the inner loop is repeated, as opposite, if the contact interface is unchanged, the solution is accepted and the iteration may proceed to the next incremental step. Due to the intrinsically dynamic nature of the active set cardinality along the deformation history, the problem size (that is the number of degrees of freedom) and, accordingly, the data structures holding the Jacobian and residual operators of the HDG formulation, need to be updated concurrently with the contact interface.

In order to identify the active set, for each face $\mathrm{F} \in \partial\Omega_{2,h}$, the distance from the obstacle Ω_1 has to be computed. If the normal gap function g_n is smaller or equal to zero along the face, the latter is inserted in the active set. In particular, $g_n < 0$ indicates that the bodies penetrate. From the computational viewpoint, we rely on the following procedure: if the integral $\int_{\mathrm{F}} g_n$ of the normal gap on the face F is equal or lower than a certain tolerance (we set 10^{-10}), that face belongs to $\mathcal{F}_h^{\mathrm{C}}$. Clearly, this requires to solve the minimum distance problem (6.2) at each quadrature point of the face. Since we consider obstacles whose surface admits an analytical description, also g_n is an analytical function.

Chapter 7. Numerical Validation of Hybridizable Discontinuous Galerkin Formulations for Hyperelastic Deformations and Frictionless Contact Constraints

This chapter deals with numerical validation of HDG method introduced in Sec. 3.4 are investigated in this chapter and its application to real life computations in the hypothesis of frictionless contact constraints.

Two and three dimensional nonlinear elasticity problems featuring frictionless contact with rigid obstacles are solved demonstrating the effectiveness of the active set strategy introduced in Sec. 6.5. As described in the previous chapter, contact with rigid obstacles is modelled by introducing a non-penetration boundary condition enforced with Lagrange Multipliers. Thanks to the analytical description of the obstacle surface (see Sec. 7.1.1, Sec. 7.1.2, Sec. 7.2.1 and Sec. 7.2.2), the expressions of the normal gap function g_n, of the normal vector $\overline{\boldsymbol{n}}_1$ and of the Hessian matrix $\boldsymbol{H}_{g_n}$ are easily derived.

The material is organized as follows. *Two dimensional computations* are collected in Sec. 7.1: the impact of a square body against a horizontal obstacle is presented in Sec. 7.1.3 while a semicircle that comes in contact with a horizontal and a circular obstacles is depicted in Sec. 7.1.4. *Three dimensional computations* are considered in Sec. 7.2: the relative motion between a thin square membrane and a spherical obstacle is portrayed in Sec. 7.2.3 and the blowing of a preform constrained in a cylindrical mould is the topic of Sec. 7.2.4.

7.1 2D computational contact mechanics computations

We first consider a horizontal planar obstacle and a circular obstacle. Expressions for the normal gap, the normal vector and the Hessian matrix are provided in Sec. 7.1.1 and Sec. 7.1.2, respectively, according to equation Eqs. (6.10) and (6.20). In the following examples, let $\boldsymbol{x}_2 = \{x_2, y_2\}$ be a point of the 2D Euclidean space located on the boundary surface of a deforming body Ω_2.

7.1.1 Horizontal planar obstacle

Consider a planar two dimensional obstacle whose top surface is modelled as the horizontal line $y = y_0$. The normal gap function is given as

$$g_n(\boldsymbol{x}_2) = y_2 - y_0.$$

This obstacle splits the 2D space in two parts. If the obstacle occupies the region of the space below the horizontal line $y = y_0$, the normal vector is

$$\overline{\boldsymbol{n}}_1 = (0, 1),$$

namely a vector pointing upwards. Being the normal constant in the space, the Hessian matrix is the null matrix.

7.1.2 Circular obstacle

We assume that the curved surface of the obstacle is modelled by the equation of a circumference with radius R and centre at $\boldsymbol{x}_0 = (x_0, y_0)$. The circumference divides the space in two regions and the obstacle occupies the circle.

The distance between the point $\boldsymbol{x}_2$ and $\boldsymbol{x}_0$ reads

$$d_{2\mathrm{D}}(\boldsymbol{x}_2) = \sqrt{(x_2 - x_0)^2 + (y_2 - y_0)^2}.$$

Accordingly, the normal gap function is defined as

$$g_n(\boldsymbol{x}_2) = d_{2\mathrm{D}}(\boldsymbol{x}_2) - R.$$

Computing the gradient of g_n respect to $\boldsymbol{x}_2$, we obtain the normal vector

$$\overline{\boldsymbol{n}}_1(\boldsymbol{x}_2) = \left(\frac{x_2 - x_0}{d_{2\mathrm{D}}}, \frac{y_2 - y_0}{d_{2\mathrm{D}}} \right). \tag{7.1}$$

Finally, the Hessian matrix is computed according to Eq. (7.1), yielding

$$\boldsymbol{H}_{g_n}(\boldsymbol{x}_2) = \begin{bmatrix} -\frac{(x_2-x_0)^2}{d_{2\mathrm{D}}^3} + \frac{1}{d_{2\mathrm{D}}} & -\frac{(x_2-x_0)(y_2-y_0)}{d_{2\mathrm{D}}^3} \\ -\frac{(x_2-x_0)(y_2-y_0)}{d_{2\mathrm{D}}^3} & -\frac{(y_2-y_0)^2}{d_{2\mathrm{D}}^3} + \frac{1}{d_{2\mathrm{D}}} \end{bmatrix}.$$

7.1.3 Square body against a horizontal planar obstacle

Consider a unit-length square computational domain $\Omega_2 : [0, 1]^2$ consisting of 512 triangular elements. A NHK-C material model with $\mu = 0.4$, $\lambda = 0.4$ and $\Theta = \ln(J)$ describes the behaviour of the body. The horizontal planar obstacle of Sec. 7.1.1 is put in place at $y_0 = -1$.

Dirichlet boundary conditions are enforced on the top surface of the domain so that, in the final configuration, the top surface of the body is modelled by the horizontal line $y = -0.3$. The lateral surfaces are stress free while the bottom surface is stress free until contact occurs. The square translates undeformed until the bottom surface gets in touch with the obstacle. Thus, the computational domain squeezes in the vertical direction. The evolution of von Mises stress distribution is depicted in Fig. 23. Results are obtained employing a first degree HDG discretization. This simulation is performed considering 100 incremental steps and setting the stabilization parameter as $\xi = 30$.

The aim of this test case is to check the active set strategy implementation. After contact, and all along the loading path, all the bottom boundary faces are stably identified as part of the active set. The normal contact reaction forces avoid the body to penetrate the obstacle while the tangential motion are frictionless.

7.1.4 Semicircular body against a planar and a circular obstacle

We consider a semicircular body of radius $r = 1$, centred at point $(0, 0)$ and discretized using 782 triangular elements. $\mu = 0.4$, $\lambda = 0.4$ and $\Theta = \ln(J)$ are the material parameters for the NHK-C model employed in these test cases. Two different obstacles are considered: a horizontal planar obstacle (see Sec. 7.1.1) with $y_0 = -2$ and a circular obstacle (see Sec. 7.1.2) with $\boldsymbol{x}_0 = (0, -3)$ and $R = 1$.

Dirichlet boundary conditions are enforced on the planar surface of the domain so that, in the final configuration, the top surface is modelled by the horizontal line $y = -1.5$, while the curved surface of the body is stress-free until contact. Figs. 24 and 25 depict two sequences of frames captured during the loading path. Simulation are performed with 60 and 100 incremental steps and with the stabilization parameters $\xi = 80$ and $\xi = 60$, respectively, for the planar and the curved obstacle.

These two test cases demonstrate that our active set strategy is able to deal with evolving contact surfaces. In fact, the number of faces included in the active set grows as the deforming body adapts to the obstacle shape. Furthermore, the normal vector associated to a point sliding over the circular obstacle changes due to the curvature of the geometry.

7.2 3D computational contact mechanics computations

We consider a spherical obstacle and a cylindrical contact surface. Expressions for the normal gap function, the normal vector and the Hessian matrix are provided in Sec. 7.2.1 and Sec. 7.2.2, respectively, according to equations Eqs. (6.10) and (6.20). In the following, let $\boldsymbol{x}_2 = \{x_2, y_2, z_2\}$ be a point of the 3D Euclidean space located on the boundary surface of a deforming body Ω_2.

7.2.1 Spherical obstacle

We assumed that the obstacle is described by the equation of a sphere with the radius R and centre at point $\boldsymbol{x}_0 = (x_0, y_0, z_0)$. As for the circumference, the sphere divides the space in two regions. In this work, the obstacle occupies the sphere.

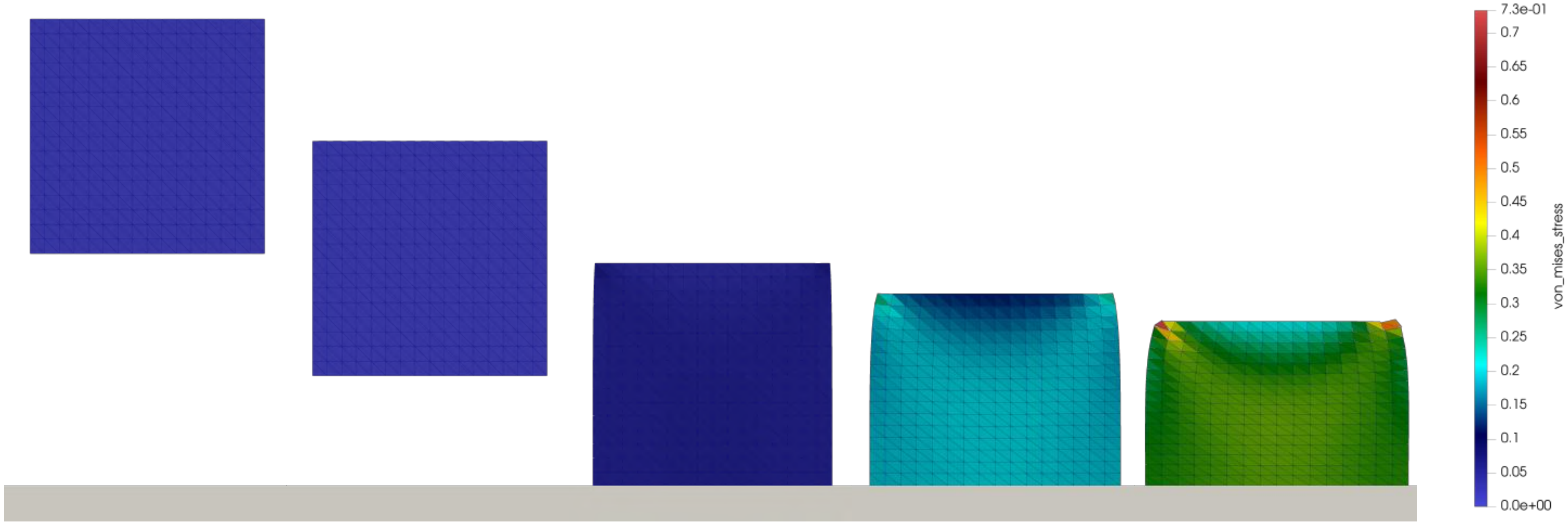

Figure 23: A square NHK-C body impacts against a horizontal planar obstacle. On the top surface, a vertical displacement is imposed while the normal contact conditions are simulated using the Lagrange Multiplier method. Colours represent the von Mises stress distribution obtained with a first degree HDG discretization.

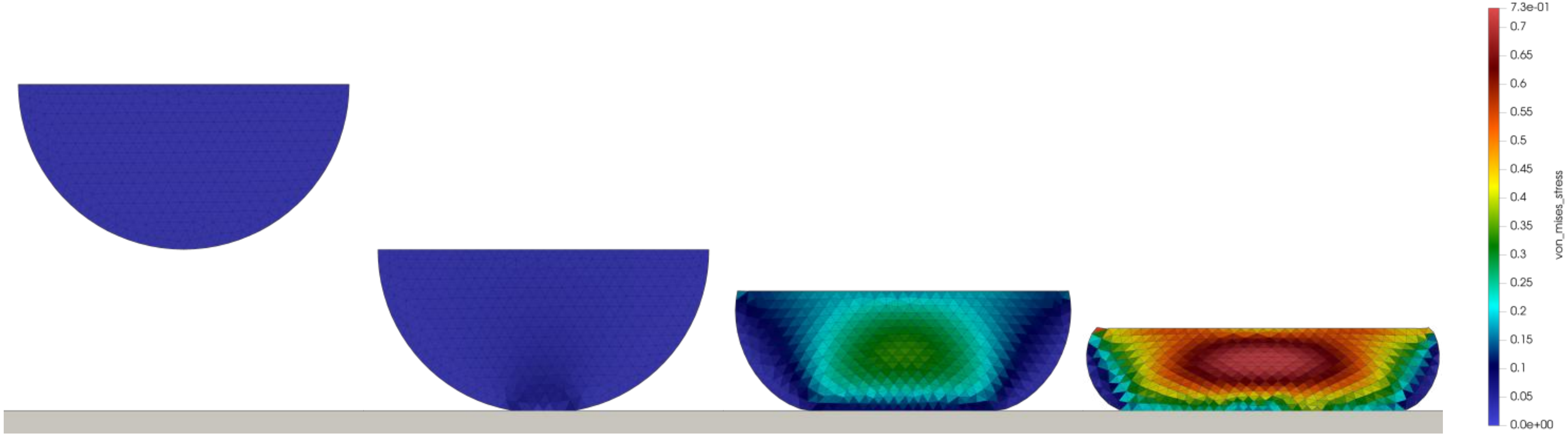

Figure 24: A semi-circle NHK-C body impacts against a horizontal planar obstacle. On the top surface, a vertical displacement is imposed while the normal contact conditions are simulated using the Lagrange Multiplier method. Colours represent the von Mises stress distribution obtained with a first degree HDG discretization.

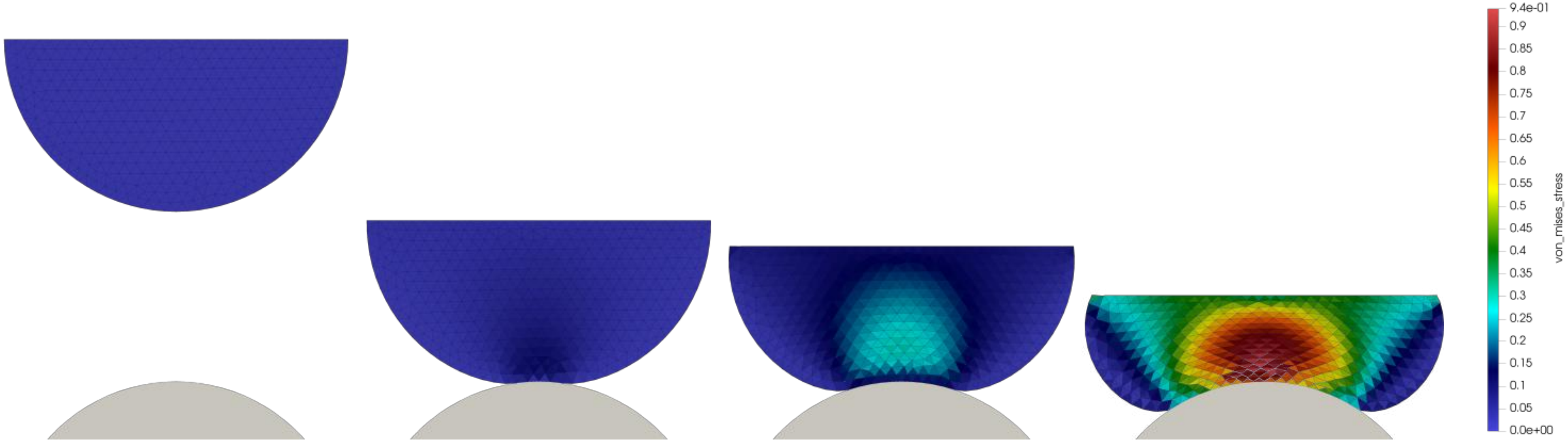

Figure 25: A semi-circle NHK-C body impacts against a circular obstacle.On the top surface, a vertical displacement is imposed while the normal contact conditions are simulated using the Lagrange Multiplier method. Colours represent the von Mises stress distribution obtained with a first degree HDG discretization.

The distance between $\boldsymbol{x}_2$ and $\boldsymbol{x}_0$ reads

$$d_{3\mathrm{D}}(\boldsymbol{x}_2) = \sqrt{(x_2 - x_0)^2 + (y_2 - y_0)^2 + (z_2 - z_0)^2}.$$

Accordingly, the normal gap function is such that

$$g_n(\boldsymbol{x}_2) = d_{3\mathrm{D}}(\boldsymbol{x}_2) - R.$$

Computing the gradient of g_n respect to $\boldsymbol{x}_2$, we obtain the normal vector

$$\overline{\boldsymbol{n}}_1(\boldsymbol{x}_2) = \left(\frac{x_2 - x_0}{d_{3\mathrm{D}}}, \frac{y_2 - y_0}{d_{3\mathrm{D}}}, \frac{z_2 - z_0}{d_{3\mathrm{D}}} \right). \tag{7.2}$$

Finally, the Hessian matrix is computed according to Eq. (7.2), yielding

$$\boldsymbol{H}_{g_n}(\boldsymbol{x}_2) = \begin{bmatrix} -\frac{(x_2-x_0)^2}{d_{3\mathrm{D}}^3} + \frac{1}{d_{3\mathrm{D}}} & -\frac{(x_2-x_0)(y_2-y_0)}{d_{3\mathrm{D}}^3} & -\frac{(x_2-x_0)(z_2-z_0)}{d_{3\mathrm{D}}^3} \\ -\frac{(x_2-x_0)(y_2-y_0)}{d_{3\mathrm{D}}^3} & -\frac{(y_2-y_0)^2}{d_{3\mathrm{D}}^3} + \frac{1}{d_{3\mathrm{D}}} & -\frac{(y_2-y_0)(z_2-z_0)}{d_{3\mathrm{D}}^3} \\ -\frac{(x_2-x_0)(z_2-z_0)}{d_{3\mathrm{D}}^3} & -\frac{(y_2-y_0)(z_2-z_0)}{d_{3\mathrm{D}}^3} & -\frac{(z_2-z_0)^2}{d_{3\mathrm{D}}^3} + \frac{1}{d_{3\mathrm{D}}} \end{bmatrix}.$$

7.2.2 Cylindrical cavity

Let R and H be, respectively, the radius and the axial extension of a cylinder. We assume that the cylinder represents a closed cavity acting as a mould. Sharp corners forms where the top and bottom circular surfaces cap the lateral curved surface of the cylinder. Accordingly, we need a strategy to define uniquely the normal gap function at each point of the cavity.

We assume that axis of the cylinder is the vertical line $x = x_0$ and the point $\boldsymbol{x}_0$ is located at the intersection between the axis and the bottom surface.

The radial distance between the point $\boldsymbol{x}_2$ and the axis of the cylinder is

$$d_R(\boldsymbol{x}_2) = \left| R - \sqrt{(x_2 - x_0)^2 + (z_2 - z_0)^2} \right|.$$

The distances between the point $\boldsymbol{x}_2$ and the two planar surfaces of the cylinder are

$$d_A^-(\boldsymbol{x}_2) = y_2 - y_0, \qquad d_A^+(\boldsymbol{x}_2) = y_2 - (y_0 + H).$$

Moreover, the minimum axial distance is defined as follows

$$d_A(\boldsymbol{x}_2) = \min\left(|d_A^-(\boldsymbol{x}_2)|, |d_A^+(\boldsymbol{x}_2)| \right).$$

The normal gap function is defined as

$$g_n(\boldsymbol{x}_2) = \tilde{s}\ \min\Big(d_R(\boldsymbol{x}_2), d_A(\boldsymbol{x}_2)\Big)$$

where $\tilde{s} = 1$ if the point $\boldsymbol{x}_2$ is inside the cylinder and $\tilde{s} = -1$ otherwise. The normal vector reads:

$$\overline{\boldsymbol{n}}_1(\boldsymbol{x}_2) = \begin{cases} \left(-\frac{x_2-x_0}{d_R}, 0, -\frac{z_2-z_0}{d_R}\right) & \text{if } d_R \leq d_A, \\ (0,-1,0) & \text{if } d_R > d_A \text{ and } d_A^- > d_A^+, \\ (0,1,0) & \text{if } d_R > d_A \text{ and } d_A^- < d_A^+. \end{cases}$$

Finally, the Hessian matrix is

$$\boldsymbol{H}_{g_n}(\boldsymbol{x}_2) = \begin{bmatrix} \frac{(x_2-x_0)^2}{d_R^3} - \frac{1}{d_{2\text{D}}} & 0 & \frac{(x_2-x_0)(z_2-z_0)}{d_R^3} \\ 0 & 0 & 0 \\ \frac{(x_2-x_0)(z_2-z_0)}{d_R^3} & 0 & \frac{(z_2-z_0)^2}{d_R^3} - \frac{1}{d_R} \end{bmatrix}$$

if $d_R \leq d_A$, or the null matrix if $d_R > d_A$.

7.2.3 Spherical obstacle against a thin membrane

This test case considers a spherical obstacle of radius $R = 0.3$ centered at point $\boldsymbol{x}_0 = (0.5, -0.5, 0.5)$ impacting on a thin hyperelastic membrane $\Omega_2 : [0,1] \times [0, 1 \cdot 10^{-2}] \times [0,1]$. The computational domain $\Omega_{2,h}$ consists of $30 \times 3 \times 30 = 2700$ uniform hexahedral elements. The behaviour of the deforming membrane is described by the means of a NHK-C constitutive law with the material parameters $\mu = 0.4$, $\lambda = 0.4$ and $\Theta = \ln(J)$.

The relative motion between the hyperelastic membrane and the spherical obstacle is obtained imposing Dirichlet boundary conditions on the four thin lateral surfaces of the membrane while the two top and bottom square surfaces are stress-free. The displacements is prescribed setting $\boldsymbol{u}_\text{D} = (0, -1, 0)$.

The incremental method counts 200 loading steps and the stabilization parameter is $\xi = 10$. Some frames captured along the loading path are depicted in Fig. 28.

The simulation is performed using first, second and third order HDG discretizations: the comparison among the final solutions with increasing polynomial order is reported in Fig. 26. The improved quality of the solution in terms of geometry approximation and von Mises stress distribution is clearly noticeable.

Fig. 27 reports the evolution of the active set along the loading path after that the contact occurs. Faces

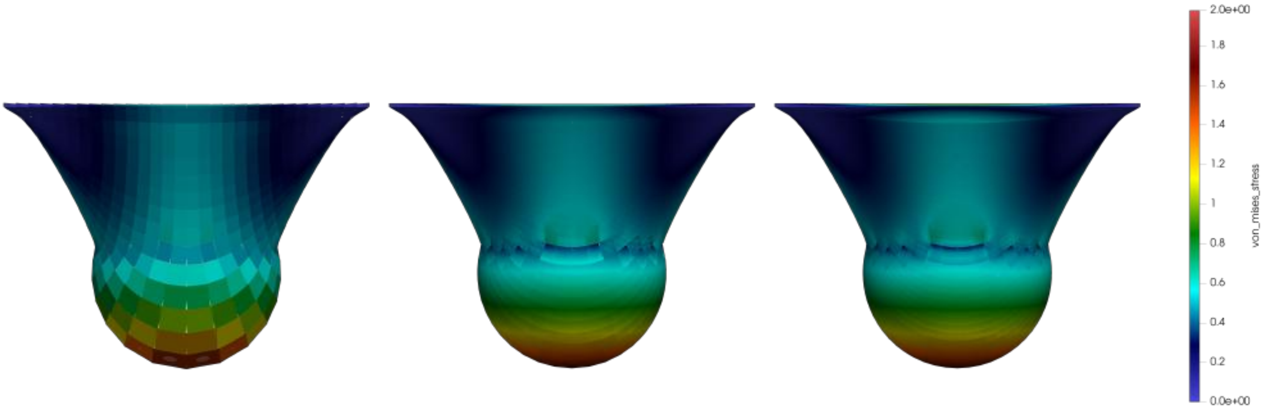

(a) $k = 1$ **(b)** $k = 2$ **(c)** $k = 3$

Figure 26: Final solutions, for different polynomial orders ($k = \{1, 2, 3\}$), of a NHK-C thin membrane deformed by a spherical obstacle. Colours represent the von Mises stress distribution obtained with increasing the polynomial order of the HDG discretization.

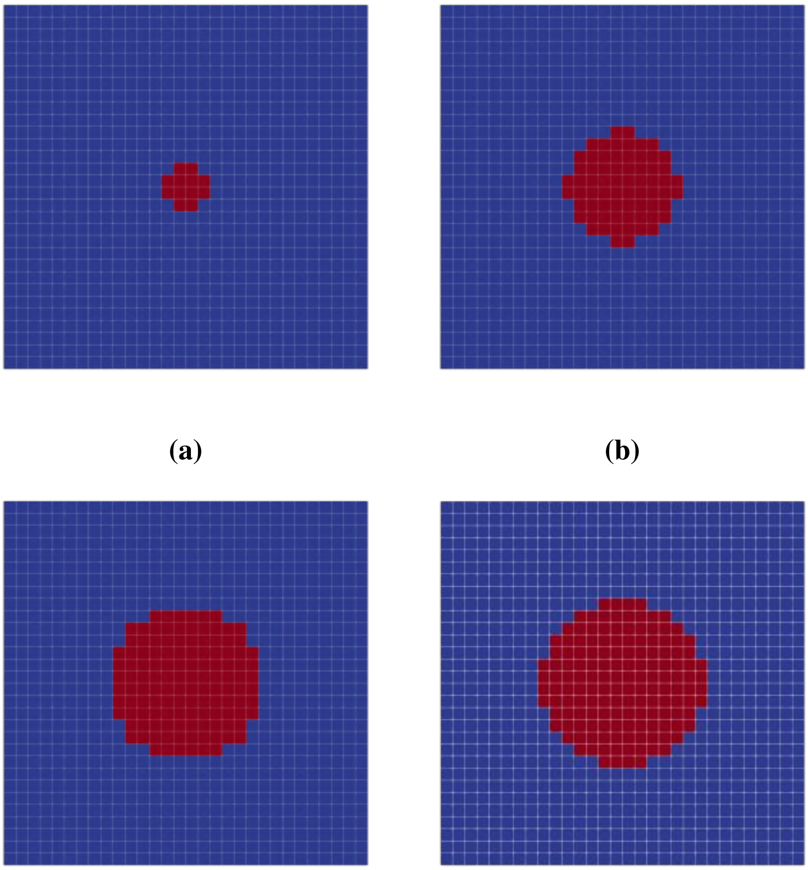

(a) **(b)**

(c) **(d)**

Figure 27: Evolution of the active set during the deformation of a NHK-C thin membrane impacting on a spherical obstacle. The active set consists of those faces highlighted in red.

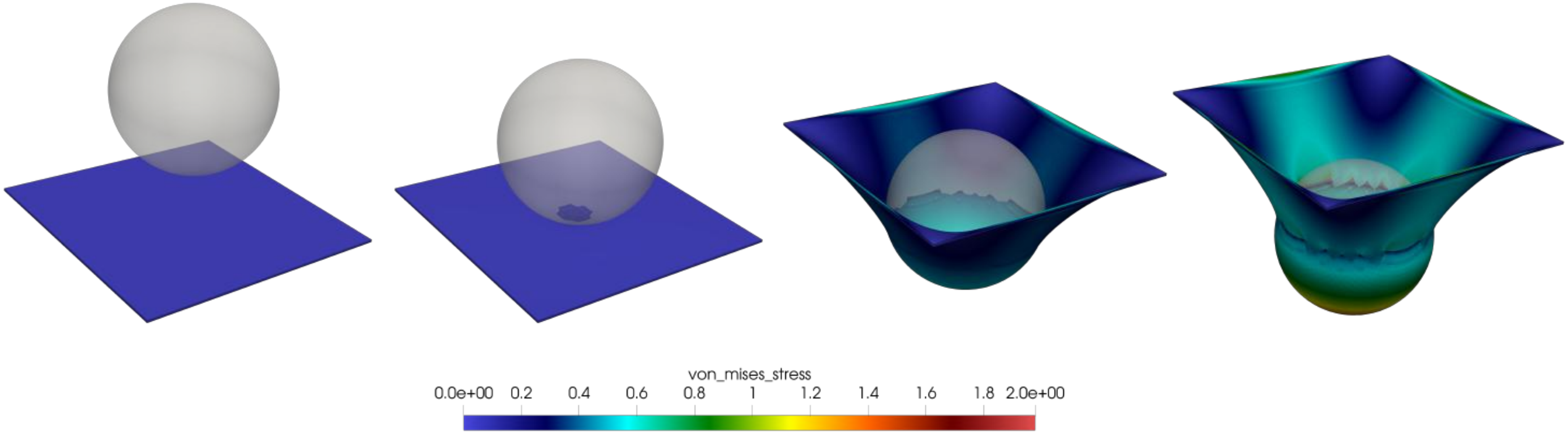

Figure 28: A spherical obstacle impacts on a NHK-C thin membrane. Relative motion is obtained through Dirichlet boundary condition while the the non-penetration constraint is rendered using the Lagrange Multiplier method. Colours represent the von Mises stress distribution obtained with a third degree HDG discretization.

highlighted in red are part of the active set, namely, the region that is considered to be in contact with the spherical obstacle. It is worth mentioning that the boundary of the active set is not a regular curve because it follows the sharp edges of square mesh faces.

An adaptive mesh refinement strategy may help to better approximate the contact surface. In particular, by splitting a face in sub-faces, the algorithm may be able to identify those sub-faces that are in contact with the obstacle. Nonconforming methods may handle this situation in a very efficient way without strongly affecting the condition number of the global matrix. Specifically, the elements whose faces have been refined can be simply be considered as general polytopes with increasingly high number of sub-faces.

7.2.4 Blowing preform in a cylindrical cavity

We consider the three dimensional preform whose geometry is described in Fig. 29.

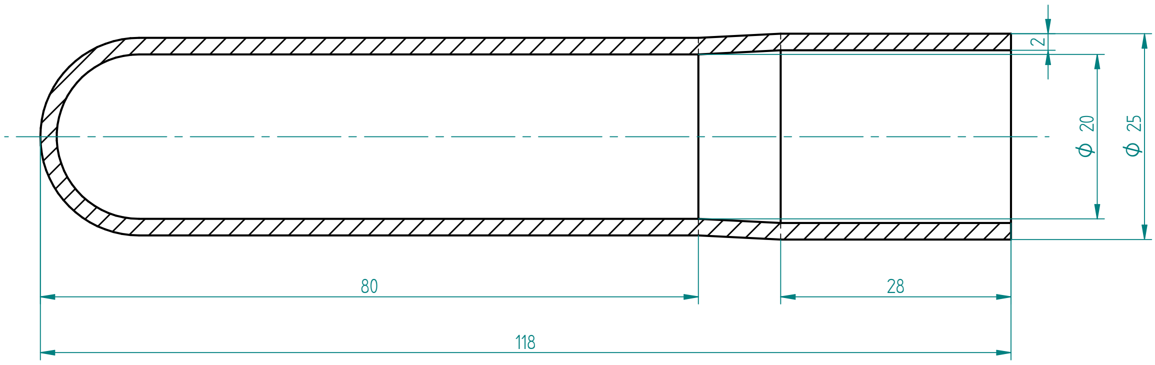

Figure 29: Preform geometry.

The computational domain is discretized with 16441 tetrahedral elements and we employ NHK-C constitutive law with the material parameters $\mu = 0.4$, $\lambda = 0.4$ and $\Theta = \ln(J)$. The preform is constrained with null displacement Dirichlet boundary condition on the top circular surface of the computational domain boundary. In order to emulate the effects of pressurized air that pushes the polymer against the internal cavity of the mould, we used a simplified Neumann boundary condition such that $\boldsymbol{T}_{\mathrm{N}} = p\,\boldsymbol{N}$ where $p = 0.54$ and $\boldsymbol{N}$ is the normal in the reference configuration. Implementation of the so-called *live load* (see [4]), namely a load that depends on the current deformation of the body will be subject of future works.

Focusing on the contact detection strategy, Fig. 30 shows a simplified blow moulding simulation realized with a second-order HDG discretization, 270 incremental steps and the stabilization parameter $\xi = 50$.

The preform comes in contact with a cylindrical cavity, (see Sec. 7.2.4) where the parameters $\boldsymbol{x}_0 = (0, 0, 0)$, $R = 38.5$ and $H = 201$ are used to described the geometry. Fig. 31 depicts some details of the final results compared with the reference configuration while Fig. 32 reports the evolution of the active set during the contact simulation. Results similar to those in Fig. 31 may reveal to be attractive in the analysis of blow moulding manufacturing processes.

7.3 Conclusions

The HDG framework has been extended to encompass CCM problems. In particular, non-penetration contact constraints are imposed by means of the CCM. The analytical description of obstacles surfaces is rendered through the normal gap functions, the normal vectors and the Hessian matrices, here reported for simple test cases. The contact detection procedure, presented in Chap. 6, proves to be effective not only in the case of simple two dimensional contact surfaces (*e.g.* horizontal obstacles) but also in the case of three dimensional curved surfaces (*e.g.* spherical obstacles). Further investigation are planned to develop a more generic active set strategy, distance computation techniques and surface description.

As demonstrated, in Sec. 7.2.4, the HDG method combined with the active set strategy have the potential of tackling real-life application. In fact, the simplified blow moulding simulation retains some of the critical challenges such as thin walls and highly stretched mesh elements in contact with the mould. It is interesting to remark that the HDG framework here proposed manages to deal with blow moulding computation without requiring further simplifying assumptions (*e.g.* shell elements, typically employed in this context).

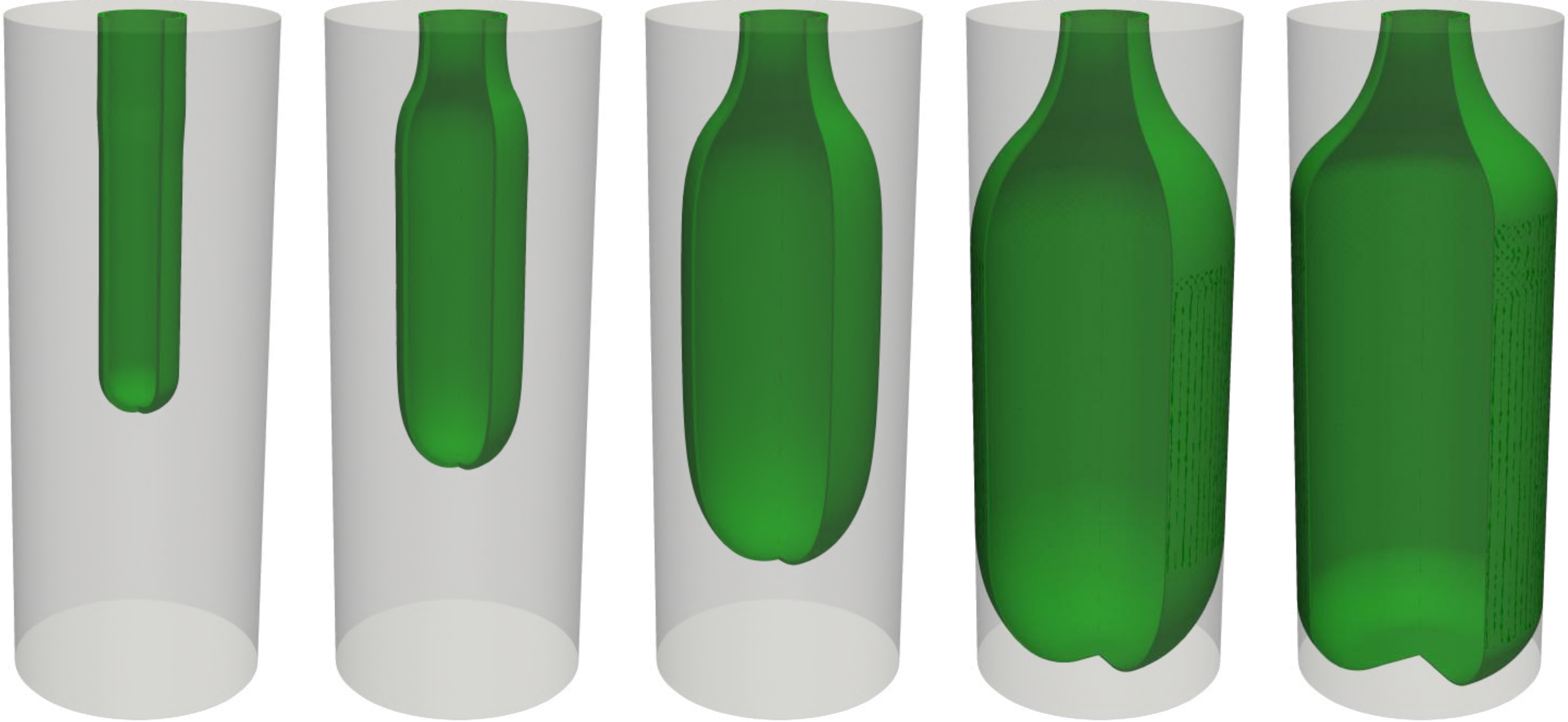

Figure 30: Sequence of frames captured during the deformation of a NHK-C preform modelled in a cylindrical cavity.

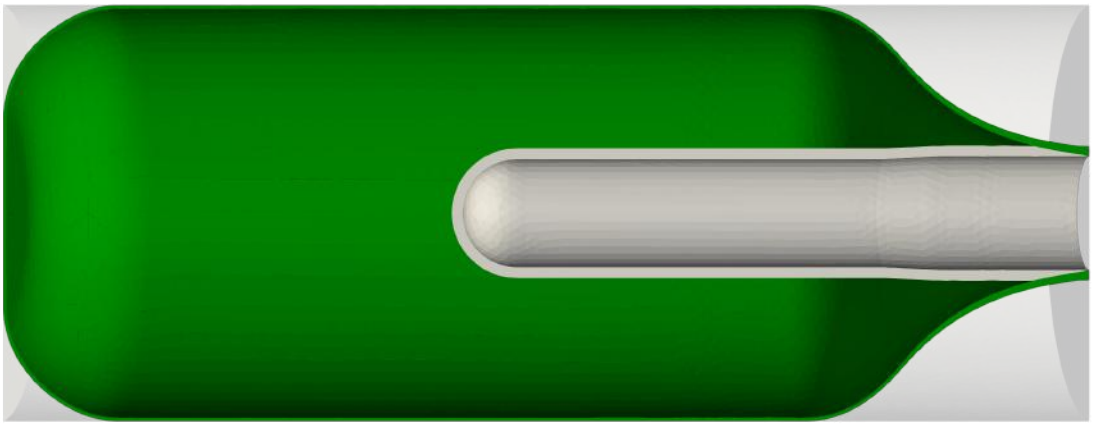

Figure 31: Section of the reference and the deformed configurations of the blowing preform modelled in a cylindrical cavity.

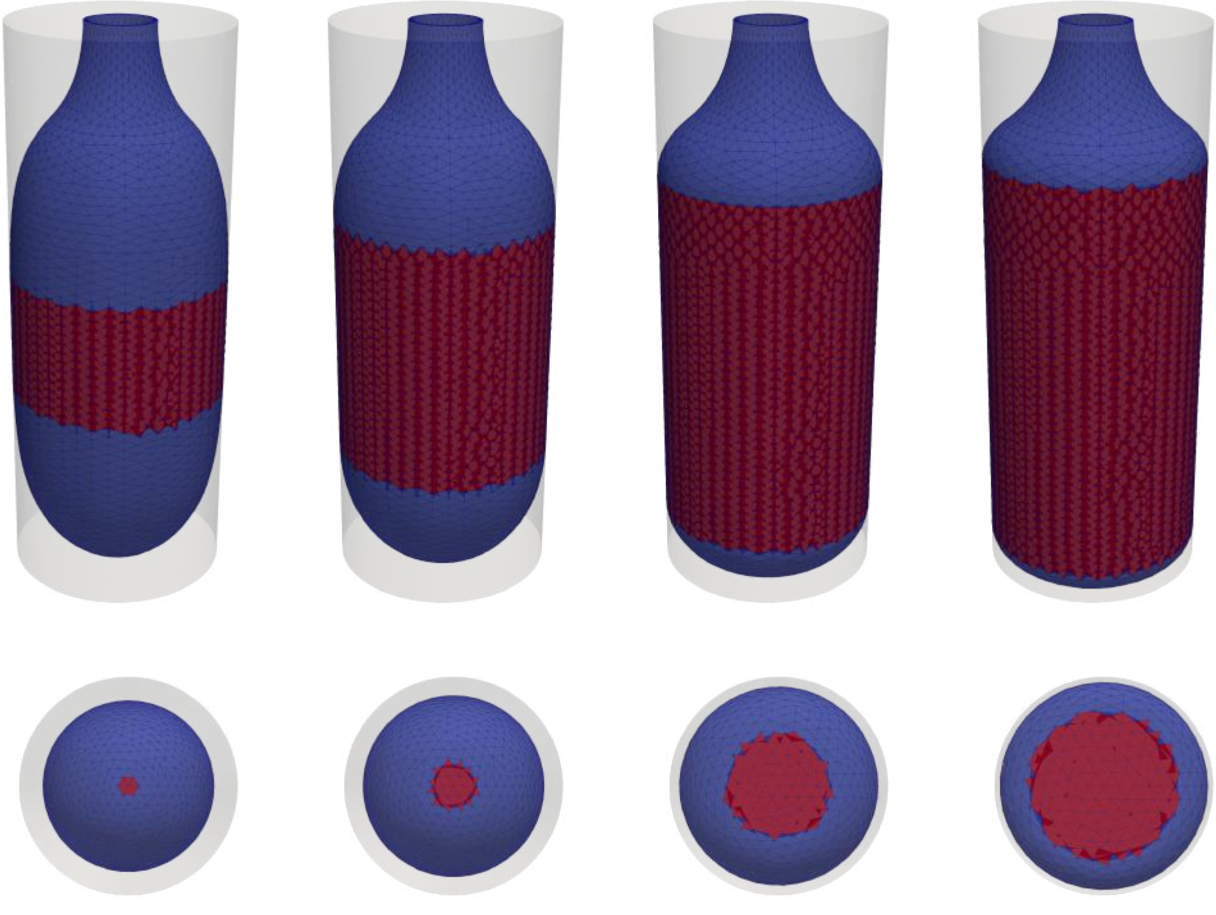

Figure 32: Evolution of the active set during the deformation of a NHK-C preform modelled in a cylindrical cavity. The active set consists of those faces highlighted in red.

Chapter 8. Final Remarks and Future Developments

In this brief chapter, we collect the final remarks and propose some future developments.

8.1 Conclusions

Based on the Lagrangian formulation of the equations of motion, three nonconforming discretizations of the nonlinear elasticity problem were implemented and tested. Neumann traction and Dirichlet displacement boundary conditions can be imposed and, in particular, the latter can be enforced by means of the Lagrange multipliers method. The BR2 dG formulation relies on broken polynomial spaces defined over mesh elements, while HDG and HHO formulations rely on broken polynomial spaces defined over mesh elements and mesh faces. Nonconforming space discretizations are introduced by defining suitable local gradient reconstruction operators and using the discrete gradient in place of the continuous gradient in the expression of the Piola-Kirchhoff stress tensor for Saint Venant-Kirchhoff and neo-Hookean materials. Stabilization terms are thus introduced in order to ensure coercivity of the formulations.

For the dG formulation, thanks to the introduction of higher-order lifting operators in the gradient reconstruction, two stabilization parameters are required: 1. coercivity is ensured by adaptively changing the amount of inter-element displacement jump penalization according to the spectrum of the fourth-order elasticity tensor; 2. inf-sup stability is provided by penalizing the jump of Lagrange multipliers on the internal edges of Dirichlet boundary surfaces. HDG and HHO formulations do not require additional penalty terms for the jumps of Lagrange multipliers on Dirichlet boundaries. For HDG and sHHO coercivity is achieved by penalizing the jumps between the trace of the elements displacements and the elements face displacements. Penalty coefficients are considered as user-defined parameters even though the scientific literature provides some guidelines for an adaptive stabilization strategy in case of HDG. The uHHO formulation is stabilization parameters free in case on small deformations thanks to a higher polynomial degree gradient reconstruction.

Extensive numerical validation of the three nonconforming formulations implementations is provided by verifying that theoretical convergence rates are achieved when considering 2D and 3D manufactured solutions in the compressible and, possibly, in the incompressible material regime. The L^2-norm of the errors on the displacement, the displacement gradient and the pressure are computed over h-refined mesh sequence and the resulting h-convergence rates are tabulated. Thanks to higher-order jump stabilization residuals, sHHO achieves one order higher convergence rates for the displacement error in L^2-norm with respect to dG, HDG, and uHHO when considering smooth analytical solutions.

Further investigations were performed applying the nonconforming formulations to 2D and 3D real-life test cases featuring finite deformations. In this context, the elasticity problem in Lagrangian formulation presents two different sources of nonlinearity: one is related to the material constitutive law and the other one is related to the geometrical transformation that maps the unloaded reference body configuration into the deformed body configuration. The static equilibrium is reached by means of an incremental load method, which is required to globalise Newton's method convergence in case of large deformations. Accordingly, the final deformed state is achieved through a sequence of intermediate equilibrium states obtained by gradually increasing the external solicitations up to the desired loading.

Thanks to the availability of efficient and flexible agglomeration-based multigrid solution strategies, a dG framework for compressible and incompressible hyperelastic materials is introduced based on the BR2 dG formulation. A fully implicit formulation for the Lagrangian equation of motion coupled with the incompressibility constraint is devised. The possibility to impose Dirichlet displacement boundary conditions by means of Lagrange multipliers is investigated and significant improvements in terms of robustness of the incremental load method are achieved using Lagrange multipliers BCs in place of Nitsche method BCs. In particular, the number of incremental steps can be reduced by orders of magnitude keeping the solution accuracy unaltered. The parabolic indentation, the cavitating voids and the torsion of a square-section bar showed the robustness of the method with respect to severe mesh distortion. The adaptive stabilization strategy proved to be effective in challenging 2D beam and hollow cylinder deformations, without requiring fine tuning of the user-dependent stabilization coefficient. In fact, the number of iterations of the agglomeration based h-multigrid preconditioned GMRES solver strategy are marginally affected by changing the stabilization coefficient.

Thanks to the increased flexibility of imposing BCs by means of the Lagrange multipliers method, an HDG framework for compressible and quasi-incompressible hyperelastic materials featuring non-penetration contact constraints is investigated. Despite the worst convergence properties, HDG is preferred to HHO because of the increased robustness demonstrated in real-life computations featuring large deformations. In particular, HDG ensures stability for wider ranges of stabilization parameter values, thereby avoiding the cumbersome trial-and-error approach. Moreover, the implementation of the adaptive stabilization strategy proposed in literature will be the subject of future work. Mimicking the Dirichlet boundary conditions approach, the Lagrange multiplier method is employed for enforcing non-penetration contact boundary conditions and an active set strategy is implemented to identify and follow the contact area all along the deformation history. The HDG framework is validated through 2D and 3D test cases tackling the impact of deformable bodies (such as a square, a semi circle and a membrane) against different rigid obstacles admitting an analytical geometrical description. The HDG framework is also applied to perform simplified blow-moulding computations: in particular, a preform is blown against a cylindrical surface emulating the mould. Those results demonstrated that the HDG method is able to handle domains with thin walls and highly stretched mesh elements in contact with the mould.

8.2 Future Developments

The robustness with respect to mesh distortion, the possibility to work with arbitrarily unstructured polytopal meshes, the ability to locally increase the solution accuracy by adjusting the polynomial degree and the availability of locking-free formulations encouraged us to use nonconforming numerical methods for Computational Solid Mechanics. Started from scratch in the context of the SpaFEDTe library, a templated C++ library for creating Discontinuous Finite Element Spaces developed by Lorenzo Botti for academic purposes, our present implementations require some further developments.

In order to apply the dG framework to nonlinear elasticity problems featuring contact constraints, implementation of suitable active set strategy for contact detection is mandatory. In fact, the strategy has to be able to identify and track the sharp corners of the domain boundary coming in contact with an obstacle in order to suitably penalize the Lagrange multipliers jumps.

Concerning the HDG and the HHO methods, adaptive stabilization strategies ought to be investigated. Up to now, the penalization parameter is is kept constant over the entire computational domain and manually adjusted with a trial and error approach in order to provide stability. In view of using an iterative solver for the solution of the linearised equations systems, it is fundamental to set the right amount of stabilization because unnecessarily high values may significantly increase the number of iterations.

Both the dG and HDG framework require improvements from the solution strategy viewpoint. As mentioned in Chap. 4, the solution of the saddle-point problem resulting from the imposition of BCs by means of Lagrange multipliers is performed with a direct solver. The latter resulted to be computationally inefficient when considering finer meshes and higher polynomial degree discretizations. The introduction of an agglomeration based h-multigrid preconditioner showed impressive improvements in terms of solution strategy efficiency when using the dG framework in combination with Nitsche method to impose Dirichlet boundary conditions. Our goal is to extend this methodology to cope with Lagrange multiplier BCs bearing in mind that the agglomeration strategy can not be easily applied to agglomerate boundary faces where the Lagrange multipliers live. Accordingly, a p-multigrid preconditioner may be applied on face unknowns and combined with the h-multigrid solution strategy for element unknowns. Similarly, the implementation of h-multigrid solution strategies for HDG and HHO discretizations is an open field of research.

In this work we considered only hyperelastic materials, nevertheless viscosity and plasticity are two of the main aspects that need to be taken into account in order to describe real material behaviours. Motivated by the results on the simplified blow moulding simulations of Chap. 7, we claim that the nonconforming dG and HDG frameworks are capable of dealing with elasto-visco-plastic computations. Indeed, the current results present more severe stress distributions with respect to those expected in realistic applications.

In order to tackle realistic blow moulding computations additional developments are required. In addition to frinctionless contact, tangential contact kinematics needs to be introduced. Analytical descriptions of obstacle surfaces is not possible when dealing with complex mould shapes, accordingly, a strategy able to manage the obstacle geometries based on their CAD representations is required.

No thermal effects were considered during this work, the thermal distributions and heat exchanges will help to enhance the simulation accuracy rendering the changes of the material properties due to temperature variations.

Further research efforts will consider the possibility to utilize the proposed nonconforming implementations within an unified high-order accurate framework for fluid-structure interaction where nonconforming methods are employed either for computational fluid-dynamics or solid mechanics.

Lists of Figures and Tables

List of Figures

List of Tables

Bibliography

References

[1] Hardik Kabaria, Adrian J. Lew, and Bernardo Cockburn. A hybridizable discontinuous Galerkin formulation for non-linear elasticity. *Computer Methods in Applied Mechanics and Engineering*, 283:303–329, jan 2015.

[2] Mickaël Abbas, Alexandre Ern, and Nicolas Pignet. Hybrid High-Order methods for finite deformations of hyperelastic materials. *Computational Mechanics*, 62(4):909–928, oct 2018.

[3] R.W. Ogden. *Non-linear elastic deformation*. Dover Publications, Inc., 1984.

[4] Philippe G. Ciarlet. *Mathematical Elasticity*. North-Holland, 1988.

[5] Morton E. Gurtin, Eliot Fried, and Lallit Anand. *The Mechanics and Thermodynamics of Continua*. Cambridge University Press, 2009.

[6] Ellad B. Tadmor, Ronald E. Miller, and Ryan S. Elliott. *Continuum Mechanics and Thermodynamics*, volume 9781107008. Cambridge University Press, Cambridge, 2011.

[7] Robert M. Hackett. *Hyperelasticity Primer*. Springer International Publishing, Cham, 2018.

[8] U. Brink and E. Stein. On some mixed finite element methods for incompressible and nearly incompressible finite elasticity. *Computational Mechanics*, 19(1):105–119, nov 1996.

[9] Thomas J. Pence and Kun Gou. On compressible versions of the incompressible neo-Hookean material. *Mathematics and Mechanics of Solids*, 20(2):157–182, 2015.

[10] T. Y.P. Chang, A. F. Saleeb, and G. Li. Large strain analysis of rubber-like materials based on a perturbed Lagrangian variational principle. *Computational Mechanics*, 8(4):221–233, 1991.

[11] A N Gent and P B Lindley. Internal rupture of bonded rubber cylinders in tension. *Proceedings of the Royal Society of London. Series A. Mathematical and Physical Sciences*, 249(1257):195–205, 1959.

[12] Béatrice Rivière and Mary F. Wheeler. Optimal Error Estimates for Discontinuous Galerkin Methods Applied to Linear Elasticity Problems. *Comput. Math. Appl*, 46, 2000.

[13] Peter Hansbo and Mats G. Larson. Discontinuous Galerkin methods for incompressible and nearly incompressible elasticity by Nitsche's method. *Computer Methods in Applied Mechanics and Engineering*, 191(17-18):1895–1908, 2002.

[14] Adrian Lew, Patrizio Neff, Deborah Sulsky, and Michael Ortiz. Optimal BV Estimates for a Discontinuous Galerkin Method for Linear Elasticity. *Applied Mathematics Research eXpress*, 2004(3):73, 2004.

[15] Bernardo Cockburn, Dominik Schötzau, and Jing Wang. Discontinuous Galerkin methods for incompressible elastic materials. *Computer Methods in Applied Mechanics and Engineering*, 195(25-28):3184–3204, may 2006.

[16] Thomas P. Wihler. Locking-free DGFEM for elasticity problems in polygons. *IMA Journal of Numerical Analysis*, 24(1):45–75, 2004.

[17] Thomas P. Wihler. Locking-free adaptive discontinuous Galerkin FEM for linear elasticity problems. *Mathematics of Computation*, 75(255):1087–1103, jan 2006.

[18] Paul Houston, Dominik Schötzau, and Thomas P. Wihler. An hp-adaptive mixed discontinuous Galerkin FEM for nearly incompressible linear elasticity. *Computer Methods in Applied Mechanics and Engineering*, 195(25-28):3224–3246, may 2006.

[19] Fatila Celiker, Bernardo Cockburn, Sukru Güzey, Ramdev Kanapady, Sew-Chew Soon, Henrik K. Stolarski, and Kummar Tamma. Discontinuous Galerkin Methods for Timoshenko Beams. In Miloslav Feistauer, , Vít Dolejší, , Petr Knobloch, , and Karel Najzar, editors, *Numerical Mathematics and Advanced Applications*, pages 221–231. Springer Berlin Heidelberg, Berlin, Heidelberg, 2004.

[20] Fatih Celiker and Bernardo Cockburn. Element-by-Element Post-Processing of Discontinuous Galerkin Methods for Timoshenko Beams. *Journal of Scientific Computing*, 27(1-3):177–187, jun 2006.

[21] S. Güzey, H.K. Stolarski, B. Cockburn, and K.K. Tamma. Design and development of a discontinuous Galerkin method for shells. *Computer Methods in Applied Mechanics and Engineering*, 195(25-28):3528–3548, may 2006.

[22] L. Noels and R. Radovitzky. A new discontinuous Galerkin method for Kirchhoff–Love shells. *Computer Methods in Applied Mechanics and Engineering*, 197(33-40):2901–2929, jun 2008.

[23] Peter Kaufmann, Sebastian Martin, Mario Botsch, and Markus Gross. Flexible simulation of deformable models using discontinuous Galerkin FEM. *Graphical Models*, 71(4):153–167, 2009.

[24] J.K. Djoko, F. Ebobisse, A.T. McBride, and B.D. Reddy. A discontinuous Galerkin formulation for classical and gradient plasticity. Part 2: Algorithms and numerical analysis. *Computer Methods in Applied Mechanics and Engineering*, 197(1-4):1–21, dec 2007.

[25] J. K. Djoko, F. Ebobisse, A. T. McBride, and B. D. Reddy. A discontinuous Galerkin formulation for classical and gradient plasticity - Part 1: Formulation and analysis. *Computer Methods in Applied Mechanics and Engineering*, 196(37-40 SPEC. ISS.):3881–3897, 2007.

[26] L. Noels and R. Radovitzky. A general discontinuous Galerkin method for finite hyperelasticity. Formulation and numerical applications. *International Journal for Numerical Methods in Engineering*, 68(1):64–97, 2006.

[27] A. Ten Eyck and A. Lew. Discontinuous Galerkin methods for non-linear elasticity. *International Journal for Numerical Methods in Engineering*, 67(9):1204–1243, aug 2006.

[28] F. Bassi and S. Rebay. A high-order accurate discontinuous finite element method for the numerical solution of the compressible Navier-Stokes equations. *Journal of Computational Physics*, 131(2):267–279, 1997.

[29] Alex Ten Eyck, Fatih Celiker, and Adrian Lew. Adaptive stabilization of discontinuous Galerkin methods for nonlinear elasticity: Analytical estimates. *Computer Methods in Applied Mechanics and Engineering*, 197(33-40):2989–3000, jun 2008.

[30] Alex Ten Eyck, Fatih Celiker, and Adrian Lew. Adaptive stabilization of discontinuous Galerkin methods for nonlinear elasticity: Motivation, formulation, and numerical examples. *Computer Methods in Applied Mechanics and Engineering*, 197(45-48):3605–3622, 2008.

[31] Jonathan P. Whiteley. Discontinuous Galerkin finite element methods for incompressible non-linear elasticity. *Computer Methods in Applied Mechanics and Engineering*, 198(41-44):3464–3478, sep 2009.

[32] Davide Baroli, Alfio Quarteroni, and Ricardo Ruiz-Baier. Convergence of a stabilized discontinuous Galerkin method for incompressible nonlinear elasticity. *Advances in Computational Mathematics*, 39(2):425–443, aug 2013.

[33] G. Becker and L. Noels. A full-discontinuous Galerkin formulation of nonlinear Kirchhoff-Love shells: elasto-plastic finite deformations, parallel computation, and fracture applications. *International Journal for Numerical Methods in Engineering*, 93(1):80–117, jan 2013.

[34] A.T. McBride and B.D. Reddy. A discontinuous Galerkin formulation of a model of gradient plasticity at finite strains. *Computer Methods in Applied Mechanics and Engineering*, 198(21-26):1805–1820, may 2009.

[35] Ruijie Liu, Mary F. Wheeler, and Ivan Yotov. On the spatial formulation of discontinuous Galerkin methods for finite elastoplasticity. *Computer Methods in Applied Mechanics and Engineering*, 253:219–236, jan 2013.

[36] Miloslav Feistauer, Martin Hadrava, Jaromír Horáček, and Adam Kosík. DGM for the Solution of Nonlinear Dynamic Elasticity. *Lecture Notes in Computational Science and Engineering*, 126:531–540, 2019.

[37] Adam Kosík, Miloslav Feistauer, Martin Hadrava, and Jaromír Horáček. Numerical simulation of the interaction between a nonlinear elastic structure and compressible flow by the discontinuous Galerkin method. *Applied Mathematics and Computation*, 267:382–396, sep 2015.

[38] Bernardo Cockburn, Jayadeep Gopalakrishnan, and Raytcho Lazarov. Unified Hybridization of Discontinuous Galerkin, Mixed, and Continuous Galerkin Methods for Second Order Elliptic Problems. *SIAM Journal on Numerical Analysis*, 47(2):1319–1365, jan 2009.

[39] S.-C. Soon, B. Cockburn, and Henryk K. Stolarski. A hybridizable discontinuous Galerkin method for linear elasticity. *International Journal for Numerical Methods in Engineering*, 80(8):1058–1092, nov 2009.

[40] N. C. Nguyen, J. Peraire, and B. Cockburn. High-order implicit hybridizable discontinuous Galerkin methods for acoustics and elastodynamics. *Journal of Computational Physics*, 230(10):3695–3718, 2011.

[41] N.C. Nguyen and J. Peraire. Hybridizable discontinuous Galerkin methods for partial differential equations in continuum mechanics. *Journal of Computational Physics*, 231(18):5955–5988, jul 2012.

[42] Bernardo Cockburn and Ke Shi. Superconvergent HDG methods for linear elasticity with weakly symmetric stresses. *IMA Journal of Numerical Analysis*, 33(3):747–770, 2013.

[43] Bernardo Cockburn and Jiguang Shen. An algorithm for stabilizing hybridizable discontinuous Galerkin methods for nonlinear elasticity. *Results in Applied Mathematics*, 1:100001, jun 2019.

[44] S. Terrana, N. C. Nguyen, J. Bonet, and J. Peraire. A hybridizable discontinuous Galerkin method for both thin and 3D nonlinear elastic structures. *Computer Methods in Applied Mechanics and Engineering*, 352:561–585, 2019.

[45] Daniele Antonio Di Pietro and Jérôme Droniou. *The Hybrid High-Order Method for Polytopal Meshes*, volume 19 of *MS&A*. Springer International Publishing, Cham, 2020.

[46] Daniele A. Di Pietro and Alexandre Ern. A hybrid high-order locking-free method for linear elasticity on general meshes. *Computer Methods in Applied Mechanics and Engineering*, 283:1–21, jan 2015.

[47] Michele Botti, Daniele A. Di Pietro, and Pierre Sochala. A Hybrid High-Order Method for Nonlinear Elasticity. *SIAM Journal on Numerical Analysis*, 55(6):2687–2717, jan 2017.

[48] Francesco Bonaldi, Daniele A. Di Pietro, Giuseppe Geymonat, and Françoise Krasucki. A Hybrid High-Order method for Kirchhoff-Love plate bending problems. *ESAIM: Mathematical Modelling and Numerical Analysis*, 52(2):393–421, 2018.

[49] Mickaël Abbas, Alexandre Ern, and Nicolas Pignet. A Hybrid High-Order method for incremental associative plasticity with small deformations. *Computer Methods in Applied Mechanics and Engineering*, 346:891–912, apr 2019.

[50] Mickaël Abbas, Alexandre Ern, and Nicolas Pignet. A Hybrid High-Order method for finite elastoplastic deformations within a logarithmic strain framework. *International Journal for Numerical Methods in Engineering*, 120(3):303–327, oct 2019.

[51] Franz Chouly, Alexandre Ern, and Nicolas Pignet. A Hybrid High-Order Discretization Combined with Nitsche's Method for Contact and Tresca Friction in Small Strain Elasticity. *SIAM Journal on Scientific Computing*, 42(4):A2300–A2324, jan 2020.

[52] Michele Botti, Daniele A. Di Pietro, and Pierre Sochala. A Hybrid High-Order Discretization Method for Nonlinear Poroelasticity. *Computational Methods in Applied Mathematics*, 20(2):227–249, apr 2020.

[53] Javier Bonet, Antonio J. Gil, and Richard D. Wood. *Nonlinear Solid Mechanics for Finite Element Analysis: Statics*. Cambridge University Press, Cambridge, 2nd edition, 2016.

[54] Ivo Babuška. The finite element method with Lagrangian multipliers. *Numerische Mathematik*, 20(3):179–192, 1973.

[55] Lorenz John, Michael Neilan, and Iain Smears. Stable Discontinuous Galerkin FEM Without Penalty Parameters. In *Numerical Mathematics and Advanced Applications ENUMATH 2015*, pages 165–173. Springer International Publishing, 2016.

[56] F Brezzi, G Manzini, D Marini, P Pietra, and A Russo. Discontinuous finite elements for diffusion problems, 1999.

[57] Douglas N. Arnold, Franco Brezzi, Bernardo Cockburn, and L. Donatella Marini. Unified Analysis of Discontinuous Galerkin Methods for Elliptic Problems. *SIAM Journal on Numerical Analysis*, 39(5):1749–1779, jan 2002.

[58] Daniele A. Di Pietro. Analysis of a discontinuous Galerkin approximation of the Stokes problem based on an artificial compressibility flux. *International Journal for Numerical Methods in Fluids*, 55(8):793–813, nov 2007.

[59] Mikhail Itskov. On the theory of fourth-order tensors and their applications in computational mechanics. *Computer Methods in Applied Mechanics and Engineering*, 189(2):419–438, sep 2000.

[60] Mikhail Itskov. *Tensor Algebra and Tensor Analysis for Engineers*. Mathematical Engineering. Springer International Publishing, Cham, 5th edition, 2019.

[61] L. Botti, A. Colombo, and F. Bassi. h-multigrid agglomeration based solution strategies for discontinuous Galerkin discretizations of incompressible flow problems. *Journal of Computational Physics*, 347:382–415, 2017.

[62] The Sage Developers. *SageMath, the Sage Mathematics Software System (Version 9.0)*, 2020.

[63] Xianmin Xu and Duvan Henao. An efficient numerical method for cavitation in nonlinear elasticity. *Mathematical Models and Methods in Applied Sciences*, 21(8):1733–1760, 2011.

[64] J. C. Simo and F. Armero. Geometrically non-linear enhanced strain mixed methods and the method of incompatible modes. *International Journal for Numerical Methods in Engineering*, 33(7):1413–1449, may 1992.

[65] Stephan Wulfinghoff, Hamid Reza Bayat, Atefeh Alipour, and Stefanie Reese. A low-order locking-free hybrid discontinuous Galerkin element formulation for large deformations. *Computer Methods in Applied Mechanics and Engineering*, 323:353–372, aug 2017.

[66] Tod A. Laursen. *Computational Contact and Impact Mechanics.* Springer Berlin Heidelberg, Berlin, Heidelberg, 1 edition, 2003.

[67] Peter Wriggers. *Computational Contact Mechanics.* Springer Berlin Heidelberg, Berlin, Heidelberg, 2nd edition, 2006.

[68] J. Haslinger, I. Hlaváček, and J. Nečas. Numerical methods for unilateral problems in solid mechanics. *Handbook of Numerical Analysis*, 4(Part 2):313–485, 1996.

[69] Barbara Wohlmuth. Variationally consistent discretization schemes and numerical algorithms for contact problems. *Acta Numerica*, 20:569–734, 2011.

[70] Alexander Popp. *Mortar Methods for Computational Contact Mechanics and General Interface Problems.* PhD thesis, Technische Universität München, 2012.

[71] J. T. Oden and N. Kikuchi. Finite Element Methods for constrained problems in elasticity. *International Journal for Numerical Methods in Engineering*, 18:701–725, 1982.

[72] N. Kikuchi and J. T. Oden. *Contact Problems in Elasticity.* Society for Industrial and Applied Mathematics, jan 1988.

[73] Roland Glowinski and Patrick Le Tallec. *Augmented Lagrangian and Operator-Splitting Methods in Nonlinear Mechanics.* Society for Industrial and Applied Mathematics, jan 1989.

[74] G. Zavarise and L. De Lorenzis. An augmented Lagrangian algorithm for contact mechanics based on linear regression. *International Journal for Numerical Methods in Engineering*, 91(8):825–842, aug 2012.

[75] Patrick Hild and Yves Renard. A stabilized Lagrange multiplier method for the finite element approximation of contact problems in elastostatics. *Numerische Mathematik*, 115(1):101–129, 2010.

[76] J. Nitsche. Über ein Variationsprinzip zur Lösung von Dirichlet-Problemen bei Verwendung von Teilräumen, die keinen Randbedingungen unterworfen sind. *Abhandlungen aus dem Mathematischen Seminar der Universität Hamburg*, 36(1):9–15, 1971.

[77] Franz Chouly, Mathieu Fabre, Patrick Hild, Rabii Mlika, Jérôme Pousin, and Yves Renard. An Overview of Recent Results on Nitsche's Method for Contact Problems. In *Lecture Notes in Computational Science and Engineering*, volume 121, pages 93–141. Springer, 2017.

[78] Rabii Mlika. *Nitsche method for frictional contact and self-contact: mathematical and numerical study*. PhD thesis, Universite de Lyon, 2018.

[79] L. De Lorenzis, Peter Wriggers, and C. Weißenfels. Computational Contact Mechanics with the Finite Element Method. In *Encyclopedia of Computational Mechanics Second Edition*, pages 1–45. John Wiley & Sons, Ltd, Chichester, UK, dec 2017.